Université de Lille

Ecole doctorale n° 104 : Sciences de la Matière, du Rayonnement et de L'Environnement

Laboratoire Unité Matériaux et Transformation – Matériaux Terrestres et Planétaires

Microstructural evolution of polymineralic aggregates deformed under high pressure and temperature: an in-situ and post-mortem study on olivine+serpentine

Evolution microstructurale d'agrégats polyminéraux déformés sous haute pression et température : une étude in-situ et post-mortem sur le système olivine+serpentine

Thèse préparée et présentée publiquement par

Tommaso Mandolini

Pour obtenir le grade de Docteur en : Milieux denses, matériaux et composants

Soutenue le 18 Novembre 2022 devant le jury composé de :

DR. Jannick Ingrin	Univ. Lille	Président de jury
MCF. Jean-Philippe Perrillat	Univ. Claude Bernard Lyon 1	Rapporteur
Pr. Holger Stunitz	The Artic Univ. Norway	Rapporteur
Pr. Muriel Andreani	Univ. Claude Bernard Lyon 1	Examinatrice
MCF. Catherine Noiriel	Univ. Paul Sabatier Toulouse	Examinatrice
Pr. Sébastien Merkel	Univ. Lille	Directeur de thèse
CR. Nadège Hilairet	Univ. Lille	Co-encadrante

Table of Contents

Résumé

Aux limites des plaques tectoniques, la lithosphère est déformée et la déformation peut se localiser jusqu'à l'échelle kilométrique, avec formation de zones de cisaillement. Cela suggère que la résistance de la lithosphère est localement réduite. La formation de couches interconnectées de minéraux plus faibles mécaniquement est un mécanisme potentiel pour parvenir à un tel affaiblissement dans la lithosphère. Les péridotites serpentinisées sont couramment présentes dans et aux limites de plaques tectoniques. Elles sont principalement composées des minéraux serpentine et d'olivine, la serpentine étant généralement considérée comme étant plus déformable que l'olivine aux taux de déformation géologiques. La déformation devrait donc se distribuer préférentiellement dans la serpentine plutôt que dans l'olivine. Cela peut conduire à la formation de couches faibles interconnectées (IWL, pour « interconnected weak layer » en anglais) de serpentine, où la contrainte se localise.

Ce travail est basé sur l'investigation microstructurale pour comprendre l'accommodation de la déformation dans les roches. Des agrégats d'olivine+serpentine sont utilisés comme proxy pour les péridotites partiellement serpentinisées. Ces agrégats sont déformés en torsion sous haute pression (HP, > 2 GPa) et hautes températures (HT, > 300°C) à un taux de déformation équivalent de 10^{-4} s^{-1}. Les expériences sont couplées avec de la tomographie in-situ par contraste d'absorption de rayons X. J'obtiens des informations microstructurales en 2D et 3D sur la connectivité et l'orientation de la fabrique de la serpentine, plus déformable. La microscopie électronique est réalisée sur les échantillons post mortem pour relier les observations de tomographie en rayons X aux propriétés plastiques des phases.

Je décris tout d'abord les procédures spécifiques, expérimentales et d'analyses d'images in situ, pour la déformation sous haute pression. Ensuite, j'étudie la déformation

des agrégats sous un cisaillement croissant à plusieurs échelles d'observation. Le but principal est d'observer la formation et le développement des IWL. Les relations entre la morphologie et les propriétés plastiques des phases dans la roche sont étudiées pour comprendre la localisation de la déformation dans la péridotite partiellement serpentinisée.

Les principaux résultats montrent que le régime de déformation dans les agrégats d'olivine + serpentine peut être décrit comme semi-fragile, la phase dominante olivine (plus résistante mécaniquement) présentant principalement une déformation fragile, tandis que la phase serpentine (plus déformable) montre un style de déformation ductile. Un cisaillement γ d'environ 4-5, une teneur en serpentine de 20 % en volume, et une fraction initiale de grands clusters (volumes de serpentine) > 15 % en volume, sont des conditions pour une configuration IWL dans les agrégats d'olivine + serpentine. Inversement, à une teneur en serpentine d'environ 10 % en volume, la configuration IWL ne se produit pas, indépendamment du cisaillement ou de la distribution de taille des clusters initiaux de serpentine. Dans ce cas, un comportement de type « load bearing framework » (LBF) est observé où les grains d'olivine se bloquent et sont broyés lors de la déformation, entraînant une réduction de la taille des grains. Ces grains réduits pourraient accommoder une grande partie de la déformation dans la roche.

Ces résultats suggèrent que des teneurs en serpentine > 10 vol.% ou ca. 20 vol.% définissent un seuil clé pour des changements cruciaux dans la morphologie de la serpentine dans les péridotites serpentinisées déformées. Celui-ci pourrait correspondre à des changements importants dans la rhéologie et les propriétés mécaniques de la roche.

Enfin, au vu de ces résultats je donne des perspectives sur la localisation de la déformation et l'initiation des zones de cisaillement dans la lithosphère.

Mots-clés : tomographie in-situ par Rayons X, microstructure, localisation de la déformation, serpentine, haute pression, roche polyminérale.

Abstract

At plate tectonic boundaries, the lithosphere is deformed and strain localization occurs up to kilometers-scale, which can manifest in form of shear zones. The strain localization suggests the strength of the lithosphere is locally weakened. The formation of interconnected layers of weaker minerals in the lithosphere is a potential mechanism to achieve such weakening. Serpentinized peridotite is commonly found within and between tectonic plates. It is mainly composed of olivine and serpentine minerals. The latter is generally accepted to be weaker than olivine at geological strain rates. During deformation, strain is thus expected to preferentially partition into serpentine than into olivine. This can lead to the formation of interconnected weak layers (IWL) of serpentine where strain localizes.

The present work is based on microstructural investigation to infer the strain accommodation in rocks. Olivine+serpentine aggregates with two compositions (10 and 20 vol.% serpentine) are used as a proxy for partially serpentinized peridotites. The aggregates are experimentally deformed in torsion at high pressures (HP, > 2 GPa) and high temperatures (HT, > 300°C) at an equivalent strain rate of 10^{-4} s^{-1}. The experiments are coupled with in-situ absorption contrast X-ray tomography. I obtain 2D and 3D information on connectivity and structural layering in the microstructure of the 'weak' serpentine. Electron microscopy is performed on recovered samples to link the in-situ X-ray tomography observations to the plastic properties of the phases.

I first outline experimental and image-data processing procedures specific to in-situ HP experimental deformation. Then, I study the deformation of the aggregates with increasing shear deformation at multiple scales of observations. The main aim is to observe the onset and development of IWL in its microstructure. The relations between

the morphology and plastic properties of the phases in the rock are investigated to understand the strain localization in serpentinized peridotite.

The main results show the deformation regime in olivine+serpentine aggregates can be described as semi-brittle, with the dominant phase of olivine ('stronger') mainly displaying brittle deformation, whereas the serpentine ('weaker') showing a dominant ductile-style deformation. A strain γ of ca. 4-5, serpentine content of ca. 20 vol.%, and initial fraction of large clusters >15 vol.% determine the condition for IWL configuration in the olivine+serpentine aggregates. Conversely, at serpentine content of ca. 10 vol.%, IWL do not occur, independently of strain or initial clusters size distribution of serpentine. This is more consistent with a load-bearing framework (LBF) behavior, where the stronger olivine grains are jammed, and during deformation crush one another, leading to grain size reduction and accommodating much of the deformation in the rock. These findings suggest contents of serpentine >10 vol.% or ca. 20 vol.% define a threshold for crucial changes in the morphology, connectivity, percolation, of the weak serpentine in serpentinized peridotites under shear. This may lead to important changes in deformation behavior and mechanical properties of the rock.

In light of these findings, I give some perspectives for strain localization and shear zones initiation in the lithosphere.

Résumé pour le grand public

Aux limites entre les plaques tectoniques, la déformation peut se localiser jusqu'à l'échelle kilométrique. Cela affaiblit la résistance mécanique de la lithosphère. Les couches connectées de minéraux plus déformables dans la lithosphère constituent un mécanisme potentiel pour parvenir à un tel affaiblissement. Dans ce travail, j'étudie la déformation d'une des roches courantes de la lithosphère, la péridotite serpentinisée. J'utilise des expériences, de l'imagerie par rayons X (tomographie en 3 dimensions), et de la microscopie électronique pour caractériser la morphologie des minéraux (microstructure) dans la roche, et comment elle évolue avec la déformation. L'objectif principal est d'observer dans quelles conditions des couches interconnectées très déformables peuvent se former dans la péridotite serpentinisée. Cela peut entraîner une localisation importante des déformations dans la roche. Avec mes résultats, je discute du régime de déformation principal de la roche, des processus de localisation des déformations et identifie les conditions spécifiques de cette localisation dans les péridotites serpentinisées. Je donne ensuite des perspectives sur la localisation des déformations dans la lithosphère.

Mots-clés : Lithosphère, localisation de la déformation, péridotite serpentinisée, microstructure, 3D, tomographie.

Plain language summary

At the boundaries between tectonic plates, deformation (strain) can localize up to kilometer-scale. This weakens the strength of the lithosphere. Interconnected layers of "weaker" (easily deformed) minerals in the lithosphere is a potential mechanism to achieve such weakening. In this work, I study the deformation of a common rock of the lithosphere, serpentinized peridotite. I use experiments, X-ray imaging (3D X-ray tomography), and electron microscopy in order to charaterize the morphology of the minerals (microstructure) in the rock, and how it evolves with strain. The main aim is to observe at which conditions interconnected weak layers can occur in serpentinized peridotite. This can result in major strain localization in the rock. With my findings, I discuss the main deformation regime of the rock, the processes of strain localization and pinpoint specific conditions for this localization in serpentinized peridotites. I further give some perspectives for strain localization in the lithosphere.

Keywords: Lithosphere, strain localization, serpentinized peridotite, microstructure, 3D, tomography.

Chapter 1

Introduction

The plate tectonics is driven by forces originating either from mantle convection or slab pull and ridge push (e.g., Turcotte and Schubert, 2002). The boundaries between tectonic plates, such as spreading ocean ridges and subduction zones are sources of most of the volcanic and seismic activities that occur across the planet, impacting the Earth at regional and planetary scale.

At plate tectonic boundaries, the lithosphere is deformed and strain localization occurs up to kilometers-scale suggesting the strength of the lithosphere is locally reduced (e.g., Turcotte and Schubert, 2002). From spreading ocean ridges to subduction zones, deformation of the lithosphere depends on compositional layering, physical properties of rocks and their deformation behavior (or rheology).

Rocks are made of multiple minerals, or phases. Each one of the phases has its own mechanical properties or shows a specific deformation behavior, which makes rocks mechanically heterogeneous. Some phases can be 'weaker' than others, with the strain preferentially localizing in the former. Strain localization in the weaker constituents of the lithosphere could result in the local strength reduction of the lithosphere.

One of the rocks commonly found in geological settings in the lithosphere, within and between tectonic plates, is serpentinized peridotite. This rock results from the serpentinization of peridotitic mantle, and can exists in both slow-spreading ocean ridges and subduction zones (e.g., Scambelluri et al., 2019). Its main mineralogical components are olivine, pyroxene and serpentine. The formers are magnesium-iron silicates, whereas the latter is a group of magnesium-rich phyllosilicates (sheet-structured minerals).

Phyllosilicates, such as serpentine, are weaker components in the lithosphere that can form interconnected 'weak' layers in deformed rocks and significantly reduce their strength (Dell'Angelo and Tullis, 1996; Niemeijer and Spiers, 2005; Holyoke and Tullis, 2006a). Laboratory experiments demonstrated the deformation of serpentines could explain the rheology weakening of the oceanic lithosphere (e.g., Escartín et al., 2001; Hilairet et al., 2007; Amiguet et al., 2012). It is generally accepted the mechanical strength of serpentine is lower than olivine at geological strain rates. This makes the serpentine weaker than olivine in serpentinized peridotite and potentially accommodate much of the strain in the rock (e.g., Hirauchi et al., 2010; Soda and Takagi, 2010; Padrón-Navarta et al., 2012; Brownlee et al., 2013; Soda and Wenk, 2014; Morales et al., 2018).

The deformation behavior of a multi-phase rock such as serpentinized peridotite can be addressed from two different points of view (Karato, 2008): i) If the volumetrically dominant phase is the 'weak' phase, then one can ask how the addition of the 'strong' phase increases the aggregate strength and influences the distribution of the strain; ii) if the volumetrically dominant phase is the 'strong' phase, then the question is how the addition of a weaker phase influences the overall strength of the rock and the strain localization in it.

The main aim of the present work is to experimentally explore the deformation of serpentinized peridotite by addressing it from the point of view ii) (above). For the purpose of the simplicity, the presence of pyroxene in natural peridotite will be ignored here, and the system investigated is olivine+serpentine. The relations between the morphology and plastic properties of the phases in the aggregates are investigated to understand the strain localization or distribution in serpentinized peridotite. I will focus the analysis on the 'weak' serpentine, and on the study of its microstructure evolution with increasing deformation. The results are obtained with an approach that incorporates multiple analytical techniques enabling the study of two-phase rocks at multiple scales of

observations. In the following, I provide background information leading to the specific objectives and approach of this work.

1.1. Deformation styles and mechanisms in rocks

Two general types of deformation exist in materials:

1) elastic deformation;

2) plastic deformation.

Elastic deformation is time independent and recoverable, whereas plastic deformation is time dependent and non-recoverable. In the elastic deformation, if the stress is removed, the material recovers and the strain (shape change in the material) returns to zero. Conversely, in the plastic deformation, the strain changes continuously with time. Even after the stress is removed, the material permanently retains some strain.

Non-recoverable (plastic) deformation is common in nature for most of the rocks in the lithosphere and asthenosphere. However, when describing the deformation behavior of rocks, the general term "non-recoverable" or "plastic" can be not enough. Deformation of rocks often results in highly heterogeneous microstructures, which requires additional terms within a general deformation type to describe the observable deforming features.

Two main deformation styles can exist in the non-recoverable (plastic) deformation for rocks:

1) "brittle" deformation;

2) "ductile" deformation.

Brittle deformation can be described as a shape change of the rock by breaking of its chemical bonds, which do not successively reform. It occurs when the applied stress surpasses the elastic threshold of the rock, and when the deformation rate is too fast to accommodate further strain without breaking of the rock (e.g., Song and Cao, 2021). In

natural rocks, the result of brittle deformation often manifests as fractures or microcracks where strain mostly localizes. One of the most common brittle flow patterns occurring in rocks is the so-called "cataclastic flow" (e.g., Passchier and Trouw, 2005). The cataclastic flow is the result of brittle deformation mechanisms occurring at the microscale (i.e., grain scale), such as grain fracturing (within a single grain or across multiple grains), grain rotation and frictional sliding. (e.g., Gomez-Rivas et al., 2020). The latter defines the ability of a grain or more to slide along grain contacts. The so-called fiction coefficient defines the resistance of a mineral to slide along contacts between grains. The lower the friction coefficient, the greater the ability of the grains to slide, and therefore promote frictional sliding in the mineral. Minerals with low friction coefficient in the range of 0.2–0.8 exhibit low-frictional behavior and are generally considered weak, such as sheet-structured minerals (e.g., phyllosilicates) (e.g., Byerlee, 1978; Moore and Lockner, 2004).

Ductile deformation refers to a shape change of the rock through bending or flowing during which chemical bonds may become broken but successively reformed into new bonds (e.g., Song and Cao, 2021). It requires an applied stress surpassing the elastic threshold of the rock, and a deformation rate slow enough to accommodate further strain without breaking of the rock (i.e., "ductility" or "plasticity") (e.g., Gueguen and Palciauskas, 1994; Passchier and Trouw, 2005). Rocks that experienced ductile deformation are often not fractured, and show a homogeneously distributed deformation. Folds, foliation, and lineations are typical features of ductile deformation in a rock (e.g., Passchier and Trouw, 2005; Philpotts, Antony R., Ague, 2009; Fossen, 2012)

Rheological laws in the ductile regime in Earth materials are often described using two main deformation mechanisms, diffusion creep and dislocation creep (e.g., Karato and Wu, 1993; Passchier and Trouw, 2005; Karato, 2008; Bhattacharya, 2022) (see section 1.1.1). However, other mechanisms that can accommodate ductile (plastic) deformation have also been proposed, such as mechanical twinning or kinking, grain

boundary sliding, and rigid body rotation (e.g., Passchier and Trouw, 2005; Song and Cao, 2021 and references therein).

Whether brittle deformation is favored over ductile deformation, or vice-versa, can depend on the strain rate and conditions with increasing depth through the Earth, e.g. temperature and pressure. Lower temperature and confining pressure, and higher strain rate usually favor brittle deformation, whereas higher temperature and pressure, and lower strain rate usually favor ductile deformation. Rocks can, however, undergo different deformation events determined by a change in strain rate, temperature or pressure. Manifestation of both brittle and ductile deformation is, therefore, possible. The coexistence of multiple phases with different rheological properties in a rock can also cause the manifestation of heterogeneous deformation, with both brittle and ductile deformation occurring (e.g., Jammes et al., 2015). For instance, the term "semi-brittle" can be used to describe the rheology of a rock with minerals being harder that their surrounding matrix. These minerals stay undeformed or show localizing fracturing associated with brittle deformation, whereas the minerals in the matrix show evidence of viscous or ductile deformation (e.g., White et al., 1980; Jammes et al., 2015). This rheology can be found for instance in naturally sheared rocks called mylonites (e.g., Passchier and Trouw, 2005), which show planar foliations and straight lineations in a 'softer', strongly deformed fine-grained matrix that surrounds secondary, 'harder' and undeformed (or fractured) coarse-grains (the so-called "porphyroclasts").

1.1.1. Main deformation mechanisms in ductile (plastic) deformation

As previously introduced in section 1.1., the two main deformation mechanisms that are often used in rheological laws in the ductile regime for Earth materials are diffusion creep and dislocation creep (e.g., Karato and Wu, 1993; Passchier and Trouw, 2005; Karato, 2008; Bhattacharya, 2022), which are described as follows.

Diffusion creep involves diffusion of vacancies (point defects) through the crystalline lattice of a mineral, leading to diffusive mass transport between the grain boundaries or within the grain. This mechanism usually changes the shape of grains by removal of mass from the most-stresses grain boundaries, diffusion through the grains or along the grain boundaries. Then, re-precipitation of this mass on less-stressed interfaces or in veins can occur. A loss from the system in flux or pore fluid can also occur. In a special case where water is present and wets the grain boundaries, the dislocation creep involving diffusive mass transport can be referred as the so-called pressure solution creep.

In contrast with diffusion creep, where deformation in the mineral is determined by diffusion of point defects through the crystalline lattice, dislocation creep involves the formation and motion of line defects through the crystalline lattice of the mineral. This linear defect is called dislocation. The movement of a dislocation allows atoms to slide over each other, which can lead to a large displacement of one part of the crystal lattice relative to another plane, along specific crystallographic planes and direction. This large displacement is called slip, and a slip system describes the set of crystallographic planes and associated slip directions for which the motion of a dislocation can easily occur. Microstructural features that can be associated with formation and motion of dislocations in grains of a mineral can be referred as intracrystalline plasticity. It can include flattened grains, wavy extinctions, deformation lamellae, subgrain formation and dynamic recrystallization (e.g., Passchier and Trouw, 2005). Intracrystalline plasticity also induces textural changes in the mineral, i.e. crystallographic preferred orientation (CPO). CPO is due to the activation of slips being confined to certain crystallographically-controlled slip system, promoted by dislocation motions. CPO can result in anisotropy in the seismic waves velocity, and creep strength, which is generally believed not to occur in deformation caused by diffusion creep (e.g., Karato and Wu, 1993, and references

therein), although the occurrence of CPO induced by diffusion creep mechanism have been reported (Miyazaki et al., 2013). Microstructural and textural features of intracrystalline plasticity can be observed and investigated through electron microscopy techniques (see section 2.4).

1.2. LBF and IWL: deformation behaviors in multi-phase rocks

A key for understanding the deformation of a multi-phase rock is the stress-strain distribution among the phases. The stress-strain distribution is sensitive to the phases morphology, which evolves with strain (e.g., Karato 2008). Studies on deformed microstructures in natural rocks show several minerals collectively determine the entire rock deformation or rheological behavior (e.g., White et al., 1980). Both stress and strain are partitioned according to the relative rheological contrast between the minerals making up the rocks. The degree of stress and strain partitioning depends on the minerals (or phases) proportion, distribution and shape, as well as on temperature, strain rate, and grain size dependencies of the main deformation mechanism in the minerals.

Pioneer studies constructed models of polymineralic materials deformation to explain the deformation behavior observed in natural rocks (e.g., Handy, 1990). A possible and simple model for multiphase rocks deformation is a two-phases system, which takes into account the relative volume proportions and rheological contrast between the two dominant phases comprising the rock. The terms "weak" and "strong" are used to define the rheological contrast between the two phases, with the weak phase being more susceptible to 'flow' than the strong phase. Based on this model, the main end-member behaviors in rocks are (Fig. 1.1): (1) a load-bearing framework (LBF), where the strong phase surrounds isolated pockets of the weak phase, and (2) interconnected weak
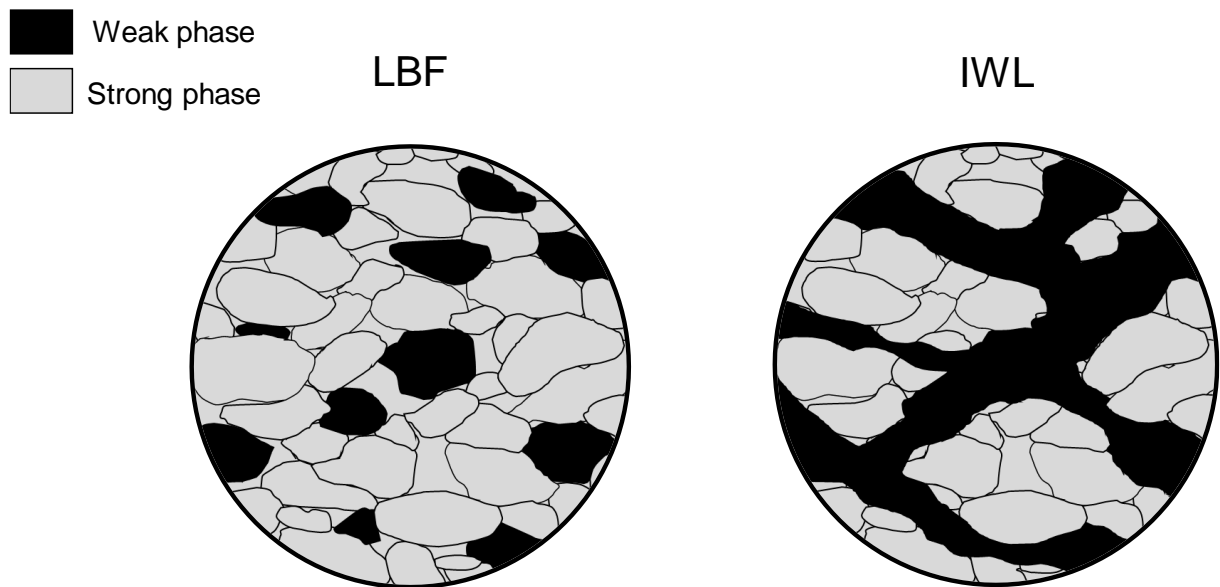
Figure 1. 1. Load bearing framework (LBF) and interconnected weak layer (IWL) configurations for multi-phase rock (after model by Handy et al., 1990, 1994).

layers (IWL), where the weak phase form a network of layers that separate clasts of the strong phase (e.g., Handy, 1990; 1994; Karato, 2008; Wang et al., 2011).

In comparison with the LBF, where the strength of the aggregate depends primarily on the strength of the strong phase, the weak phase controls the rheology of the rock in the IWL. The interconnection of weak layers determines localized regions where deformation or stain rate can be higher at constant stress, therefore where there could be strain localization, which could in turn lower the overall strength of the rock at specific conditions.

1.2.1. Strain localization and IWL

Strain localization in rocks manifest in form of shear bands or zones, and are characterized by large shear strain analogous to the simple shear geometry. Shear zones are common in the lithosphere, and can be present at many scales in the Earth (e.g., Paterson and Olgaard, 2000, and references therein), from millimeter-sized up to km-sized, or tectonic-plate scale (such as subduction zones).

Shear zones can be regarded as a manifestation of the weakening of the lithosphere. However, the processes that lead to the rheological weakening of the lithosphere remain up to now uncertain. Multiple possible mechanisms leading to lowering the strength of the lithosphere have been suggested, such as shear heating (Thielmann and Kaus, 2012; Lu et al., 2015) and grain size reduction (Bercovici, 2003; Bercovici and Ricard, 2014). In nature, multiple mechanisms are likely to combine. A structural transition has been demonstrated, as previously noted (see section 1.2), where the weakest phase in the rock forms interconnected layers (IWL). The IWL can play a dominant role in efficiently localize strain, even enabling shear zones to a tectonic level (e.g., Montési, 2013).

The deformation and development of interconnected layers in the major weak minerals constituents of the lithosphere (such as serpentines in serpentinized peridotites) could, therefore, be a key to understand shear zone and strain localization dynamics in the lithosphere.

1.3. Deformation in serpentinized peridotites

The deformation behavior or rheology of serpentinized peridotite could be determined by the rheological contrast between its main components, here considered to be olivine and serpentine. In the following sub-sections, a background on deformation of olivine (section 1.3.1) and serpentine (section 1.3.2) is first given. Then, previous work on deformation of serpentinized peridotite (olivine+serpentine) relevant for the present study will be presented (section 1.3.3).

1.3.1. Olivine deformation

Olivine can constitute over the ca. 50 % of the Earth's upper mantle volume, and is one of the most common Earth's minerals by volume (McDonough and Rudnick, 1998). The olivine deformation behavior has been extensively investigated (e.g., Bai et al., 1991;

Hirth and Kohlstedt, 1996, 2003; Mei and Kohlstedt, 2000a, 2000b; Demouchy et al., 2009; Faul et al., 2011). At higher temperature, olivine usually show deformation accommodated by association of dislocation glide and diffusion creep processes. Well-defined flow-laws have also been constructed (e.g., Kohlstedt and Goetze, 1974; Durham and Goetze, 1977; Bai et al., 1991; Demouchy et al., 2009). However, at lower temperatures, and higher differential stresses relevant for the lithosphere, olivine behaves differently (e.g., Raleigh, 1968; Goetze and Evans, 1979; Demouchy et al., 2009), usually showing a dominant brittle and work hardening (or strain hardening) behavior. Studies on experimentally deformed olivine have shown low-temperature plasticity (intracrystalline plasticity) occurring in single crystal- and polycrystalline samples (e.g., Gaboriaud et al., 1981; Druiventak et al., 2011; Idrissi et al., 2016; Hansen et al., 2019). The early study by Gaboriaud et al. (1981) reported results on micro-hardness indentation experiments on olivine single crystal. TEM images showed low-temperature plasticity occurring along with fracturing at temperatures between 20°C and 900°C, with [001](100) and [001](110) slip systems being activated. The latter prevailed at temperatures higher than 600° C, whereas the former at <600° C.

A recent study (Idrissi et al., 2016) has shown similar findings on dislocations structures in an oriented olivine single crystal under in-situ TEM mechanical testing. At lower temperature, the plasticity of olivine was dominated by glide of [001] screw dislocations on (110) and (100) planes. At controlled imaging conditions relative to the tensile direction, the resolved shear stress on [001](110) slip system was close to maximum. Idrissi and colleagues also integrated their TEM findings with numerical modelling to obtain critical stresses for plastic flow of olivine as a function of temperature, spanning from 0°C to 1000°C. The main conclusion was intrinsic ductility of olivine at lower temperature being significantly lower than previously reported values at strain-hardened conditions.

Finally, deformation of polycrystalline olivine has been performed on natural dunite by carrying out experiments on a Griggs-apparatus at low temperature (20°C, 300°C and 600°C) and high stress conditions (Druiventak et al., 2011). At these conditions, dunite showed maximum differential stresses in the range of 1.0 to 2.9 GPa, indicating semi-brittle behavior. Microstructures at higher experimental temperatures showed evidence of low-temperature plasticity of olivine in the form of pronounced undulatory extinction associated with high dislocation densities, with pile-up of dislocations leading to the formation of either fracture arrays at 300 °C or deformation lamellae and cellular structures at 600 °C, indicating intragranular work-hardening. Strain hardening in olivine that has also been suggested to be associated with dislocation interaction was reported in a more recent experimental, deformation study investigating low-temperature plasticity in olivine single crystals and aggregates (from room temperature to ca. 1200°C, at 5 to 9 GPa) (Hansen et al, 2019). They reported one of the key phenomena in low-temperature plasticity of olivine to be the significant strain hardening until an approximate steady-state flow stress was reached, independently of the grain size (Hansen et al, 2019).

1.3.2. Serpentine deformation

The common serpentine varieties are chrysotile, lizardite and antigorite. Each one of them shows a specific crystallographic structure (e.g., Evans et al., 2013), which influences their individual rheological and geophysical properties (Guillot et al., 2015). The early work by Raleigh and Paterson (1965) showed that serpentine is generally a weak material and remains ductile even at low temperature. Since their work, a large number of studies have been reported to constrain the deformation behavior of the serpentine minerals (e.g., Guillot et al., 2015 and refrences therein).

Lizardite is stable at low-pressure (<1 GPa) and low-temperature (up to 300°C) conditions (e.g., Guillot et al., 2015). It is the most common serpentine variety at low-

temperature, and often found to form mesh-like texture surrounding or pseudomorphing the olivine grains (e.g., Evans et al., 2013; Guillot et al., 2015; Viti et al., 2018). Lizardite can show a transition from brittle to ductile regime at low confining pressure (200 to 400 MPa) (e.g., Escartín et al., 1997). The deformation of lizardite can be described as a frictional deformation with relatively low friction coefficient between 0.3 and 0.5 (e.g., Reinen et al., 1994; Moore et al., 1997). This is due to its crystallographic structure involving weak interaction between OH and silica layers (e.g., Evans et al., 2013; Hirth and Guillot, 2013). The relatively low frictions can promote easy gliding on the basal plane associated with kinking (e.g., Amiguet et al., 2014). The amount of deformation due to kinks at the microscopic scale was found to be similar to the total macroscopic sample strain, suggesting homogenous plastic flow occurring in lizardite (Amiguet et al., 2012). Gliding on the basal plane of lizardite associated with kinking observed in experiments is consistent with observations of the lizardite basal plane in the foliation plane of weak shear zones (e.g., Amiguet et al., 2012, 2014).

Chrysotile, as lizardite, is generally stable at low-pressure (<1 GPa) and low-temperature (up to 300°C). The frictional coefficient of chrysotile is, however, generally lower than the one of lizardite (from 0.1 to 0.5; e.g., Moore et al., 2004). This is due to the chrysotile tendency to absorb large amount of water that acts as lubricant during deformation (e.g., Moore et al., 2004; Moore and Lockner, 2007). The absorption of large amount of water is related to the crystal structure exposing the $(OH)^-$ ions on the outer layers (e.g., Moore et al., 2004, and references therein; Evans et al., 2013). However, with increasing temperature and pressure, the water is driven off the chrysotile, leading to an increase in the friction coefficient and strength of the mineral. At dry conditions, the friction coefficient can be up to 0.7, similar as, or even higher than the one of lizardite (e.g., Moore et al., 1997, 2004).

Antigorite is the high-pressure, high-temperature variety of the serpentine group (e.g., Auzende et al., 2002, Evans et al., 2013; Hirth and Guillot, 2013; Guillot et al., 2015). It is stable down to ca. 180 km depth, and is common in cold subduction zones and at the mantle wedge (e.g., Ulmer and Trommsdorff, 1995). Antigorite is thought to show a ductile behavior at intermediate temperature (>300°C) and high confining pressure (up to 4 GPa), especially during seismic events (e.g., Guillot et al., 2015). Naturally deformed antigorite was found to show crystallographic preferred orientation (CPO) consistent with a dislocation creep mechanism accommodating the deformation (e.g., Padrón-Navarta et al., 2012). Pressure solution creep was also suggested as plastic deformation mechanism for naturally deformed antigorite (Auzende et al., 2015; Tulley et al., 2022). However, different ideas arise when antigorite is experimentally deformed, with studies debating over the main deformation mechanism responsible for accommodating plastic deformation (e.g., Chernak and Hirth, 2010; Amiguet et al., 2014; Auzende et al., 2015, Idrissi et al., 2020; Hansen et al., 2020), as well as the main observable deformation regime (brittle or ductile) and the conditions of transition from brittle to ductile regimes (e.g., Raleigh and Paterson, 1965; Escartín et al., 1997; Hilairet et al., 2007; Amiguet et al., 2014; Auzende et al., 2015; Proctor and Hirth, 2016; Shao et al 2021).

In early experimental studies (Raleigh and Peterson, 1965; Escartín et al., 1997), antigorite was found to deform by macroscopically ductile processes at confining pressure of >500 MPa, based on observations of a transition from localized to distributed deformation and decreasing friction coefficients with increasing pressure. Conversely, other experimental studies stated that antigorite could never achieve fully ductile flow or plastic deformation mechanism based on i) an insufficient number of dislocation glide planes (i.e., the so-called Von Mises criterion is not met), ii) the observation that differential stresses during deformation remain above the confining pressure (i.e., the so-called Goetze's criterion is not met), and iii) the presence of semibrittle microstructures

in naturally deformed serpentinites (e.g., Chernak and Hirth, 2010; Auzende et al., 2014). More recently, new insight on mechanical data using micro-mechanical testing have been provided to constrain the plastic deformation mechanism accommodating the macroscopically observable deformation in antigorite (Hansen et al., 2020; Idrissi et al., 2020). Hansen et al. (2020) showed dislocation gliding on the basal plane or shear fracturing involving delamination (Hansen et al., 2020). On the other hand, Idrissi et al. (2020) suggested the grain boundary sliding as the main deformation mechanism in antigorite to possibly explain its ductility. Later, Shao et al. (2021) reported microstructural observations revealing the indication of ductile behavior by kinking and bending of the originally straight foliation in antigorite, with formation of Riedel shear (S-C' fabric; Passchier and Trouw, 2005) and microcracking, which are consistent with a semi-brittle deformation regime.

1.3.3. Serpentinized peridotites: fabric and strength reduction

In natural serpentinized peridotite, with olivine and serpentine as main components, the serpentine likely accommodates most of the deformation (e.g., Hirauchi et al., 2010; Soda and Takagi, 2010; Padrón-Navarta et al., 2012; Brownlee et al., 2013; Soda and Wenk, 2014; Morales et al., 2018). This implies that a microstructural transition of IWL fabric (see section 1.2) displayed by the serpentine surrounding olivine clasts can occur in serpentinized peridotite.

It has been demonstrated the weak phase abundance in the aggregate strongly influences the transition to IWL (see section 1.2), with the occurrence of strain localization or strength reduction in rocks (e.g., Handy, 1990; 1994; Handy et al., 1999). In serpentinized peridotite, previous studies show that a content of <20% of serpentine is enough to see relevant microstructural or mechanical changes in the rock (e.g., Escartín et al., 2001). With laboratory axial compression tests (pressure <1GPa; room temperature) on partially serpentinized peridotite cores with 10-15 vol.% of serpentine,

they determined the influence of serpentine content on the strength and deformation mechanism of the rock (Escartín et al., 2001). They have found the only presence of 10 vol.% of serpentine being enough to dramatically reduce the strength of a partially serpentinized peridotite compared to that of a pure serpentinite. According to their main results, one can speculate that a content of 10 vol.% in the weaker phase is sufficient to possibly enable an IWL mechanical behavior and the onset of deformation localization in serpentinized peridotites.

However, in a more recent work of controlled deformation experiments on olivine+antigorite-rich serpentine aggregates at different antigorite contents, (Ferrand et al., 2017) suggested that connected clusters or serpentine (antigorite) could occur at lower (i.e., ca.6 vol.% at 1.1 GPa) or higher (i.e., ca.18 vol.%, at 3.5 GPa) contents than 10 vol.%, at temperature of <600°C.

To our knowledge, there is no other study documenting the serpentine microstructural evolution and its critical abundance above which interconnected weak layers are likely to form and surround olivine clasts during shear deformation. Further experimental constrains are needed at different deformation stages to locate the onset of an IWL behavior (see section 1.2) in serpentinized peridotite, and possibly explain strain localization development for shear zones and strain localization in the lithosphere.

1.4. Aim and approach

Microstructural observation is a key to infer the strain accommodation in minerals and rocks. The present work is based on microstructural observation and analysis, and can be divided in two main parts that are described as follows.

The first part outlines specific experimental and image-data processing procedures I choose to study the evolution of deformed microstructures in multi-phase rocks under shear deformation (chapter 3). I test and perform these procedures in two

different aggregates.   I provide examples of experimentally exploring large shear deformation in multi-phase rocks at high pressures (HP, 4-5 GPa) and high temperatures (HT, 300-400°C) using *in-situ* X-ray tomography, in order to investigate the evolution of their internal structural features with perspective for shear zone dynamics.

The second part is the main aim of this work, which to study the deformation behavior of serpentinized peridotite under shear deformation (chapter 4). Aggregates of olivine+serpentine are used as a proxy for partially serpentinized peridotites. The aggregates are hot-pressed and then sheared through torsion at equivalent strain rates of 10^{-4} s^{-1} at HP-HT. I follow the evolution of their microstructure with increasing deformation using *in-situ* X-ray tomography, focusing on the 'weak' serpentine. The main objective is to observe at which conditions an IWL-like behavior (see section 1.2) can be achieved, and infer how strain is localized in partially serpentinized peridotite, depending on the transferred strain and serpentine content. To link the X-ray tomography observations to the plastic properties of the minerals, I then perform *post-mortem* electron microscopy on recovered samples of interest.

Chapter 2

Materials and techniques

2.1. Starting materials

The majority of the experiments were performed on the aggregates of olivine+serpentine (chapters 3, 4), used as a proxy for partially serpentinized peridotite (see sections 1.3.3, 1.4). The employed starting materials were powder mixtures of:

i)   Serpentine from a natural serpentinite rock

ii)   Crystals of San Carlos olivine.

The two minerals were separately crushed and sieved to obtain a final particle sizes range of ca. 50-100 μm. The portion of powder particles <3 μm was removed by ethanol suspension, and not used for the experiments. One powder mixture was prepared with ca. 10 vol.% of serpentine, and another with ca. 20 vol.% of serpentine.

Serpentine and olivine were chemically characterized using the Electron micro-probe analyzer (EPMA, model CAMECA SX 100) at the Plateforme de microscopie electronique de Lille (PMEL, University of Lille, https://pmel.univ-lille.fr/). The calculated chemical formula for serpentine is $(Mg_{0.93}Fe_{0.04}Al_{0.033})_3(Si_{0.99})_2O_5(OH)_4$, whereas for olivine is $(Mg_{0.87}Fe_{0.13})_2SiO_4$. To detect the mineralogical varieties of serpentine, microstructural characterization was performed on the serpentine powder in a Transmission electron microscope (TEM, model JEOL JEM-2100) at the Plateforme d'imagerie cellulaire et tissulaire, on the BiolMaging Center de Lille (BICeL, University of lille, https://bicel.univ-lille.fr/microscopie-electronique). The acquired TEM images (Fig. 2.1) revealed the presence of crystals consistent with the structure of chrysotile (Fig. 2.1a, b), lizardite (Fig. 2.1c) and antigorite (Fig. 2.1d).
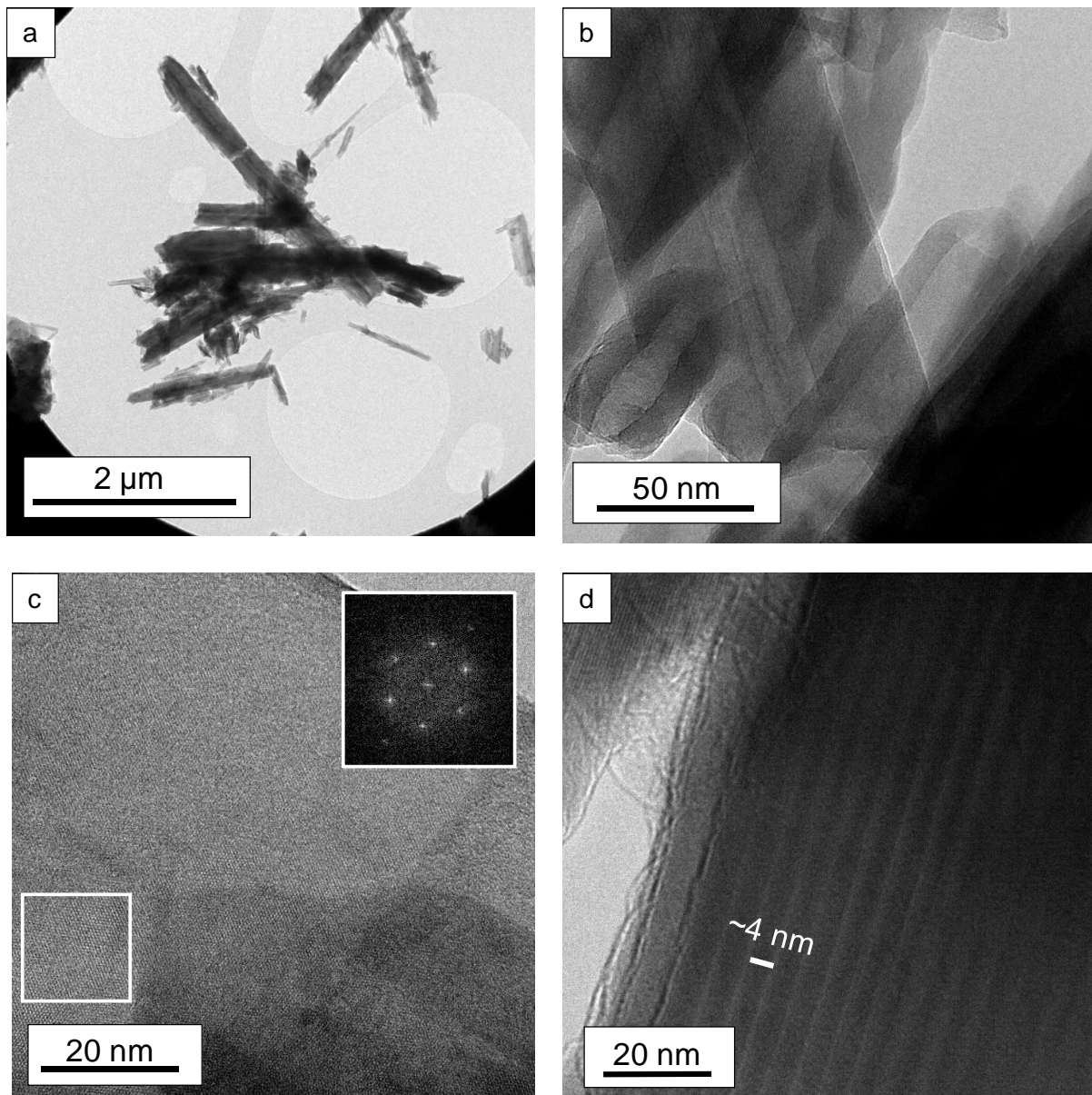
Figure 2. 1. Micrographs of the starting material serpentine acquired through transmission electron microscopy (TEM). a) cluster of long crystals consistent with chrysotile crystals. b) detail of chrysotile with central hollow area. c) High-resolution TEM (HRTEM) image with Fast fourier transform (FFT) pattern (upper-right corner) obtained for the area in the white square. The isotropic shape of the FFT pattern is consistent with the crystal structure of lizardite for the crystallographic basal plane (e.g., Mellini, 1982; Auzende et al., 2006). d) detail of a crystal showing a structural feature consistent with antigorite crystal structure with lattice modulation of ca. 4 nm (e.g., Auzende et al., 2002).

To characterize the volume proportions of the serpentine varieties, X-ray diffraction (XRD) analysis was performed on the serpentine powder using a Bragg-Brentano geometry diffractometer with detector Rigaku HyPix-3000, in the department of Plateau technique rayon X (PTRX, University of Lille, https://uccs.univ-lille.fr/index.php/en/presentation-of-uccs/resources/2-non-categorise/59-diffraction-

28

x). Unfortunately, because of the presence of many peaks overlapping for the three different serpentine varieties in the XRD, the refinement led to inclusive results. On the basis of the position and intensity of the main peaks in the XRD (Fig. 2.2) and the TEM observations, the first most abundant mineralogical variety is likely lizardite (possibly >50 vol.%), with chrysotile likely being the second most abundant ($\lesssim$40 vol.%), and antigorite the least abundant (<10 vol.%).
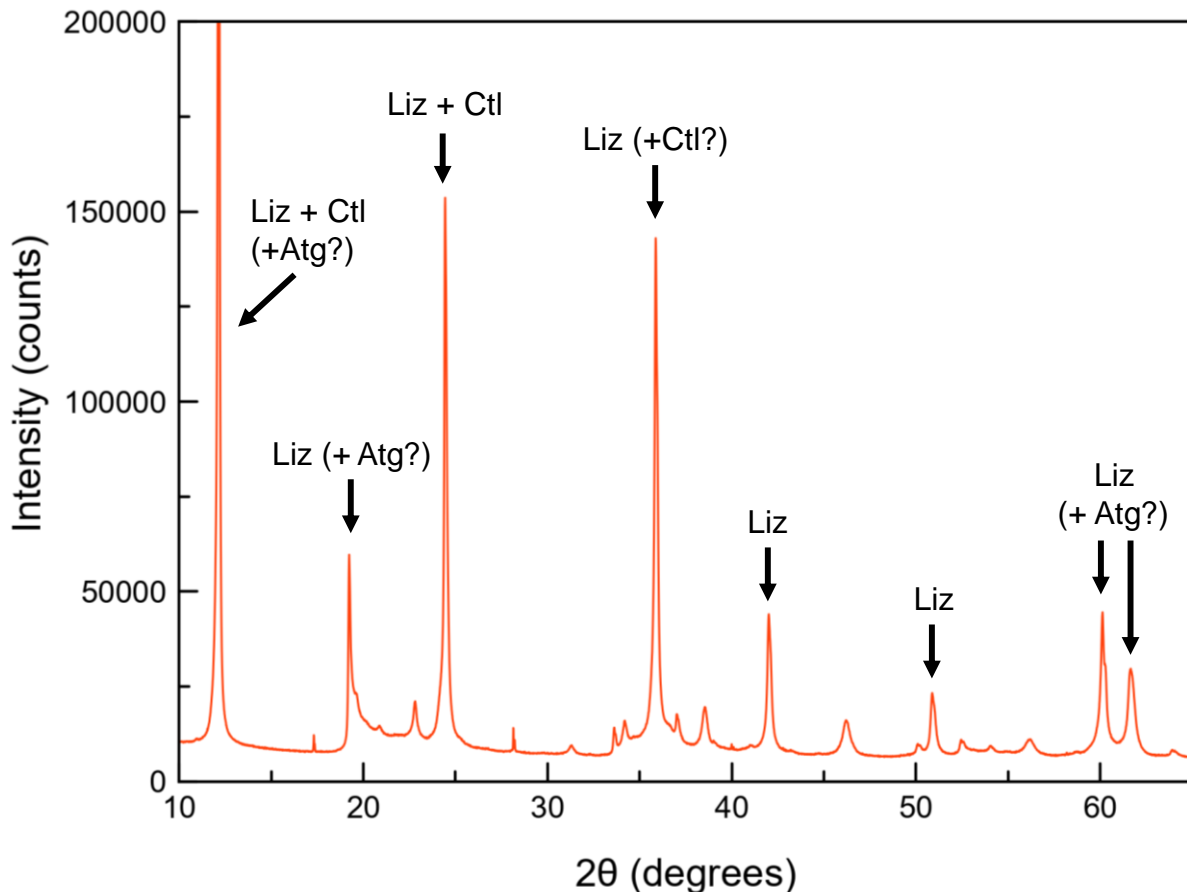
Figure 2. 2. X-ray diffraction (XRD) collected for the serpentine powder showing the main peaks (higher-intensity peaks) that are consistent with the serpentine varieties. Liz is lizardite. Ctl is chrysotile. Atg is antigorite.

Other experiments (chapter 3) were performed on aggregates representative for eclogitic rocks (e.g., Philpotts et al., 2009). The starting materials were:

i)   Cores (diameter of ca. 1.5-2 mm).

ii)   Powder mixtures of Na-rich pyroxene (omphacite)+garnet.

The cores (i) were made out of a selected natural eclogitic rock (donated by Ph.D. M. Locatelli) from the Monviso region, Italy (Locatelli et al., 2018) (Fig. 2.3a). This rock

comprises ca. 30 vol.% of garnet (including atoll-shaped garnet grains), ca. 65 vol.% of pyroxene (omphacite), and 5 vol.% of additional minerals, such as quartz (SiO_2) and rutile (TiO_2) (Locatelli et al., 2018).

The powder mixture of Na-rich pyroxene (omphacite)+ garnet (ii) was used as a proxy for eclogite composition. The two minerals were retrieved from a natural eclogite (Fig. 2.3b) sampled in the Western Gneiss region (Fjortoftvika, Norway) (donated by Ph.D. M. P. Terry; Robinson et al., 2003, geological survey report no. 2003.057). The Na-rich pyroxene (omphacite) and garnet were separately crushed and sieved to obtain a final particle sizes range of ca. 50-100 μm. The portion of powder particles <3 μm was removed by ethanol suspension, and not used for the experiments. One powder mixture was prepared with ca. 30 vol.% of garnet, and another with ca. 70 vol.% of garnet. The two minerals were chemically characterized using the EPMA-CAMECA SX 100 (PMEL, University of Lille). The calculated formula for pyroxene is $(Ca_{0.68}Na_{0.27})_{0.95}(Mg_{0.22}Fe^{2+}_{0.09}Al_{0.29}Fe^{3+}_{0.4})Si_2O_6$, whereas the garnet is $(Mg_{0.52}Fe^{2+}_{0.36}Ca_{0.12})_3(Al_{0.99}Fe^{3+}_{0.01})_2Si_3O_{12}$.
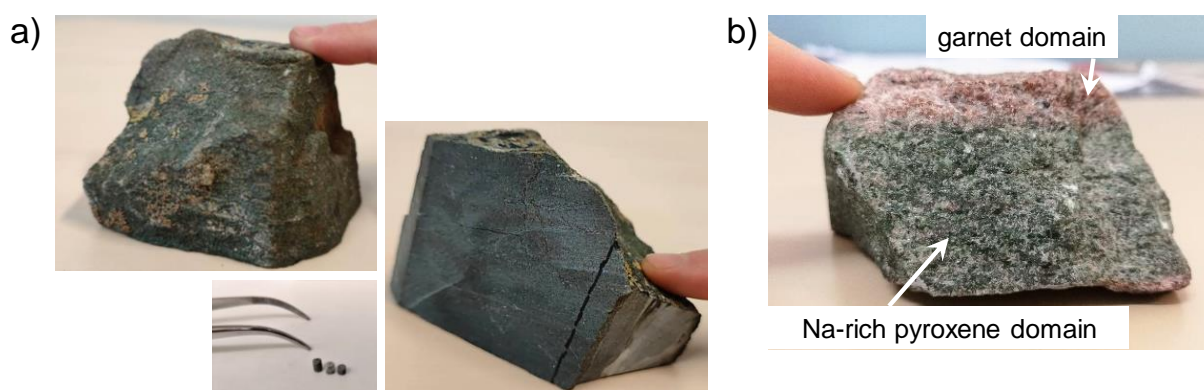
Figure 2. 3. Rock specimens used for the pyroxene+garnet starting material. a) Eclogite specimen (from 'L-30' sampling series in Locatelli et al., 2018) used to retrieve cores samples (see text). b) Eclogite specimen (from '4-1' sampling location in Robinson et al., 2003) used to make the powders mixture (see text).

The starting materials of power mixtures (olivine+serpentine, pyroxene+garnet) and cores (pyroxene+garnet) were hot-pressed at HP-HT prior starting the deformation

experiments. The apparatus used for both hot-pressurization and deformation at HP-HT is introduced in the next section (section 2.2).

2.2. The RoToPEc apparatus

All the experiments were conducted in the apparatus "Rotating Tomography Paris-Edinburgh cell" (RoToPEc) (Philippe et al., 2016; Álvarez-Murga et al., 2017). In this section, I give information on the design and technical features of this apparatus. Further details can be found in e.g. Philippe et al. (2016).

The RoToPEc is a portable, HP-apparatus comprising anvils that are rotated under a uniaxial load, which is transmitted by thrust bearings. The apparatus allows HP-HT (e.g., up to HP of ca. 10 GPa, and HT up to ca. 2200 °C) torsion experiments (potentially simple shear $\gamma > 2$ or $\gamma > 3$) (Philippe et al., 2016; Álvarez-Murga et al., 2017). The apparatus design is thought to be easily be coupled with *in-situ* X-ray tomography on large-volume samples (at least 2 mm^3; Philippe et al., 2016) (see section 2.3 for a background information on X-ray tomography). The design is a result of modifications made to the traditional V7-type Paris-Edinburgh-type (PE) (e.g., Le Godec et al., 2009), with implementation of a new rotating module inspired by the cell developed by Bromiley et al. (2009).

The RoToPEc apparatus is shown in Figure 2.4. It consists of two-opposed rotating anvils placed at the equatorial plane of the apparatus vertical stack, which comprises an upper and lower frame component (Fig. 2.4a). In the lower frame of the stack, a hydraulic ram transfers the force from a piston to a thrust bearings system (inside the conical spacer; Fig. 2.4a) in order to transmit a uniaxial load and pressurize the sample between the opposed-anvils (Fig. 2.4.a). The oil pressure in the ram can be generated by a computer-controlled hydraulic pump with a capacity of 3000 oil bars, which potentially results in transferring a pressure up to ca. 10 GPa to the sample at HT if tungsten-carbide
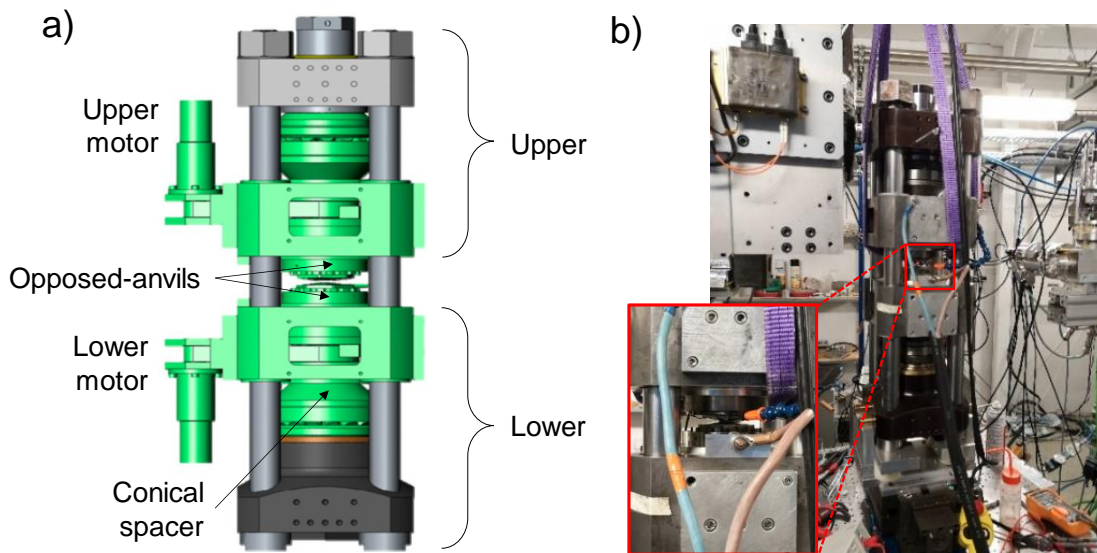
Figure 2. 4. RoToPEc apparatus used in the present work for hot-pressurization of the starting materials and subsequent deformation experiments with in-situ X-ray tomography. a) render of the RoToPEc (modified after Philippe et al., 2016) showing the main components of the apparatus (see text for description). The hydraulic pump that transfers the pressure to the anvils and sample is placed in the lower frame, inside the conical spacer. b) Photograph of the RoToPEc apparatus on the PSICHE beamline (SOLEIL synchrotron, France) to perform experiments with in-situ X-ray tomography. The close-up shows the anvils, the cooling system (orange-tip cable) shooting cooled-air flow to the anvils, and the heating system (light-blue and light brown electric cable attached to the anvils housing frame.

anvils are employed (Philippe et al., 2016; Álvarez-Murga et al., 2017) Two rotating motors systems, one on the upper- and another on the lower-frame (Fig. 2.4a), allows the rotation of the anvils under the uniaxial load. The rotation system has an angular resolution of 0.005°, and allows a full rotation angle of the anvils (i.e., 360°). The motors can be controlled individually permitting three types of anvils motions (see Fig. 11 in Philippe et al., 2016): i) one anvil rotates (around the vertical axis of the press, or torsion axis) while the other remains fixed in the frame for inducing torsion (or twist) to the sample (the so-called "shearing mode"; e.g., Álvarez-Murga et al., 2017); ii) both anvils rotates with opposite direction to one another for potentially inducing greater torsion in the sample than the previous mode (i); iii) both anvils rotates in the same direction for acquisition of the sample tomographic image. These modes of anvils motions imply it is not possible to collect the tomographic image while inducing torsion (mode (i) or (ii)), which has to be stopped before initiating the simultaneous anvils rotation (mode (i)).

The heating system of the RoToPEc consists of an electrical feed-through attached to the upper and lower housing of the anvils (Fig. 2.4b). The connection system is thought for not interfering with the anvil motion or the acquisition of the tomography (Philippe et al., 2016). A cooling system is installed to prevent the anvils, motors and bearings from damaging during HT experiments. This cooling system can prevent the anvils from exceeding a temperature of ca. 60°C when the sample is at ca. 2000°C (Philippe at et al., 2016).

The sample assembly employed for the RoToPEc has similar design as the one used for the PE apparatus. The details on the specific assembly design and components employed in my work are reported in chapter 3 (section 3.3.1). Ones of the most important features of this type of assembly, essential for a successful HP-HT torsion experiment with *in-situ* X-ray tomography, are its external components. They consist of a boron epoxy transmitting medium or gasket, transparent to X-ray, and Poly-ether-ether-ketone (PEEK) or Lexan ring, which is placed around the gasket. This ring limits the lateral extrusion of the cell assembly during pressurization or torsion (Philippe et al., 2016).

2.3. The X-ray tomography (XRT)

In this section, I give a general background and the main concepts of the X-ray tomography (XRT) (or X-ray computed tomography, XCT). Concepts and equations are from Kastner and Heinzl (2018). Information on how X-ray beams are usually generated (i.e., the source of X-ray beams) in laboratories or facilities for X-ray tomography goes beyond the purpose of this section. Further details can be found in e.g., Kastner and Heinzl (2018).

The XRT is a powerful, non-destructive tool for collecting 3-d information on internal structural features, or heterogeneities, in a large variety of materials. Nowadays, high-resolutions XRT systems are installed and available in multiple laboratories and

facilities, employing different kind of set-ups or geometry depending on the main field of study, samples size or resolution to accomplish. One of the most common (standard) set-up geometries used for X-ray tomography is the cone beam XRT geometry (Fig. 2.5).
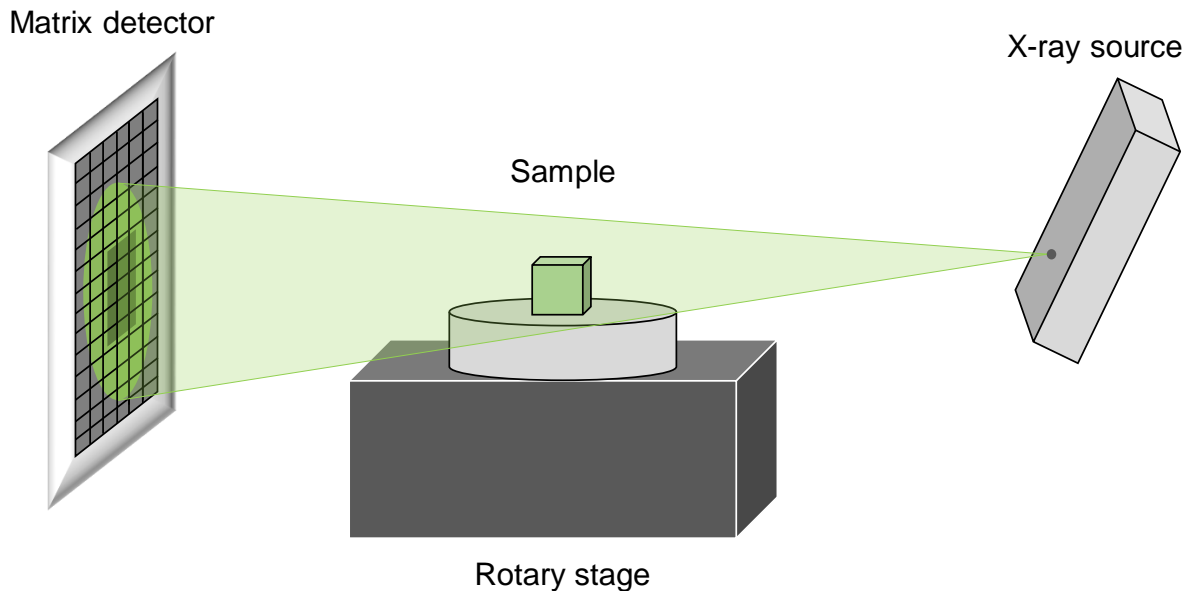
Figure 2. 5. Simple representation of the cone beam configuration for X-ray tomography acquisition.

A sample is placed on a high-precision rotation stage between the X-ray tube (source) and the digital matrix detector. The X-ray source generates a conic beam of photons that penetrate the sample to be analyzed. A magnified penetration image (i.e., the 2D radiograph or projections) is recorded by the X-ray matrix detector. The sample is rotated step by step to acquire the projection images at each angular position. Typically, projections widths in the order of fractions of a degree are collected, during a full rotation of 360° of the stage.

The achievable resolution of an XRT scan of a sample generally depends on the geometrical magnification m, which determines the opening cone beam angle (Fig. 2.6). Geometrical magnification m depends on the source-detector distance (SDD) and source-object distance (SOD) (Fig. 2.6) according to the following equation (Kastner and Heinzl, 2018):

$$m = \frac{SDD}{SOD} \quad (2.1).$$
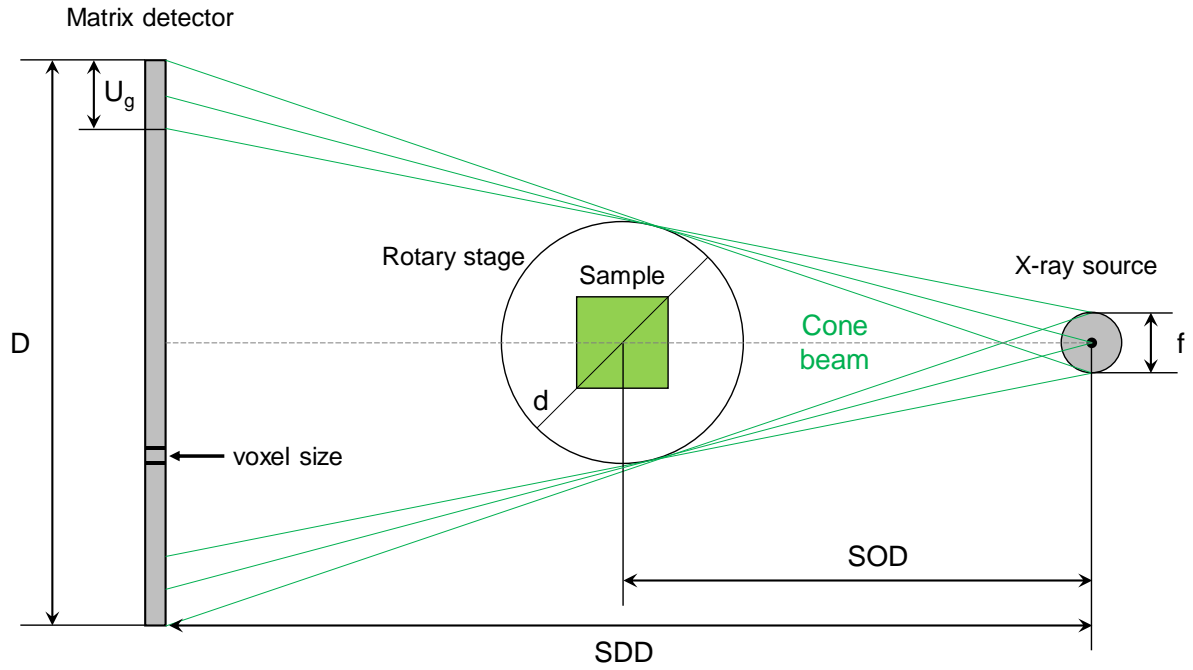
Figure 2. 6. Geometry and components of the cone beam configuration for X-ray tomography acquisition (Fig. 2.5) (after Kastner and Heinzl, 2018). Geometrical magnification is determined by the source-object distance (SOD) and source-detector distance (SDD), as well as the effective detector width D and the diameter d of the measuring volume. f is the focal spot size, and Ug is the geometric unsharpness in the penetration image in relation to the focal spot size f.

The closer to the source a sample is positioned, the higher is the geometrical magnification and the resolution of the XRT scans. Additionally, the resolution of the scans can be affected by the size of the focal spot and the quality of the rotation axis. For instance, for the cone beam XRT geometry, the highest accuracy is achieved in the beam that is perpendicular to the rotary axis, going through the focal spot of the X-ray source.

The volumetric dataset from XRT scans is constituted by volumetric elements, called 'voxels'. The size of a voxel s is determined by the detector pixel size p according to the following equation (Kastner and Heinzl, 2018):

$$s = \frac{p}{m} \ (2.2).$$

Typical voxel sizes are in range between 1 μm and 0.2 mm. For high-resolution XRT systems, the minimum voxel size s can be 100 nm or even lower.

In order to accurately collect the tomography image, the entire sample must remain within the field of view and the cone beam during the rotation. It should be noted that the maximum geometrical magnification m (defined above) of an XRT system is also

limited by the ratio of the detector width D and the sample diameter d (Fig. 2.6). Therefore, it can be also expressed according to the relation:

$$m = \frac{D}{d} \ (2.3).$$

In the collection of the scans, the geometrical unsharpness U_g also occurs (Fig. 2.6), depending on the focal spot size f and on the magnification m following the relation (Kastner and Heinzl, 2018):

$$U_g = f(m - 1) \ (2.4).$$

2.3.1. The parallel beam XRT geometry: Synchrotron-based XRT

Here, I introduce the XRT employed in synchrotron facilities, which differs from a standard geometry.

Synchrotron tomography itself is known since the 1990 (e.g., Kastner et al., 2010a; Kastner and Heinzl, 2018 and refrences therein). Nowadays, high-quality imaging capabilities of synchrotron radiation are available to a number of facilities all over the world (e.g., PETRA III at ESRF (European Synchrotron Radiation Facility) in Grenoble; SLS (Swiss Light Source) in Villigen; Hasylab in Hamburg; Elettra Sincrotrone in Trieste; NSLS (National Synchrotron Light Source) and APS (Advanced Photon Source) in the USA; SOLEIL in France).

The XRT employed in synchrotrons (or the so-called s-XCT in Kastner and Heinzl, 2018) shares the same theory and principles as the ones of a common XRT (section 2.3). However, the feature that makes the difference between the two is that the synchrotron-based XRT involves a nearly parallel beam (Fig. 2.7) of high brilliance.

Synchrotron sources deliver a very high flux that is at least 1000 times larger than X-ray tubes at small source size (e.g., Kastner et al. 2010a). The spatial resolution can be increased by applying 'pink' or monochromatic radiation, which also allows the generation of phase contrast of internal interfaces between phases. A parallel, 'pink' or
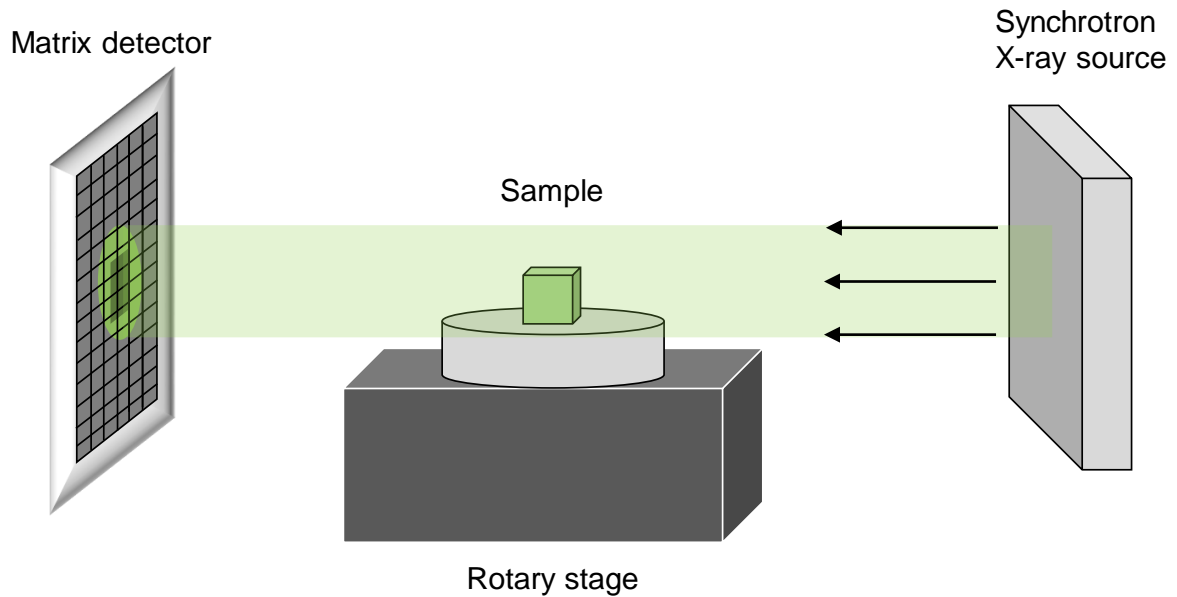
Figure 2. 7. Simple representation of the parallel beam configuration for X-ray tomography acquisition at synchtron facilities.

monochromatic beam set-up allows to generate an exact and quantitative reconstruction, free of geometrical and beam hardening artifacts, also reaching resolutions well below 1 µm.

2.3.2. The XRT data reconstruction

Reconstruction algorithm(s) are usually implemented in XRT facilities to obtain the 3D image from the collected 2D radiograph. The early work by Feldkamp (1984) describes an approximating reconstruction algorithm to retrieve 3D data from a series of 2D radiographs for circular cone beam tomography, based on a filtered back-projection algorithm. Nowadays, a large number of other reconstruction techniques exist, such as three-dimensional Fourier-based reconstruction methods, as well as algebraic and statistical reconstruction methods (e.g., algebraic reconstruction technique, and direct iterative reconstruction) (Kastner and Heinzl, 2018 and references therein).

In the present work, the majority of the XRT images were reconstructed at the PSICHE beamline (King et al., 2016, 2019) that employs a code of PyHST-2018 routines. The PyHST-2018 routines are based on the hybrid distributed code PyHST2 (Mirone et al., 2014), which employs a filtered back-projection algorithm (e.g., Feldkamp, 1984), and

iterative reconstruction techniques with *a priori* knowledge (e.g., Soleimani and Pengpen, 2015). As input, the code takes raw data and human readable parameters file (Mirone et al., 2014). This includes the rotation axis parameter, which is calculated or adjusted by the user beforehand. Then, the data undergo pre-processing steps before launching the reconstruction in the PySHT-routines. A description of the pre-processing is given as follows (from Mirone et al., 2014).

The first part of the pre-processing involves the removal of the signal coming from the detector dark-current background-noise. The dark-current is an image giving the averaged signal measured by the detector when no beam is present. Additionally, the correction for the beam spatial inhomogeneity is performed in this first treatment, the so-called flat-field correction (e.g., Mirone et al., 2014; Álvarez-Murga et al., 2017). The flat-field images are recorded in the absence of the sample. They, therefore, are images of the beam. Several flat-fields can be acquired at different times during the scans to track the beam shape drifts. Flat field corrections are applied dividing every radiography by the flat-field obtained. After correction for the flat field, the signal can still contain noise, which can be regularized by a median filter. The concept of the median filter is the following: if the median of the pixel neighbors is smaller than the pixel value by more than a given threshold, then the pixel value is substituted with the neighbors' median. After the flat-field correction and application of the median filter, the Paganin filtering method is implemented for phase contrast enhancement (Paganin et al., 2002).

After the above pre-processing, the radiographies are rearranged in a sequence of the so-called "sinograms" (e.g., Kastner and Heinzl, 2018), with one sinogram corresponding to a detector line perpendicular to the rotation axis (Mirone et al., 2014).

Before launching the 3D reconstruction of the sample dataset, a last pre-processing can consist in reducing artifacts, such as the so-called "ring artifacts" (e.g., Koeberl et al., 2002; Wang et al., 2011; Gharbi and Blunt, 2012; Mirone et al., 2014; Berg et al., 2018;

Kastner and Heinzl, 2018). Ring artifacts belongs to the group of motion artifacts that be observable in images. They are mainly due to irregularities of neighboring detector pixels, caused by the rotation or internal motions of the sample during acquisition (Fig. 2.8).
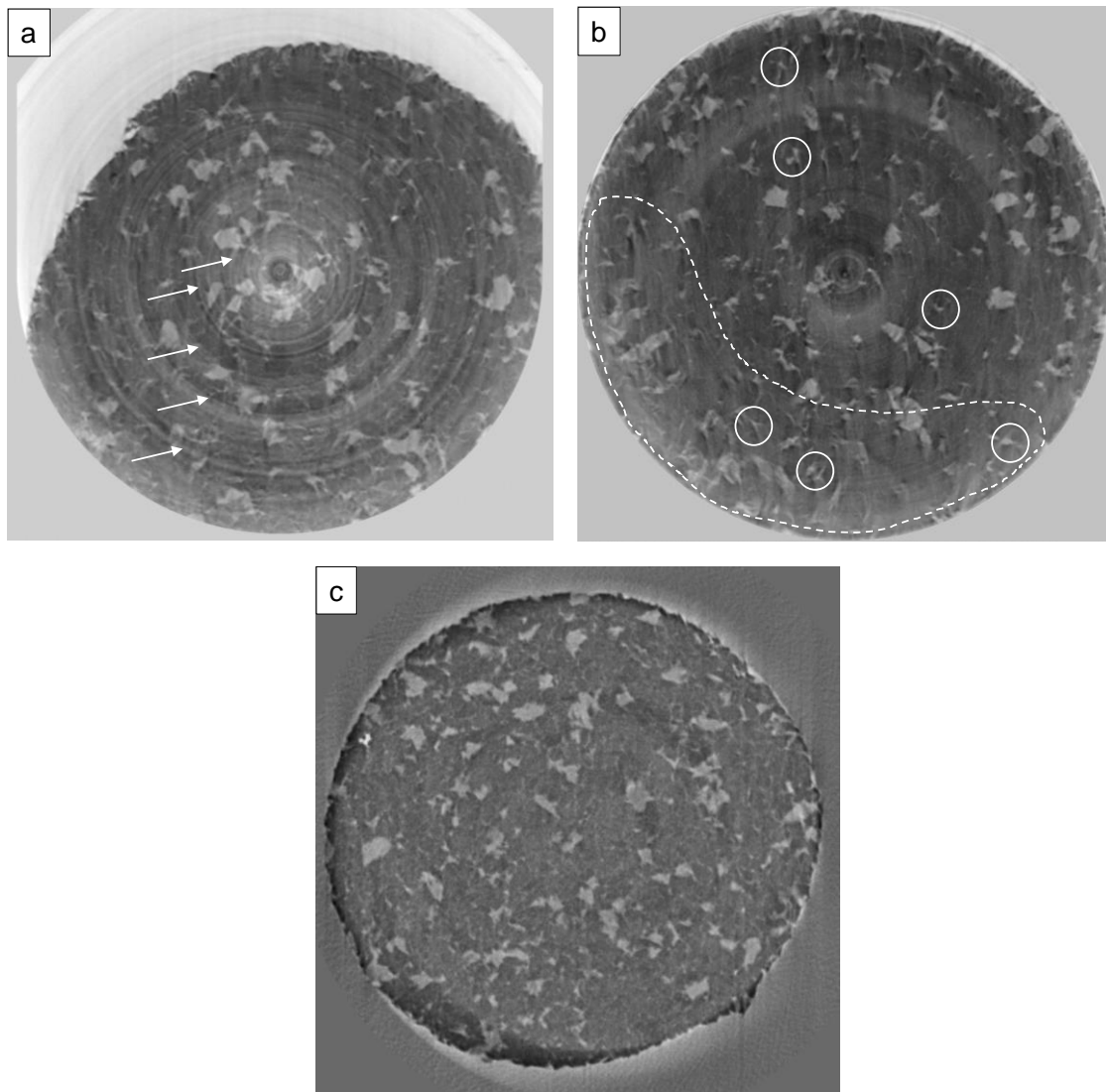
Figure 2. 8. Tomographies images (negative contrast) of the present work (samples of olivine+serpentine; serpentine is brighter (olivine is darker) showing motion artifacts (a-b) in comparison with an image with no visible artifacts (c) obtained during reconstruction processing. a) pronounced ring artifacts (white arrows) The position of the zone axis of rotation in the image is off because of the high extent of sample motion during acquisition. b) the white-dotted line area shows the location where sample motions artifacts ("blurriness" and shadings) are concentrated. White-solid circles show a type of motion artifact ("triple-point" or "Mercedes" structures) related with motion of punctiform structure (see text).

In my work the sample motions during acquisition were often present, and mainly caused by the sample responses to the transferred deformation. In some cases, the internal motions were extensive and developed in the whole sample, which resulted in

the position of the zone axis of rotation to be completely off in the images (Fig. 2.8a). In these cases, the adjustment of the zone axis of rotation during pre-processing was rather difficult, and it was necessary to repeat the acquisition. In other cases, where the position of the zone axis was considered satisfactory, the main issue was the presence of "image blurriness", shading and "triple-point" structures (or the so-called "Mercedes" structures) (Fig. 2.8b), along with some remaining ring artifacts. In comparison with the common ring artifacts that can be reduced by the application of flat-field filters (e.g., Mirone et al., 2014), the others cannot. For these, a solution could be relying on the "triple-point" structures, if enough present and visible (Fig. 2.8b). The so-called "Mercedes" correction filter (see also section 3.3.2) in the PyHST-2018 routine at the PSICHE beamline can be used (A., King, pers. communication). The filter relies on the selection of multiple "triple-point" structures, and uses them as "hot-spots" to correct the image and reduce the remaining motion artifacts. However, this filter worked well locally, and it was not always possible to correct these motions artifacts everywhere in the area of the sample (Fig. 2.8b). A specific pre-processing tool or filter to fully correct motion artifacts different from common ring artifacts is still not available or documented (A., King, pers. communication). Any remaining motion artifacts at this stage were, therefore, corrected during post-processing treatment (see section 3.5), after the reconstruction.

, and is either done by filtered back projection or by the advanced *a priori* knowledge technique (e.g., Mirone et al., 2014). After reconstruction of the 3D XRT data, these are post-processed in an external software for treating 3D image and performing quantitative analysis. The steps for post-processing used in the present work are given in chapter 3 (section 3.5).

2.4. The electron microscopy

I investigate the recovered samples from deformation experiments using the electron microscopy techniques of i) scanning electron microscopy (SEM) with electron back-scattered diffraction (EBSD), and ii) transmission electron microscopy (TEM). In the following sections, I give main concepts of these techniques (corresponding information from Passchier and Trouw, 2005, and Williams and Carter, 2009), as well as provide the sample preparations and analytical settings.

2.4.1. Scanning electron microscopy (SEM) and electron back-scattered diffraction (EBSD)

The scanning electron microscope (SEM) is an important tool for the study of microstructures. Nowadays, its accessibility in many laboratories and relatively easy use makes the SEM a powerful tool to complement and sometimes replace the optical microscope. This is also due to the SEM significantly greater magnifications than those of a common optical microscope.

A representation of the SEM is given in Figure 2.9. A sample is placed in a chamber under vacuum, and investigated by scanning a beam of electrons across the sample. The electrons can be either scattered back from the surface of the sample (back-scattered electrons, BSE), or cause the sample to emit secondary electrons (SE). Both types of electron signal are collected by detectors. The electrons that strike the detectors are used to build up grey-scales images of the sample on a monitor. The amount of SE and BSE generated by the sample is directly proportional to the atomic number (Z) of the constituent elements in the minerals, with heavier elements yielding more electrons. This results, for instance, in visible brighter tones on the built-up BSE-images for the minerals comprising heavier elements, and otherwise darker tones for the minerals containing lighter elements. Therefore, identifying the individual minerals in the sample is possible
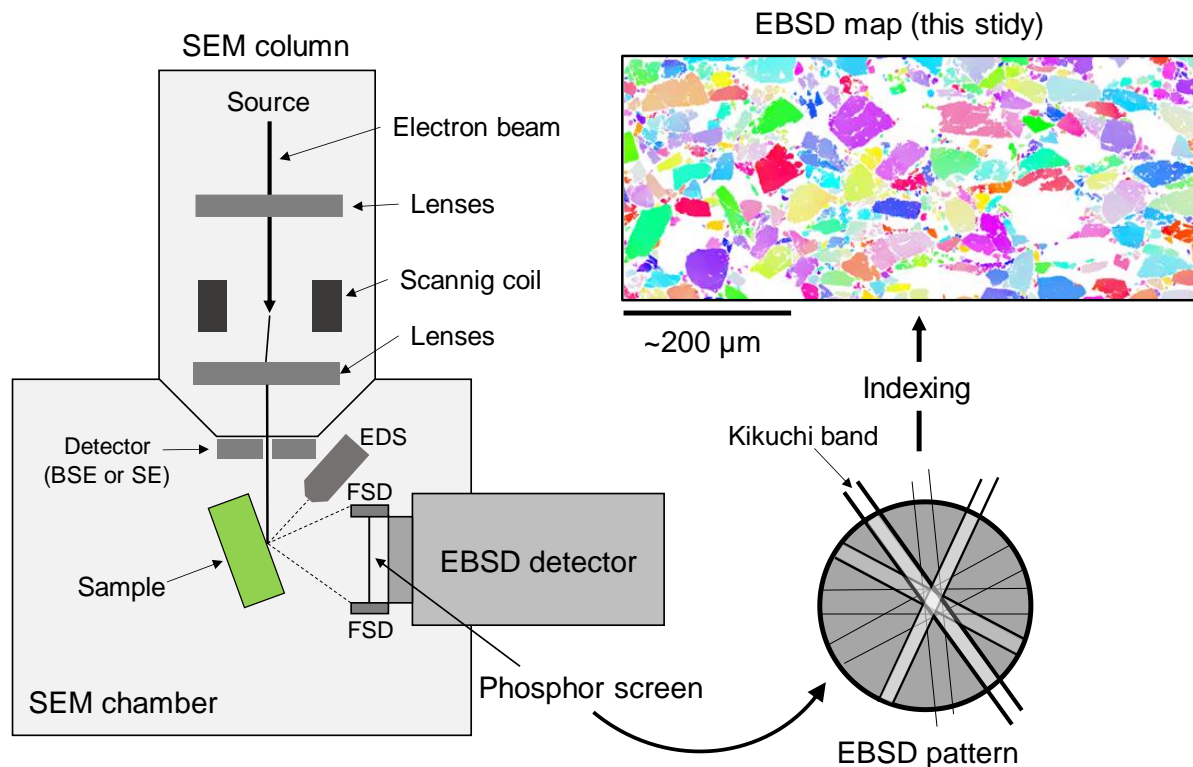
Figure 2. 9. SEM geometry and EBSD acquisition setting. The sample is titled at ca. 70° inside the vacuum chamber. The beam hits the sample at an angle of ca. 20° with respect to the sample surface. The EBSD detector collect forward scatter electrons with upper and lower detectors (FSD), as well as the EBSD pattern thanks to the phosphor screen. The available software in the microscope process the EBSD pattern collected across the sample, indexing the recorded Kikuchi bands with the theoretical crystal structure information to obtain the EBSD map. Here it is shown an example of EBSD map obtained in the present work for olivine showing different crystallographic orientation (color-coded). Collection of energy dispersive spectroscopy (EDS) for chemical analysis during EBSD acquisition is possible. BSE is back-scattered electrons. SE is secondary electrons.

through simple imaging in the SEM. Furthermore, diagnostic of the minerals in the sample can be done by complementing the imaging with chemical analysis. This is usually done with energy dispersive spectroscopy (EDS). This tool measures the energy of X-rays emitted by the irradiated sample, and can identify the elements in the sample, so that the chemical composition can be determined both qualitatively and quantitatively.

Information on the crystal structure and orientation of minerals can be obtained through one of the uses of the back-scattered electrons in the SEM, i.e. by electron back-scattered diffraction (EBSD) (Fig. 2.9). The EBSD provides quantitative microstructural information about the crystallographic nature of materials. It reveals grain size, grain boundary character and grain orientation, as well as texture and intracrystalline plasticity

features (see section 1.1.1). Centimeter-sized samples with millimeter-sized grains, to metal thin films with nanograins can be analyzed. The usual nominal angular resolution limit is ca. 0.5° and the spatial resolution is related to the resolution of the SEM, but for modern field-emission SEMs (FE-SEMs), 20 nm grains can be measured with reasonable accuracy. SEM-EBSD technique usually operates at an acceleration voltage of 10-30 kV, and incident beam current of 1-50nA.

The principle behind the EBSD analysis is the detection and study of a specific diffraction pattern called 'Kikuchi-pattern' or simply EBSD pattern (Fig. 2.9). The pattern consists of straight bright bands, also called 'Kikuchi bands', which have a direct relation to the lattice planes of the diffracting crystal: the center line of each of the bands directly corresponds to the gnomonic projection of the lattice planes. The width of the Kikuchi band is approximately proportional to the electron diffraction angle on the related lattice plane. The band intensity profile corresponds to the dynamic electron diffraction intensity obtained in a rocking experiment across the related lattice plane.

The EBSD pattern can be generally and easily detected if a specific geometry in the SEM chamber between the primary electron beam, sample and EBSD detector is respected. The sample is tilted at ca. 70° (or >50°) with respect to the horizontal in the SEM chamber. The vertical electron beam hits the titled sample surface whose axis is oriented at ca. 20° with respect to the vertical of the primary electron beam (Fig. 2.9). When the primary beam interacts with the crystal lattice of the sample, low energy loss back-scattered electrons are channeled and are subject to path differences that lead to constructive and destructive interference. The geometry between the electron beam and the tilted sample satisfy the production of the most intense cone of back-scattered electrons diffracted and emanated from the sample. The EBSD detector has to be placed in the path of the diffracted electrons and in a short distance from the titled sample, so that the diffraction pattern can be captured. The EBSD detector is usually a digital camera

and employs a phosphor screen. The CCD chip of the camera is illuminated by the phosphor screen that intersects the spherical diffraction pattern. The phosphor, therefore, converts the diffracted electrons into light suitable for the CD camera to record, and the EBSD pattern can be finally seen.

In order to find the crystal orientation from the pattern and obtain information on the crystal lattice, the lines (Kikuchi bands) in the pattern must be *indexed*, i.e. the corresponding lattice planes should be identified. This is usually done by the implemented EBSD software available for the microscope. The software matches the experimental (detected) EBSD pattern with the theoretical crystal structure information previously loaded in the software.

2.4.1.1. Samples preparations and analytical setting

The quality of the EBSD analysis and detection of a good EBSD pattern strongly depends on the surface quality of the sample. Therefore, a careful sample preparation must be performed.

In the present study, recovered samples from deformation experiments are first covered with water-like viscosity super-glue and then let them dry overnight for about 8-12h. This is to harden the sample and improve its integrity, to avoid unnecessary embrittlement during the cutting procedure that follows. The cutting of the sample is done to retrieve a slice of specific surface (orientation) to be analyzed. In the present work, I chose the slice surface that corresponds to the plane approximately parallel to the applied shear direction of the experiments (see e.g. chapter 4, section 4.3.1). The cutting is done by using a diamond wire saw. After embedding the selected slice(s) in ca. 1-inch diameter epoxy mold, these are mechanically and chemically polished. The chemical polishing is crucial to obtain a good-quality surface for EBSD analysis. I employ a colloidal-silica polishing using the VibroMet2 vibratory polisher with non-crystallizing colloidal silica suspension (0.05 µm particle size). This polishing is carried out for ca. 8-12 h.

The EBSD analysis were carried out on two different microscopes of the PMEL at the University of Lille, both with field-emission gun (FEM-SEMs). One is the JEOL JSM-7800F-LV, and the other is the HITACHI SU-5000. The procedure employed in both SEMs consists of first tilting each sample until ca. 70°, collecting high-resolution pictures in forward-scattering mode (FSE) mode and then using the software-in house "AZtec" (Oxford instruments, https://nano.oxinst.com/products/aztec) to collect the 'Kikuchi pattern', index it and acquire EBSD maps (Fig. 2.9).

The EBSD data are acquired in the range of 20-30 KV, with beam current of ca. 2-30 nA, working distance of ca.10-15 mm, and low vacuum conditions of ca. 10-15 Pa.

In the JEOL, drifting or shifting of the EBSD mapping can happen during acquisition. To avoid this, the 'auto-lock' mode on the microscope software is employed. This mode corrects for the possible shifting or drifting of the scanning beam, correcting it during acquisition. However, this mode drastically increases the timing of the map acquisition. For instance, using a step size of ca. 0.3 µm for a good-quality map of ca. 200 x 150 µm, the acquisition time can be up to ca. 20 h. Because of this downside of the JEOL, I acquire larger EBSD maps on the HITACHI, which does not show issues correlated with drifting or shifting of the scanning beam, and has a higher scanning beam frequency than the one of the JEOL. Using the HITACHI with a scanning beam step size of ca. 0.5-1.5 µm, larger good-quality maps (up to ca. 700 x 400 µm) are acquired within ca. 2 h.

2.4.2. Transmission electron microscopy (TEM)

Transmission electron microscopy allows observations of structures as small as a few nanometers at magnifications up to ca. 350 000X. TEM employs high speed electrons accelerated at a voltage of ca. 200-300 kV, which interact with small thin-foil sample permitting the transmission electron mode. Structure of single dislocations (line defects), deformation lamellae, subgrain, grain boundaries and twins can be imaged and

investigated in relation with their orientation and the crystal lattice. This can allow to properly characterize and quantify the deformation mechanism in minerals and rocks.

Nevertheless, TEM can be a destructive technique that can damage the sample of interest. Some minerals can be very sensitive to high-voltage electron beam such the one in TEM. This is, for instance, the case for serpentine (e.g., Van De Moortèle et al., 2010), i.e. one of the minerals in the aggregates investigated in the present work (see sections 1.4, 2.1). Therefore, extra care must be taken during the analysis in TEM. A considerable experience to carry out the analyses efficiently and in a fair amount of time depending on the kind of sample is required. Moreover, the TEM is most useful to identify and study microstructures on the grain scale, or to determine the mineral content and microstructure of very fine-grained rocks (<1 μm) that are difficult to study by SEM. The limitation of TEM is, therefore, the small amount of volume material that can be studied. If one has to obtain information on crystal structure/orientation or deforming microstructures on a large or bulk sample-scale, the SEM with EBSD technique (see section 2.4.1) is generally considered more suitable and less time consuming.

A sketch overview of the TEM is given in Figure 2.10. A beam of high velocity electrons passes through the thin foil sample suspended in a high vacuum. The electron beam is deflected by electronic lenses, which enlarge the image, and the result is focused onto a fluorescent screen, photographic plate or CCD camera.

The sample-holder in TEM can be rotated in all directions. In certain orientation and observation modes, electron diffraction patterns can be imaged. These can be used to determine the crystallographic orientation of the crystal/sample, as well as to determine the good orientation conditions to image and interpret dislocations. Moreover, specific imaging mode are possible to observe dislocations. For instance, dislocations can be visible as shadows in an otherwise bright (transparent) matrix, or as bright lines in an
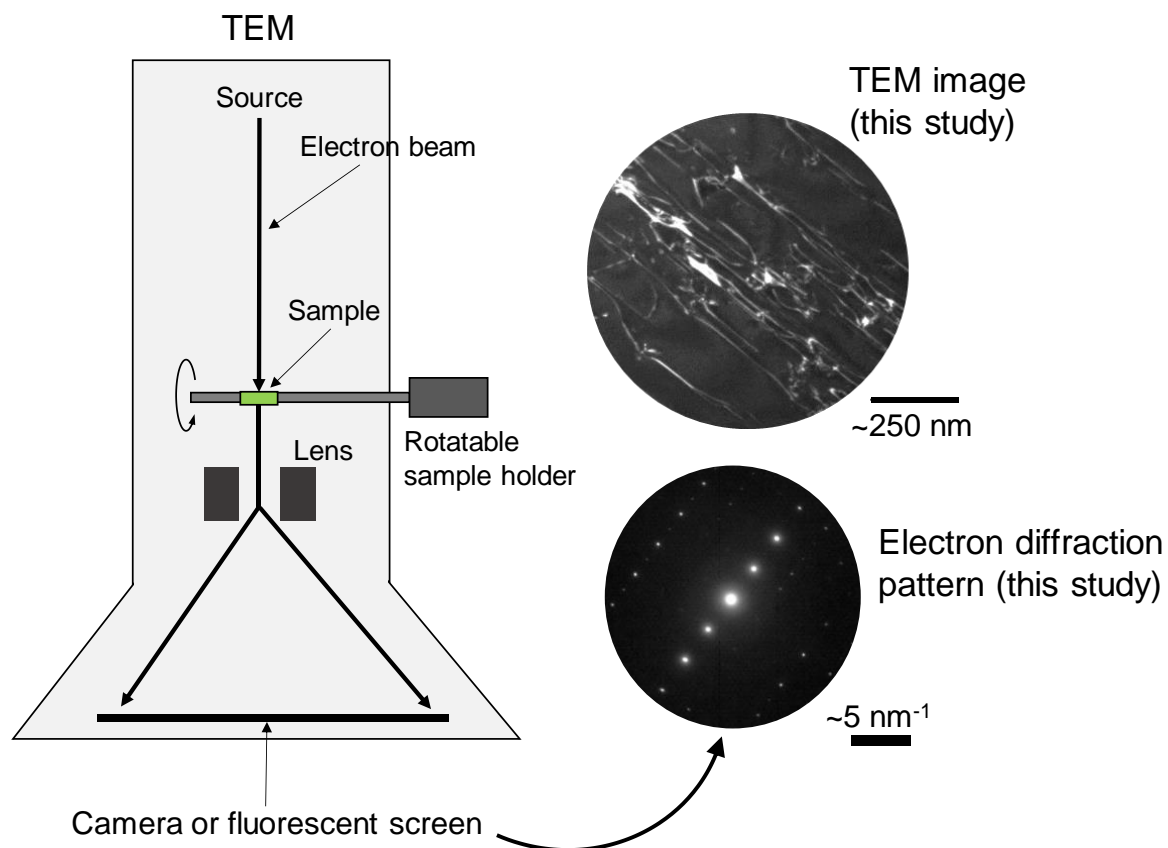
Figure 2. 10. Simple representation of the TEM geometry for standard imaging and diffraction. The high-velocity electrons pass through the sample, then the lens transmits the transmitted beam to the camera or fluorescent screen to obtain the electron diffraction pattern (right, on the bottom) or images (right, top). The given diffraction pattern is an example of a zone axis collected in the present work for an olivine single crystal. The central (brighter) spot corresponds to the primary transmitted beam (000), whereas the others correspond to reflections of the diffracted planes in the crystal (hkl). The given image on the top is a dark-filed (DF) image (see text) acquired in the present work for the same crystal of olivine showing liner defects in the crystal lattice, i.e. dislocations (bright). It is acquired by selecting a specific diffraction spot of the electron diffraction pattern (i.e., DF-imaging mode, see text).

otherwise dark matrix. This latter is the case if a specific imaging mode is performed in the TEM, i.e. the dark-field (DF) mode. This is done by selecting (or exciting) a specific spot reflection (specific *hkl* plane) in the electron diffraction pattern to acquire the image. The reflection of a selected *hkl* plane of interest in the electron diffraction pattern is often referred as g reflection, with the *g* vector perpendicular to the lattice plane of interest. The DF image shows bright-contrast features or lattice defects in the sample belonging to that selected or excited plane (Fig. 2.10). The DF mode is commonly used to image and characterize dislocations.

2.4.2.1. Analytical and imaging setting

In the present work, focused ion beam-SEM (FIB-SEM) is used to make lamellae (thin-foil samples) out of a selected experimental product (specifics and results given in sections 4.3.3, 4.4.1).

TEM imaging is carried out with the microscopes FEI Tecnai G2-20 equipped with FE-gun, and a FEI TITAN Themis 300 that permits scanning transmission microscopy (i.e., STEM). The common dark-field (DF, e.g., Fig. 2.10) imaging is used to image the dislocation in the present work. Additionally, another imaging mode is tested for dislocation characterization to possibly reach optimum dislocation contrast, i.e. the weak-beam DF (WBDF) (e.g., Williams and Carter, 2009). In this imaging methodology, after an appropriate zone axis is visible, it is necessary to tilt the sample until the so-called two-beam condition is satisfied. This condition implies that that only two *hkl* reflections are visible, and only one *hkl* reflection of interest is strongly excited. From this conditions, it is necessary to slightly keep on tilting the sample until the so-called *g/3g* condition is satisfied (i.e., the standard method to obtain high quality WBDF image; e.g., Williams and Carter, 2009). This latter is obtained by bringing the *g* reflection of interest in the optical axis, or under the so-called kinematical diffraction condition *s > 0*, with *s* indicating the angular deviation of the primary electron beam wave vector k from the Bragg conditions; the *3g* reflection is instead excited, and satisfies the Bragg condition *s = 0* (Fig. 2.11).

The DF or WBDF imaging are used at different *g* reflections to characterize the dislocations, i.e. to infer their Burgers vector. It corresponds to the measure of the lattice distortion caused by the presence of the dislocation in the crystal lattice, and is used to
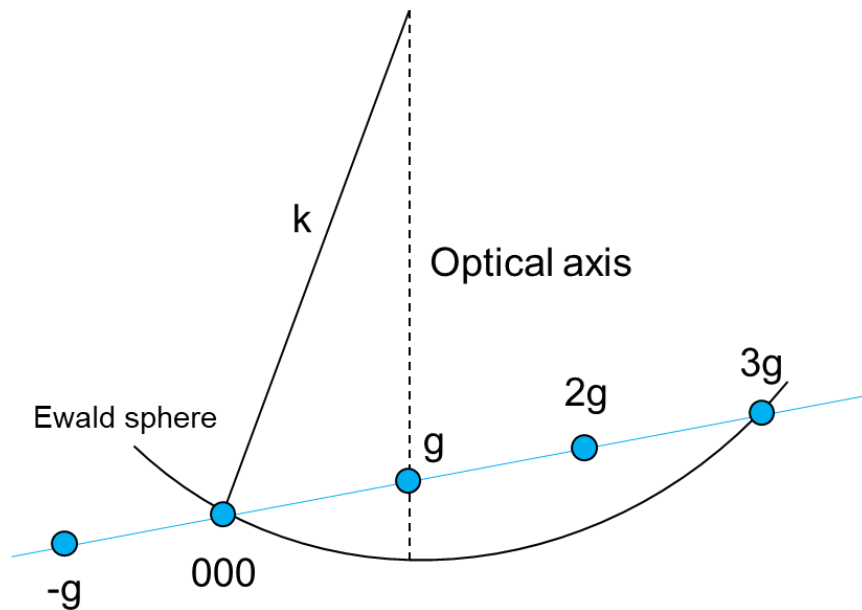
Figure 2. 11. Simple illustration of the g/3g conditions in the TEM. The g refection is in the optical axis with a large deviation from the Bragg conditions, which is represented by the intersection of the g spots with the theoretical Ewald sphere. The 3g satisfy the Bragg conditions and is therefore excited. k is the primary, transmitted electron beam (000 spot, or origin of the electron diffraction pattern).

determine the possible slip system active in the mineral of interest. A dislocation is visible only if its Burgers vector has a particular orientation with respect to the electron beam. It is necessary to rotate the crystal and selecting/exciting different g reflections using DF or WBDF imaging to see at which g reflections the dislocation becomes invisible, therefore determining at which g it becomes otherwise visible. This together with determination of the diffraction pattern of the crystal allows determination of the Burgers vector for that dislocation. This standard method is called invisibility criteria (e.g., Williams and Carter, 2009 and references therein) for g reflections of interest.

Chapter 3

Deformation of two-phase aggregates: the use of the RoToPEc with *in-situ* high-pressure, high-temperature X-ray tomography

3.1. Introduction

Because of the complexity of rocks deformation, three-dimensional information are often needed to reconstruct the spatial distribution and alignment of fabrics and minerals in rocks (Fusseis et al., 2014). For this, serial sectioning techniques are traditionally employed (e.g., Bryon et al., 1995; Mock and Jerram, 2005; Holzer et al., 2006; Jerram and Higgins, 2007; Morales et al., 2018). However, these are destructive techniques damaging the sample volume, and can require long data acquisition.

X-ray tomography (XRT) (see section 2.3) can allow three-dimensional investigation of internal structures without damaging the samples in a large range of materials, including rocks for the study of their petrography and deformation microfabrics (e.g., Denison and Carlson, 1997a, 1997b; Van Geet et al., 2001; Koeberl et al., 2002; Tarplee et al., 2011). Nowadays, the coupling of *in-situ* XRT with deformation devices is been implemented, or under development, in laboratories (e.g., McBeck et al., 2020; Shi et al., 2020; Shi et al., 2021) and been possible in synchtron facilities (e.g., Wang et al., 2011; Kareh et al., 2012; Fusseis et al., 2012; Fusseis et al., 2014; Philippe et al., 2016; Butler et al., 2020; Colombier et al., 2020; Dobson et al., 2020; Marone et al., 2020).

Deformation experiments with *in-situ* XRT permits to image and quantify microstructural information at different deformation stages (time-resolved), removing part of the ambiguities in the interpretation of rock deformation behavior and evolution with strain.

Among deformation devices, torsion systems and set-ups with *in-situ* XRT exist for the study of rock deformation (Wang et al., 2005, 2011; Le Godec et al., 2012; Fusseis et al., 2014; Di Genova et al., 2016; Yu et al., 2016; Philippe et al., 2016; Renard et al., 2016; Voltolini et al., 2019; Dobson et al., 2020). Torsion tests can transfer much higher strains than other devices, and can be conventionally used to experimentally explore features associated with large geological shear strain (Paterson and Olgaard, 2000). Nowadays, torsion devices can be found coupled with *in-situ* synchrotron-based XRT. These devices are either "low" pressure torsion systems (Di Genova et al., 2016; Dobson et al., 2020) or apparatuses based on higher pressure, large volume presses (e.g., Wang et al., 2005, 2011; Le Godec et al., 2012; Yu et al., 2016; Philippe et al., 2016; Álvarez-Murga et al., 2017). In comparison with "low" pressure torsion systems enabling confining pressures in the order of a MPa, torsion apparatuses are capable of inducing large shear deformation at confining pressures greater than a GPa together with high temperatures up to ca. 1000°C or more. Therefore, in conjunction with *in-situ* XRT, they allow to image evolving microstructures associated with large geologically-relevant shear strains at high pressure and temperature conditions of the Earth interior.

Nowadays, only few synchrotron beamline facilities enable the use of high-pressure torsion apparatuses coupled with *in-situ* X-ray tomography (e.g., Wang et al., 2005, 2011; Álvarez-Murga et al., 2017; Philippe et al., 2016). The devises used consist in an opposed-anvils design that allow for 360° access to the sample in the equatorial plane. Rotation of the motorized anvils allow for either tomography acquisition, if both anvils are rotated simultaneously, or torsion, if a single anvil is rotated while the other remains

fixed in the press frame. A high-pressure torsion apparatus, the Drickamer module (e.g., Wang et al., 2005, 2011), is coupled with a high-pressure X-ray Tomography Microscope (HPXRTM) at GeoSoilEnviro-CARS (GSECARS) in the Advanced Photon Source (Argonne National Laboratory, IL, USA). The other high-pressure torsion apparatus is the RoToPEc (Philippe et al., 2016; Álvarez-Murga et al., 2017; see section 2.2). The RoToPEc has been tested and used in various synchtron experimental facilities (Philippe et al., 2016), including the ID27 beamline at ESRF synchrotron (Grenoble, France), the I12 beamline at DIAMOND synchrotron (Didcot, Oxfordshire, UK), and the PSICHE beamline (Philippe et al., 2016; King et al., 2016; 2019) at SOLEL synchrotron (Saint-Aubin, France).

In the present work, I use the RoToPEc apparatus on the PSICHE beamline at SOLEIL synchrotron. In section 2.2, I introduced the RoToPEc design for experiments with *in-situ* X-ray tomography. In this chapter, I provide details on the specific methodology and approach I use to study time-resolved deformation of two-phase aggregates, carrying out torsion with *in-situ* X-ray tomography at high pressures, high temperature (HP-HT, ca. 4-5 GPa, ca. 300-400°C, respectively). The motivation for this chapter is a result of the scarce documentation on the use of the RoToPEc for the study (through imaging) of microstructure evolution and deformation of multi-phase rocks with strain.

The RoToPEc was previously employed for the study of metal phase transition (Boulard et al., 2020) and melt percolation (Berg et al., 2018) at high confining pressure and temperature. Previous work only provided a proof-of-concept of the apparatus potential to deform samples at transferred large simple shear strain (i.e., $\gamma > 3$), as well as to *in-situ* image some deforming microstructural features (Philippe et al., 2016). There is, however, a previous work reporting the use of a variation of the RoToPEc, the roPEc (rotating PEc), to induce torsion in rocks in conjunction with X-ray tomography (Berg et al., 2017). Yet, they could not perform time-resolved study of microstructural evolution, since the roPEc does not allow the *in-situ* tomographic acquisition.

The following sections define contents that are intended for a technical paper. I first report results on temperature calibration performed at PHSICHE for the RoToPEc. Then, I provide the experimental procedure on torsion in the RoToPEc with *in-situ* X-ray tomography at PSICHE. Afterwards, I report how I estimate the evolving strains transferred to the samples with increasing deformation. I subsequently outline the specific tomographic image processing I chose for studying deformed microstructures in torsion configuration. I also provide representative examples of three-dimensional quantifications on the evolving microstructures of the phases of interest in the aggregates with increasing deformation. Finally, I discuss the experimental set-up shortcomings along with possible improvements for the instruments and methodology.

3.2. RoToPEc: temperature calibration at PSICHE

3.2.1. Motivation

The RoToPEc apparatus with *in-situ* XRT has been tested and used on the PSICHE beamline at SOLEIL or in other facilities for studies of materials under high confining pressures and temperatures (Le Godec et al., 2012; Philippe et al., 2016; Álvarez-Murga et al., 2017; Berg et al., 2018; Boulard et al., 2020). However, the temperature conditions in the assembly are poorly constrained for the RoToPEc.

Previous work that conducted experiments with Paris-Edinburgh cell (PEc)-type apparatuses used unpublished data of temperature calibrations that were obtained *in-situ* at synchrotron facilities (Morard et al., 2007; Bromiley et al., 2009; Le Godec et al., 2012; Philippe et al., 2016; Berg et al., 2017, 2018; Boulard et al., 2020; Giovenco et al., 2021). Most of them relied on *in-situ* cross calibrations obtained with calibrants with well-known equation of state (Morard et al., 2007; Bromiley et al., 2009; Le Godec et al., 2012; Philippe et al., 2016; Berg et al., 2017, 2018). Others used power-temperature relations obtained with a thermocouple (Boulard et al., 2020; Giovenco et al., 2021). The

currently documented temperature calibrations and gradient variation in the cell mainly regard the common PEc (e.g., Riva et al., 2018). To our knowledge, a temperature calibration that exists for the RoToPEc has been performed and tested ex-situ, i.e. outside the synchtron facility using a DC power supply (at Sorbonne University, IMPMC lab, Paris, unpublished data, Y., Le Godec, pers. communication). No temperature calibration had been yet performed in the RoToPEc on the PSICHE beamline at SOLEIL, which employs an AC power supply.

In deformation experiments, the issue of a large uncertainties on temperature can hamper the interpretation of the microstructural evolution in the aggregates investigated in the present work. Therefore, a better constrain of the temperature is necessary. Moreover, a temperature calibration for the RoToPEc could be of an interest for other potential users carrying out experiments at the PSICHE beamline.

In the following I give the methods and results of offline temperature calibration experiments carried out at SOLEIL on the PSICHE beamline in the RoToPEc using a thermocouple. Conditions of confining pressure are ca. 4 GPa and ca. 2 GPa.

3.2.2. Materials and experimental procedure

The assembly design for the temperature calibration experiment is given in Figure 3.1. The basic design is similar as the one employed in previous work using the RoToPEc, roPEc or PEc (Morard et al., 2007; Bromiley et al., 2009; Le Godec et al., 2012; Philippe et al., 2016; Berg et al., 2017, 2018; Boulard et al., 2020). This kind of assembly design is also employed for the actual deformation experiments in the present work (see section 3.3.1). A Boron-epoxy mixture (5:1) was used to make the gasket (or pressure medium), which was sandwiched between the opposed anvils and surrounded by a PEEK ring (see also section 2.2). This was placed in the equatorial plane of the gasket (Fig. 3.1). The PEEK contains or reduces the sideways expansion (or lateral expansion/extrusion) of the assembly being squeezed during pressurization or torsion under high pressure and

temperature. The extremities of the thermocouple wires were bent to make a junction between the wires, and placed at the center of the assembly (Fig. 3.1). Below the thermocouple junction, within the hBN (hexagonal boron nitride) sleeve, a sintered MgO (magnesium oxide) plug was placed, whereas a compacted fine-grained powder of MgO was used to completely surround the thermocouple junction in the cell (Fig. 3.1). The thermocouple wires were inserted from opposing sides of the assembly through the PEEK ring, gasket, heater and sleeve (Fig. 3.1). To keep the PEEK ring in place and prevent it from breaking during pressurization, some sticky tack was placed on two opposite sides of the PEEK ring (Fig. 3.1).
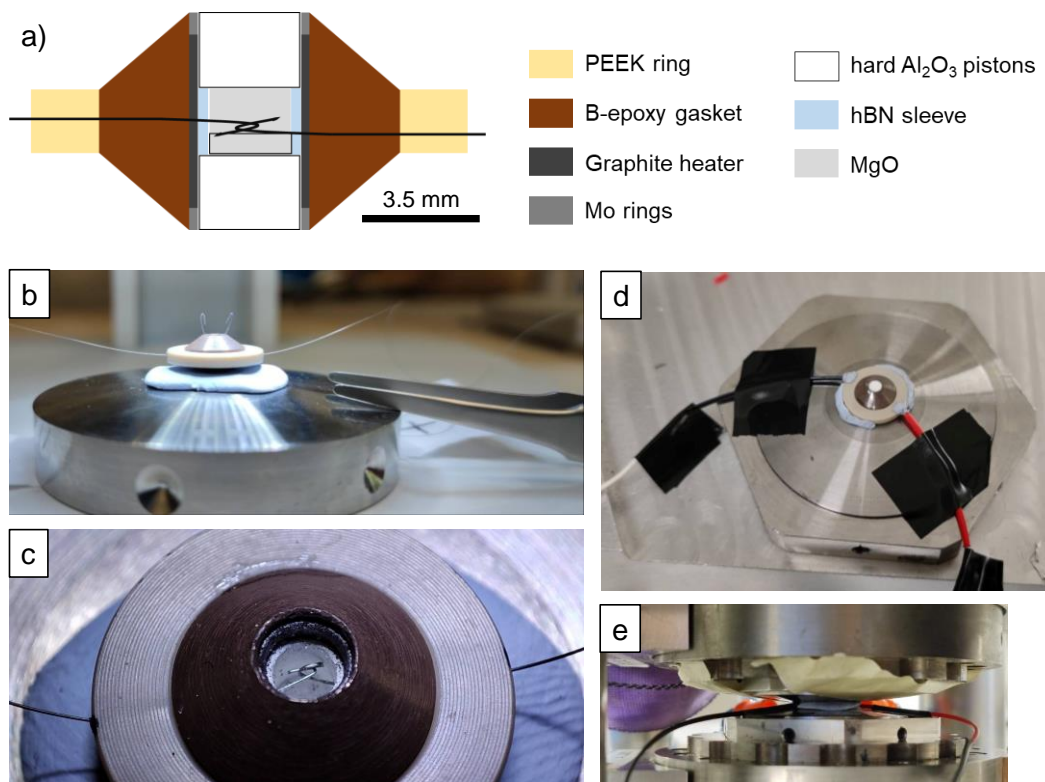
Figure 3. 1. Assembly design and preparation for the offline temperature-calibration experiments in the RoToPEc on the PSICHE beamline at SOLEIL synchrotron (France). a) Sketch showing the assembly design and parts, with the thermocouple wires (black) extremities forming a junction (or contact) at the center of the assembly. b) photograph showing a step in the preparation of the assembly placed on top of one of the anvil. Each wire of the thermocouple is let pass through the cell parts and then pulled up outside the cell to make the hook for the junctions. c) photograph showing the detail of the junction between the wires at the center of the cell. c) assembly design ready with the thermocouple wires, placed on one of the anvil before putting them in the RoToPEc. The sticky tack (light-blue) surrounds the PEEK, and covers the holes where the thermocouple passes through. e) assembly under pressure sandwiched between the anvils in the RoToPEc.

Four different runs were performed, during which the assembly was cold-pressed up to pressure of interest (see next section 3.2.3) before heating. Thermocouple measurements were recorded during cycles of heating and cooling.

3.2.3. Results

Out of the four different runs performed, only one was successful and used to record the temperature inside the cell during multiple cycles of heating and cooling. Power (W) vs. temperature (°C) data points were collected during this run at two different pressures, first at 250 bars, and then at 150 bars, corresponding to ca. 4 GPa and ca. 2 GPa of confining pressure, respectively. Figure 3.2 shows the power (W) vs. temperature (°C) data points collected during this run for the two pressures.
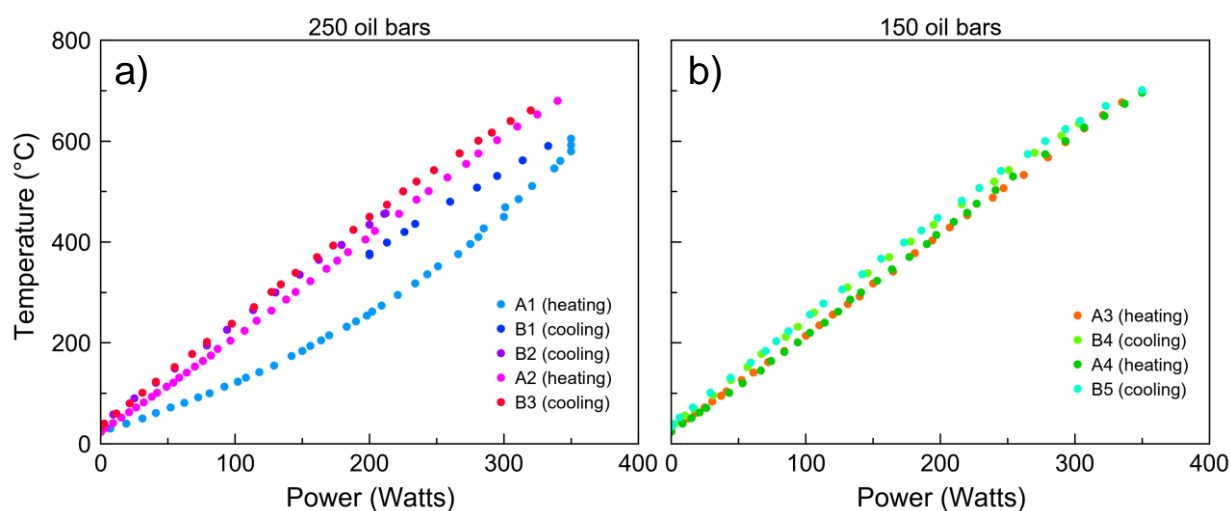
Figure 3. 2. Diagram showing the power vs temperature data points collected during different cycles of heating and cooling in the same run at the two different pressures. a) data points collected at higher oil pressure (corresponding to ca. 4 GPa). Trends A1(heating) and B1 (cooling) show different trends with respect to the others (from B1 to B3), which instead agree with each other. b) data points collected at lower oil pressure (corresponding to ca. 2 GPa). Here, the all data points agree with each other.

In the data collected at higher pressure, the first cycles of heating and cooling (trends A1 and B1; Fig. 3.2a) show different trends compared to the ones that follow (from trend B2 to B3, Fig. 3.2a), which instead agree with each other. The change in slope visible in A1 (Fig. 3.2a) could be an indication of a change of heater efficiency: below ca. 100 W, the slope (efficiency) is linear and much lower. The heater gains the best efficiency

after the cycle B1, with the subsequent trends showing a certain stability (Fig. 3.2a, b). The trends A2 and B3 at 42.5 tons (ca. 4 GPa) (Fig. 3.2a) and the ones from A3 to B5 at 25.5 tons (ca. 2 GPa) (Fig. 3.2b) were fitted using a linear relation between the temperature (°C) and the power (W). Table 3.1 shows the linear fit parameters for each of the two pressures. The highest power value of 350 W corresponds to a temperature of 723.40$\pm$14.65°C at ca. 4 GPa (42.5 tons or 250 bar in load), and 719.62$\pm$14.58°C at ca. 2 GPa (25.5 tons or 150 bar in load).

Table 3.1. Linear relation between the power (W) and the temperature (°C) used to fit the trends in Fig. 3.2a, b.

Load (bar)	Pressure (GPa)	Fit: T(°C)=aP(W)+b		Residual Std. Dev.	R^2
		a	b		
250	~4	1.981	29.901	14.657	0.994
150	~2	1.963	32.551	14.581	0.995

T is temperature. P is power. R^2 defines the goodness of the fits.

The obtained temperature calibration based on thermocouple measurements is used to obtain the temperature conditions for all the deformation experiments performed in the RoToPEc at the PSICHE beamline (see section 3.3, and chapter 4).

Figure 3.3 is given to compare the power-temperature relation of the present work with other available relations from previous studies (Riva et al., 2018; Y., Le Godec, pers. communication). Riva et al. (2018) obtained power-temperature relations for PEc-type assembly designs. Y., Le Godec (pers. communication) provided a calibration for the RoToPEc assembly that was performed ex-situ (outside synchtron facility).
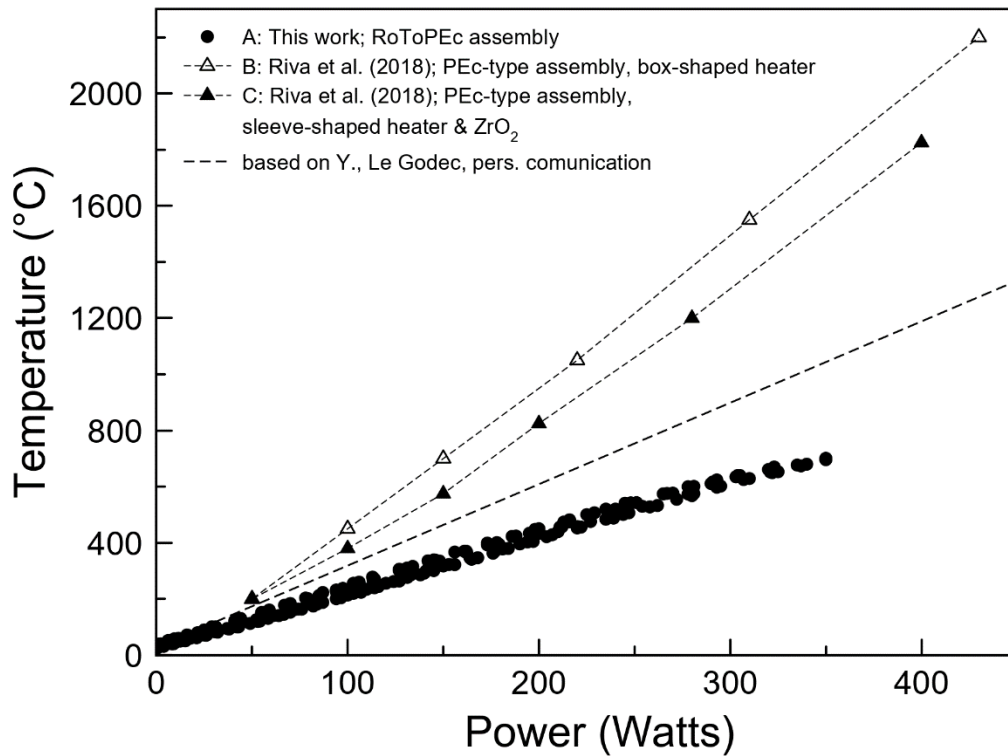
Figure 3.3 Diagram showing the comparison between the power –temperature relation of the present work (RoToPEc at PSICHE beamline) and other relations from previous work for Pec-type assemblies (Fig. 6 in Riva et al., 2018), and from a calibration provided by Y., Le Godec (pers. communication) for the RoToPEc.

The power-temperature relation obtained in the present work does not agree with the one obtained by Y., Le Godec (pers. communication) (Fig. 3.3), suggesting his calibration may not be suitable to use for RoToPEc experiments at the PSICHE beamline.

The power-temperature relation obtained in the present work (A in Fig. 3.3) shows high discrepancies with respect to the power-temperature relations by Riva et al. (2018) (B and C in Fig. 3.3). These significant discrepancies could be due to differences in materials used for the assembly cell parts, which are discussed as follows.

For one of their power-temperature relations, Riva et al. (2018) (B in Fig. 3.3) employed an assembly with a box-shaped graphite heater, which encloses the area around the sample from all sides (Fig. 2 in Riva et al., 2018: assembly "aB_hBN"). In the present work, the assembly has a sleeve-shaped graphite heater (Fig. 3.1). A box-shaped heater could be more efficient in conducting heat to the sample than a sleeve-shaped heater. However, the use of a box-shaped heater for our experiments has to be excluded

beforehand, since its shape could compromise the coupling between the anvils and the sample. This coupling is necessary to transfer the deformation to the sample in our experiments in the RoToPEc.

For the other reported power-temperature relation (C in Fig. 3.3) Riva et al. (2018) employed an assembly with zirconia as part of the gasket (pressure medium), and with a sleeve-shaped graphite heater (Fig. 2 in Riva et al., 2018: assembly "Zirc_Dia"). In the present work, the gasket of the assembly is entirely made of boron-epoxy mixture (Fig. 3.1), which is less insulating than zirconia. Therefore, in this case the use of the zirconia is likely responsible for the difference between the power-temperature relation of the present work (A in Fig. 3.3) and the one by Riva et al. (2018) (C in Fig. 3.3).

The results on temperature calibration presented here suggest the employed assembly (Fig. 3.1, see also section 3.3) is the least efficient compared to other studies (Fig. 3.3). I suggest that future work on temperature calibration for the RoToPEc should test the zirconia as insulating material to partly replace the boron-epoxy mixture for the gasket of the assembly. This could potentially make the assembly more efficient to transfer heat to the sample during HT-HP experiments in the RoToPEc.

3.3. Experiments with *in-situ* X-ray tomography

3.3.1. Materials and deformation experiments

Each of the experimental aggregates I investigate for the deformation experiments are made of two minerals. The first is an olivine + serpentine aggregate, and the second a pyroxene + garnet aggregate (see section 2.1). For olivine + serpentine aggregate, starting materials of powder mixtures are used, whereas for the pyroxene + garnet aggregate, core samples made out of a selected rock sample (Locatelli et al., 2018) are used (see section 2.1). A list of the experiments carried out during this thesis project is given in Table 3.2.

The experiments are carried out in the RoToPEc at SOLEIL synchrotron on the PSICHE beamline. A detailed description of the beamline specifics can be found elsewhere (e.g., King et al., 2016, 2019).

The assembly for the hot-pressurization of the starting materials and subsequent deformation (torsion) is given in Figure 3.4.
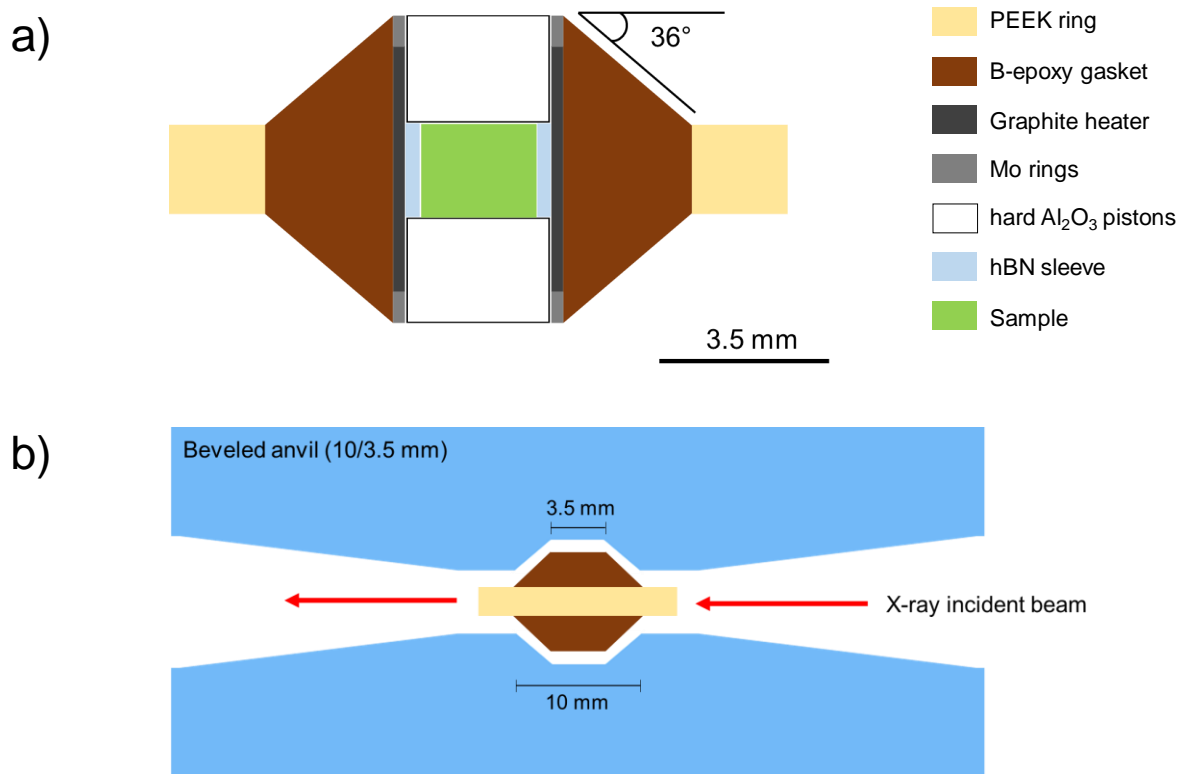
Figure 3. 4. Assembly and anvils designs employed in the RoToPEc apparatus for torsion experiment with in-situ X-ray tomography acquisition. (a) cross-section showing the assembly parts. (b) sketch showing the anvils design with the assembly and direction of incoming X-ray beam. The PEEK thickness approximately corresponds to the X-ray tomography view when the assembly is squeezed between the anvils, before torsion is applied.

Table 3. 2. Summary of the runs conducted in the RoToPEc apparatus for the two aggregates investigated in the present work.

Run (#)	Analysis	Aggregate	Composition (vol.%)	Grain size (µm)	Measured oil pressure (bars)		Calculated/estimated pressure (GPa)		Power (W)	Temperature (°C)	Anvil Twisting	
					Max.	Min.	Max.	Min.			Max. angle (°)	Rate (°s^{-1})
15	in-situ XRT	olivine+serpentine (powder)	Se10Ol90 Se: 9.9±0.5*	50-100	250		~4	1.4	150 (AC)	~330	90	0.02
15b (ex-situ)	post-mortem XRT	olivine+serpentine (powder)	Se10Ol90 Se: 10.4*	50-100	240		~4		96 (DC)		225	0.02
16	in-situ XRT	olivine+serpentine (powder)	Se10Ol90	50-100	150		~2	≤0.8	200 (AC)	~430	90	0.02
16b (ex-situ)		olivine+serpentine (powder)	Se10Ol90	50-100	143		~2		143 (DC)		225	0.02
16c (ex-situ)	post-mortem EM	olivine+serpentine (powder)	Se10Ol90	50-100	143		~2		144 (DC)		No twist	
17	in-situ XRT post-mortem EM	pyroxene+garnet (core)	Grt35Omp60	up to 200	190		~3	~1	200 (AC)	~430	216	0.02
18	in-situ XRT post-mortem EM	olivine+serpentine (powder)	Se20Ol80 Se: 16.6±0.9*	50-100	250		~4	~3	170 (AC)	~370	225	0.02
18b (ex-situ)	post-mortem EM	olivine+serpentine (powder)	Se20Ol80	50-100	243		~4		114 (DC)		No twist	
19	in-situ XRT	pyroxene+garnet (powder)	Grt15Omp85	> 50	~250		4.7	2.4	280 (AC)	~500	168	0.02
20 FAILED		pyroxene+garnet (powder)	Grt70Omp30	> 50								
21	in-situ XRT	pyroxene+garnet (powder)	Grt70Omp30	> 50	~250		4.5	1.6	280 (AC)	~500	270	0.02
22	in-situ XRT	pyroxene+garnet (core)	Grt35Omp60	up to 200	190		~3	0.8	336 (AC)	~710	135	0.02
23	in-situ XRT post-mortem EM	olivine+serpentine (powder)	Se10Ol90 Se: 9.6±1.6*	50-100	250	130	5.2	4.2	170 (AC)	~370	225	0.02
24	in-situ XRT	olivine+serpentine (powder)	Se20Ol80 Se: 18.9±2.5*	50-100	250	130	5.3	4.5	150 (AC)	~330	225	0.02
25	in-situ XRT post-mortem EM	olivine+serpentine (powder)	Se10Ol90 Se: 10.6±1.3*	50-100	250	130	~5	~4	200 (AC)	~430	225	0.02
26	in-situ XRT	olivine+serpentine (powder)	Se20Ol80	50-100	250		~4		300 (AC)	~630	135	0.02

'ex-situ' refers to experiments not performed at the synchrotron beamline, i.e. without in-situ X-ray tomography (XRT). For run #15b, post-mortem XRT is performed at the University of Lille (see section 3.5). 'EM' refers to electron microscopy analyses. Se is serpentine. Ol is olivine. Grt is garnet. Omp is omphacite, i.e. pyroxene. AC refers to alternative current. DC referes to direct current. (*) refers to phase volume amount obtained from image processing of the tomograhies (see section 3.5).

Torsion is generated by rotating one of the anvil at a speed of 0.02°/s while the other remains fixed in the press frame. In this study, the experiments aim for a confining pressure of ca. 4 GPa and temperatures of ca. 300-400°C. Confining pressure is determined by *in-situ* X-ray diffraction on h-BN (assembly sleeve, Fig. 3.4). Temperatures in the samples are determined through the off-line experiments performed at the PSICHE beamline using a thermocouple presented in the previous section (section 3.2).

The experiments in the RoToPEc are coupled with *in-situ* XRT acquisition carried at a specific interval of anvil twisting angle. To acquire the tomography scans, the torsion in the RoToPEc needs to be stopped, and only later the rotation of both anvils to collect the full tomography is possible. Before each acquisition of the tomography scans, the sample is quenched by shutting down the power supply and waiting a fair amount of time (between 15 to about 40 min.) to let the sample stabilize. Preliminary series of experiments were carried out by keeping the sample at HT after stopping the torsion, and quenching proved to be necessary in our experimental conditions to reduce the sample motion and reconstruct properly the X-ray tomographies (see section 3.5, 3.7). After the collection of the tomography, the sample is again heated up to the target temperature and deformed to higher anvil twisting angle. The twist interval is either 45° or 90°. These steps are repeated for the whole duration of each deformation experiment until the maximum angle of twist is reached. This latter mainly depends on the gap between the opposed anvils (Fig. 3.4). Because of sideways expansion of the assembly during torsion, the opposed anvils tend to approach each other and the gap shortens. This gap corresponds to the X-ray tomography view, which does not match with the actual sample length (or height) during torsion (see sections 3.4, 3.7).

3.3.2. In-situ X-ray tomography acquisition

In-situ X-ray tomography acquisition is performed using pink-beam illumination at the PSICHE beamline (e.g., King et al., 2016, 2019). The beam is filtered with a mirror

to cut the high energies, then aluminum and tin filters are used to define the spectrum. This gave an average X-ray beam energy of 39 keV, with beam size of ca. 2.8 x 2.8 mm^2. With this setting, 1 voxel corresponds to ca. 2 μm^3 in the later reconstructed tomography images. Each acquired X-ray image is corrected for inhomogeneous illumination using a white-field image taken prior to each tomography scan and from the electronic noise by a dark-current image.

A speed of anvil rotation of 0.15°/s is used to collect ca. 3000 projections from 0° to 180° rotation. Each X-ray tomography image is reconstructed using the in-house PyHST-2018 routines at the PSICHE beamline. A Paganin filter (e.g., Paganin et al., 2002) is chosen to reduce the rings artefacts (e.g., Kastner and Heinzl, 2018). A so-called "Mercedes" correction is performed to reduce as much as possible the sample motion artefacts (e.g., Kastner and Heinzl, 2018). The final reconstructed slices are later stacked to render 3-d images in Avizo 9.0 software. The further processing of the images is given in section 3.

3.4. Strain and strain rate

During deformation experiments, strain is an important parameter to be quantified. The anvil twisting angles shown in Table 3.4 do not correspond to the actual strains in the samples. The deformation is partly taken up by the cell parts or lost in frictions at the interfaces. In this section, I report how to measure the evolution of the actual strain transferred to the samples during torsion as the angle of twist increases in the RoToPEc.

One of the common ways to obtain the simple shear strain in a rock during torsion is adding in the cell assembly one or more strain marker(s) to measure their relative displacement, or motion. These strain marker(s) can usually be observed in the plane parallel to the transport direction of the torsion or shear direction (analogue to the plane

defined as the longitudinal tangential section in Paterson and Olgaard, 2000). The marker(s) can give an angle between the top and bottom surfaces of the sample in the plane parallel to the shear direction Then, the relation to obtain the simple shear strain can be $\gamma = \tan \alpha$ (e.g., Fossen, 2012), where γ is the simple shear strain and α the angle shown by the strain marker(s). Previous work on rock deformation with the Drickamer module showed examples of this methodology (e.g., Wang et al., 2011; Girard et al., 2016). Wang et al., (2011) used the relative displacement of two metal-alloy particles placed at the top and bottom of the sample to obtain the angle. Girard et al. (2016) measured the angle on the profile of a torqued metal foil marker placed in the assembly and with the same height as the one of the sample. However, in the present study with the RoToPEc apparatus none of the two methods given above are possible. This is because of the gap reduction between the opposed anvils during the experiment. The shadow of the anvils partially covers the sample along its height in the *in-situ* radiographs, as the gap between them reduces from top and bottom. Additionally, in the present work I used starting material powders hot-pressed *in-situ*, and in this case inserting a metal foil as a strain marker and keeping it fixed within the powder is difficult. In a previous work on deformation using a variation of the RoToPEc, the roPEc, Berg et al. (2017) estimated the strain by a digital measure of the anvil rotation (or anvil twisting angle) during off-line experiments. They overcome the problem of the anvil decoupling from the cell and sample by checking the strain on platinum strain markers in the recovered samples. In fact, the roPEc does not allow the *in-situ* tomography since the rotation of both anvils is not possible. Here, I take advantage of the *in-situ* tomography in the RoToPEc to estimate the simple shear strain transferred to the samples by tracking the motion of a marker at each anvil twisting angle.

Multiple particles of a phase with a higher density than the sample are loaded inside the assembly sleeve along with the sample powder. This phase should not react

with the sample under the experimental conditions. The particles are placed in multiple locations within the sample powder, i.e. close to either the center or the rims of the sleeve, and at different heights. Then, the reconstructed X-ray tomography images are used to locate at least one particle marker that should be visible for the whole experiment as the angle of twist increases. This implies that it is necessary to locate a particle close to the center of the sample along its height, since the central area of the sample along its height can be visible for the whole duration of the experiment despite the gap reduction between the anvils as twisting increases.

An overview of the methodology used to calculate the strain is given below in Figure 3.5.
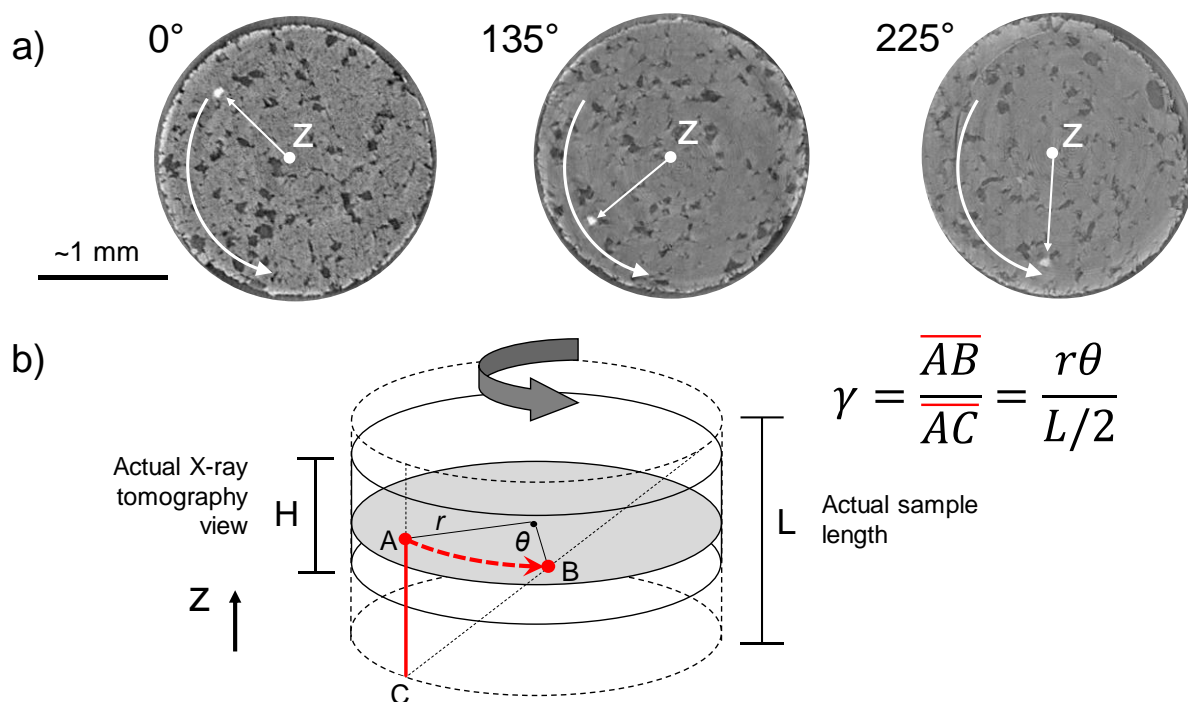
Figure 3. 5. Method to estimate the simple shear strain transferred to the samples in the RoToPEc. Z is the torsion axis. (a) reconstructed X-ray tomography images of a sample showing the motion of the grain marker (white arrow) with increasing anvil twisting angle. (b) Sketch of the theoretical transfer of simple shear strain in a cylindrical sample under torsion showing the simple shear strain calculated in our study. H is the image height (X-ray tomography view). L is the actual height of the sample. r is the radius to the marker location. θ is the measured twisting angle in the sample. Red-dotted arrow shows the observed marker motion (AB) defining the arc length of θ. Red vertical line corresponds to half of the height of the sample (AC). γ is the simple shear strain.

First, the total γ can be calculated by measuring the total motion of the marker on tomography images, which correspond to the plane where the transport of the torsion lies, perpendicular to the torsion axis (Fig. 3.5a). It is analogue to the plane defined as transverse section (TS) in Paterson and Olgaard (2000) for torsion experiments. The motion of the marker gives the real twisting angle θ transferred to the sample. Then, the relation to obtain γ is

$$\gamma = \frac{r\theta}{L/2} \ (3.1),$$

with θ expressed in radians, r being the radius from the center to the location of the marker, and L being the length (or total height) of the recovered sample after deformation (Fig. 3.5b). The marker is located close to the center of the sample along L (Fig. 3.5b). The product of $r\theta$ gives the arc length that defines the marker motion (Fig. 3.5b). The r is here taken as an average value since the marker tends to move away from the center of the sample assembly as the twisting increases. This is due to a sample lateral expansion linked to the uniaxial compression component in the sample during torsion. The uniaxial strain component ε is calculated with the relation

$$\varepsilon = \frac{\Delta L}{L_0} \ (3.2),$$

with ΔL being the difference between the final (after deformation) and initial (before deformation) lengths of the sample. The initial sample length L_0 is measured on a sample recovered from a static (i.e., no twisting of the anvil) *ex-situ* experiment performed on the RoToPEc at similar values of P and T. The length L_0 is used as a representative initial length of reference to estimate ε in all the experimentally deformed samples.

The *ex-situ* deformation experiments in the RoToPEc are also used to estimate the simple shear strain rate $\dot{\gamma}$ and the uniaxial strain rate $\dot{\varepsilon}$. The *in-situ* deformation (i.e., the twisting) needs to be stopped at the beamline to acquire the X-ray tomography at different twisting steps (see section 3.3.2). Therefore, obtaining the actual duration of the

deformation at the beamline is not straightforward. On the other hand, *ex-situ* deformation can be carried out continuously, and the actual duration of the deformation during torsion can be obtained. For the *ex-situ* experiments, I use the same speed of anvil rotation as for *in-situ* experiments (i.e., 0.02°/s; see section 3.3.2).

Using the $\dot{\varepsilon}$ obtained, an actual length L' is estimated for the sample at each anvil twisting angle. With ε' the uniaxial strain at a specific twisting angle, and Δt the time interval to a specific twisting angle, the relations are

$$\varepsilon' = \dot{\varepsilon}\Delta t, \qquad L' = L_0(1 - \dot{\varepsilon}\Delta t) \ (3.3).$$

Finally, the value of L' and the angle θ' (real twisting angle measured at each twisting step, Fig. 3.5a) can be used to calculate the simple shear strain γ' at each anvil twisting step using the form of equation 3.1.

Since both components of uniaxial and simple shear strains are present in our samples, the equivalent strain ε_E and the equivalent strain rate $\dot{\varepsilon}_E$ are estimated following the relations

$$\varepsilon_E = \sqrt{\varepsilon^2 + \frac{4}{3}\gamma^2}, \qquad \dot{\varepsilon}_E = \sqrt{\dot{\varepsilon}^2 + \frac{4}{3}\dot{\gamma}^2} \ (3.4),$$

where $\dot{\varepsilon}$ is the uniaxial strain rate, and $\dot{\gamma}$ is the simple shear strain rate.

It should be pointed out that the above methodology to obtain simple shear and uniaxial strains at each twisting step assumes a constant uniaxial compression strain rate (equation 3.3), while in reality it can vary with time.

Table 3.3 shows the estimates of strains and strain rates along with the twisting angles in three samples where the markers are used. The estimates refer to markers located close to the edge of the samples (Fig. 3.5). In one run I could also track a marker closer to the center of the sample, which gave lower γ and ε_E than for the marker close to the edge (run #24, Table 3.5). This is consistent with the expected strain gradient along the radius of the samples. The highest value of simple shear strain γ transferred to the

sample close to the edge is ca. 5 at a strain rate $\dot{\gamma}$ of 10^{-4} s^{-1} and a real twisting angle θ of ca. 100°(225°anvil twisting angle), whereas the uniaxial strain ε is ca. 0.5 at a strain rate $\dot{\varepsilon}$ of 10^{-5} s^{-1} (run #23; Table 3.5). The corresponding equivalent strain ε_E is ca. 600% at $\dot{\varepsilon}_E$ of 10^{-4} s^{-1} (run #23; Table 3.5).

Table 3. 3. Strain and strain rates with anvil and sample twisting angles calculated from in-situ X ray tomography in three experimental runs. Pressure and temperature conditions are also given.

Run (#)	Composition (vol.%)	Measured oil pressure (bars)		Calculated/estimated pressure (GPa)		Power (W)	Temperature (°C)	Twisting angle (°) and rate (s⁻¹)			Strains			Total strain rates (s⁻¹)		
		Max.	Min.	Max.	Min.			Anvil twist angle	Anvil twist rate	Sample twist angle (θ)	ε^a	γ	ε_E (%)^b	ε	γ	$\varepsilon_E{}^b$
23	Se10Ol90 Se: 9.6±1.6*	250	130	5.2	4.2	170 (AC)	~370	0	0.02							
								90		47	0.2	1.5	177.1			
								135		59	0.3	2.2	255.5			
								225		102	0.5	5.1	592.6	3.9×10^{-5}	4.7×10^{-4}	5.5×10^{-4}
24	Se20Ol80 Se: 18.9±2.5*	250	130	5.3	4.5	150 (AC)	~330	0	0.02							
								90		45	0.2	1.2 / 1.1	143.5 / 132.1			
								135		60	0.3	1.9 / 1.5	217.4 / 172.9			
								225		103	0.4	4.1 / 2.9	479.5 / 334.3	3.9×10^{-5}	$3.8 \times 10^{-4} / 2.7 \times 10^{-4}$	$4.4 \times 10^{-4} / 3.1 \times 10^{-4}$
25	Se10Ol90 Se: 10.6±1.3*	250	130	~5	~4	200 (AC)	~430	0	0.02							
								90		61	0.2	1.4	160.8			
								135		74	0.3	2.0	228.3			
								225		118	0.5	4.5	516.8	4.9×10^{-5}	4.1×10^{-4}	4.8×10^{-4}

Se is serpentine. Ol is olivine. ε is uniaxial strain. γ is simple shear strain. ε_E is equivalent strain. In run #24, the two values between the " / " for γ, ε_E and their total rates indicate calculation from marker close to the edge of the sample (first value), and calculation from marker close to the center of the sample (second value). ([a]) values at 90° and 135° anvil twists are estimated from total uniaxial strain rate, values at 225° anvil twist are calculated from recovered samples (see text). ([b]) calculated using equations 3.4 (see text). (*) calculated in the software Avizo (see text, section 3.5).

3.5. X-ray tomography processing and analysis

An overview of the workflow on processing and analysis methods is given in Figure 3.6. The workflow consists in: selection of a representative volume (RV) in the whole sample image; application of various filters; segmentation and binarization; post-segmentation processing; quantitative analysis.
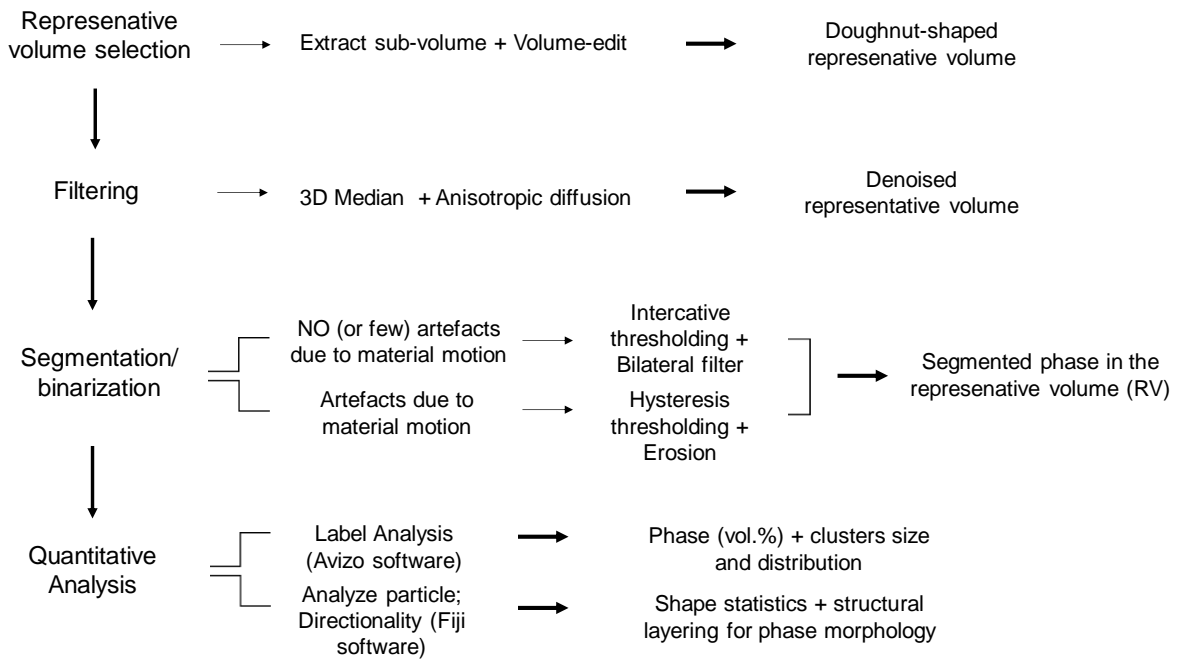
Figure 3. 6. Workflow overview of the X-ray tomography image processing and analyses using Avizo and Fiji softwares. See text for details.

In the following sub-sections, a detailed description of each of these steps is given. The first steps determine the quality of the subsequent quantitative analysis.

All steps before the analysis are performed in the software of commercial use Avizo 9.0 for FEI Systems (Avizo Software | Materials Characterization Software | Thermo Fisher Scientific - FR) available at the University of Lille on the department of "Plateforme des Microscopies Electroniques de Lille" (PMEL). Some tomographies were processed on Avizo 8.0 and 9.0 at the department of "ISIS4D" (https://isis4d.univ-lille.fr/) at the University of Lille. The ISIS4D facility was also used to acquire a post-mortem XRT of a

sample recovered from an ex-situ experiment (i.e., not conducted at the synchrotron beamline, namely run #15b in Table 3.2).

The quantitative analyses on XRT images are both performed in Avizo and Fiji. The latter is a specific distribution of the open-source program ImageJ (ImageJ (nih.gov)).

3.5.1. The representative volume (RV)

The investigated volume should be as representative of the sample as possible in order to avoid biasing the final statistics. I make the choice of a representative volume (RV) as close to the sample geometry as possible to preserve the torsional deformation geometry in the deformed microstructure.

The choice of the RV is further constrained by two factors in my work, which are partly linked to the experimental set-up: (1) presence and distribution of artefacts and (2) smaller image of the sample at higher angles of twist.

Some tomography artefacts remain difficult to avoid during reconstruction even with filtering and denoising modules. In my reconstructed images, the artefacts are usually more pronounced in the inner and outer regions of each cylindrical image. The inner region tends to show ring artefacts and/or scatter dots, whereas the artefacts towards the outer regions are mainly due to material motion during tomography collection. If the latter are anyway present at this stage, I choose to crop out the areas containing them.

The other constraint regards the gap between the opposed anvils, which shortens during the torsion (Fig. 3.5). The window for X-ray tomography becomes smaller leading to a reduced volume size of the tomography (e.g., Fig. 3.7a). For the purpose of observation and statistics consistencies, I select similar values of RVs among the different tomographies (at different twisting step) for each sample. The size of the RV for each sample is chosen on the basis of the height of the last image at the highest twisting angle.
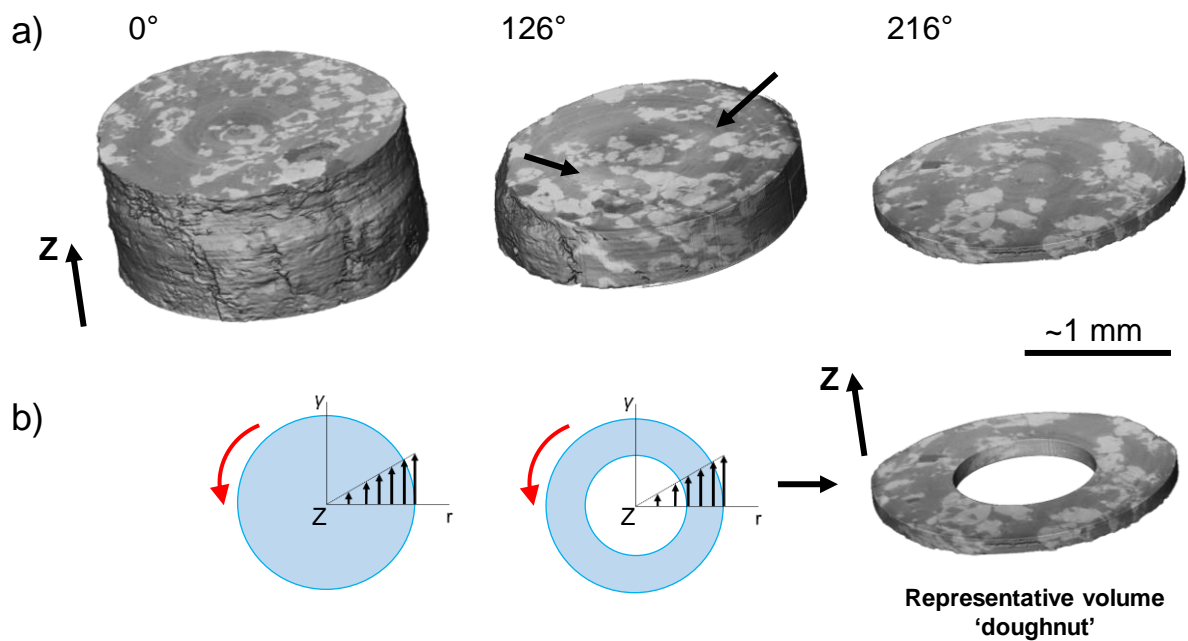
Figure 3. 7. Change in the reconstructed X-ray tomography volume with increasing twisting angle (a), theoretical transfer of the strain in a solid cylinder and in the representative volume (RV) (b). Z is the torsion axis. a) Arrows showing presence of rings and shading artifacts. Note the decreasing volume size (decrease in height of the image) with increasing anvil twisting angle due to the gap reduction. Phases in the sample image from brightest to darkest: Garnet (secondary mineral); Pyroxene (or omphacite, Omp; matrix mineral); Quartz (accessory mineral). b) γ is strain. r is radius. Red arrow showing the sense of torsion. Black arrows showing the strain gradient along the radius.

The "Extract sub-volume" and the "Volume-edit" tools available in Avizo 9.0 are used to obtain the RV. The first is used to define the bounding box containing the actual sample and remove portions of the tomography image including parts of the assembly or the anvils. The second is used to apply a user-defined cropping based on a 3-d mesh. Using a cylindrical mesh, two cropping are made at two different radii to remove the outer and inner regions of the sample, i.e. the two regions where the artefacts are more pronounced. The resulting cropped volume obtained at this stage is a hollow cylinder. This cylinder is then cropped along the height, leading to a doughnut-shaped volume (e.g., Fig. 3.7b) with boxes of ca. 1600 x 1600 x 150 voxels on average.

The representative doughnut-shaped volume can allow a microstructure investigation which is consistent with the deformation geometry (torsion geometry; e.g.,

see Fig. 3.5b) and where the strain gradient is theoretically lower along the radius sector (Fig. 3.7b).

For detailed observations of the 3-d microstructure at smaller scale in selected regions within these "doughnuts", extraction of volume boxes (ca. 150 x 150 x 100 voxels) are also made using the "Extract sub-volume" tool.

3.5.2. Image filtering and segmentation thresholding

Noise-reduction and edge-preserving filters are then used to erase, or reduce, some of the remaining artefacts in the RVs. The basic "3-d Median" filter is often used in this study. I also run the "Anisotropic diffusion" module to smooth rings artefacts, if still present.

User's choices of filters parameters applied to the grey-levels images can be non-unique, and result in uncertainties on the quantitative analysis performed on the segmented RV. The influence of these choices can be estimated by iterating over a range of filter parameter values, from visual inspection of the filtered image. An uncertainty range is therefore obtained above and below which image filtering is considered incorrect. The filtering uncertainties are then taken into account for estimating the total quantifications uncertainties during quantitative analyses performed on the segmented RV (see section 3.6.2).

After filtering, the doughnut images are transformed into binary by applying image segmentation through thresholding tools, assigning specific grey level ranges to each phase. In this study, I mainly use the Interactive and Hysteresis thresholding available in Avizo 9.0. Figure 3.8 shows a comparison between both modules used in the reconstructed images. The Interactive module prompts the user to set the grey level intervals manually with visual feedback. However, this tool does not work well on the noisier images, since some artefacts can remain in the resulting segmentation. In these cases, one solution is a post-segmentation filter, such as a bilateral filter. Alternatively, I

use the Hysteresis thresholding, where a grey level threshold is selected above which the segmentation will be applied. This implies this tool works well when the mineralogical phase of interest has the highest grey levels in the image. When the phase of interest has the lowest intensities, a grey scale inversion (negative contrast) is necessary.
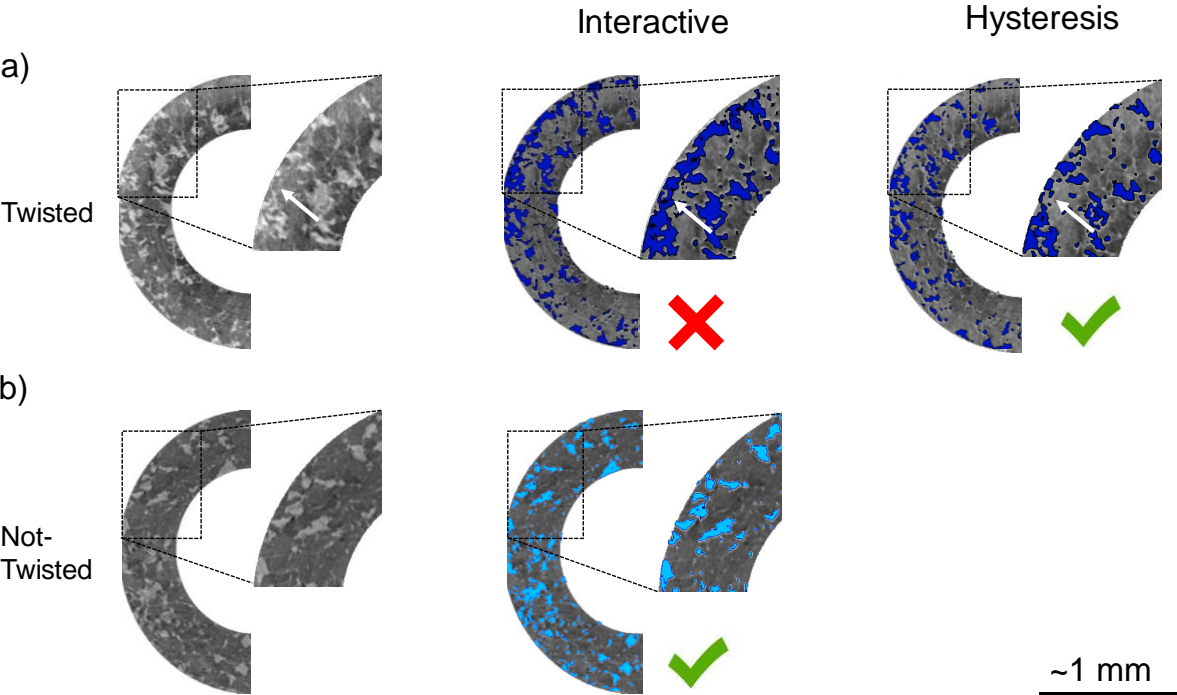
Figure 3. 8. Comparison between two different thresholding segmentation tools, Interactive and Hysteresis, showing when one works better than the another depending on the image quality and/or presence of artefacts. Scale bar refers to a) and b). a) tomography acquired after twisting where artefacts due to sample movements in the grey-scale image are present. In this case, Hysteresis is used. White arrow showing presence of unwanted segmentation that are present if Interactive is used. Note that the unwanted segmentation is not present if Hysteresis is used b) tomography acquired before twisting where no artefacts are observed. In this case, interactive is used.

Figure 3.9 gives a representative example of selection of thresholding values for both Interactive and Hysteresis. I also estimated segmentation uncertainties (Fig. 3.9) with the same strategy as for filtering uncertainties. These estimations are based on user's choices of thresholding parameters to segment the contouring of the phase of interest from visual inspection. An uncertainty ranges on image grey levels (Fig. 3.9) is therefore obtained above and below which segmentation is visually considered incorrect. The visually estimated thresholds and uncertainty ranges do fall where there is a change of slope on the grey levels histograms (Fig. 3.9). The change of the slope indicates the

74

boundary between the different phases. The segmentation uncertainty range obtained from visual inspection (Fig. 3.9) is then taken into account for estimating the total quantifications uncertainties during quantitative analyses performed on the segmented RV (see section 3.6.2).
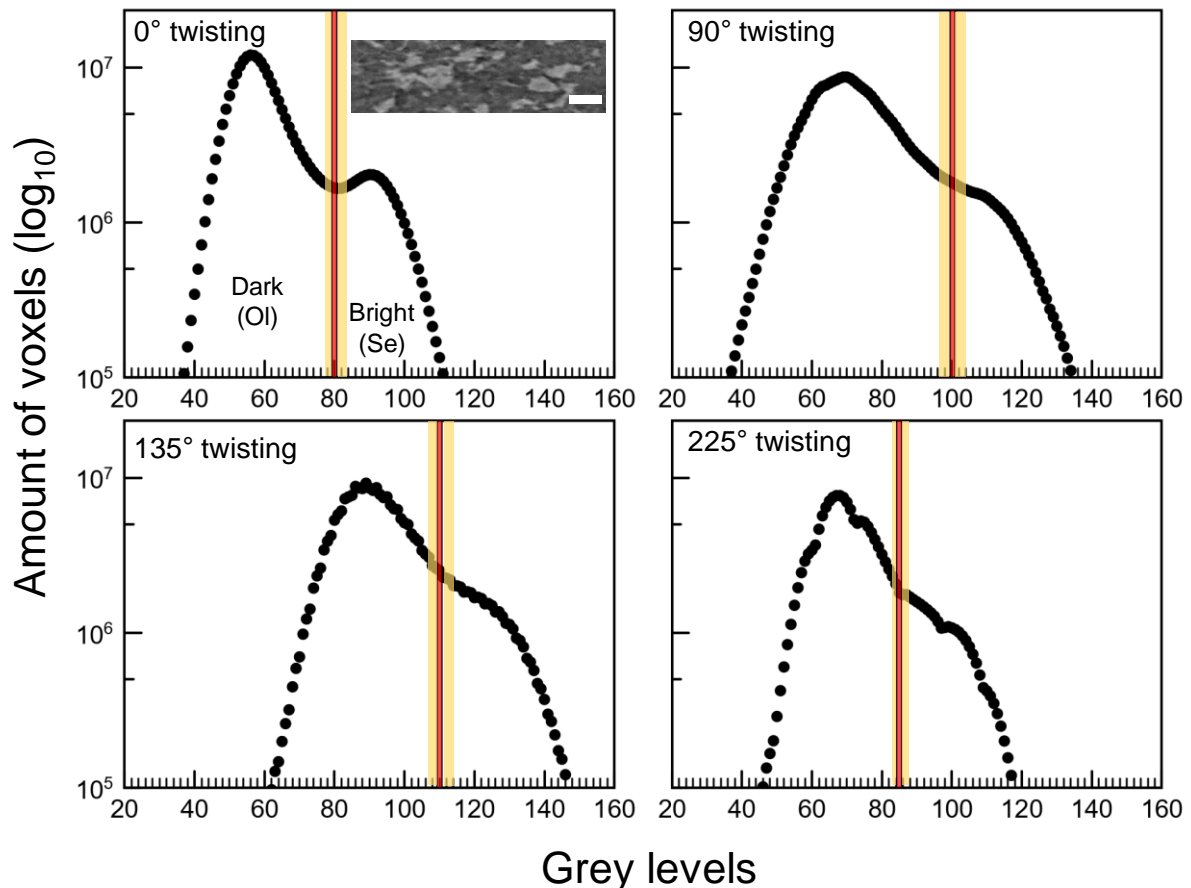
Figure 3. 9. Histograms of grey-levels (negative contrast) of images at different anvil twisting angle showing the selected thresholding values (red-shaded line) with uncertainties (yellow-shaded regions) to segment the brighter phase (Se, serpentine) in the sample. Ol is olivine. Upper-left quadrant: subset showing representative image of the sample in negative contrast with white scale bar corresponding to 100 μm.

3.5.3. Post-segmentation

After thresholding, to further improve the segmentation to be as close as possible to the actual contouring of the phase of interest, the "Erosion" tool is used when necessary and often where Hysteresis thresholding is previously used. This is because the Hysteresis thresholding does not always preserve the edges of the phase.

Finally, whether the applied segmentation in each image gives or not a satisfactory result is judged firstly on the basis of a visual feedback. When the sample volume is known beforehand, and when it is safe to assume that no chemical reactions and nucleation of new phases occurred during the experiments (i.e. temperature well within the stability field of minerals investigated, low temperature), I also rely on the resulting total volume percentage of the segmented phase.

The analyses are then run on the "clusters" of the segmented phase. The term "cluster" indicates individual aggregates of pixels (if in 2-d) or voxels (if in 3-d) in the segmented (binary) image. Each cluster can be an individual particle or structure of the segmented phase with its own morphology and size, observed and identified in 2-d or 3-d. In Table 3.4, I give the (arbitrary) classification of the clusters size. For the 2-d investigation, I take into account the area of the clusters (in pixel or microns). For the 3-d investigation, I take into account the order of magnitude of voxels amount making up the clusters (1 pixel is 1.3 µm; 1 voxel is 1.3 x 1.3 x 1.3 µm). For comparison, the volume of the RV (representative volume) is in the order of 10^8 voxels or µm³.

Table 3. 4. Arbitrary classification of clusters size for the 2-d and 3-d image investigation.

Units	Clusters 2-d			Unit	Clusters 3-d		
	Small	Medium	Large		Small	Medium	Large
µm²	$50 \leq x < 100$	$100 \leq x < 1000$	$x \geq 1000$	voxels	$10^1 < x \leq 10^3$	$10^4 \leq x \leq 10^5$	$10^6 \leq x \leq 10^7$
pixel²	$\sim30 \leq x < \sim60$	$\sim60 \leq x < \sim590$	$x \geq \sim590$				

3.6. The deformed microstructures

3.6.1. Description of analysis tools and quantifications

The first part of the analysis is run on the 3-d image of the doughnut-shaped RV using Avizo software. The 3-d analysis on the RV is to i) obtain phase volume proportions, ii) observe the evolution in size and shape of the clusters, and iii) obtain the degree of connectivity of the clusters of the phase of interest with increasing deformation. One way to estimate the degree of connectivity of the phase of interest, following Kaercher et al.

(2016), is taking into account the size of the largest cluster. The connectivity is calculated by dividing the volume of the largest cluster by the total volume of the phase present in the sample RV (after Kaercher et al., 2016).

The second part of the analysis is run on selected 2-d images extracted from the RV, and loaded into the software Fiji. The 2-d images are unrolled sections that follow the doughnut perimeter, and are extracted at a selected doughnut radius using a Matlab script developed by Ph.D. M. Thielmann from the University of Bayreuth (BGI, Germany). The selected geometries of the doughnut-shaped RV and the extracted unrolled sections can allow a microstructural analysis consistent with the torsional deformation geometry in cylindrical samples along the whole perimeter (e.g., Fig 3.5b, 3.7b). The 2-d analysis on the unrolled sections is to obtain i) statistics on shape descriptors of the clusters and ii) quantify the structural layering (orientations) of the clusters with respect to the shear direction (see section 3.6.2).

For i), the shape descriptors (Analyze Menu (nih.gov)) used here for the clusters corresponds to:

1) Area (μm^2).

2) Aspect ratio, the ratio of the major axis over the minor axis of the cluster fitting ellipse. It gives information on shape anisotropy.

3) Circularity, with formula $4\pi \, area \, (\mu m^2)/P(\mu m)^2$, where P is the perimeter of the clusters (or the length of the contouring of clusters). It can range from values of 0 to 1, where 1 represents a perfect circular shape. In comparison with the aspect ratio, the circularity takes into account the complexity of the clusters morphology that is described by the contouring of the clusters.

For ii), the structural layering refers to:

1) The orientation in angle (°) of individual clusters with respect to the horizontal direction of the section. The angle (°) of the clusters refers to the major axis orientation (from -90° to 90°) of the fitting ellipse with respect to the reference (0°) (Analyze Menu (nih.gov), i.e. the horizontal. The horizontal of the section corresponds to the shear direction.

2) The orientation in angle (°) of the clusters boundaries obtained through the "Directionality" tool in Fiji (Directionality (imagej.net). Instead of the orientation of the major axis of fitting ellipses (1), the directionality gives the distribution of the orientation (from -90° to 90°) of each segment of clusters boundaries (for further information on directionality see Liu, 1991) with respect to the reference horizontal. The directionality is useful for obtaining the orientation of inter-phase boundary, between the phase of interest (secondary phase) and the phase in the matrix.

3.6.2. Results

Here I give examples of deformed microstructures and related quantifications in 2-d and 3-d (see section above, 3.6.1) on two aggregate systems: olivine+serpentine and pyroxene+garnet. The results focus on the secondary phase (less abundant) in the matrix of the aggregates.

Serpentine microstructure (from olivine+serpentine aggregate)
3-d results

The 3-d microstructure of serpentine shows the size of the largest cluster increasing with increasing anvil twisting angle (Fig. 3.10). Figure 3.11 shows the evolution of the largest cluster connectivity (see section 3.6.1) with increasing twisting angle (deformation). At first, the connectivity of serpentine seems constant from 0° to 90° anvil twisting angle, with values ca. 30%. Above 90° twist, the trend becomes steeper with

78

values changing from ca. 30% to ca. 90% of connectivity at 225° anvil twisting angle (Fig. 3.11).
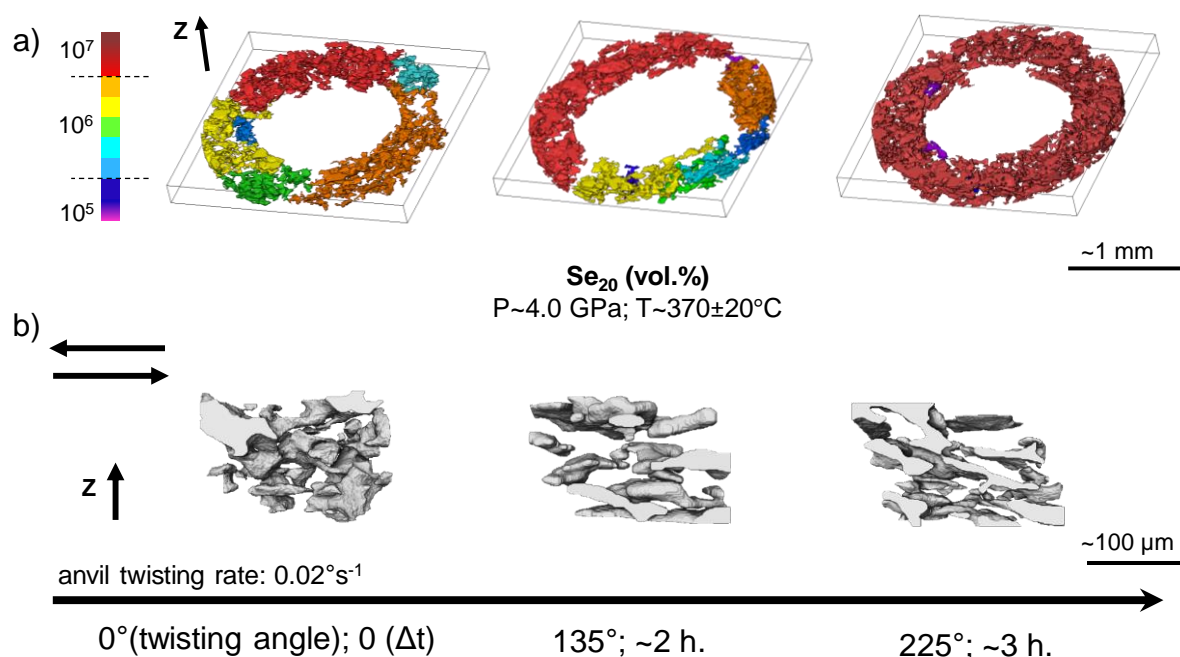
Figure 3. 10. 3-d renders showing the serpentine morphology evolution in a representative sample with increasing anvil twisting angle (a) Serpentine morphology in the representative volume (doughnut). The color-coded bar shows the voxel amount in the clusters. The bounding boxes are ~ 1600 x 1600 x 150 voxels (b) Smaller regions of interest within this representative volume. The bounding boxes are 150 x 150 x 100 voxels. For a) and b) Z is the torsion axis, the black arrow indicates increasing anvil twisting angle, and Δt is the time interval corresponding to the twisting duration for each step. P-T conditions and serpentine (Se) volume content of the sample are also given.
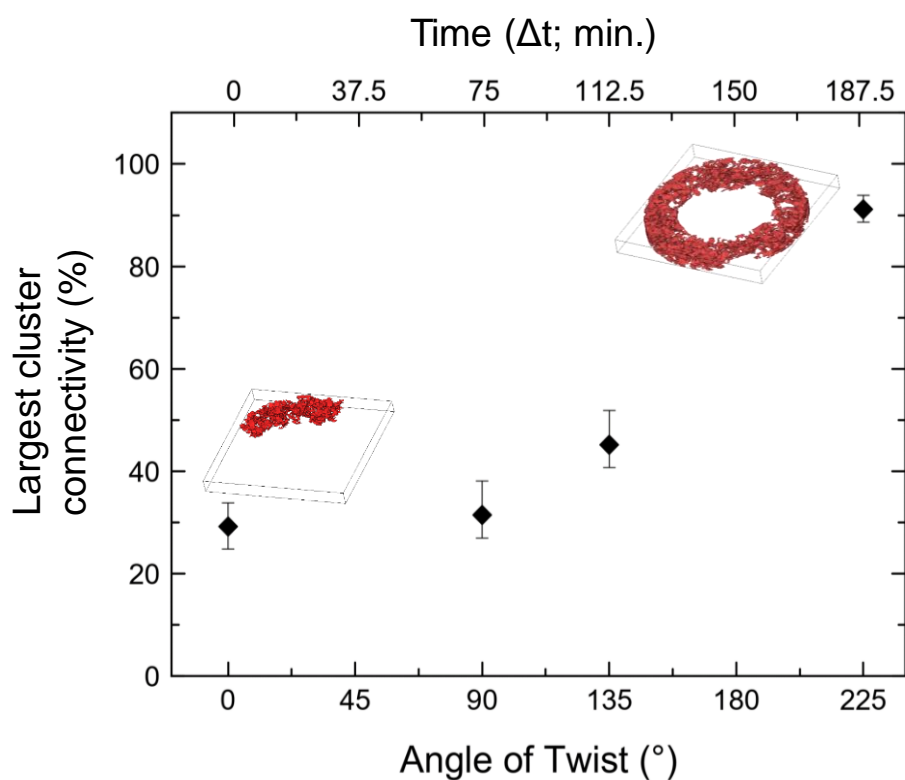
Figure 3. 11. Diagram showing the connectivity evolution of the biggest cluster (Fig. 3.10a) with increasing anvil twisting angle (angle of twist) and twisting duration (time). Error bars show the total connectivity (%) uncertainties from Table 3.7.

The uncertainties on connectivity (%) are also evaluated taking into account the uncertainties ranges estimated for image segmentation and filtering (see section 3.5.2). This uncertainty ranges influence the result of the segmented phase volumes, and in turn the connectivity (%) calculation, as well. These uncertainties remain low with respect to the connectivity (%) values (Fig. 3.11, Table 3.5).

Table 3. 5. Uncertainties estimation of the biggest cluster connectivity (%).

Anvil twisting angle (°)	Total representaive volume (mm³)*	Se volume (mm³)*	Calculated Se (vol.%)*	Largest cluster connectivity (%)	Connectivity (%) uncertainties				Tot. Connectivity (%) uncertainties	
					Thresholding			Filters***		
					Tool**	+	-	(+ and -)	+	-
0	0.462	0.071	15.4	29.2	Interactive	3.2	3.0	1.4 / 1.4	4.6	4.4
90	0.396	0.066	16.7	31.4	Hysteresis	5.3	3.1	1.4 / 1.4	6.7	4.5
135	0.442	0.077	17.4	45.2	Hysteresis	5.3	3.1	1.4 / 1.4	6.7	4.5
225	0.382	0.065	17.0	91.2	Interactive	1.3	1.1	1.4	2.7	2.5
Avg	0.4	0.1	16.6							
Stdv	0.04	0.006	0.9							

All the uncertainties (+ and -) refers to connectivity (%). The total connectivity (%) uncertainties corresponds to error bars in Figure 3.11. Se is serpentine. (*) calculated in the software Avizo 9.0. (**) segmentation tools used in the software Avizo 9.0 (see text, section 3.5.2). (***) refers to "Median" and "Anisotropic diffusion" filters tools (see text).

2-d results

Figure 3.12 shows the 2-d evolving microstructure of the serpentine with increasing deformation in the unrolled sections extracted from the doughnut-shaped RV. The 2-d microstructure shows elongated serpentine clusters parallel or sub-parallel to the shear direction (corresponding to the images horizontal). The population of these clusters increases between 0° to 90° anvil twisting angles (Fig. 3.13). Beyond 90° twist, the overall directionality distribution of serpentine skews towards negative angles of ca. 10-20° (Fig. 3.13). This indicates that beyond 90° of anvil twisting there is a greater population of clusters boundaries describing preferential orientations at certain angles with respect to the shear direction (i.e., corresponding to 0° directionality, Fig. 3.13), therefore showing deviations from the shear (parallel to the sections, Fig. 3.12).
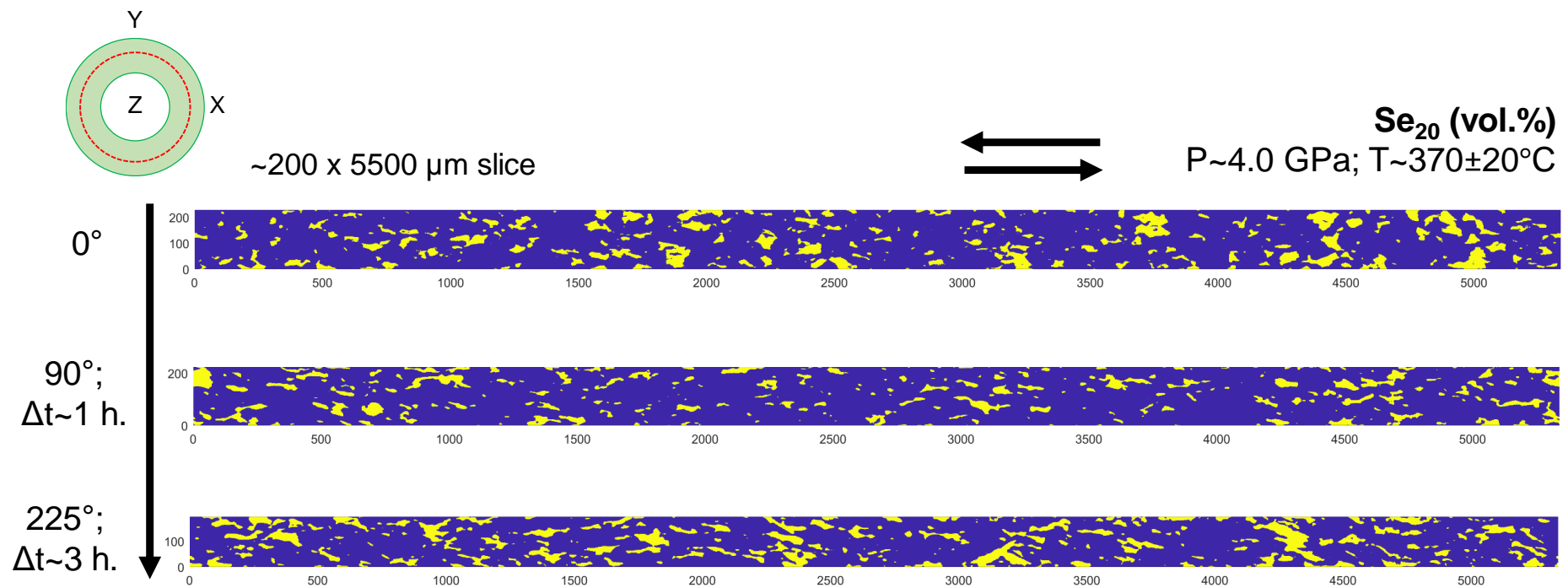
Figure 3. 12. 2-d serpentine microstructure evolution (yellow) with increasing anvil twisting angle (°) in the unrolled sections extracted from the doughnut-shaped representative volume. Red-dashed line in the upper-left subset showing the approximate location from where the unrolled sections are extracted. Z is the torsion axis. P-T conditions and serpentine (Se) volume content of the sample are also given. Arrows on top showing the sense of shear. Number labels of the unrolled sections corresponds to approximate dimensions in microns (μm). Δt is the time interval corresponding to the twisting step duration
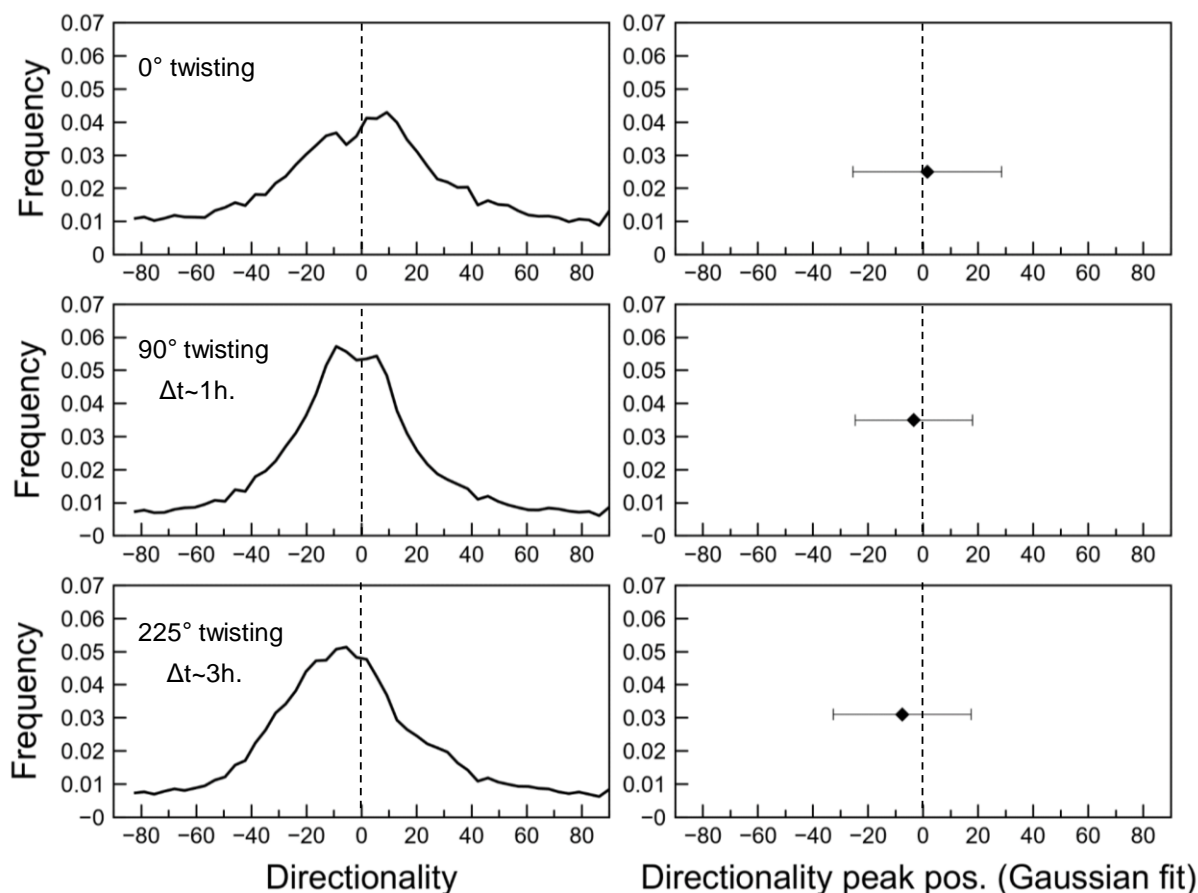
Figure 3. 13. Directionality distributions at different anvil twisting angles (°) showing preferred structural layering in the serpentine microstructures (yellow, Fig. 3.12) with respect to the shear direction (i.e., 0° in the directionality axis, corresponding to horizontal direction of the unrolled sections images in Fig. 3.12). Quadrants on the right showing the peak position and HWHM (half-width-half-maxima, error bars) from Gaussian fits done on the directionality distributions. Δt is the time interval corresponding to the twisting step duration.

The statistics on shape descriptors (area, aspect ratio, circularity) (Fig. 3.14) show the population of smaller serpentine clusters decreasing with increasing twisting angle, while the aspect ratio frequency increases around values of 4 to 8 with increasing twisting angle. The aspect ratio also shows an increase in frequency of lower aspect ratios values at the last stage of deformation (around 2-3; Fig. 3.14).

The circularity distribution is skewed towards values close to zero at 225° anvil twisting angle. This indicates an increasing population of serpentine structures deviating from a perfect sphere shape, with their morphology becoming more complex at the last stage of deformation (Fig. 3.14).
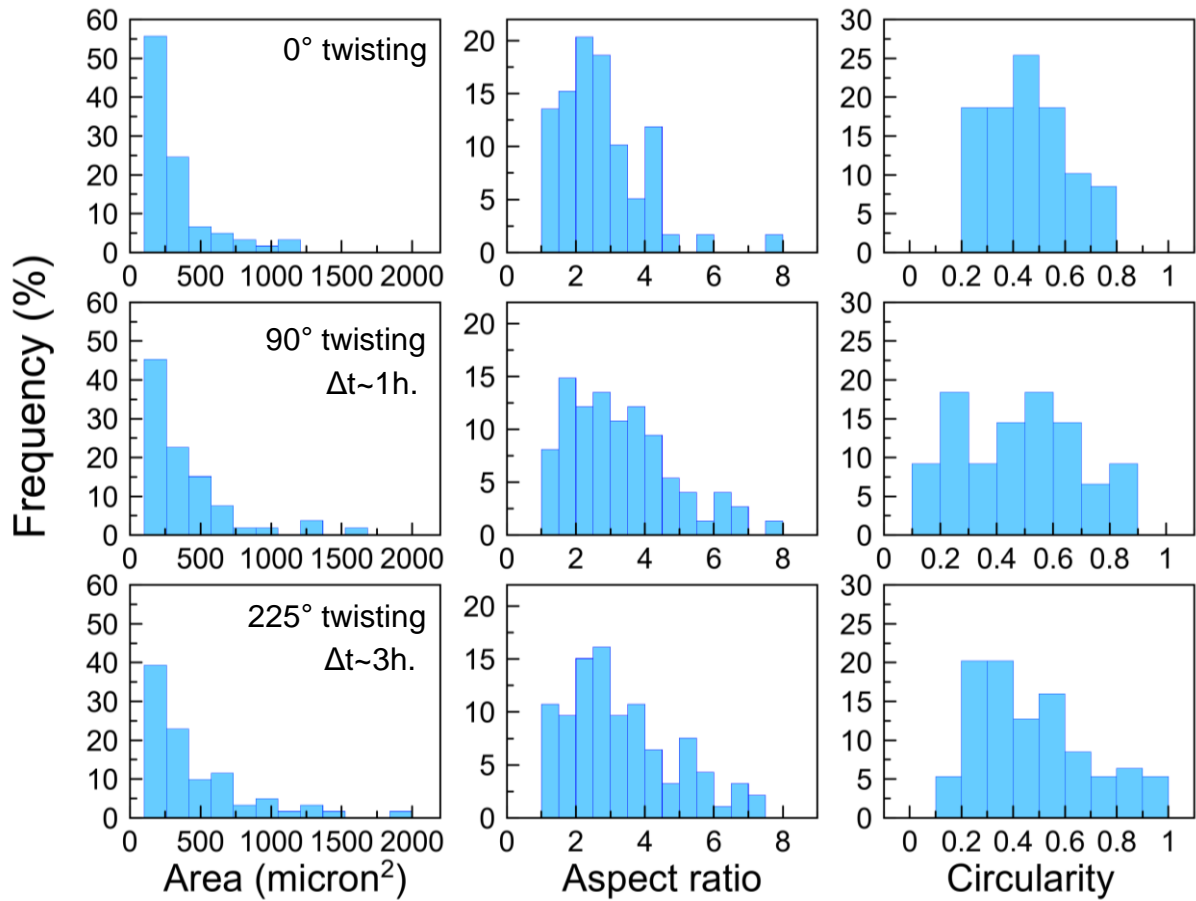
Figure 3. 14. Histograms showing the evolving area, aspect ratio and circularity of the serpentine microstructure shown in Fig. 3.12 with increasing anvil twisting angle (°). Aspect ratio is defined as the ratio of major axis/minor axis of the fitting ellipse to any single serpentine structure. Circularity is defined as the ratio of 4π area/perimeter2 of any single serpentine structure.

With increasing twisting angle and transferred simple shear strain, the above observations suggest the serpentine developing a more complex microstructure after 90° of twisting, with the clusters aligning along preferential orientation at certain angles with respect to the shear direction rather than only aligning parallel (or subparallel) to the shear direction. The increasing complexity of the microstructure can be linked with the evolving interconnectivity among neighboring clusters that can occur along specific directions with respect to the shear direction. The increasing interconnectivity eventually leads to a larger high-connectivity cluster distributed in the whole RV at the last stage of deformation (Fig. 3.10a, 3.11).

Garnet microstructure (from pyroxene+garnet aggregate)

In the aggregate made of pyroxene matrix + garnet, I follow the motion of an atoll-shaped garnet grain with increasing deformation.

2-d results

Figure 3.15 shows the atoll-shaped garnet rotating in the pyroxene matrix at different twisting angles. This suggests the grain behaves as a clast, i.e. a rigid body within the pyroxene matrix. This is in agreement with usual observations on deformed garnet and pyroxene bearing rocks (i.e., eclogite; e.g., Philpotts and Ague, 2009; Passchier and Trouw, 2005), where the garnet behave as a clast.

Grt$_{35}$ (vol.%)
P~3.0 GPa; T~427±20°C

anvil twisting rate: 0.02°s^{-1}

0°(twisting angle); 0 (Δt)   126°; 1.75 h.   216°; 3 h.
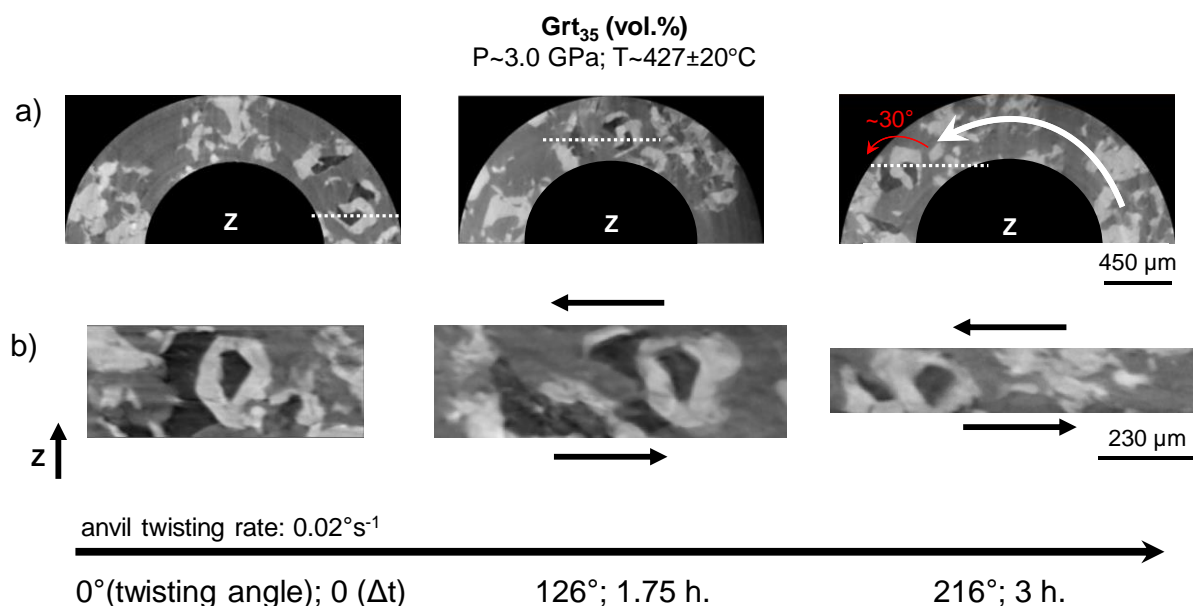
Figure 3. 15. 2-d grey-levels images showing the atoll-shaped garnet clast motion with increasing anvil twisting angle (black arrow at the bottom). For a) and b) Z is the torsion axis. P-T conditions and garnet (Grt) volume content of the sample are also given. Δt is time interval in the experiment corresponding to specific anvil twisting step duration. Phases in the sample image from brightest to darkest: Garnet (secondary mineral); pyroxene (or omphacite, Omp; matrix mineral); quartz (accessory mineral). a) observed motion (white arrow) and rotation (red arrow) of the clast with increasing anvil twisting angle. (b) view of the clast in cross-cutting (location shown by the white dashed lines in (a)). Black arrows showing the sense of shear.

3-d results

Figure 3.16 shows the 3-d render of the garnet clast and gives a reconstruction of the overall motion of the clast in 3-d space with increasing deformation.

anvil twisting rate: 0.02°s⁻¹

0°(twisting angle); 0 (Δt)   126°; 1.75 h.
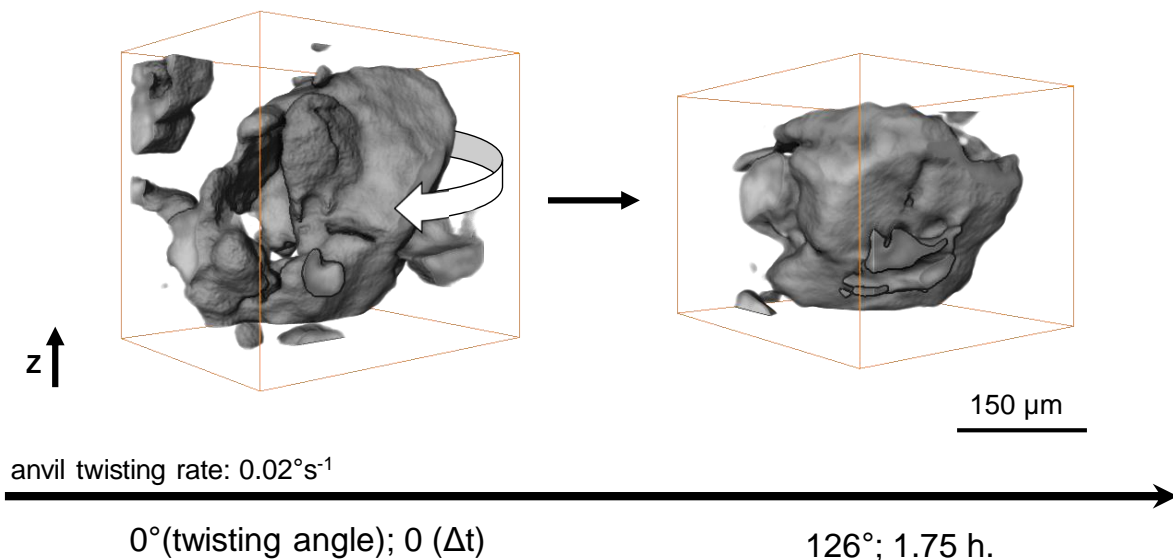
Figure 3. 16. 3-d render showing the evolving morphology of the atoll-shaped garnet clast (Fig. 3.15) with increasing anvil twisting angle (black arrow at the bottom). White arrow showing the possible rotation in 3-d space. Z is the torsion axis. Δt is time interval in the experiment corresponding to specific anvil twisting step duration.

The clast indicates a rotation of at least ca. 30° (Fig. 3.15) visible in the expected shearing plane (i.e., where the motion of the material lies; Fig. 3.15a) and the plane parallel to the shear direction (Fig. 3.15b) The 2-d and 3-d observations suggest a total rotation with 2 components, i.e. one parallel (Fig. 3.15a, 3.16) and one perpendicular (Fig 3.15b) to the torsion axis.

3.7. Discussion

3.7.1. Deformation experiments

One of the major difficulties of experiments conducted with PEc-type apparatuses is the sideways expansion of the cell assembly and sample during the experiment. This extrusion is related with a loss of the apparatus oil pressure in the absence of regulation, and the reduction of the gap between the opposed anvils (gap H; Fig. 3.5b).

In the RoToPEc, where twisting is performed in addition to compression, this effect is expected to be even more pronounced than a "static" experiment with no deformation. For conducting a deformation experiment, this results in the following shortcomings:

- The potential loss of pressure can make the interpretation complex in terms of deformation behavior.

- The deformation field in the sample is a result of combined uniaxial shortening/lateral expansion, and torsion (e.g., see section 3.4). The microstructure can be affected in multiple locations or in the whole volume of the sample, which also makes the interpretation of deformation behavior complex.

- The decrease of the anvil gap limits the window for the X-ray tomography analysis (e.g., Fig. 3.5b; Fig. 3.7a). The decreasing gap can ultimately result in the anvils touching for large twists/high temperature experiments, limiting the duration of the deformation experiment and possibly leading to an anvil blow-out. A good compromise has to be found between achieving large shear strains and keeping a field of view wide enough for the microstructural investigation.

Figure 3.17 shows the evolution with increasing anvil twisting angle of the anvil gap, oil pressure, sample lateral expansion, and calculated uniaxial shortening.

The decrease of the anvil gap with increasing anvil twisting angle (Fig. 3.17a) is more pronounced at the beginning of the twisting. The experiments reported here are stopped when a gap of ca. 300 μm is reached in order to keep a field of view suitable for microstructural interpretations. The apparatus oil pressure follows a similar trend as the gap reduction, decreasing with increasing anvil twisting angle, with most of the apparatus oil pressure loss occurring at the beginning of the torsion (Fig. 3.17b). This could imply that the actual confining pressure transferred to the sample decreases as torsion is performed, and prompt us to regulate the oil pressure to maintain the hydrostatic pressure inside the assembly. In turn, increasing oil pressure at this stage could involve an even greater decrease of the anvil gap and early experiment termination.

However, the need for such a regulation is not so straightforward. In the experiments reported in this study, the pressure is monitored *in-situ* using X-ray
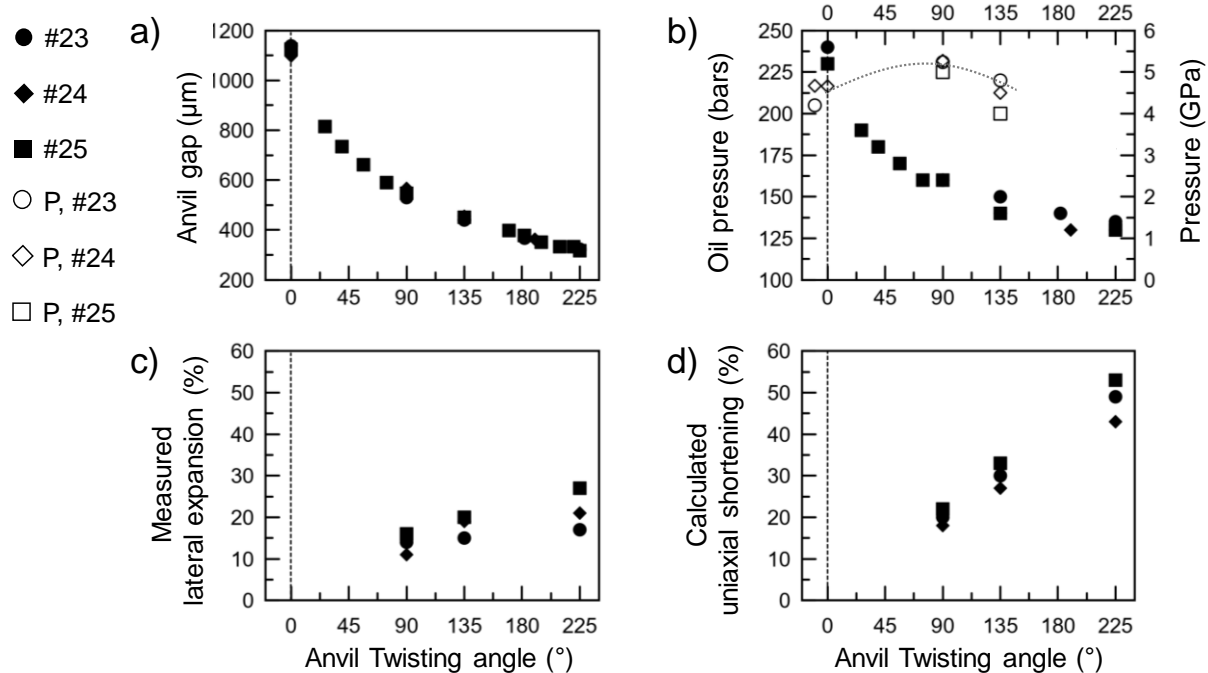
Figure 3. 17. Diagrams showing a) the anvil gap reduction, b) oil pressure of the press, corresponding confining pressure in the cell/sample in GPa, c) measured sample lateral expansion and d) calculated uniaxial strain with increasing anvil twisting angle in three different runs (see Table 3.5) carried out in RoToPEc. The straight black dashed line in each diagram defines the beginning of the deformation (0° anvil twisting angle). The curved dashed line in (b) is a guide-to-the-eye for the calculated confining pressure trend.

diffraction on the h-BN of the sample sleeve (see section 3.3). I did not observe a clear decrease in pressure with increasing anvil twisting angle or duration of the experiments. Instead, the pressure increases in the order of 1 GPa or more during the first step of twisting (i.e., from 0° to 90° anvil twisting angles, Fig. 3.17b). From the start to the end of twisting, I observed either an overall pressure increase of ca. 0.7 GPa (e.g., run #23; Table 3.4, 3.5; Fig. 3.17b) or an overall slight pressure decrease of ca. 0.2 GPa (e.g., run #24; Table 3.4, 3.5; Fig. 3.17b). Note that in another set of experiments (not presented here), where tomography acquisition was performed under HT, I observed a continuous and larger decrease in pressures from the start to the end of deformation. The total decrease in pressure is ca. 2 GPa, from a starting pressure of ca. 4 GPa. This could be explained by the longer exposure of the assembly to HT, which caused the gasket to be less effective and flow more.

The largest increase in pressure occurring at the beginning of the deformation could be related to the measured sample lateral expansion not fully compensating the calculated uniaxial shortening (run #23; Fig. 3.17c, d). This suggest that the sample gains pressure rather than experiencing shear at this stage, i.e. at ≤ 90° anvil twist. At this twist condition, the simple shear strains transferred to the sample are low (e.g., Table 3.5), with the microstructures mostly showing cluster elongation (flattening), and suggesting a pure shear configuration transferred to the sample rather than simple shear. The noticeable changes indicating effective transfer of simple shear occur after 90° twist, i.e. when rotation in the microstructure occur, reflecting the transferred sense of shear (e.g., Fig. 3.10b, 3.12).

Therefore, in the RoToPEc, after an initial stage of pressurization and increase of friction in the assembly parts, I suggest that the coupling between the rotating anvil inducing torsion and the sample becomes really effective at ≥ 90°. Although the strain rates are different, this value seems consistent with the low strains by Berg et al., 2017, on samples recovered from experiments in the roPEc.

Overall, from the start to the end of the twisting, I suggest the RoToPEc is efficient in transferring the simple shear strain to the samples rather than the uniaxial strain. The transfer of the simple shear strain is faster than the transfer of the uniaxial strain during the experiments in this study (total strain rates in Table 3.5).

As in the RoToPEc, in the Drickamer, another high-pressure torsion apparatus (e.g., see sections 3.1), the deformation field in the sample is a result of combined uniaxial shortening/lateral expansion, and torsion (e.g., Yamazaki and Karato, 2001; Wang et al., 2011; Girard et al., 2016). In a previous work on rock deformation with the Drickamer at maximum pressure of 6 GPa, Wang et al. (2011) in an experiment reported values of ca. 60% of uniaxial strain at ca. 65° of actual twisting angle (measured with markers in the sample) and ca. 2.5 of the corresponding simple shear strain (Table 1 in Wang et al.,

2011). In this study, at a maximum pressure of ca. 5 GPa, twisting angles of ca. 60-70° and simple sear strain of ca. 2 (corresponding to the stage of 135° of anvil twisting angles, Table 3.5), the uniaxial strain reported is 30%, i.e. half of the one reported by Wang et al. (2011) for similar values of transferred twisting angles and simple shear strain. This suggest that, in comparison with the Drickamer, the RoToPEc could be more efficient in transferring less amount of uniaxial strain to the samples at similar twisting angles and simple shear strains. However, the opposed-anvil design of the Drickamer permits to perform longer duration of torsion experiments (higher simple shear strain in the recovered samples) at higher pressure and temperature, with the X-ray tomography field of view corresponding to the actual length of the sample for the all duration of the twisting (e.g., Wang et al., 2011).

The above observations state the importance of having a proper instrumental setting in terms of assembly or anvils design depending on the aim of the experiment, or the study. In the RoToPEc, to counter the shortcomings and their influences on the data, I suggest future work is needed to reduce the sideways expansion related to the potential loss of pressure and reduction of the X-ray tomography field of view, or gap, during torsion. For instance, a possibility can be a variation of the assembly design.

The in-situ X-ray tomography acquisition

Regarding the *in-situ* X-ray tomography acquisition in the RoToPEc, I suggest that one of the major difficulties regards the acquired and processed images, with their artefacts due to physical motions in the sample caused by deformation. These artefacts are difficult to avoid during acquisition, and erasing them during either reconstruction, processing or post-processing revealed to be difficult. They can hamper the proper investigation on the microstructure evolution and shape descriptors. One solution is to let the sample stabilize after each deformation step (i.e., anvil twisting angle) before acquiring the X-ray tomography (see section 3.3.2). Another solution is to carry out the

tomography fast enough to minimize the motion in the samples. Recent developments at the high-pressure PSICHE beamline (SOLEIL synchrotron) have allowed studies using high-speed X-ray tomography (in the order of less than a second for a complete tomogram) coupled with a high-pressure, high-temperature apparatus, the UToPEC, another variation of the PEC design (e.g., Boulard et al., 2018; King et al., 2019; Giovenco et al., 2021). Therefore, a coupling of the new high-speed tomographies settings with the RoToPEc or similar apparatus designs could be realized.

3.7.2. Summary and perspective

In this chapter, I showed how to process and analyze X-ray tomography data acquired *in-situ* in two-phase aggregates. The aggregates were experimentally deformed in torsion on the RoToPEc apparatus at HP-HT on the PSICHE beamline, at SOLEIL synchrotron.

I successfully imaged and followed the microstructure evolution in the two aggregates at different steps of torsional deformation. I observed and quantify evolving features and heterogeneities in the microstructures consistent with the symmetry of the torsion geometry transferred to the samples at HP-HT. I provided some quantifications that can be used to interpret multiphase rock deformation dynamics and microstructural behaviors in highly sheared zones in nature. I suggest the RoToPEc with *in-situ* X-ray tomography might be a powerful tool to experimentally investigate microstructures at simple shear strains comparable to those of large geological shear deformation environments.

When performing *in-situ* tomography together with deformation in the RoToPEc, I suggest that quenching before tomography acquisition to this date remains strongly necessary. This is valid for the quality of the acquisition, as well as to reduce lateral expansion, loss in pressure, and maximize the final strain.

Future work on a different assembly design should be needed to counter the loss of oil confining pressure and the gap reduction between the anvils, which corresponds to the reduction of the X-ray tomography field of view.

The missing of potentially important information in the sample due to the reduction of the X-ray tomography field of view could lead to misinterpretation of the X-ray tomography data. For this, *post-mortem* electron microscopy analysis on the bulk, recovered samples can be a solution (see chapter 4).

The integration of *in-situ* X-ray tomography data with *post-mortem* electron microscopy can bring new insights on mechanical, microstructural evolution and behavior in the samples, possibly constraining strain localization and deformation mechanism at multiple scales of observation in multi-phases rocks representative for large geological shear strains.

In this chapter, I also reported for the first time an offline temperature calibration conducted on PSICHE beamline employing a thermocouple during static experiments (no twisting). The results showed the assembly and its materials used in the present work are the least efficient in conducting heat to the sample compared with other calibration from previous work (Fig. 3.3). I suggest the assembly of the present work could be improved by employing a more insulating material than boron-epoxy mixture for the gasket (pressure medium), such as zirconia. A future work can also be to compare and integrate these results with cross calibration experiments employing calibrants to infer the conditions, and potential variation, of temperature during torsion in the RoToPEc.

Chapter 4

Deformation and microstructure evolution of the olivine+serpentine aggregate

4.1. Introduction

A key in the deformation of a multi-phase rock is the stress-strain distribution among the phases, which is sensitive to the phases morphology that evolves with strain (e.g., Karato 2008). Two general end-member configurations exist (e.g., Jordan, 1987; Handy, 1990, 1994; Ji et al., 2004; Montési, 2007, 2013) : i) a dispersed fabric where the strain is distributed uniformly and stress is controlled by the strong phase, and ii) a layered fabric, where stress is uniform and also controlled by the weakest phase. The change from a dispersed fabric to a layered fabric can be associated with a high shear localization that can depend on the minerals involved (Montési 2013).

The configuration of a layered fabric can correspond to the IWL configuration presented by Handy (e.g., 1990, 1994; see section 1.2), in which the stress-strain distribution of the two phases in a rock (one phase being weaker and the another stronger under deformation) is related to the morphology of the phases, specifically their morphological network, or framework (see section 1.2). The IWL configuration describes a specific layered fabric where the weak phase forms an interconnected layer within the stronger phase matrix (see Fig. 1.1), and where strain is localized, governing the bulk rheology of the rock (e.g., Handy 1990, 1994).

In this chapter, I investigate at which conditions the configuration of IWL can be observable in olivine+serpentine aggregates during shear deformation experiments. I use

olivine+serpentine as a proxy for serpentinized peridotites (see section 1.4). I present results on the evolving microstructure (or fabric) in the olivine+serpentine aggregates with increasing strain, focusing on the secondary weak phase, serpentine.

Table 4.1 below gives the summary of the experimental runs on olivine+serpentine aggregates for which the results are presented in this chapter. Figure 4.1 shows the pressure temperature conditions (P-T) of the experimental runs. Figure 4.2 shows the evolution of the transferred strain (shear strain and equivalent strain) to the samples with anvil twisting angles.

Table 4. 1. Summary of the experimental runs for the olivine+serpentine aggregates performed in the RoToPEc apparatus.

Run (#)	Batch/experiment session	Composition (vol.%)	Measured oil pressure (bars) Max.	Min.	Calculated/estimated pressure (GPa) Max.	Min.	Power (W)	Temperature (°C)	Anvil twist angle	Anvil twist rate	Sample twist angle (θ)	ε^a	γ	ε_E (%)[b]	ε	γ	ε_E[b]
15	1	Se10Ol90 Se: 9.9±0.5*	250		~4	1.4	150 (AC)	~330	90	0.02							
15b	1	Se10Ol90 Se: 10.42*	240		~4		96 (DC)		225	0.02							
18	1	Se20Ol80 Se: 16.6±0.9*	250		~4	2.6	170 (AC)	~370	225	0.02		0.5					
18b	1	Se20Ol80	243		~4		114 (DC)		No twist								
23	2	Se10Ol90 Se: 9.6±1.6*	250	130	5.2	4.2	170 (AC)	~370	0	0.02							
									90		47	0.2	1.5	177.1			
									135		59	0.3	2.2	255.5			
									225		102	0.5	5.1	592.6	3.9 X 10^{-5}	4.7 X 10^{-4}	5.5 X 10^{-4}
24	2	Se20Ol80 Se: 18.9±2.5*	250	130	5.3	4.5	150 (AC)	~330	0	0.02							
									90		45	0.2	1.2 / 1.1	143.5 / 132.1			
									135		60	0.3	1.9 / 1.5	217.4 / 172.9			
									225		103	0.4	4.1 / 2.9	479.5 / 334.3	3.9 X 10^{-5}	3.8 X 10^{-4} / 2.7 X 10^{-4}	4.4 X 10^{-4} / 3.1 X 10^{-4}
25	2	Se10Ol90 Se: 10.6±1.3*	250	130	~5	~4	200 (AC)	~430	0	0.02							
									90		61	0.2	1.4	160.8			
									135		74	0.3	2.0	228.3			
									225		118	0.5	4.5	516.8	4.9 X 10^{-5}	4.1 X 10^{-4}	4.8 X 10^{-4}

Runs from #15 to #18b represent a first set of experiments, whereas runs from #23 to #25 represent the second set. The difference between the two sets is the batch (1 and 2) of mixed powders used. Runs #15b and 18b refers to experiments performed ex-situ (i.e., not at the synchrotron). For run #15b, post-mortem XRT was performed. Se is serpentine and Ol is olivine. (*) refers to serpentine volume calculated in the software Avizo for tomography processing (see section 3.5). Pressure (GPa, gigapascal) was calculated from in-situ X-ray diffraction on h-BN during the experiments (see section 3.3). AC is alternate current (at the synchrotron, in-situ). DC is direct current (for ex-situ experiments). Strains calculation was performed in the second session of experiments (runs #23, #24, #25), where strain markers were used (see section 3.4). ε is uniaxial strain. γ is simple shear strain. ε_E is equivalent strain. In run #24, the two values between the "/" for γ, ε_E and their total rates indicate calculation from marker close to the edge of the sample (first value), and calculation from marker close to the center of the sample (second value). ([a]) values at 90° and 135° anvil twists are estimated from total uniaxial strain rate, values at 225° anvil twist are calculated from recovered samples (see text in section 3.4). ([b]) calculated using equations 3.4 (see text in section 3.4).
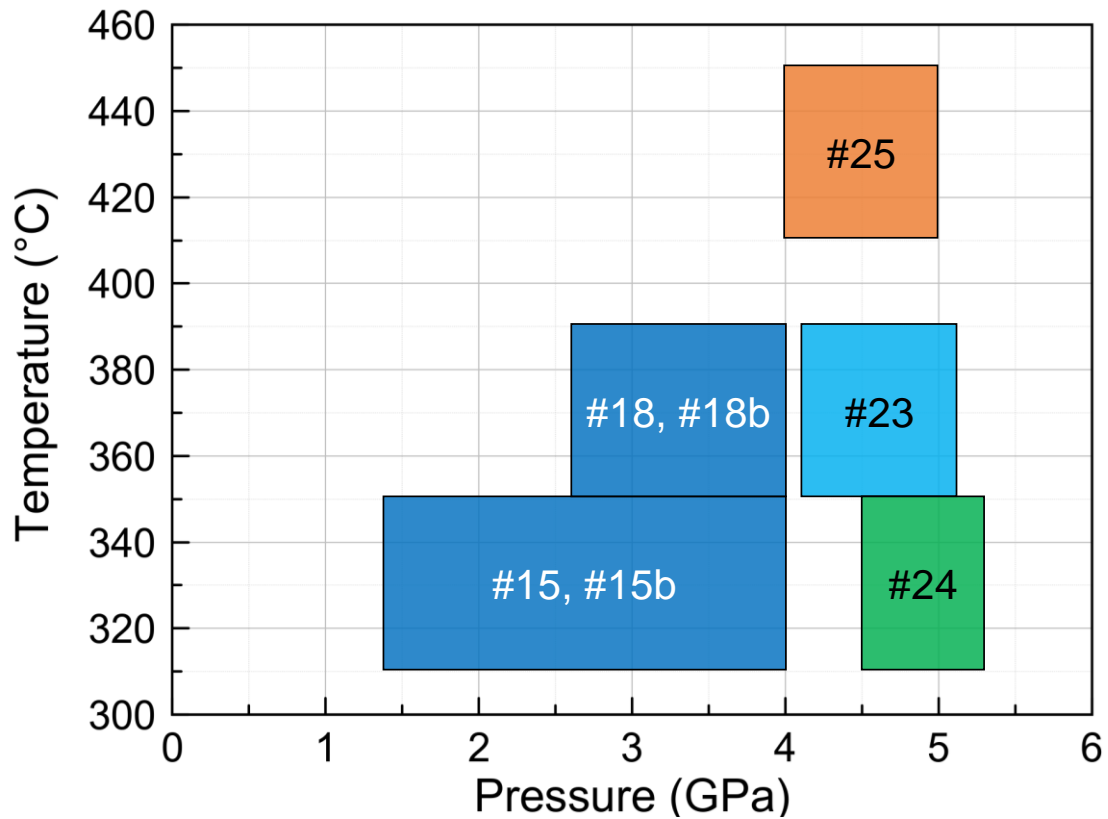
Figure 4. 1. Diagram illustrating the P-T conditions of the runs shown in Table 4.1. Approximate uncertainties on temperature are also shown ($\pm$ ca. 20° C), and are based on temperature calibration reported in section 3.2.3 in the present work.
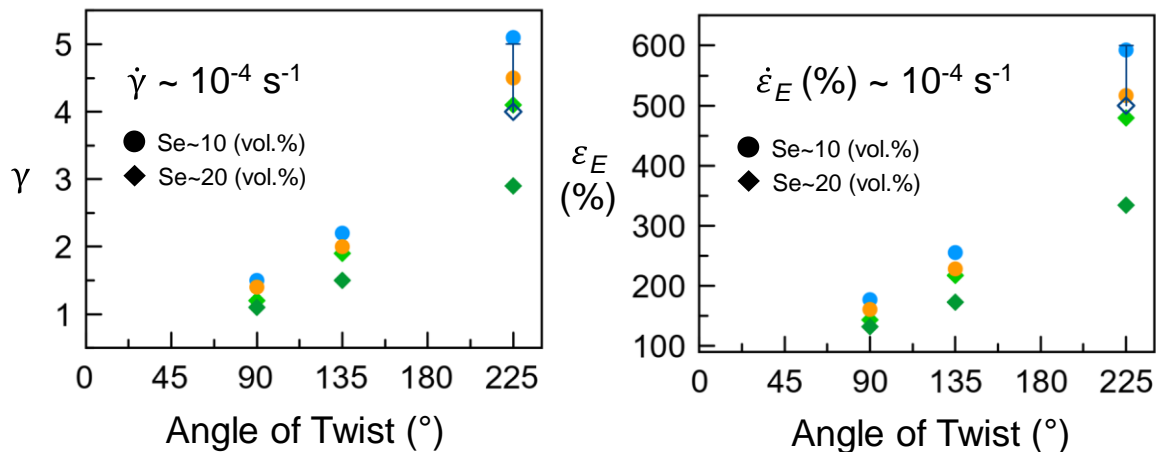
Figure 4. 2. Diagram showing the simple shear strain (γ) and equivalent strain (ε_E) transferred to the samples with increasing anvil twisting angles (see strains calculation in section 3.4) for runs #23, #24, and #25, plotted in Figure 4.1 and shown in Table 4.1. Color-coding is the same as the one in Figure 4.1. Se is serpentine. $\dot{\gamma}$ and $\dot{\varepsilon}_E$ are simple shear strain rate and equivalent strain rate, respectively. For run #24, two trends are shown (light-green and dark-green diamond-shaped symbols). These two trends correspond to two different calculations for the transferred strains along the sample #24 radius (see Table 4.1). For runs #15, 15b and #18b, only the estimated strain for the last angle of twist is shown (empty diamond symbol, with positive error bar), since for these runs strain markers were not used. Run #18b is not shown because is a static experiment (no deformation, see Table 4.1).

4.2. Background: percolation theory

This section concerns the percolation theory (e.g., Stauffer and Aharony, 2003). The concepts of percolation theory are used in the present work to investigate and discuss the interconnectivity and percolation of serpentine. This is to locate the condition of IWL in the aggregates. A background on percolation theory is, therefore, necessary before presenting the results.

Percolation theory is one of the models in which one can treat the behavior of a two-phase mixture with the phases presenting large contrast in properties (e.g., Karato, 2008) such as the case for the olivine+serpentine aggregate I investigate.

The main purpose of the percolation theory is to find the critical volume fraction of a phase of interest (such as the 'weak' phase in the mixture) at which a cluster of interconnected particles of that phase occurs, percolating from one end to another of the mixture or aggregate. This critical volume fraction corresponds to the so-called percolation threshold (e.g., Stauffer and Aharony, 2003), which leads to a drastic change in the bulk properties of the aggregate (e.g., Karato, 2008). One of the central interests of the percolation theory is to calculate the size of the cluster, i.e. the number of sites or interconnected phase particles making up the cluster, and define the conditions at which the cluster approaches to infinity (i.e., at the percolation threshold) (e.g., Karato, 2008; Stauffer and Aharony, 2003).

Percolation theory has found its application and discussion in multiple studies of heterogeneous rocks and their deformation, mostly concerning development and distribution of cracks or fractures (e.g., Guéguen et al., 1997; Reuschlé, 1998; Liu and Lieb, 2021), melt fraction (e.g., Karato, 2008, and references therein) or pores size and their interconnectivity (e.g., Gueguen and Palciauskas, 1994; Liu and Lieb, 2021).

In this work, the concepts of percolation theory are used to investigate and discuss the percolation of the 'weaker' serpentine within the 'stronger' olivine matrix, based on X-ray tomography observations. Applications of percolation theory to X-ray tomography of rocks are recent (Ikeda et al., 2000; Nakashima and Kamiya, 2007; Navarre-Sitchler et al., 2009; Pringle et al., 2009; Liu et al., 2009; Liu and Lieb, 2021). These applications include, for instance, i) the shape of crystals and the correlations function of a granite sample (Ikeda et al., 2000), ii) the connectivity of pores and anisotropic tortuosity of rocks (Nakashima and Kamiya, 2007), iii) the percolation threshold of the brine of sea ice in a series of samples at different temperature (Pringle et al., 2009).

In a rock investigated through X-ray tomography, the percolation threshold can correspond to the minimum concentration of the phase of interest at which a percolating cluster occurs (Liu and Lieb, 2021). This minimum concentration can simply correspond to the phase volume (Karato, 2008; Liu and Lieb, 2021), or the number of particles (density) of that phase. A percolating cluster is when the phase of interest is observed to percolate from one end to another of the sample boundaries, or from one boundary to another of a defined representative volume (RV) in the XRT image. However, the structure of the phase of interest in the imaged rock specimen is static. To locate when a percolating cluster occur and define the conditions approaching to the percolation threshold, one has to investigate the structure as it evolves with changing parameters. Unless one has access to repeated scans of developing microstructure, the percolation threshold is *a priori* unknown for a static structure (Liu and Lieb, 2021). The datasets of the present work capture a developing microstructure with increasing transferred strain thanks to *in-situ* X-ray tomography. Therefore, the conditions at which a percolating cluster forms can be located.

Percolation theory includes multiple theoretical models and properties to compute and extrapolate for a given media, depending on the purpose and the field/topic of

interest. In the following section, I provide the theoretical explanation on the percolation threshold and cluster size in a specific model relevant for my experiments. The explanation of other models or properties to compute from percolation theory are beyond the scope of this section. Further details or supporting information can be found in Stauffer and Aharony (1992, 2003) and Guegen and Palciauskas (1994).

4.2.1. The Bethe lattice model

Analytical results on cluster size and percolation threshold in a mixture can be obtained considering the geometrical model of the Bethe lattice (Bethe, 1935). The Bethe lattice concerns sites connected to z neighboring sites (z as the coordination number) through bonds. The relations on the Bethe lattice model that follows are from Stauffer and Aharony (1992, 2003), Guegen and Palciauskas (1994) and Karato (2008).

To construct the Bethe lattice, a site as the origin O has to be connected, for instance, to four other adjacent sites A, therefore defining the Bethe lattice coordination number as $z = 4$ (Fig. 4.3). From every site A, there are four bonds or branches: one connected to the origin O (branch of level A), and $(z - 1) = 3$ connected to new sites B (branches of level B). Each of the new sites B is connected to $(z - 1) = 3$ new sites C (branches of level C), and so on to other sub-levels of connections that obey $(z - 1) = 3$.
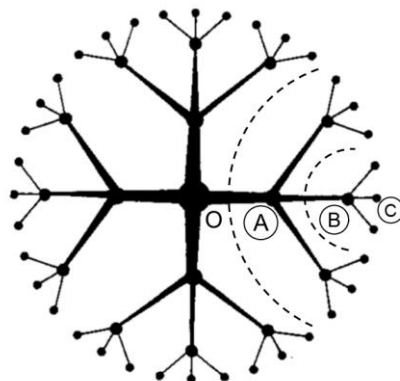
Figure 4. 3. Modified after Guégen and Palciauskas (1994). Bethe lattice model geometry with 4 branches ($z = 4$) at the origin (O), and the sub-branches levels A, B and C.

98

Now, it is necessary to introduce the probability p to find the phase of interest in the sites or bonds of the Bethe lattice network. For the purpose of the present work (see sections 1.4, 4.1), p can correspond to the volume fraction of the weak phase (e.g., Karato, 2008), or density of the weak phase particles in a specific region of interest or volume of the aggregate.

The percolation threshold p_c in a Bethe lattice depends on how the lattice is constructed, i.e. the coordination number and sub-level connections. For a given site or bond, the probability of them to be occupied by the weak phase is $(z - 1)p$. Repeating this process to the neighboring sites, the probability to find an occupied bond or site at the n-th step is $[(z - 1)p]^n$. If $(z - 1)p < 1$, then $[(z - 1)p]^n \to 0$ as $n \to \infty$. This implies that the probability for an infinite cluster spanning the Bethe lattice is zero. Therefore,

$$p_c = \frac{1}{z - 1} \quad (4.1).$$

In the Bethe lattice geometry considered here (i.e., $z = 4$), p_c is equal to 1/3. This result is valid for both the site and bond percolation problem.

Now, it is necessary to introduce the so-called average cluster size S from percolation theory in a Bethe lattice (Stauffer and Aharony, 1992, 2003; Guegen and Palciauskas, 1994; Karato, 2008). It can be defined as the average number of sites/bonds occupied by the weak phase in the Bethe lattice (e.g., Karato, 2008). The interest is to calculate S when p is near the threshold p_c, considering there are four branches from the origin O leading to the sub-branches (Fig. 4.3). Let us first introduce T as the average size of the cluster, i.e. the average number of sites occupied by the weak phase to which the origin is connected to a single branch A. A single branch can be further subdivided into three other infinite branches. There are three neighboring sites, B, that extend further away (Fig. 4.1). Leaving site A, a neighbor site is either an unoccupied site with probability $(1 - p)$, or occupied with probability p. The unoccupied sites contribute 0 to the size of the

cluster, whereas the occupied sites contribute $(1 + 3T)$: 1 for the site itself, and $3T$ for the three branches emanating from that site. Therefore

$$T = (1 - p)0 + p(1 + 3T), \qquad T = \frac{p}{1 - 3p} \quad (4.2).$$

The size of a cluster emanating from the origin is 0 if the site is empty, and $(1 + 4T)$ if the origin is occupied. Therefore:

$$S = (1 - p)0 + p(1 + 4T), \qquad S = \left(\frac{1 + p}{1 - 3p}\right) \quad (4.3).$$

If one presumes there is an infinite cluster above the percolation threshold p_c, it is plausible that slightly below p_c the average cluster size is very large, and indeed the denominator of the equation 4.3 vanishes for $p = 1/3 = p_c$, giving:

$$S \propto \frac{1}{p_c - p} \quad (4.4).$$

This states that the average cluster size S tends to infinity as it approaches to the percolation threshold p_c (e.g., Stauffer and Aharony, 1992, 2003; Guegen and Palciauskas, 1994; Karato, 2008).

4.3. Results (I): Microstructure of the serpentine

4.3.1. Microfabrics and structural layering (in-situ X-ray tomography)

4.3.1.1. Observations

Figure 4.4 and 4.5 show the evolution of serpentine microstructure with increasing strain, in 2-d unrolled sections parallel to the direction of shear. The sections are extracted from the tomography image of the representative volume (RV; see sections 3.5.1, 3.5.3).

The starting, non-sheared ($0°$ twist, $\gamma = 0$) microstructure shows some local pre-existing structural features or discontinuities dipping at ca. 20-30° angle with respect to the horizontal direction of the sections reference frame (Fig. 4.4, 4.5). These features are inferred by local distribution of serpentine clusters along or around what can be fractures, which could develop prior deformation. The two samples with higher serpentine content (20 vol. %), i.e. runs #24 and #18 (see Table 4.1), visibly show evident differences in the starting ($0°$ twist, $\gamma = 0$) cluster size distribution between one another. The former visibly shows an initial greater population of larger clusters in the section than the latter (Fig. 4.5). This feature is not visible in the starting microstructure of the two samples with lower serpentine content (10 vol. %, Fig. 4.4).

Two main kind of structures are visible in the sheared serpentine (e.g., Fig 4.4, at 225° twist; Fig. 4.5, at 135° and 225° twist):

(i)   shear-localized bands dipping at moderate to high angles with respect to the direction of shear;

(ii)   sigmoidal serpentine structures, or lenses, defining the sense of the transferred shear.

Some of the locations and orientations of the shear bands ((i)-type structure) coincide with the ones of the pre-existing fractures developed due to hot-compression (at $0°$ twist; Fig. 4.4, 4.5).
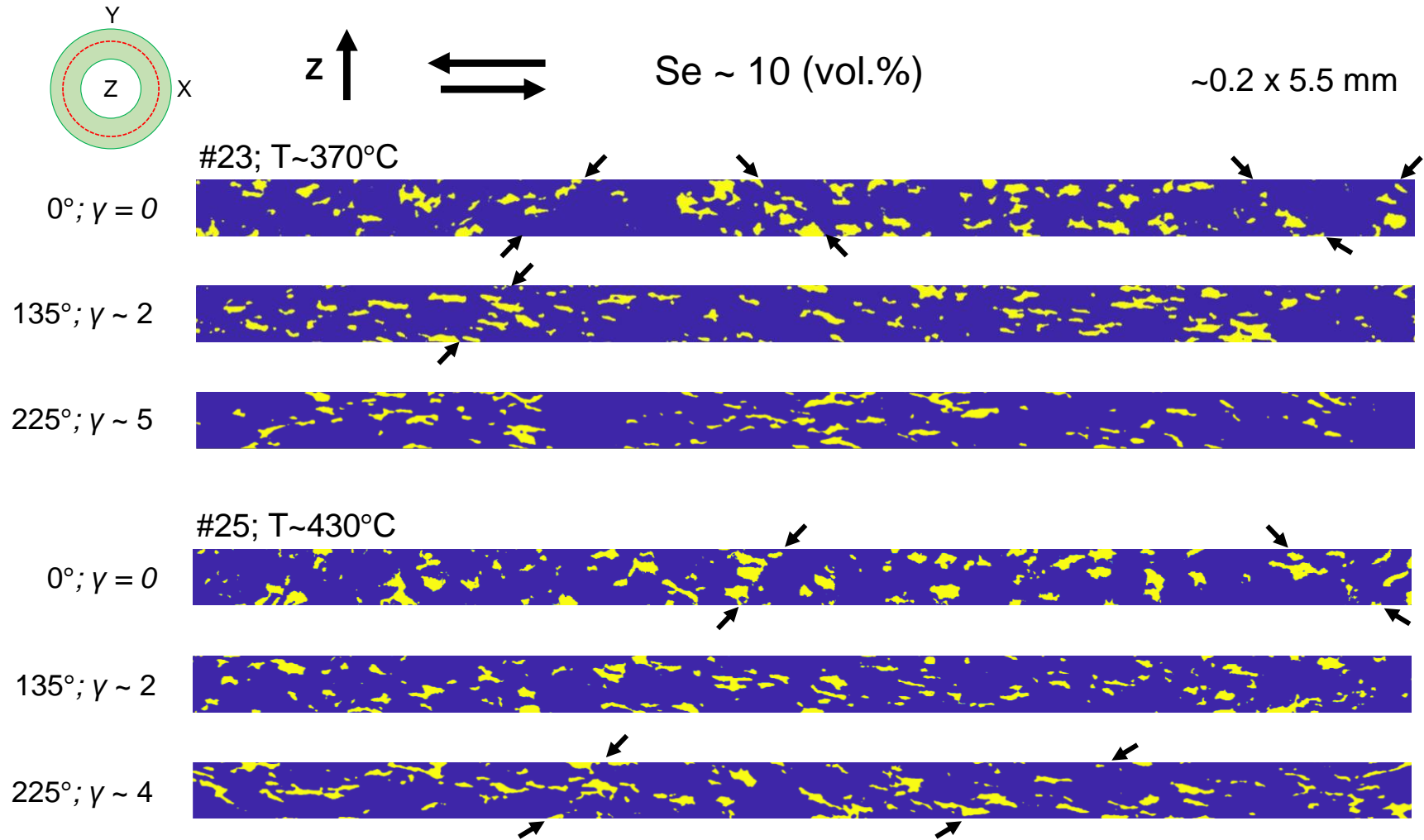
Figure 4. 4. Serpentine microstructure described by the 2-d clusters (yellow) observed in the unrolled sections with increasing deformation, in two samples (#23 and 25, see Table 4.1) with serpentine (Se) content ~10 vol.%, and at two different temperatures. The inset in the upper-left corner shows the location of the unrolled section along the radius of the RV doughnut (red-dashed line). Z is the torsion axis. Arrows on top indicate the sense of shear. Opposing arrows on the sections delineate oblique structural features or discontinuities, which can correspond to shear bands boundaries at the last stage of deformation in run #25. Numbers in degrees (°) are the angle of twist of the anvil. γ is the simple shear (see section 3.4).
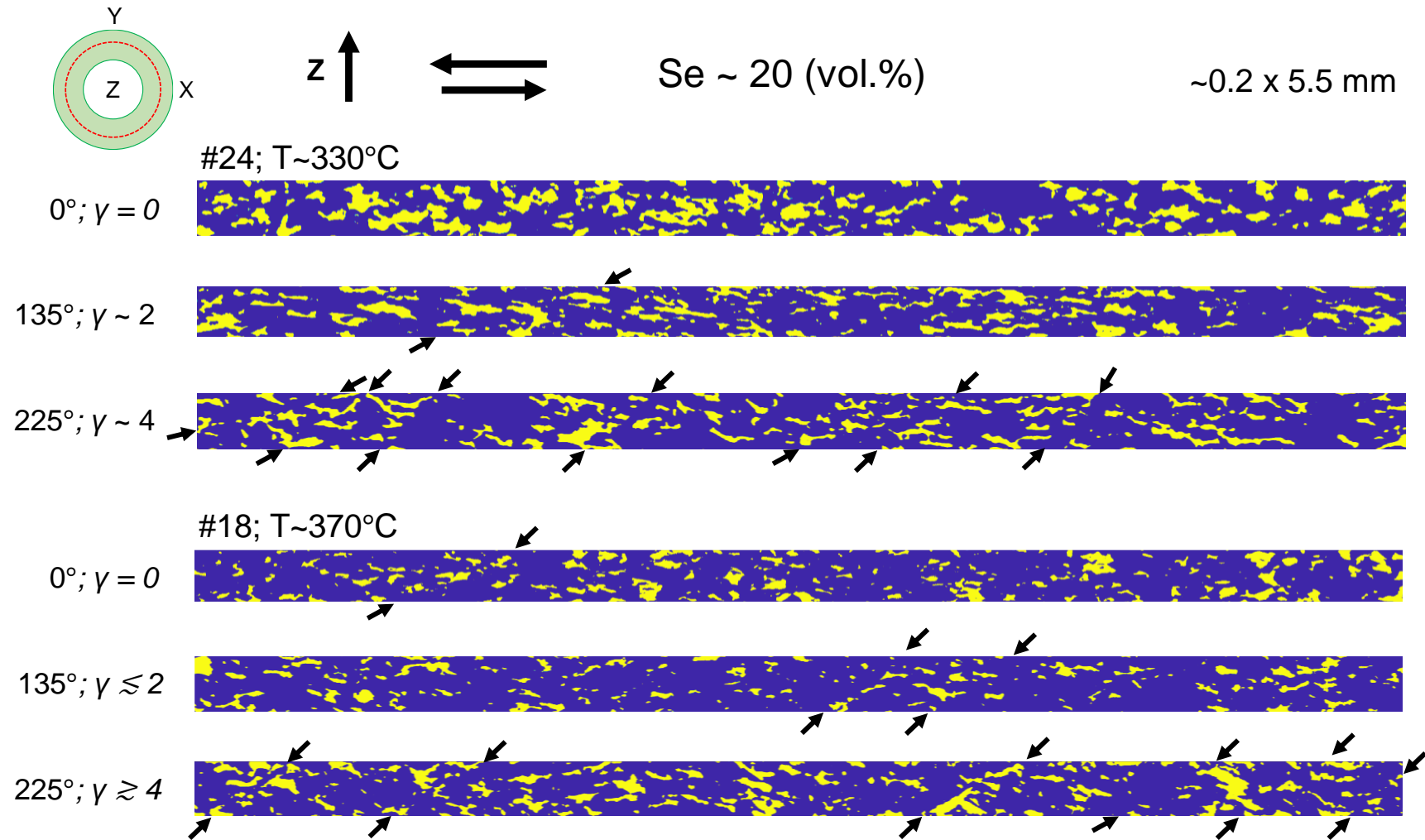
Figure 4. 5. Serpentine microstructure described by the 2-d clusters (yellow) observed in the unrolled sections with increasing deformation, in two samples (#24 and #18, see Table 4.1) with serpentine (Se) content ~20 vol.%, and at two different temperatures (T). The inset in the upper-left corner shows the location of the unrolled section along the radius of the RV doughnut (red-dashed line). Z is the torsion axis. Arrows on top indicate the sense of shear. Opposing arrows on the sections delineate oblique structural features or discontinuities, which correspond to shear bands boundaries (in #24 at 225°, in #18 at 135° and 225°) within which sigmoidal serpentine clusters develop and define the sense of shear. Numbers in degrees (°) are the angle of twist of the anvil. γ is the simple shear (see section 3.4).

The structural features that develop as deformation increases depend on the serpentine content. In the samples with lower serpentine abundance (10 vol. %, Fig. 4.4), the microstructure tends to maintain an overall structural alignments parallel, or subparallel, to the shear, with lack of developed shear bands ((i)-type structure, above). Locally, developed sigmoidal serpentine lenses ((ii)-type structure, above) are observable at the last stages of deformation (Fig. 4.4). Overall, the extension/elongation of the serpentine clusters aligned along the shear direction prevails over the formation of (i)-type distributed shear bands. In the samples with higher serpentine abundance (20 vol.%, Fig. 4.5), structures (i) and (ii) are visible before the last stage of deformation, and develop in conjunction with networking, or clustering, among neighboring clusters, forming in some cases complex and large structures that tend to percolate from one boundary to another of the unrolled sections, as well as describing the sense of shear (e.g., run #18 at 225° twist, Fig. 4.5).

I also perform 3-d observation on the serpentine morphology at a smaller scale. Selected regions (boxes) of interest (ROI) within the RV are extracted (Fig. 4.6).

At this scale of observation, the samples present a starting morphology characterized by a dispersed distribution of the clusters. With increasing strain, the samples with higher serpentine content (20 vol.%) first show an increase in clusters size, and alignment along the shear direction. Then, at the last stage of deformation, clusters rotation and formation of sigmoidal elongated structures occur. Here, in some cases, the elongated clusters percolate from one end to another of the ROI and defining well the sense of shear (e.g., run #18 at 225, Fig. 4.6). On the other hand, in the samples with lower serpentine content (10 vol.%), the clusters predominantly align parallel or subparallel to the shear direction with increasing deformation.

At the first (90° twist) and intermediate (135° twist) stages of deformation, it is possible to observe a peculiar local vertical (perpendicular to the shear direction)

T~330°C

#15; ~10 vol.%

#15b

$\gamma \gtrsim 1$

$\gamma \gtrsim 4$

#24; ~20 vol.%

$\gamma \sim 1$

$\gamma \sim 2$

$\gamma \sim 4$

T~370°C

#23; ~10 vol.%

$\gamma \sim 1$

$\gamma \sim 2$

$\gamma \sim 5$

#18; ~10 vol.%

$\gamma \gtrsim 1$

$\gamma \lesssim 2$

$\gamma \gtrsim 4$

T~430°C

#25; ~10 vol.%

$\gamma \sim 1$

$\gamma \sim 4$

~200 µm

z

anvil twisting rate: 0.02°s^{-1}

0°(twist angle); 0 (Δt min.)   90°; 75   135°; 112.5   225°; 187.5
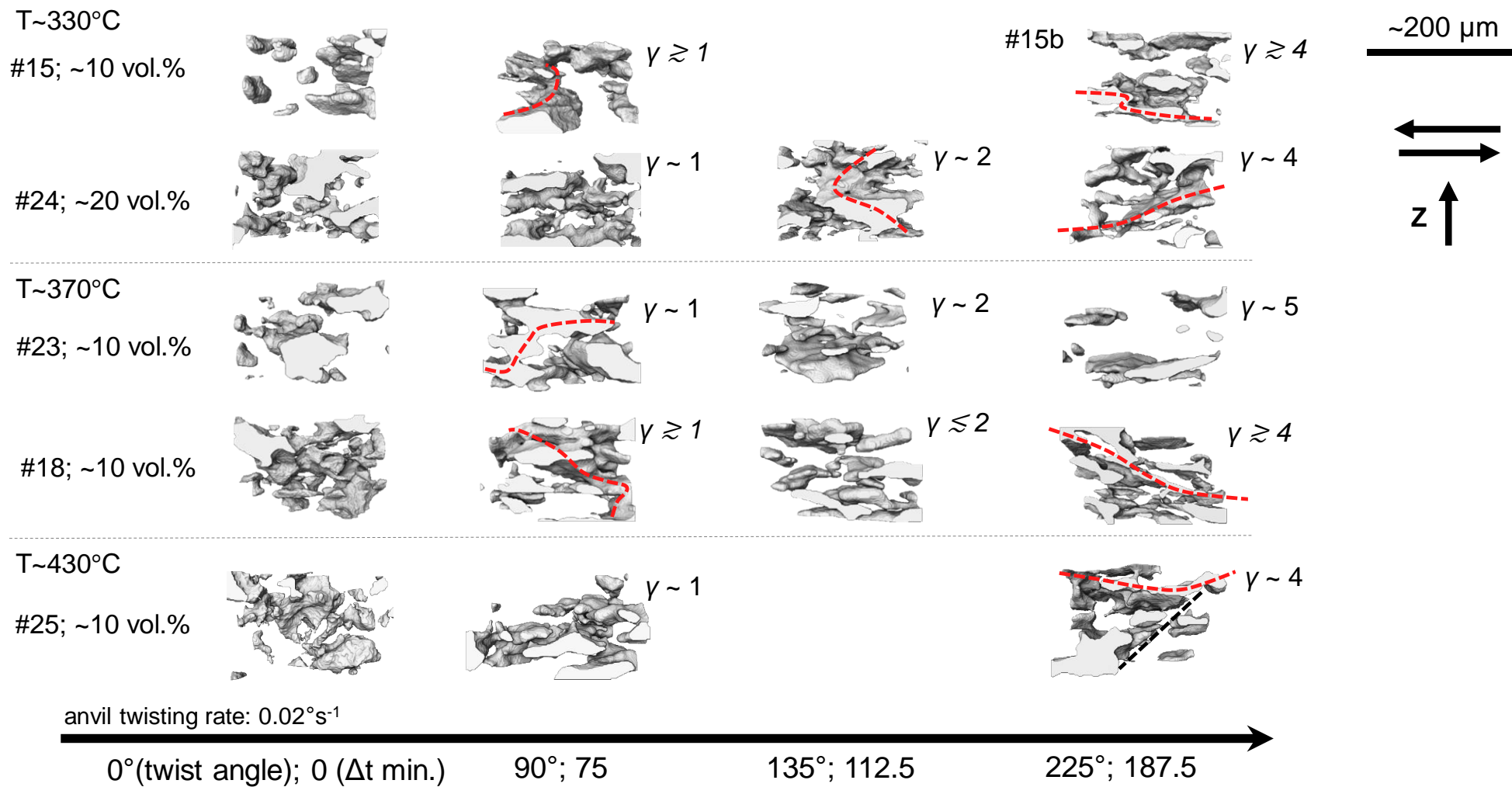
Figure. 4.6. Local serpentine microstructures described by renders of 3-d clusters (shaded-grey) observed in regions of interest (ROI, 150 x 150 x 100 voxels) within the RV. On the right-side, Z is the torsion axis, the arrows show the sense of shear. The clusters morphology is shown for the two serpentine contents (10 and 20 vol.%) at different temperatures (T) with increasing deformation (arrow on the bottom). γ is the simple shear (see section 3.4). Δt is the time interval between the start of the twisting and a specific twisting angle (°), without counting the time spent for the tomography acquisition. For the renders of sample #15 at 225°, the tomography acquisition was performed ex-situ (see section 3.3) on sample #15b (see Table 4.1). The red-dashed lines highlight: i) interconnecting clusters percolating vertically and forming 'pile-up' structures at 90° (samples #15, #23, #18) and 135° (sample #24); ii) interconnecting or elongated clusters percolating horizontally and following the shear direction at 225° (samples #15, #24, #18, #25). The black-dashed line highlights an oblique structural feature or discontinuity between the clusters (sample #25, at 225°) corresponding to the features delineated by opposing back arrow on the sections in Fig. 4.2 (sample #25, at 225°).

percolation or networking among neighboring clusters in both kind of samples (both serpentine contents; samples #15, #24, #23, #18, Fig. 4.6). These "pile-up" structures developing along the vertical direction are especially visible at the first stages of deformation (90° twist, samples #15, #23, #18, Fig. 4.6). The vertical percolation with pile-ups is not visible at the last stage of deformation.

4.3.1.2. Quantifications

Here, I present quantifications obtained from the serpentine microstructure in the 2-d unrolled sections parallel to the shear direction. The quantifications regard cluster size distribution and evolving shape, as well as their preferred structural layering, or orientation, with respect to the shear direction.

Cluster size distribution

I first provide below in Table 4.2 the arbitrary classification of clusters in 2-d (see also section 3.5.3) based on their area in microns and pixel.

The clusters area distribution (in μm^2) is given as a histogram for the samples at lower serpentine content (ca. 10 vol.%, samples #23 and #25; Fig. 4.7), and for the samples at higher serpentine content (ca. 20 vol.%, samples #24 and #18; Fig. 4.8, 4.9) with increasing deformation and as a function of increasing temperature.

Table 4. 2. Classification of the serpentine clusters in 2-d.

	Clusters 2-d		
	Small	Medium	Large
μm^2	$50 \leq x < 100$	$100 \leq x < 1000$	$x \geq 1000$
$pixel^2$	$\sim 30 \leq x < \sim 60$	$\sim 60 \leq x < \sim 590$	$x \geq \sim 590$
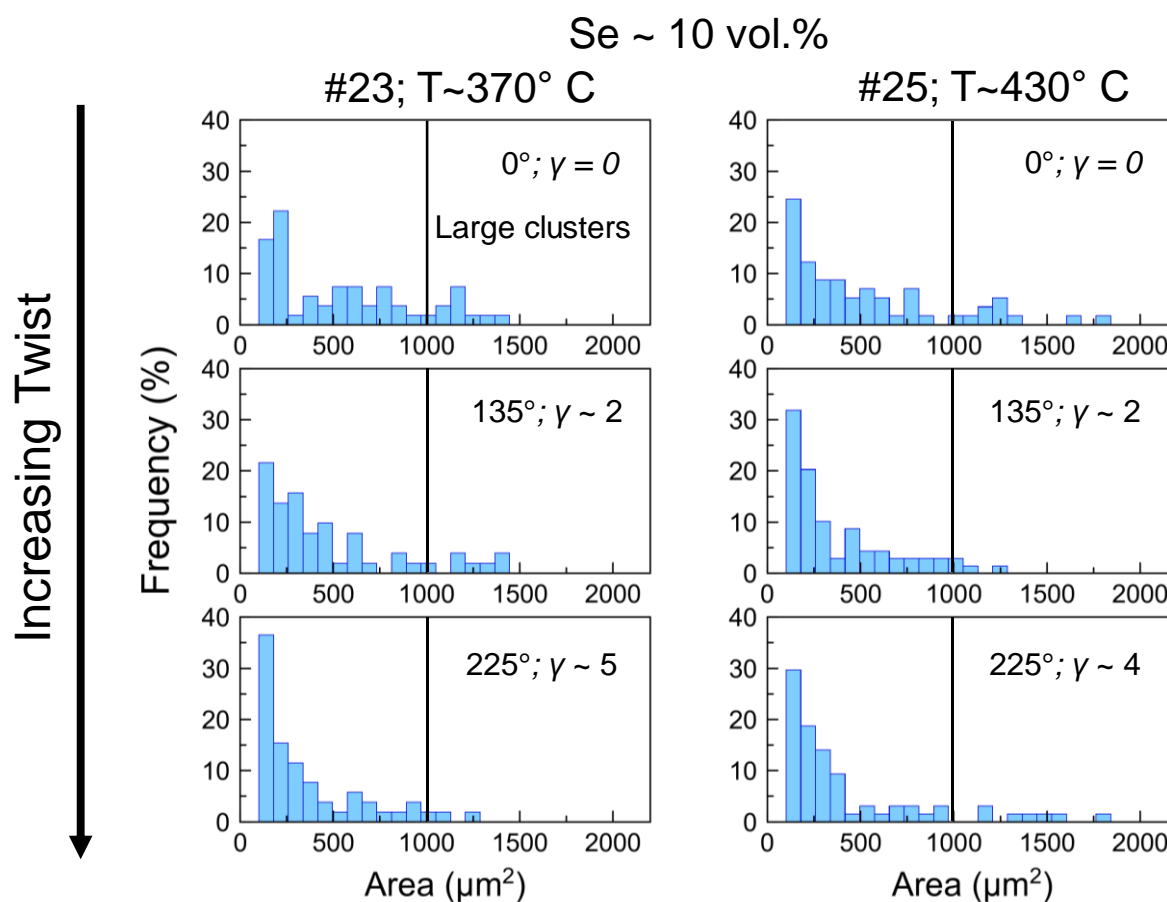
Figure 4. 7. Serpentine clusters size (area) distribution in the unrolled sections of two samples (#23 and #25), shown for two temperatures (T) at lower serpentine (Se) content (~10 vol.%) with increasing deformation. Numbers in degrees (°) are the angle of twist of the anvil. γ is the simple shear.

At ca. 10 vol.% of serpentine (Fig. 4.7), the initial clusters distribution at higher temperature (#25) is slightly broader than the one at lower temperature (#23). Sample #23 shows a homogeneous distribution from ca. 250 to 1500 μm^2, with low frequency (<10%), of the large and part of the medium clusters. With increasing deformation, the clusters in both samples (#23 and #25) overall show a shift towards lower areas, and therefore an overall increase of the population of the small and medium clusters.

At ca. 20 vol.% of serpentine (Fig. 4.8), the initial cluster distribution at higher temperature (#18) clearly shows a larger population of the smallest clusters than the one
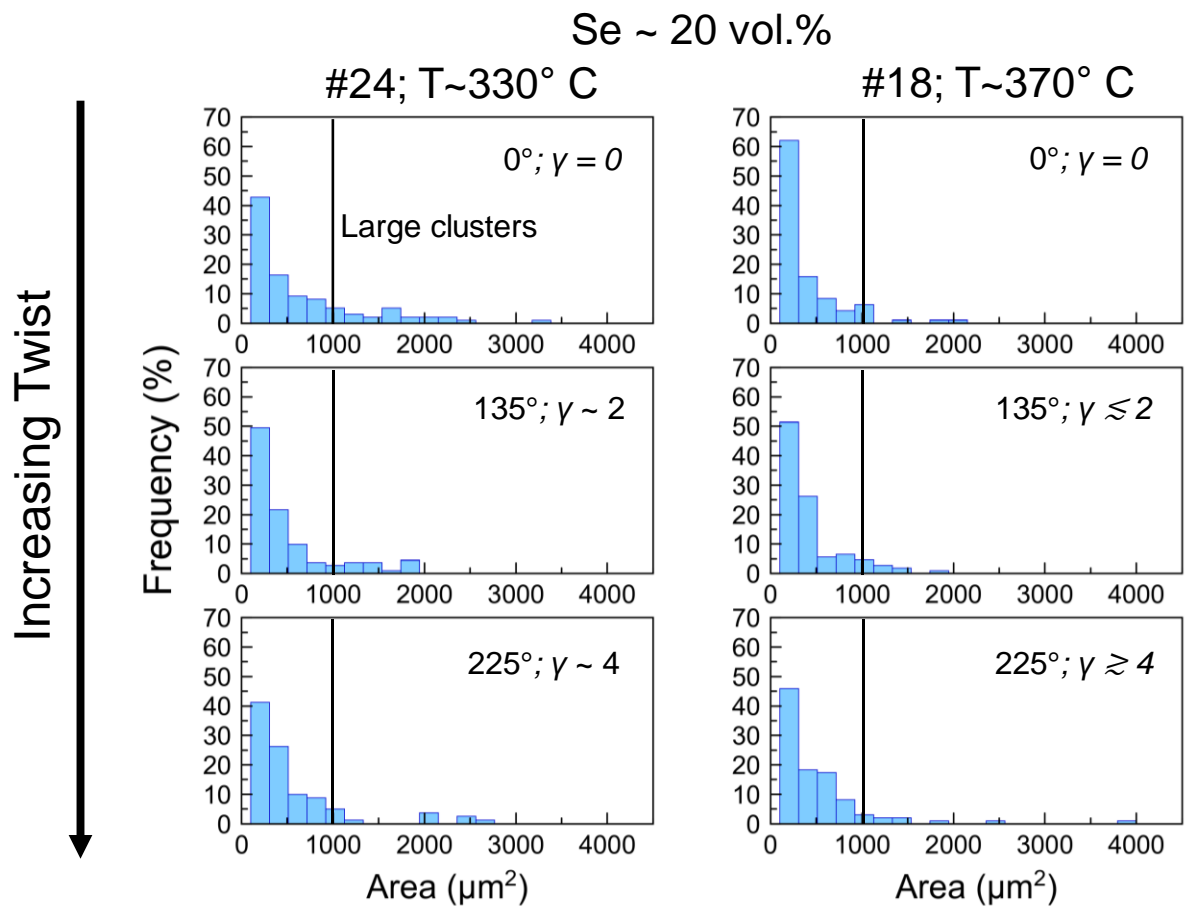
Figure 4. 8. Serpentine clusters size (area) distribution in the unrolled sections of two samples (#24 and #18). It is shown for two temperatures (T) at higher serpentine (Se) content (~20 vol.%) with increasing deformation. Numbers in degrees (°) are the angle of twist of the anvil. γ is the simple shear.

in the sample at lower temperature (#24), with the former showing a frequency of 40% and the latter a frequency of 60%. With increasing deformation, this initial difference in population and distribution is not visible anymore, with both samples overall showing similar distribution from small to large clusters (Fig. 4.8). Figure 4.9 shows the cluster size distribution of the same samples #24 and #18 but only in the large cluster size range (≥1000 μm^2, Table 4.2). Here, the clusters in sample #18 overall increase with increasing deformation, even though their distribution temporarily shifts to, and concentrate around smaller areas between 1000 and 2000 μm^2 with total frequency of ca. 80%, at the intermediate stage of deformation (Fig. 4.9). In sample #24, the increase in the large cluster with increasing deformation is less obvious (Fig. 4.9). Slight changes in frequency

and distribution concerns the clusters around 1000 and 3000 µm², with few bigger clusters outlying around 4000 and 5000 µm² (frequency of ca. 10%) (Fig. 4.9).
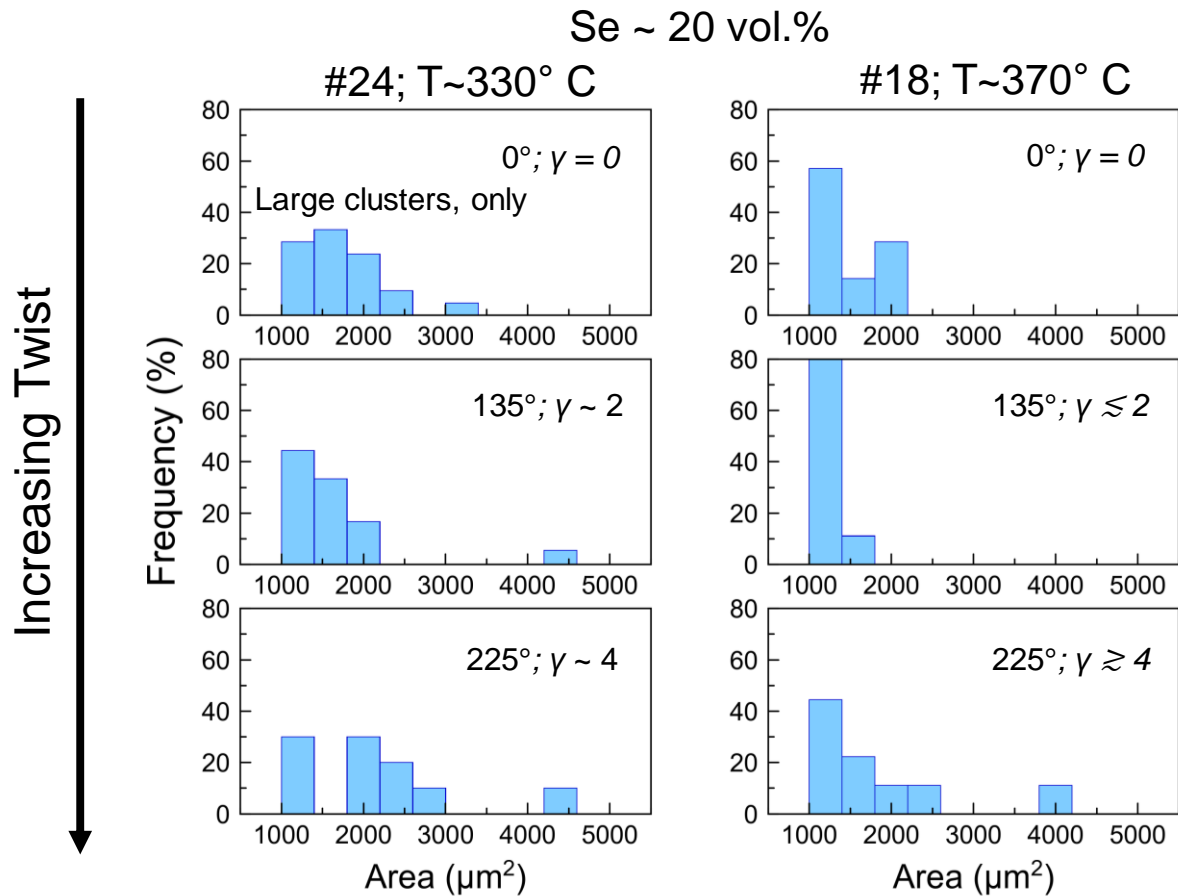
Figure 4. 9. Serpentine clusters size (area) distribution in the unrolled sections of two samples (#24 and #18) only concernig the large clusters. It is shown for two temperatures (T) at higher serpentine (Se) content (~20 vol.%) with increasing deformation. Numbers in degrees (°) are the angle of twist of the anvil. γ is the simple shear.

Individual clusters morphology and orientation

The morphology of the individual clusters was obtained from the image processing program Fiji (Particle Analysis (imagej.net); see also chapter 3, section 3.6.1). Parameters taken into account here are:

1) Perimeter (µm), the contouring length of each cluster.

2) Aspect ratio, the ratio of the major axis over the minor axis of the ellipse fitting each cluster. It gives information on shape anisotropy of the clusters.

3) The orientation distribution in angle (°) of the clusters. It is computed considering the major axis orientation of the ellipses fitting the individual clusters. The

orientation is from -90° to 90° with respect to the horizontal direction of the unrolled sections (i.e., 0°), which corresponds to the shear direction.

4) The orientation distribution in angle (°) of the clusters boundaries with respect to the shear direction (from -90° to 90°). This is obtained through the so-called "directionality" tool in Fiji (Directionality (imagej.net); see also chapter 3, section 3.5.3). Specifics on the tool can be found elsewhere (e.g., Liu, 1991). The directionality is useful for obtaining inter-phase boundary orientations, between the serpentine clusters and the olivine in the matrix.

The results concerning the above parameters are described in the sections below, as follows: a) as a function of serpentine content and with increasing deformation, at constant temperature of ca. 370°C (Fig. 4.10, 4.11); b) as a function of temperature and with increasing deformation, for i) the lower serpentine volume in the aggregates (ca. 10 vol.%; Fig. 4.12, 4.13), and ii) the higher serpentine volume (ca. 20 vol.%, Fig. 4.14, 4.15).

(a)   Constant temperature (ca. 370°C)

The perimeter distribution of the serpentine clusters (Fig. 4.10) extends to higher values with increasing deformation, from a maximum of 190 μm for both samples (#23 and #18, ca.10 and 20 vol.% of serpentine, respectively), to a maximum of 260 μm, for the sample with lower serpentine content (#23, ca. 10 vol.%), and a maximum of 540 μm, for the sample with higher serpentine content (#18, ca. 20 vol.%). In this latter, at the last stage of deformation (225° twisting; $\gamma \gtrsim 4$), the population of the smallest cluster perimeters (around 50 μm) decreases, and the few outliers clusters of larger perimeter appear (ca. 330 and 540 μm).

The aspect ratio distribution (Fig. 4.10) overall shift towards higher values (up to 7-8) with increasing deformation at both serpentine contents. The sample at higher serpentine content initially shows a significantly higher frequency of clusters with aspect ratio around 1 than the sample at lower serpentine content. At 135° twisting ($\gamma \sim 2$), the
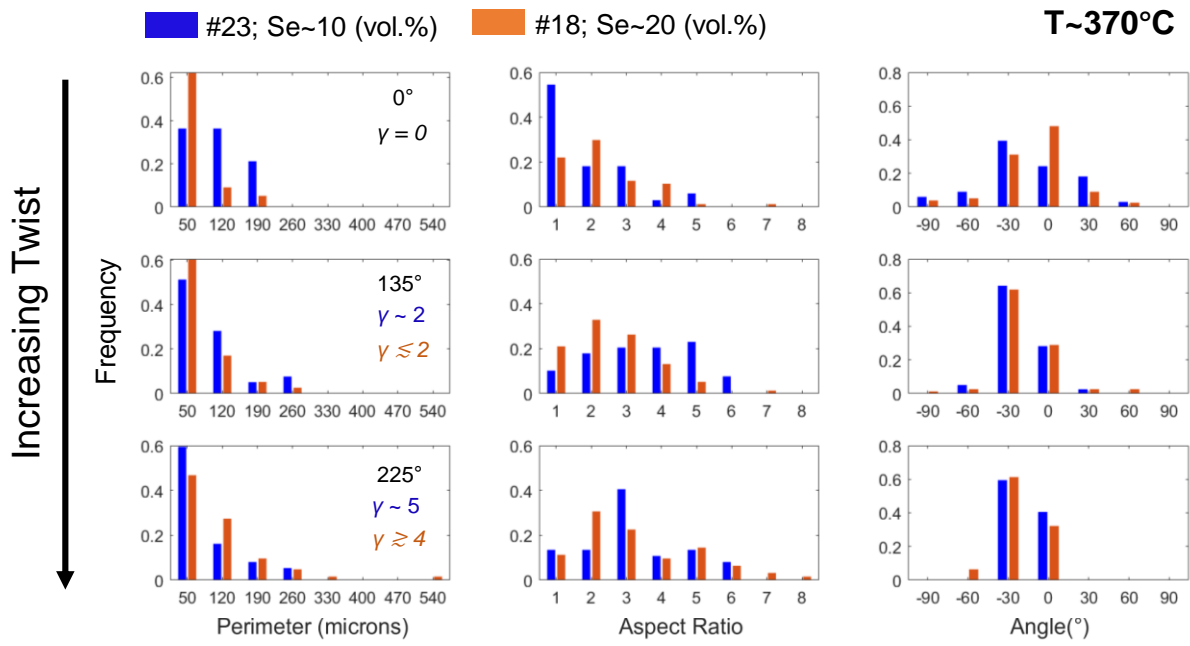
Figure 4. 10. Histograms distributions of serpentine clusters morphology described by perimeter (μm, left), aspect ratio (middle), and angle of orientation (°, right) with respect to the shear direction (0°) of the fitting ellipse to each individual cluster. Histograms are shown for the two serpentine (Se) contents (~10 and 20 vol.%, samples #23 and #18, respectively; Table 4.1) at the same temperature (T) with increasing twisting angle of the anvil (°).

sample at lower serpentine content shows higher frequency of clusters with moderate to high aspect ratios (around 4, 5 and 6), whereas the sample at higher serpentine content shows higher frequency of clusters with low aspect ratios (ca. 1, 2 and 3). At the last stage of deformation, the aspect ratio distribution of the sample at lower serpentine content shifts back towards low to moderate values, showing a maximum peak at ca. 3, whereas in the sample at higher serpentine content the maximum peak is located ca. 2, even though its aspect ratio distribution also extends towards higher values, with few clusters showing aspect ratio of 6, 7 and 8. The orientation distribution (°) of the clusters (Fig. 4.10) shows pre-existing preferential orientations in both samples. The sample at higher serpentine content shows a greater population of clusters parallel or sub-parallel to the shear direction (ca. 0°) than the sample at lower serpentine content. This latter instead shows a greater population of cluster oriented at about -30° than the sample at higher serpentine. With increasing deformation, the two samples show a consistent distribution

around -30°. This orientation prevails over the one parallel to the shear (0°) in both samples until the last stage of deformation.

The orientation distribution (°) of the clusters boundaries (directionality, Fig. 4.11) in both samples overall shows an increase around 0° (i.e., parallel to the shear direction) during the first stage of deformation (90° twisting).
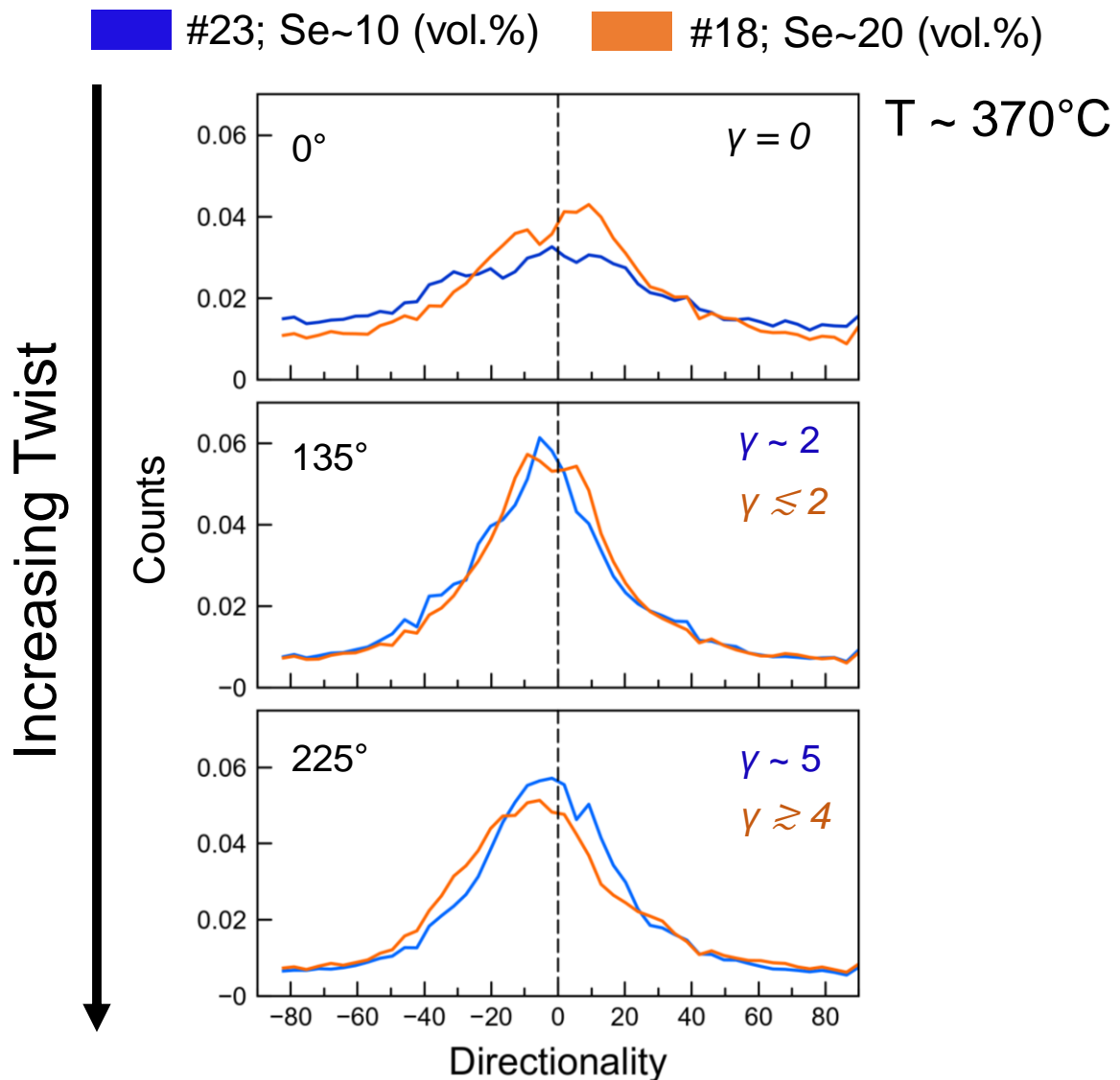
Figure 4. 11. Distribution of orientation of the serpentine clusters boundaries with respect to the shear direction (0°). The distributions are shown for the two serpentine (Se) contents (~10 and 20 vol.%, samples #23 and #18, respectively; Table 4.1) at the same temperature (T) with increasing deformation. Numbers in degrees (°) are the angle of twist of the anvil. γ is the simple shear.

In the sample at higher serpentine content (sample #18, Fig. 4.11), pre-existing (0° twisting) peaks are visible at +10° and −10°, with population at +10° being slightly higher. This feature disappears at the first stage of deformation (90° twisting). At the last

stage of deformation (225° twisting, $\gamma \gtrsim 4$), the distribution skews to negative angles with respect to the shear in the same sample (sample #18). Here, it is also possible to see a shoulder in the distribution at positive angles from ca. 10 to 40°. On the other hand, the distribution in the sample at lower serpentine content (sample #23, Fig. 4.11) does not show any clear change or anisotropy as deformation increases, except for the occurrence of a secondary peak around 10°.

(b.i)   Constant serpentine content (ca. 10 vol.%)

At ca. 10 vol. % of serpentine, the perimeter distribution (Fig. 4.12) overall shifts to higher values (up to 470 μm), with increasing deformation in both samples at the two different temperatures (samples #23 and #25, ca. 370 and ca. 430 °C, respectively).
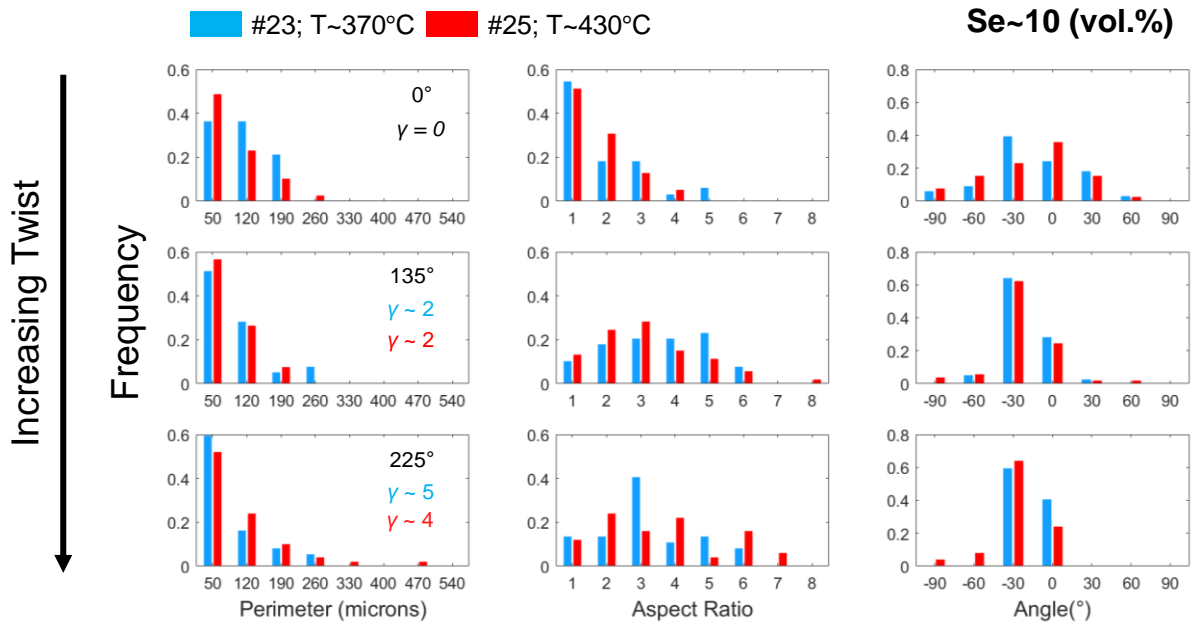
Figure 4. 12. Histograms distributions of serpentine clusters morphology described by perimeter (μm, left), aspect ratio (middle), and angle of orientation (°, right) with respect to the shear direction (0°) of the fitting ellipse to each individual cluster. Histograms are shown for two temperature (T) (~370°C and 430°C, samples #23 and #25, respectively; see Table 4.1) at lower serpentine (Se) content (~10 vol.%) with increasing twisting angle of the anvil (°).

At the last stage of deformation (225° twisting; $\gamma \gtrsim 4$) and with increasing temperature, the population of the smallest cluster perimeters (ca. 50 μm) slight decreases, and the appearance of few outliers clusters with big perimeter occurs (ca. 330 and 470 μm).

The aspect ratio distribution (Fig. 4.12) overall extends towards higher values with increasing deformation at both temperatures. The sample at higher temperature initially shows a significantly higher frequency of clusters of aspect ratio around 2 than the sample at lower temperature. At 135° twisting ($\gamma \sim 2$), the sample at lower temperature shows slightly higher frequency of clusters with moderate to high aspect ratios (ca. 4, 5 and 6), whereas the sample at higher temperature shows higher frequency of clusters with aspect ratio from 1 to 3. At the last stage of deformation, the aspect ratio distribution within the sample at lower temperature is heterogeneous and peaks at 40%, for an aspect ratio of 3, standing out with respect to the overall distribution. Conversely, at higher temperature, the aspect ratio presents an overall more homogenous distribution within the whole range, with higher frequency of around 20% at 3 and 4, and few clusters ($\leq$10% frequency) showing aspect ratio of 7.

The angle (°) distribution (orientation of the major axis of the fitting ellipse) in both sample (Fig. 4.12) initially shows clusters with pre-existing preferential orientations at 0°, i.e. parallel to the shear, and -30° with respect to the shear. The sample at higher temperature shows a greater population of clusters parallel to the shear, whereas the sample at lower temperature shows a greater population of cluster at the -30°. With increasing deformation, the two samples show a consistent distribution around the -30° orientation. This latter prevails over the orientation parallel to the shear (0°) in both samples until the last stage of deformation.

The orientation of the clusters boundaries (directionality, Fig. 4.13) in the two samples overall shows an increase in counts at the first stage of deformation around 0°, i.e. parallel to the shear direction. This is followed by a shift in the distribution to negative angles with respect to the shear as the transferred strain increases in the sample at higher temperature. At the last stage of deformation, a shoulder in the distribution appears covering angles ranges from -40° to -10°. On the other hand, the distribution in the sample
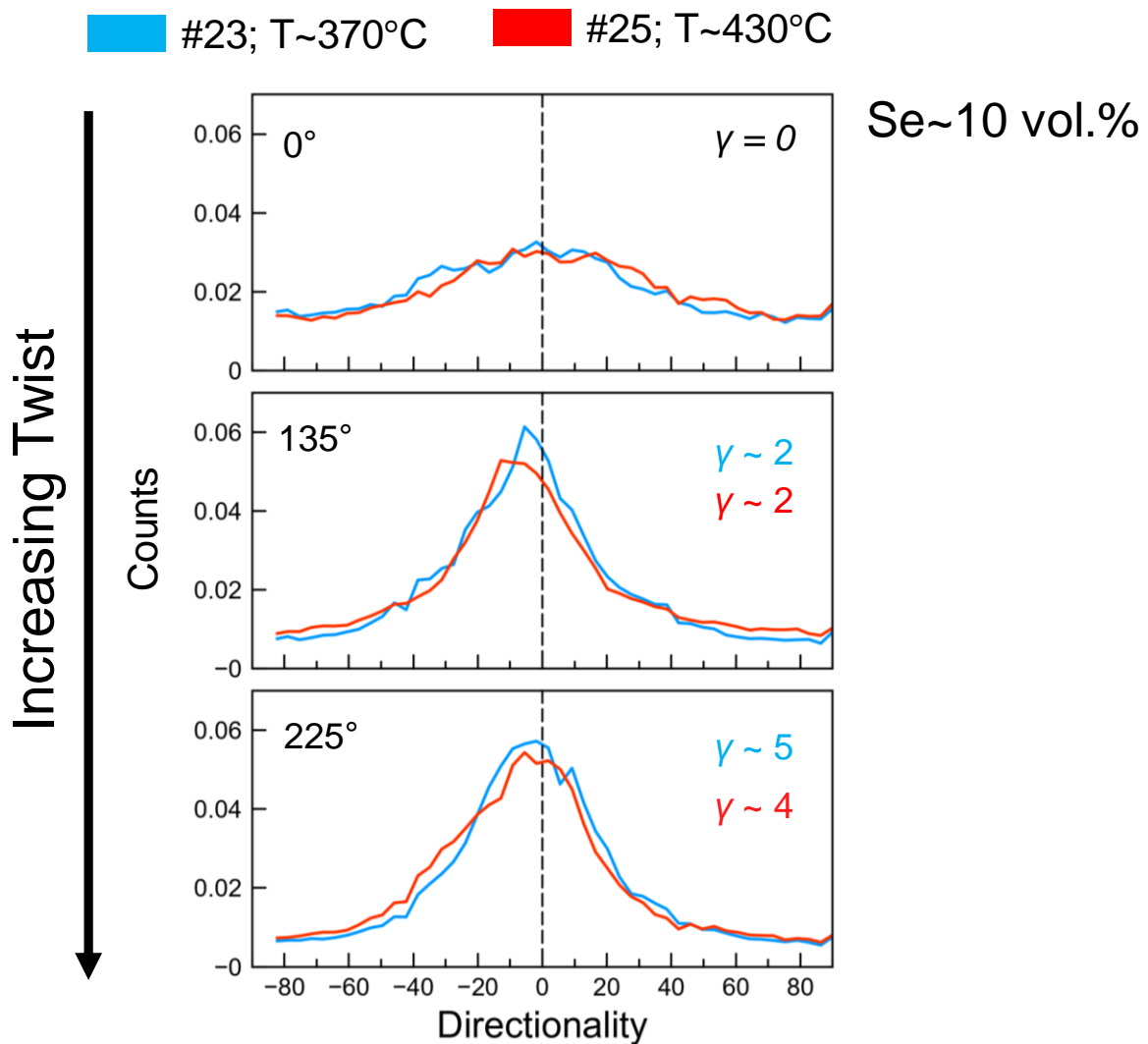
Figure 4. 13. Directionality distribution of the serpentine clusters boundaries with respect to the shear direction (0°). The directionality distributions are shown for two temperatures (T) (~370℃ and 430℃, samples #23 and #25, respectively; Table 4.1) at lower serpentine (Se) content (~10 vol.%) with increasing deformation. Numbers in degrees (°) are the angle of twist of the anvil. γ is the simple shear.

at lower temperature does not show any clear change or anisotropy as deformation increases, except for the occurrence of an additional feature, or secondary peak, around 10°.

(b.ii)   Constant serpentine content (20 vol.%)

At ca. 20 vol. % of serpentine, the perimeter distribution (Fig. 4.14) overall shows an increase in frequency of pre-existing cluster populations ≥120 μm (present at 0° twisting, γ = 0) with increasing deformation in both samples at the two different temperatures (samples #24 and #18, ca. 330 and ca. 370 ℃, respectively).
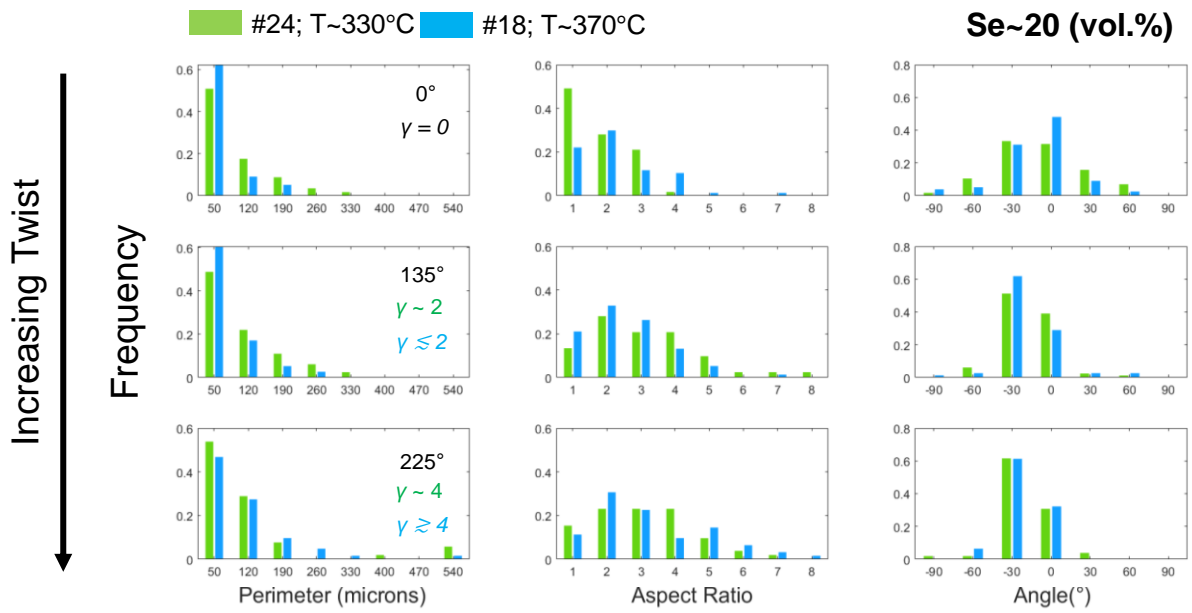
Figure 4. 14. Histograms distributions of serpentine clusters morphology described by perimeter (μm, left), aspect ratio (middle), and angle of orientation (°, right) with respect to the shear direction (0°) of the fitting ellipse to each individual cluster. Histograms are shown for two temperature (T) (~330°C and 370°C, samples #24 and #18, respectively; see Table 4.1) at higher serpentine (Se) content (~20 vol.%) with increasing twisting angle of the anvil (°).

In sample #18, the population of the clusters around 50 μm perimeter decreases with increasing deformation, whereas the one sample #24 remains somewhat stable. At the last stage of deformation (225° twisting) both samples show the occurrence of few big clusters in the range ca. 400 to 540 μm perimeter.

The aspect ratio distribution (Fig. 4.14) overall extends towards higher values with increasing deformation at both temperatures. The sample at lower temperature initially shows a high frequency of clusters of aspect ratio around 1, which disappears with increasing deformation. At 135° twisting ($\gamma \sim 2$), the sample at lower temperature shows slightly higher frequency of clusters around 4 and 5 than the sample at higher temperature, as well as few, quite elongated clusters up to 8 in aspect ratio. In the sample at higher temperature, most frequently clusters have an aspect ratio around 2, which is valid until the end of the deformation.

The fitting-ellipse angle (°) distribution (Fig. 4.14) in both samples initially shows clusters with pre-existing preferential orientations at 0°, i.e. parallel to the shear, and -30°

116

with respect to the shear. The sample at higher temperature shows a greater population of clusters parallel to the shear than the sample at lower temperature. The two samples show a similar frequency for the -30° orientation. With increasing deformation, the two samples show a consistent distribution around the -30° orientation. This latter prevails over the orientation parallel to the shear (0°) in both samples until the last stage of deformation.

The clusters boundaries orientation (directionality, Fig. 4.15) in the two samples overall shows an increase in counts at the first stage of deformation around 0°, i.e. parallel to the shear direction. In the sample at higher temperature (sample #18), pre-existing (prior deformation; 0° twisting) peaks are visible at positive and negative angles up to ca.10°, with the counts of the former being slightly higher.
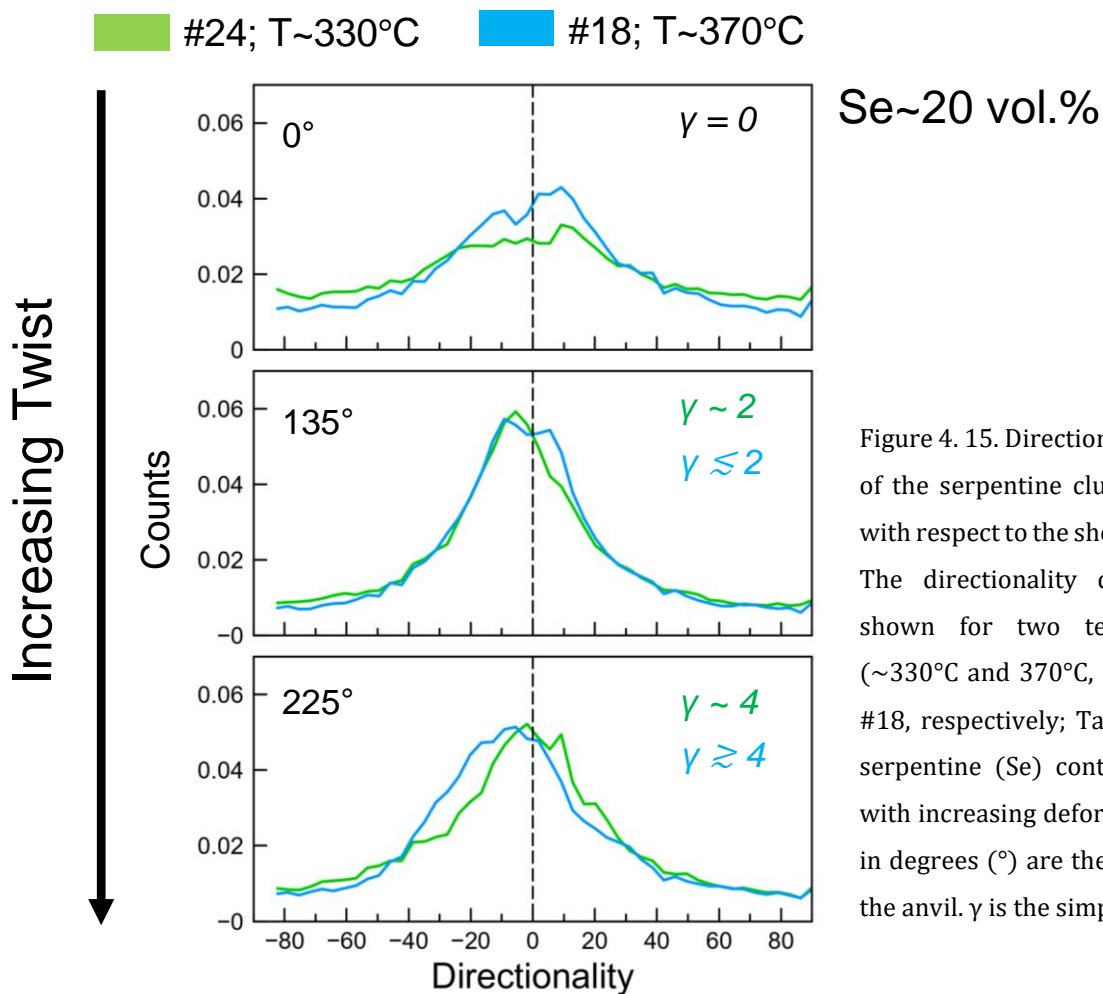
Figure 4. 15. Directionality distribution of the serpentine clusters boundaries with respect to the shear direction (0°). The directionality distributions are shown for two temperatures (T) (~330°C and 370°C, samples #24 and #18, respectively; Table 4.1) at lower serpentine (Se) content (~20 vol.%) with increasing deformation. Numbers in degrees (°) are the angle of twist of the anvil. γ is the simple shear.

This feature disappears at the first stage of deformation (90° twisting) where the counts increase. At the last stage of deformation (225° twisting, $\gamma \gtrsim 4$) the same sample (sample #18) displays a skewness to negative angles with respect to the shear. Here, the occurrence of a small shoulder at positive angles is also visible. On the other hand, the distribution in the sample at lower temperature (sample #24) does not show any clear change or anisotropy as deformation increases, and maintain its overall distribution around 0°, except for the occurrence of a secondary peak around 10°.

2-point function: numerical approach for clusters morphology and orientation

In this section, I provide the results on the serpentine morphology obtained from a numerical approach, i.e. using the functions of 2-point probability (e.g., Torquato, 2002) and 2-point cluster (Torquato et al., 1988; Jiao et al., 2009; Torquato, 2010; Thielmann et al., 2020). The script to compute these results was written by PhD. M. Thielmann (BGI, University of Bayreuth, Germany). The script was run on the 2-d unrolled sections (given in Fig. 4.4, 4.5).

The 2-point probability function answers to the question: What is the probability of finding two arbitrary points x_1 and x_2 within the same phase i? The 2-point cluster function incorporates the information given by the 2-point probability function, and additionally answers to the question: What is the probability of finding two arbitrary points x_1 and x_2 within the same cluster of phase i? The former gives information on phase distribution. The latter additionally gives information on phase morphology, based on the distance and location of the two points in a single cluster of the phase. The functions can be used to statistically determine the whole morphology of random heterogeneous two-phase mixtures in an image, capturing their isotropic or anisotropic nature (e.g., Thielmann et al., 2020).

Here, to quantify the degree of morphological anisotropy of the serpentine, the so-called correlation lengths of the cluster function are computed (e.g., Thielmann et al.,

2020). They are defined as the distance over which two arbitrary points within the serpentine phase, or within the same cluster of serpentine phase (x_1 and x_2, see above), decreases by 1/e (e.g., Taconet and Ciarletti, 2007). The anisotropic feature of the cluster function is described by the 1/e-isoline exhibiting an elliptical shape (e.g., Thielmann et al., 2020). This can be fitted to an ellipse whose semi-major and semi-minor axes corresponds to the two correlation lengths (e.g., Thielmann et al., 2020).

I use the two correlation lengths to obtain the aspect ratio as a morphological descriptor of the serpentine. Additionally, I use the angle of the semi major axis with the horizontal (i.e., the shear direction) to get information about the average orientation (or structural layering) of the serpentine. The aspect ratio and angle are given with increasing deformation for the two serpentine contents and three temperatures conditions investigated (Fig. 4.16).

The serpentine aspect ratio trends (Fig. 4.16) suggest a linear increase with increasing deformation, until reaching a plateau at angles of twist between 90° and 135° (Fig. 4.16). After this point, the aspect ratio indicates a constant trend around a value of 3 up to the highest twisting angle. This is valid for all samples investigated, and the individual trends do not indicate any dependency of either temperature, serpentine content, or transferred strain.

The serpentine structural layering with respect to the horizontal shear direction (or average orientation, in angle; Fig. 4.16) indicates linear increase with increasing deformation. Afterwards, in the region between twisting of 90° and 135°, the angle of orientation starts to show two different kinds of development: (i) two trends that reach a maximum at 135° of twist and later remain somewhat stable, showing an angle of orientation around 5° until the last stage of deformation (blue-circle and green diamond
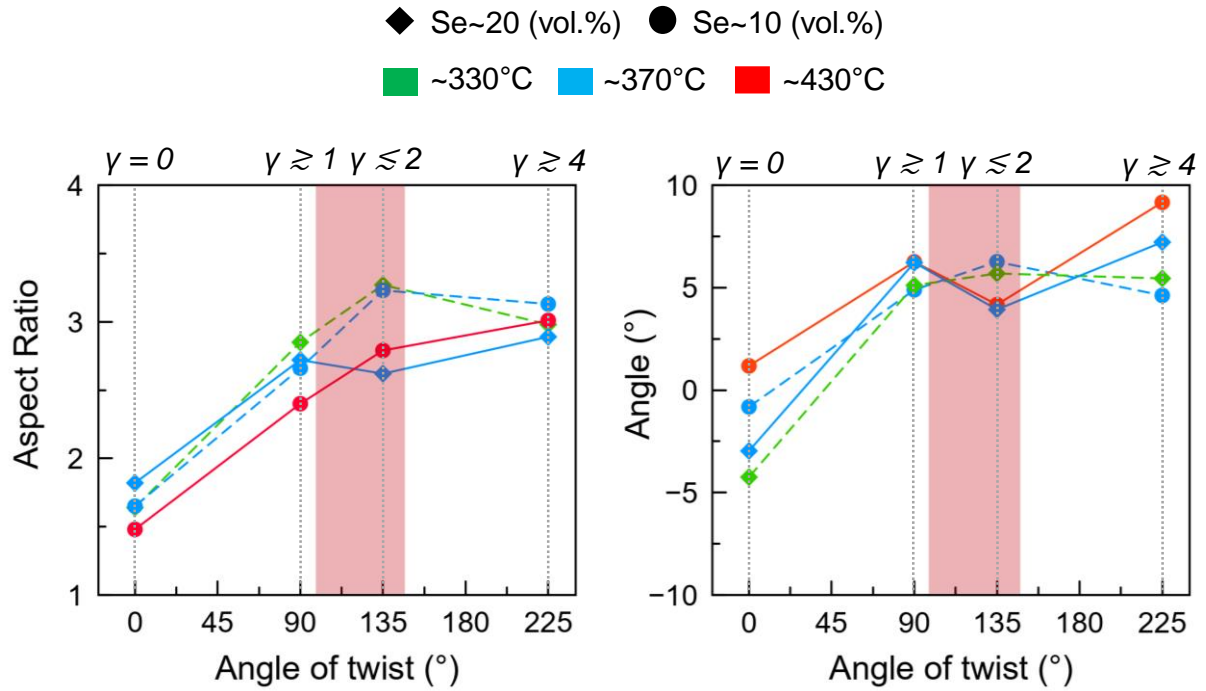
Figure 4. 16. Aspect ratio and the angle (structural layering) of the serpentine microstructure in the unrolled sections from 2-point cluster function (see text) for the three temperatures and the two serpentine contents with increasing deformation. The angle of twist refers to the anvil twist. γ is the simple shear. The red-shaded area highlight the region within which, or after which, the aspect ratio and the angle reach stable trends.

samples, see legend in Fig. 4.16), and (ii) two trends that first show a slight decrease from twist 90° to 135°, and later increase until the last stage of deformation, showing angles of orientation 7-10° (blue-diamond and red-circle samples, see legend in Fig. 4.16). This two kinds of development, however, do not indicate a dependency of either temperature, serpentine content or transferred strain. Therefore, the only clear aspect is the change in evolution with increasing deformation occurring between 90° and 135° of twisting, as for the aspect ratio trends described previously.

The overall results from the 2-point cluster function can indicate the serpentine microstructure showing a stable morphology and structural layering in the all samples from a certain degree of deformation, i.e. 1< γ ≤ 2 (with γ being the simple shear), corresponding to the interface between 90° and 135° of twist (Fig. 4.16).

4.3.2. Interconnectivity (in-situ X-ray tomography)

Here, I present the results describing the interconnectivity of the serpentine with increasing transferred strain, in both 2-d and 3-d.

4.3.2.1. Clusters in 2-d: skeletons density, length and junctions

In this section, I show the 2-d serpentine clusters in form of skeletons. In morphological analysis, the skeleton of a structure is a thin version (branch) of that structure that is equidistant to the structure boundaries. In image processing, this is referred as skeletonization of an image component or structure. Here, I use skeletonization to investigate the extent of branching of the 2-d serpentine clusters, therefore their degree of interconnectivity. The skeletonized microstructure is obtained using the skeletonization plugin available for the Fiji program (AnalyzeSkeleton (imagej.net); Arganda-Carreras et al., 2010).

Figure 4.17 shows the serpentine skeletonized microstructure with increasing deformation in two samples at the same temperature but different serpentine contents (run #18, ca. 20 vol.% serpentine, and run #23, ca. 10 vol.% serpentine; Table 4.1).

Sample #18 show higher numbers of skeletons than sample #23. With increasing deformation, the skeletons in the former become denser and new longer skeletons form, which branch with neighboring skeletons (Fig. 4.17). In sample #23, the skeletons become longer with increasing deformation, and they alight with the shear direction. The branching, however, is local and is not as developed as in sample #18 (Fig. 4.17).
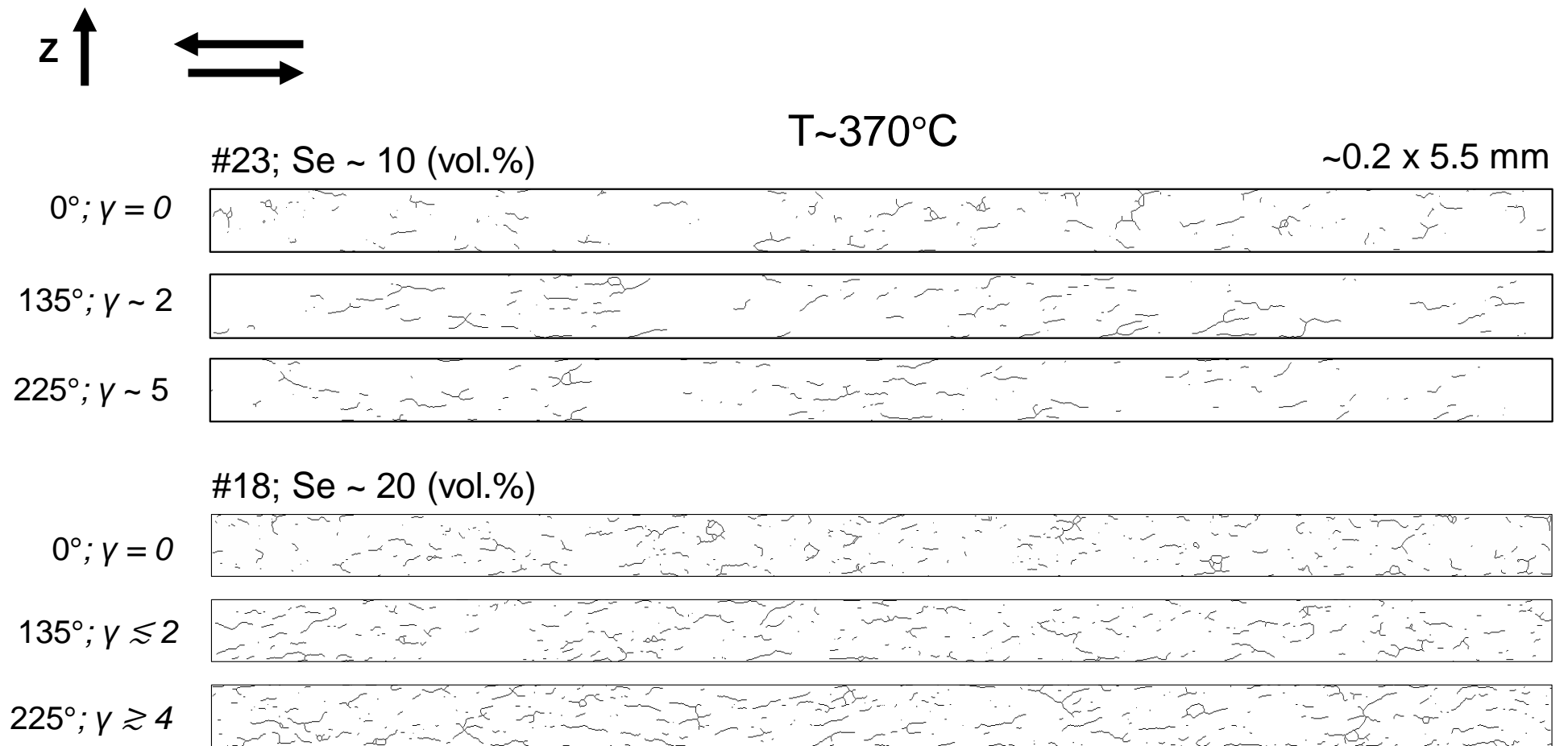
Figure 4. 17. Serpentine microstructure described by the skeletons of the 2-d clusters (yellow in Fig. 4.4, for sample #23, and Fig. 4.5, for sample #18) for the two serpentine (Se) contents (vol.%) at the same temperature (T) with increasing deformation. Z is the torsion axis. Arrows on top indicate the sense of shear. Numbers in degrees (°) are the angle of twist of the anvil. γ is the simple shear.

The analysis tool of the skeletonization plugin (e.g., Arganda-Carreras et al., 2010) returns the list of skeletons with associated junctions (present or not present). It is possible to identify four categories of serpentine skeletons:

i) Single skeletons, i.e. individual branches not creating any connections (no junctions) with neighboring structures

ii) Triple-junction skeletons, which are formed by main branches and sub-branches connected through triple-point junctions;

iii) Quadruple-junction skeletons, which are formed by main branches and sub-branches connected through quadruple-point junctions.

iv) Skeletons structures resulting from the combinations of ii) and iii).

To interpret the interconnectivity of the serpentine skeletons, I used the latter as a proxy for the branches of the Bethe lattice geometry, from percolation theory (e.g., Fig. 4.3; sections 4.2, 4.2.1). The numbers of main branches and sub-branches in a Bethe lattice depends on the kind of junction at the origin of the lattice, which can either be a triple junction ($z=3$) (e.g., Stauffer and Aharony, 2003) or a quadruple junction ($z=4$) (Fig. 4.3) (e.g., Guegen and Palciauskas, 1994). From the list of skeletons obtained with the skeletonization plugin (e.g., Arganda-Carreras et al., 2010), I took into account the skeletons of categories ii), iii) and iv) (described above). Then, I selected those giving numbers of branches and associated junctions that can agree with the construction of a Bethe lattice-like geometry, assuming that branches of lower order-junctions (triple-junctions) cannot give sub-branches of higher-order junctions (quadruple-junctions), but only vice-versa.

Table 4.3 below gives the list of numbers of branches and associated junctions I selected for skeletons of categories ii), iii) and iv) (described above) that agree with the construction of a Bethe lattice-like geometry.

123

Table 4. 3. List of possible number of branches and junctions (triple- and quadruple-point) I considered on the basis of the Bethe lattice geometry type (see section 4.2.1).

	Bethe lattice (if z = 3)				Bethe lattice (if z = 4)		
z + sub-branches	Total branches number	Junction number III	IV	z + sub-branches	Total branches number	Junction number III	IV
z + 0	3	1	0	z + 0	4	0	1
z + 1	4			z + 1	5		
z + 2	5	2	0	z + 2	6	1	1
z + 3	6			z + 3	7	0	2
z + 4	7	3	0	z + 4	8		
z + 5	8			z + 5	9	1	2
z + 6	9	4	0	z + 6	10	0	3
z + 7	10			z + 7	11		
z + 8	11	5	0	z + 8	12	1	3
z + 9	12			z + 9	13	0	4
z + 10	13	6	0	z + 10	14		
z + 11	14			z + 11	15	1	4
z + 12	15	7	0	z + 12	16	0	5
z + 13	16			z + 13	17		
z + 14	17	8	0	z + 14	18	1	5
z + 15	18			z + 15	19	0	6
z + 16	19	9	0	z + 16	20		
z + 17	20			z + 17	21	1	6
z + 18	21	10	0	z + 18	22	0	7

z is the number of branches at the origin of the Bethe lattice geometry (see Fig. 4.1). III and IV refers to triple- and quadruple-point junctions, respectively, and corresponds to skeletons of categories ii) and iii) (see text), respectively.

Finally, I obtained the density (in mm^{-2}) and length (in mm) of the skeletons of category i), and those selected of categories ii), iii) and iv). I defined the density of the skeletons as the ratio of the number of skeletons in the unrolled section over the area (in mm^2) of the section. For the contribution in density of skeletons of categories ii), iii) and iv) in the samples, I took into account the number of the individual branches making up the skeleton. For their length, two types of lengths given by the skeletonization analysis tool were considered: the average length, i.e. the average of the lengths of the individual branches making up the skeleton (see AnalyzeSkeleton (imagej.net)), and the shortest path length, i.e. the shortest distance computed from the two end-points of the skeleton (e.g., Polder et al., 2010). A detailed summary of these results is given in Table 4.4.

Table 4. 4. Summary of the skeletonization results showing the length and density of the branches, and the density of the junctions with increasing deformation.

Run (#)	Se content (vol.%)	Temperature (°C)	Anvil Twist (°)	Simple shear γ	Branches Number				Junctions Number			Branches Length (mm)			Branches Density (mm^{-2})		Junctions Density (mm^{-2})		
					Single	III	IV	III + IV	III	IV	III + IV	Single	III + IV (avg. length)	III + IV (shortest path)	Single	III + IV	III	IV	III + IV
18	~20	~370	0	0	31	44	4	48	15	1	16	1.13	0.39	1.00	0.11	0.17	0.05	0.00	0.06
			135	≤2	54	63	0	63	22	0	22	2.28	0.44	1.28	0.19	0.22	0.08	0.00	0.08
			225	≥4	60	81	12	93	30	3	33	2.62	0.69	2.05	0.21	0.33	0.11	0.01	0.12
23	~10	~370	0	0	22	37	0	37	13	0	13	0.97	0.24	0.69	0.07	0.12	0.04	0.00	0.04
			135	2.2	35	21	4	25	7	1	8	1.69	0.33	0.84	0.12	0.08	0.02	0.00	0.02
			225	5.1	38	20	0	20	7	0	7	1.67	0.17	0.43	0.13	0.07	0.02	0.00	0.02
24	~20	~330	0	0	37	97	0	97	35	0	35	1.51	0.65	2.01	0.12	0.32	0.12	0.00	0.12
			135	1.9	61	97	0	97	36	0	36	2.51	0.68	2.04	0.20	0.32	0.12	0.00	0.12
			225	4.1	49	95	4	99	36	1	37	2.36	0.59	2.21	0.16	0.33	0.12	0.00	0.12
25	~10	~430	0	0	20	73	4	77	27	1	28	0.78	0.34	1.07	0.06	0.24	0.08	0.00	0.09
			135	2.0	44	38	0	38	13	0	13	1.80	0.30	0.75	0.13	0.12	0.04	0.00	0.04
			225	4.5	40	48	0	48	19	0	19	1.96	0.31	1.10	0.12	0.15	0.06	0.00	0.06

For sample #24, only the maximum calculated γ for each anvil testing angle (°) is reported (see Table 4.1 for minimum and maximum calculated for sample #24). Single branches refer to category i) of the skeletons (see text). III and IV corresponds to branches connected through triple- and quadruple-junctions, respectively (skeletons of categories ii) and iii); see text). III+ IV corresponds to skeletons of category iv) (see text). For III + IV, the average length (avg. length) is the average among the lengths of the individual branches making up the skeleton, whereas the shortest path length is the shortest distance computed by the image processing program (Fiji) from the two end-points of the network (see text; see also AnalyzeSkeleton (imagej.net)).

Figure 4.18 gives the relation between the measured density and length of the skeletons with increasing deformation. Three main trends are visible, which are described as follows. One trend is defined by the single skeletons of category i) (Fig. 4.18a, b). Another trend is defined by the skeletons of triple- and quadruple-junctions or combination of those, when the average length of the skeletons is considered (Fig. 4.18a). The third trend is defined by the skeletons of triple- and quadruple-junctions or combination of those, when the shortest path length of the skeletons is considered (Fig. 4.18b).
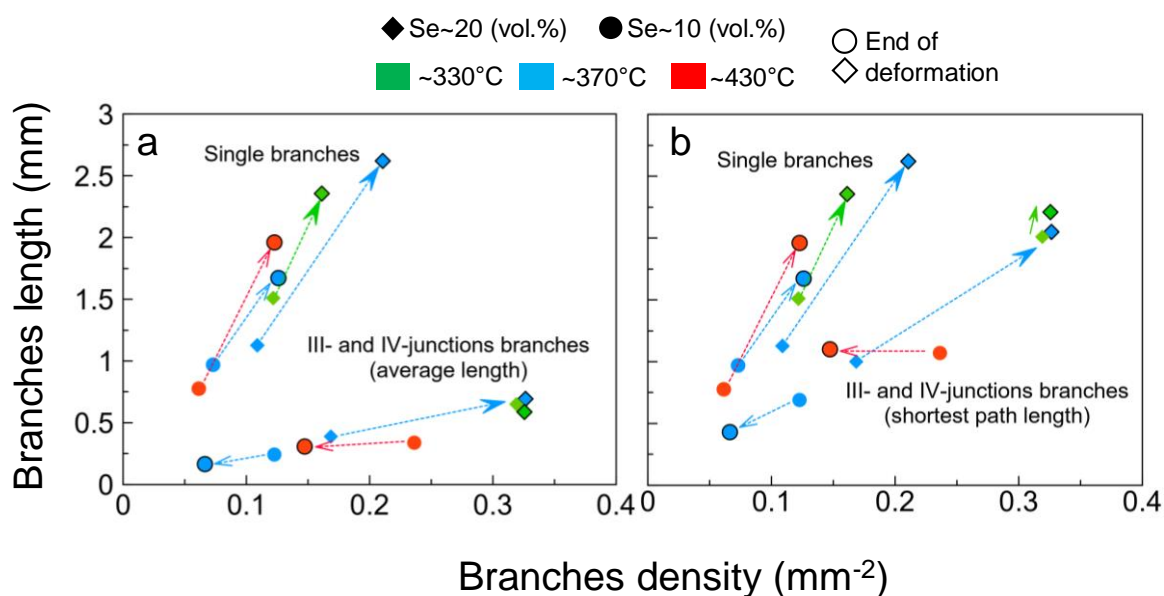
Figure 4. 18. Density vs. lengths of the skeletons branches for the two serpentine (Se) contents (vol.%) and three temperatures (°C). Light-grey dashed lines are guides-to-the-eye for the density-length trends. 'Single' refers to single skeletons (category i); see text). 'III- and IV-junctions' refer to skeletons with branches connected through triple- and quadruple-junctions, respectively, or combination of both (categories ii), iii), iv); see text). (a) the branch length plotted for III- and IV-junctions is the average branch length (see text), whereas in (b) is the shortest path length (see text). In both diagrams, the arrows indicate trends with increasing deformation. Symbols without lining indicate before deformation, whereas bold-line symbols indicate the end of deformation.

The single skeletons trend is the steepest among the three trends (Fig. 4.18a, b). This indicates the single skeletons in all samples tend to increase in length rather than in density with increasing deformation. At the last stage of deformation, higher single skeletons lengths and densities are found in the samples with higher serpentine content (ca. 20 vol.%).

The group of skeletons of triple- and quadruple-junctions or their combination show different behaviors as deformation increases depending on the serpentine content. In the sample with lower serpentine content (ca. 10 vol.%), density and lengths (average length and shortest path length) of the skeletons decrease with increasing deformation (Fig. 4.18a, b). In the samples with higher serpentine content (ca. 20 vol.%), density and lengths either increase (Fig. 4.18a, b; at temperature of ca. 370°C), show similar values (Fig. 4.18a; at temperature of ca. 330°C) or slightly increase (Fig. 4.18b, at temperature of ca. 330°C) as deformation increases.

Figure 4.19 shows the trends, as deformation increases, of the number of single branches (Fig. 4.19a), number of branches forming triple- and quadruple junctions (Fig. 4.19b), as well as number of junctions (Fig. 4.19c) in all the samples.
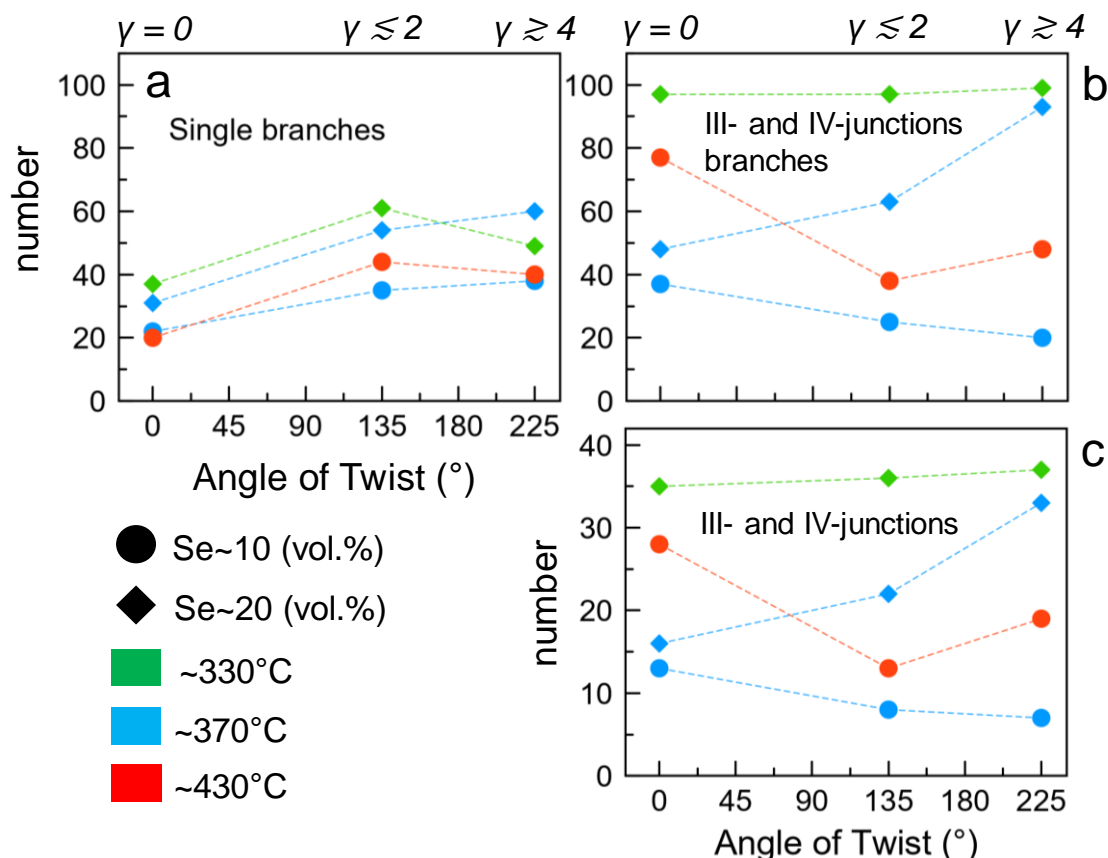
Figure 4. 19. Diagrams showing the evolution with increasing deformation of number of single branches (a), number of branches forming triple (III) and quadruple (IV) junctions (b), number of junctions in the samples, for th two contents (vol.%) of serpentine (Se) and the three temperature (°C). Angle of twist (°) refer to anvil twisting angle. γ is the simple shear.

All the samples show an increase in number of single branches until anvil twisting angle of 135° ($\gamma \lesssim 2$) (Fig. 4.19a). Above this stage, the number of single branches (Fig. 4.19a) either slightly decreases (ca. 20 vol.% of serpentine and 330 °C; sample #24 in Table 4.1), slightly increases (ca. 20 vol.% of serpentine and 370 °C; sample #18 in Table 4.1), or shows similar values (ca. 10 vol.% of serpentine at 370° and 430°C, sample #23 and #25, respectively in Table 4.1)

One of the samples with ca. 20 vol.% of serpentine (330 °C; sample #24 in Table 4.1) show high, pre-existing (prior deformation) numbers of branches with their junctions (Fig. 4.19b, c), which are maintained for the whole duration of the deformation. Conversely, in the other sample with ca. 20 vol.% of serpentine (370 °C; sample #18 in Table 4.1) the numbers of branches with their junctions (Fig. 4.19b, c) increase with increasing deformation.

The samples with ca. 10 vol.% (370° and 430°C, sample #23 and #25, respectively in Table 4.1) show decreasing numbers of branches with their junctions with increasing deformation (Fig. 4.19b, c).

4.3.2.2. Clusters in 3-d: distribution, morphology and connectivity

Here I show the 3-d morphology of the serpentine clusters in the whole RV (for RV definition, see section 3.5.1), and investigate their evolution in size and degree of interconnectivity with increasing deformation (see section 4.3.2.2). The 3-d image processing and observations of the serpentine clusters in the RV was performed in Avizo.

I first recall the classification of the 3-d clusters based on the order of magnitude of voxels amount (see section 3.5.3, Table 3.3). The categories are as follows: small ($10^1 < x \leq 10^3$ voxels), ii) medium ($10^4 \leq x \leq 10^5$ voxels) and iii) large ($10^6 \leq x \leq 10^7$ voxels). For comparison, the size of the RV is in the order of magnitude of 10^8 voxels.

In Table 4.5, I give the evolution of the serpentine clusters fractions in the RV (in vol.%, small, medium and large clusters) with increasing strain.

Table 4. 5. The total serpentine content (vol.%), and clusters size fractions (vol.%, small, medium and large) in the RV with increasing deformation.

Run (#)	Twist and Strain			Se content (vol.%) in the RV		Se Cluster size fraction (vol.%) in the RV					
				Expected	Measured						
	Anvil twist (°)	γ	ε_E (%)		Tot. Se (10 -10^7 voxel)	=	Large (10^6 - 10^7)	+	Medium (10^4 - 10^5)	+	Small (10 - 10^3)
18	0	0		~20	16.3		12.8		2.6		0.9
	135	≲2			18.4		14.7		2.8		0.7
	225	≳4	≳500%		17.4		15.3		1.5		0.6
24	0	0		~20	19.5		17.7		1.7		0.2
	135	1.9	217.4		16.1		15.7		0.3		0.1
	225	4.1	479.5		16.4		15.6		0.7		0.1
25	0	0		~10	13.1		2.6		8.8		1.8
	135	2.0	228.3				4.9		4.3		0.6
	225	4.5	516.8				7.1		3.1		0.6
23	0	0		~10	13.0		4.5		7.3		1.2
	135	2.2	255.5				3.6		4.5		0.6
	225	5.1	592.6				4.5		3.8		0.0

γ is simple shear. ε_E is equivalent strain (see text in section 3.4). Se is serpentine. For sample #24, only the maximum calculated γ and εE for each anvil testing angle (°) are reported (see Table 4.1 for minimum and maximum calculated for sample #24). RV is representative volume (doughnut). 'Measured' refers to the measured voxel amount obtained in the softwares Avizo (see text in section 3.5).

In the samples with higher serpentine contents (ca. 20 vol.%), the large clusters almost make up for the whole serpentine present in the RV (Table 4.5). The medium and small clusters represent only <3% and <1% of the RV, respectively. With increasing deformation, the large clusters fraction either increases (from 13% to 15%, run #18, Table 4.5) or does not show any clear trend (run #24, Table 4.5). When the large clusters fraction increase, the medium cluster fraction decreases with increasing deformation (from 3% to 1.5%, run #18). In the samples with lower serpentine content (ca. 10 vol.%), the medium clusters initially represent a larger portion of the whole serpentine abundance than the large clusters. With increasing deformation and at higher temperature, the large cluster fraction increases (from 3% to 7%, run #25, Table 4.5), whereas the medium clusters decrease (from 9% to 3%, run #25). At lower temperature, there is no visible trend in the large clusters with increasing deformation (run #23, Table 4.5), whereas the medium clusters again show a decrease with increasing deformation (from 7% to 4%, run #23). Here, a decrease in the small clusters fraction (from 1% to <0.1%) is also visible.

In Figure 4.20, I give a representative, visual comparison of clusters morphology between two samples at different serpentine contents (#23 at ca. 10 vol.%; #18 at ca. 20 vol.%) but same temperature (ca. 370 °C), showing the renders of the clusters in the RV with increasing deformation. For clarity, only the large and part of the medium clusters are shown in the RV (color bar: from 10^5 to 10^7 voxels). The smaller fraction of the medium clusters (10^4 voxels) and the small clusters (10^1 - 10^3 voxels) are not shown.
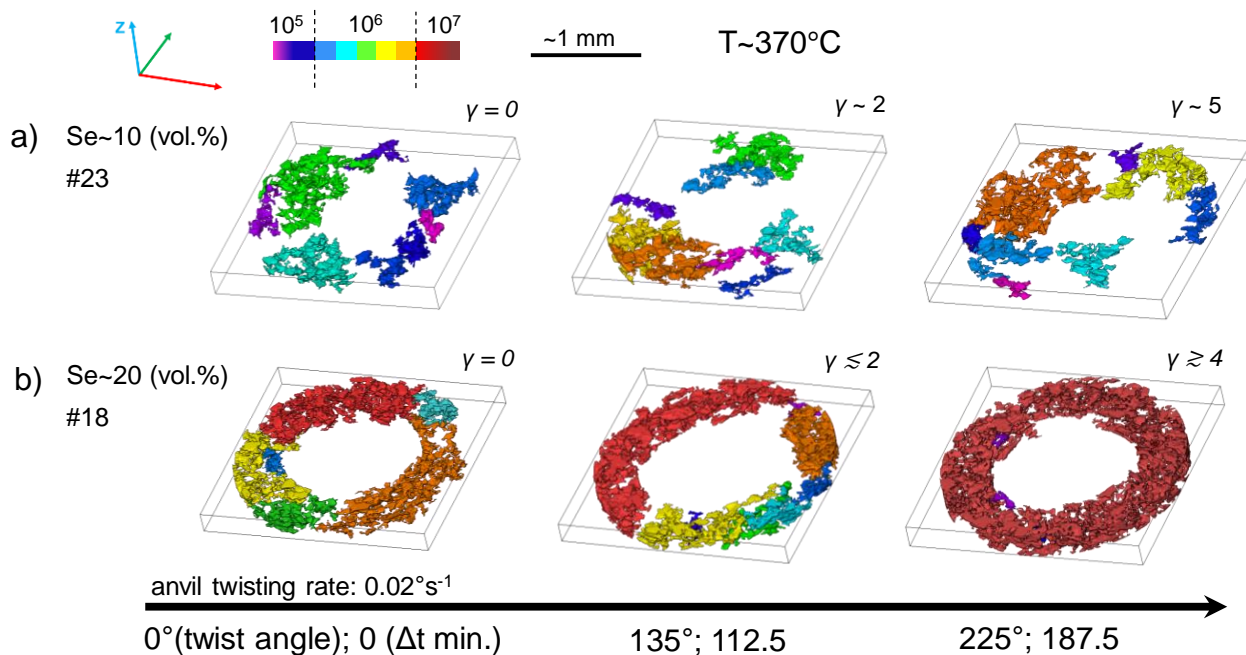
Figure 4. 20. Renders of large serpentine clusters in the RV (doughnut) for the two serpentine (Se) contents (vol.%; samples #23 in a, and #18 in b), same temperature (T) and with increasing deformation (arrow at the bottom). γ is the simple shear. Δt is the time interval between the start of the twisting and a specific twisting angle (°), without counting the time spent for the tomography acquisition. Z is the torsion axis. Color bar shows the order of magnitude of voxels amount (10n) of the clusters. Different colors within the same order of voxels magnitude indicate different sizes of clusters within that order of magnitude.

The density of the large clusters is lower in sample #23 than in sample #18 (Fig. 4.20). In the latter, initially the clusters in the order of 10^6 voxels cover most of the RV, and one big cluster in the order of 10^7 voxels is present (red in sample #18, Fig. 4.20). With increasing deformation, this largest cluster evolves in size until incorporating the other smaller neighboring clusters, and finally forming one large interconnected cluster developing in the whole RV. At this stage, only few medium clusters remain separated from the largest cluster. In sample #23, it is possible to observe an increase in the number

of the large clusters (10^6 voxels) with increasing deformation, but not any clear increase in their individual size or interconnection to neighboring clusters. Here, the maximum size at the last stage of deformation remains in order of 10^6 voxels.

In order to quantify the degree of interconnectivity of the large serpentine clusters with respect to the serpentine abundance in the samples, I obtained the connectivity percentage, which can be defined as the ratio of the volume of the large cluster(s) of a phase over the volume of that phase in the sample (after Kaercher et al., 2016; see also section 3.6.1). Following this, I obtained two connectivities (%): i) one taking into account all the large serpentine clusters (i.e. the sum of the individual large clusters volume), which I define as 'total connectivity', and ii) another taking into account only the biggest cluster among the large clusters, defined as 'largest cluster connectivity'.

The results are shown in Figure 4.21 comparing the connectivities (%) in the samples with increasing deformation, as a function of serpentine content and temperature. The uncertainties for connectivities are also given (see section 3.5 for uncertainties estimations).
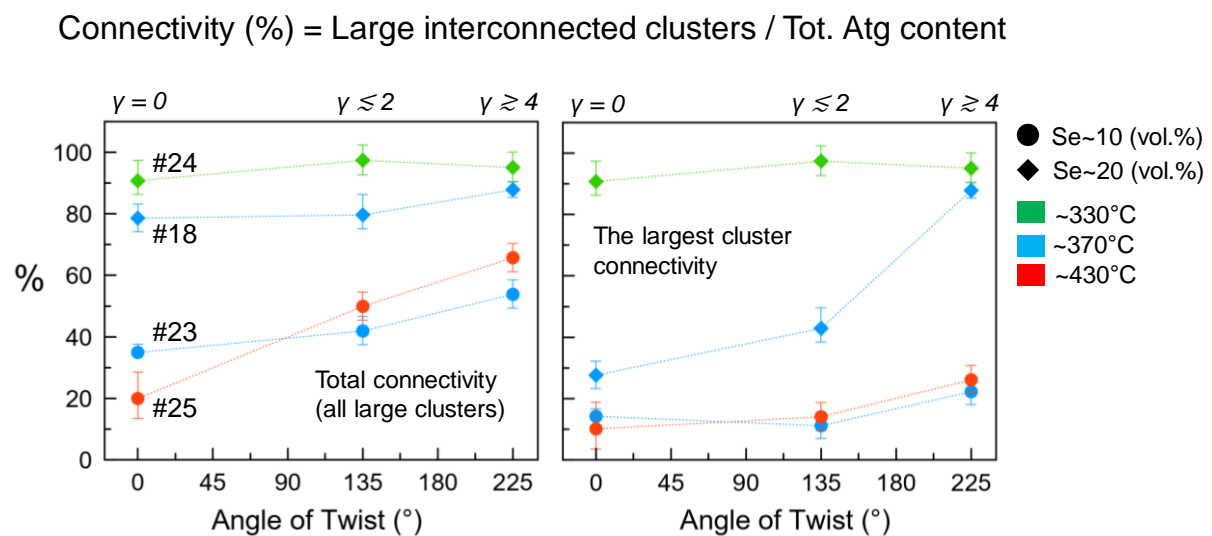
Figure 4. 21. The two connectivity (%) of the large clusters (see text) for the two serpentine (Se) contents (vol.%) and three temperatures (°C) with increasing deformation. The angle of twist refers to the one of the anvil. γ is the simple shear.

Both connectivities strongly depend on the serpentine content. The higher the serpentine abundance, the higher the initial and final connectivity with increasing strain. No temperature dependency seems to be present. However, in one case concerning the total connectivity (%) (left, Fig. 4.21), at lower serpentine content and with increasing deformation, the sample at higher temperature (#25, see Table 4.1, 4.5) shows a steeper trend than the sample at lower temperature (#23, see Table 4.1, 4.5). This indicates a possible influence of the temperature on the degree of interconnectivity of the large clusters when the serpentine abundance is lower. This is, however, not visible in the largest cluster connectivity (%) (right, Fig. 4.21), where the two samples at the lower serpentine content (#23 and #25) show similar trends with increasing deformation.

Alternatively, it is possible to observe an important difference in the largest cluster connectivity (%) between the two samples at higher serpentine content and different temperature (#18 and 24, see Table 4.1, 4.5). The sample at higher temperature (#18) shows an important evolution in the largest cluster connectivity from ca. 30% to 90% with increasing deformation (corresponding to the red-color coded cluster shown previously in Figure 4.20), whereas the sample at lower temperature (#24) surprisingly shows an initial largest cluster connectivity already at ca. 90%. The latter shows a slight increase until a maximum close to 100% at 135° twist (i.e., at $\gamma \sim 2$).

The largest cluster connectivity of sample #24 (right, Fig. 4.21) corresponds to its total connectivity (left, Fig. 4.21). This means only one large interconnected serpentine cluster belonging to the class of the large clusters develops in sample #24, from the beginning of the deformation until the end, making up for the whole serpentine abundance at already intermediate stages of the deformation. Sample #18 differs, with its total connectivity (left, Fig. 4.21) and the largest cluster connectivity (right, Fig. 4.21) presenting two different trends. This emphasizes that one large interconnected cluster

making up for almost the whole serpentine abundance is only formed at the last stage of deformation in the #18.

4.3.3. Recovered microstructure (electron microscopy)

Post-mortem electron microscopy on deformed serpentine was made on a recovered sample of interest with serpentine content of ca. 20 vol.% (sample #18, Table 4.1). Figure 4.22 shows the back-scattered electrons (BSE) images acquired on a section of the sample parallel to the shear. It is analogue to the section defined as longitudinal tangential section (LTS) in Paterson and Olgaard (2000) for torsion deformation.
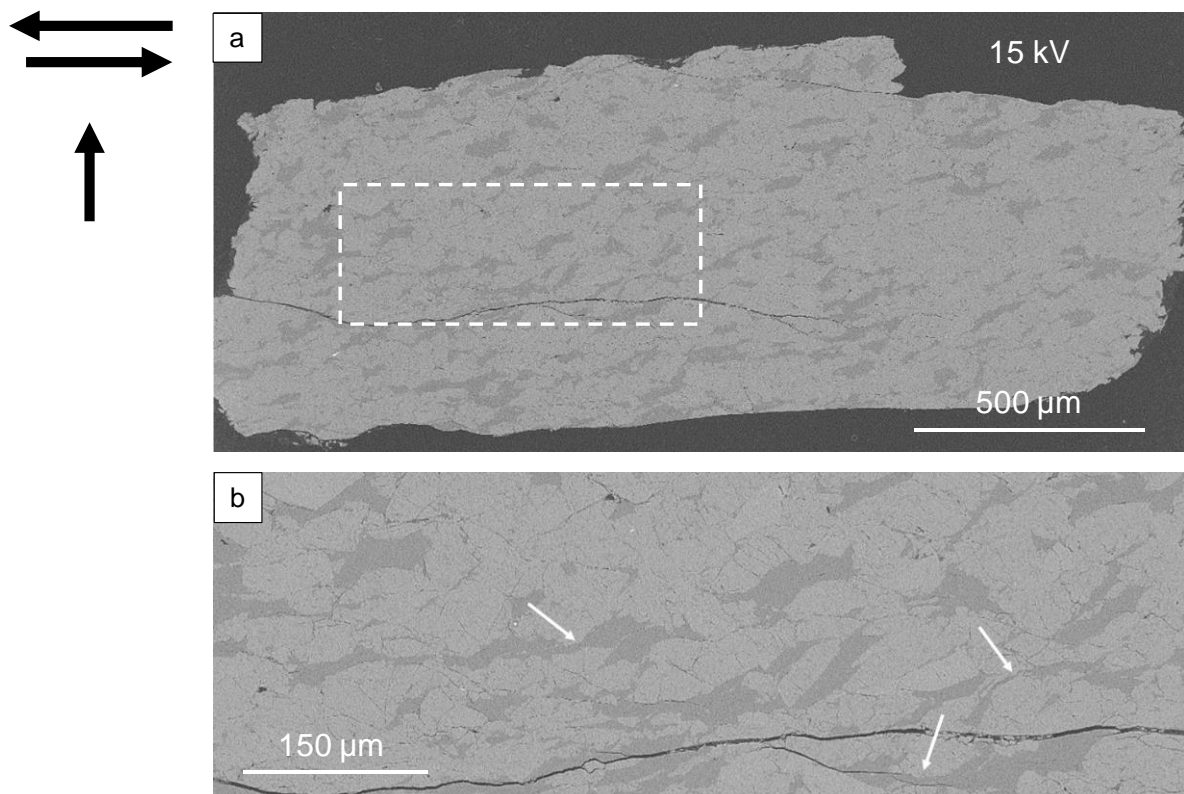
Figure 4. 22. BSE contrast images of the recovered sample #18 (sample section parallel to the shear direction) showing the sheared serpentine microstructure (dark grey) in the olivine matrix (light grey). On the upper-left corner, the pair of arrows defines the sense of shear, whereas the individual vertical arrow defines the torsion axis. a) overview of the sample section. b) close-up corresponding to area of white-dashed square in a), and showing details of serpentine sheared clusters. The white arrow show examples of interconnections between neighboring clusters.

The deformed serpentine shows elongated clusters forming connections with the neighboring clusters (Fig. 4.22b). This agree with the microstructure observed through

in-situ X-ray tomography on the same sample at the last stage of deformation (e.g., Fig. 4.5, sample #18).

The ability of the deforming serpentine to elongate and form interconnection with neighboring clusters suggest a distributed deformation in the mineral, invoking ductile deformation occurring at the clusters or sample scale. To infer the main deformation regime and mechanism in serpentine, EBSD mapping (see section 2.4.1) was at first employed. However, the recovered serpentine either happened to show very weak signal or absence of EBSD pattern.

Because of this, microstructural observations through TEM was performed. Focused ion beam-SEM (FIB-SEM) was used to make two lamellae out of the sample in the section parallel to the shear (Fig. 4.22), across a grain boundary between olivine and serpentine (Fig. 4.23). One FIB-lamella corresponds to a portion of the plane where the transport of the torsion lies, perpendicular to the torsion axis (lamella G1, Fig. 4.23b). It is analogue to a portion of the plane defined as transverse section (TS) in Paterson and Olgaard (2000). The second FIB-lamella is cut perpendicular to the section parallel to the shear (lamella G2, Fig. 4.23b).
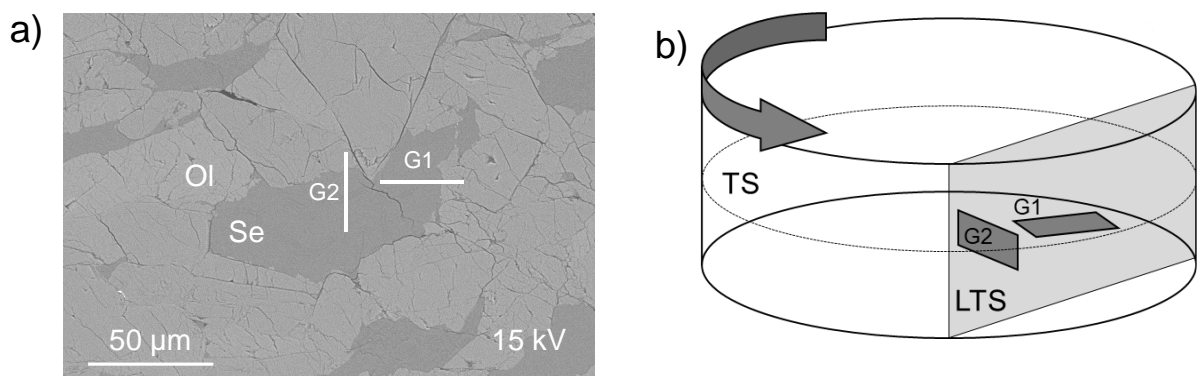
Figure 4. 23. FIB-samplings (G1 and G2) performed across serpentine (Se) and olivine (Ol). a) BSE image showing the location of FIB-samplings. b) Sketch (not in scale) showing the orientation of G1 and G2 with respect to the torsion configuration. LTS stands for longitudinal tangential section, whereas TS stands for transverse section (after Figure 7 in Paterson and Olgaard, 2000). The light grey section is the LTS corresponding to the sample section in Figure 4.22. G1 corresponds to a portion of a TS, whereas G2 is perpendicular to the LTS.

Figure 4.24 shows TEM images of serpentine acquired in the two lamellae. The circular-shaped sections of the chrysotile crystals (see also Fig. 2.1a, b, section 2.1) are observable and distributed in the deformed serpentine (Fig. 4.24a).
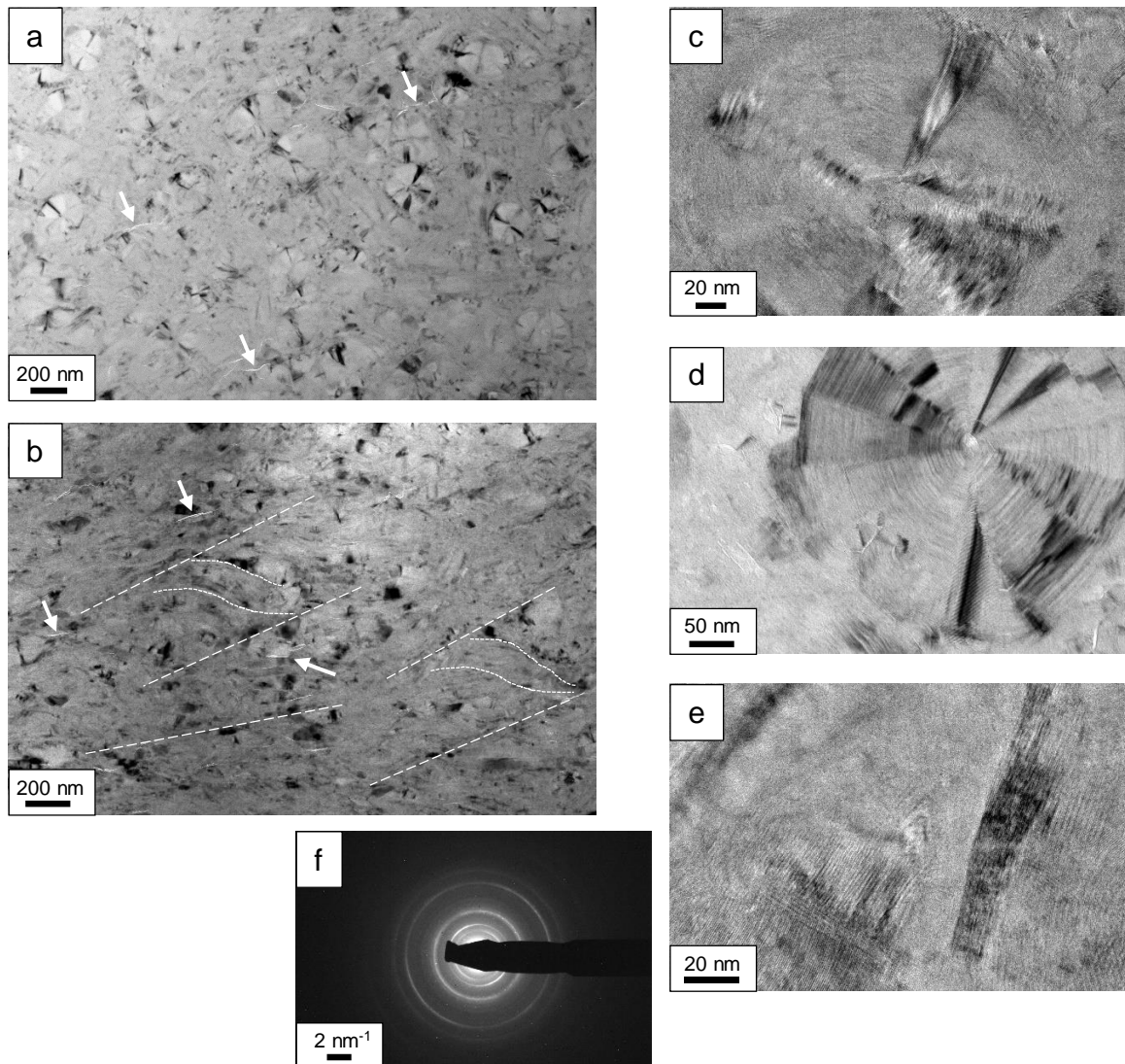
Figure 4. 24. TEM images of deformed serpentine. a) microstructure in G2 lamella (cut perpendicular to LTS, Fig. 4.23) showing the circular-shaped chrysotile crystals in the serpentine. White arrows indicate microcracks. b) microstructure in G2 lamella showing shear bands fabric (white-dashed lines). White arrows indicate microcracks. c) HRTEM image of a chrysotile crystal in G2 lamella. d) HRTEM image in G1 lamella (perpendicular to torsion axis, where shear flow lies, Fig. 4.23) showing another chrysotile crystal, or a polygonal serpentine (e.g., Baronnet and Devouard, 2005) with 15-16 sectors. e) HRTEM image of serpentine locally showing absence of lattice plane traces or crystal ordering (upper-side of the image) in G1 lamella. f) Electron diffraction pattern acquired in G1 lamella showing continuous rings and few, clear diffraction spots.

The serpentine shows few localized microcracks (brittle-like features) (Fig. 4.24a, b) and otherwise predominant micro shear bands (Fig. 4.24b). The latter are analogue to the so-called ductile Riedel shear or C' shear bands (e.g., Marques et al., 2010), and can be,

therefore, consistent with ductile deformation features. High-resolution TEM (HRTEM) images reveals locally the absence of lattice plane traces of serpentine (e.g., Fig. 4.24e). This invokes lacks of crystal ordering or (almost) amorphization in serpentine. The acquired electron diffraction pattern (Fig. 4.24e) shows continuous rings, suggesting an extremely fine-grained serpentine microstructure, or corroborating the hypothesis on the lack of crystal ordering in the sheared serpentine.

4.4. Results (II): Microstructure of the olivine

In this section, I give observations and quantifications on the microstructure of olivine (i.e., the stronger phase) investigated through *post-mortem* electron microscopy.

Four samples recovered from experiments at confining pressure of ca. 4 GPa were investigated (#18b, #18, #23 and #25, Table 4.1). The #18b is the only one that is not sheared, but only hot-pressed (ca. 370° C) under pressure. The recovered microstructure of the #18b was used as a reference and comparison for the sheared microstructures of the other deformed samples (i.e., #18, #23 and #25). Beside the influence of the transferred shear on the recovered microstructure, I chose these samples to additionally investigate i) the increasing serpentine content influence (if any) on the microstructure at a constant pressure (ca. 4 GPa) and temperature (ca. 370 °C) (#23 vs. #18, ca. 10 vol.% and 20 vol.% of serpentine, respectively) and ii) the increasing temperature influence (if any) on the microstructure at a constant pressure (ca. 4 GPa) and serpentine content (ca. 10 vol.%) (#23 vs. #25, ca. 370 °C vs. 430°C, respectively).

The recovered microstructures were analyzed with EBSD and TEM techniques (see section 2.4). For the processing of the acquired EBSD maps, I used the MTEX toolbox incorporated in Matlab (Documentation | MTEX (mtex-toolbox.github.io)). I used a code based on scripted commands and functions given in Mainprice et al. (2015). The crystallographic information file used as a starting point for olivine in the MTEX script is

retrieved from Merli et al. (2001). For the grain detection, I used a segmentation angle (e.g., Mainprice et al., 2015) of 10°. For the grains filtering, I removed from the acquired maps the grains that give a mean angular deviation (MAD, e.g., Documentation | MTEX (mtex-toolbox.github.io)) lower than 1.5°, as well as those grains giving less than 10 indexing points (see e.g., Mainprice et al., 2015). These removed grains were either too small, or considered as results from errors during EBSD mapping.

4.4.1. Recovered microstructure and grain analysis

The olivine recovered microstructure was investigated through EBSD on sections parallel to the transport direction of the torsion, or shear direction (section analogue to LTS section in e.g. Paterson and Olgaard, 2000; see Fig. 4.21, Fig. 4.23b).

Figure 4.25 shows the band-contrast maps of olivine microstructures in the samples investigated. In comparison with the undeformed sample (Fig. 4.25a), the microstructures of the deformed samples (Fig. 4.25b, c, d) indicate a dominant brittle behavior occurring in olivine, which shows fracturing and an overall grains embrittlement (grain reduction) at the interface between bigger grains. This invokes the occurrence of a cataclastic flow as deformation was taking place.
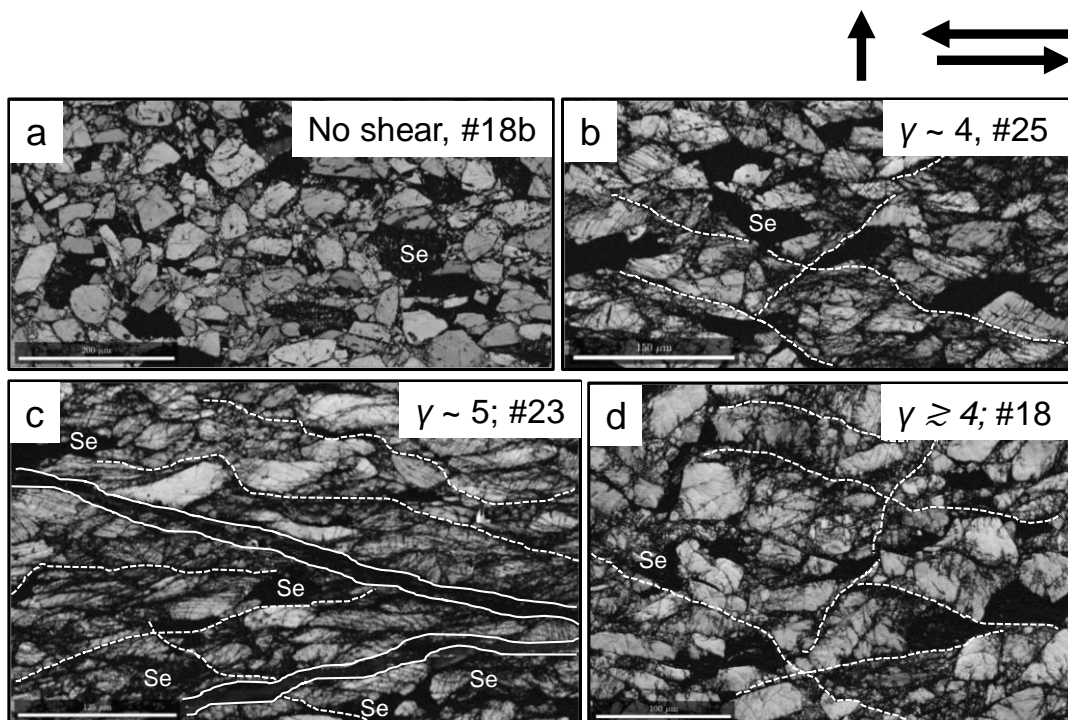
Figure 4. 25. EBSD-BC (band-contrast) maps showing the recovered microstructure of the olivine grains in the four samples of interest deformed at a confining of ca.4 GPa. In all maps, black areas correspond to serpentine (Se). γ is the simple shear strain. a) the non-sheared sample of reference, #18b. Scale bar is 200 µm. b) sample #25 (ca. 10 vol.% of serpentine; ca. 430°C). Scale bar is 150 µm. c) sample #23 (ca. 10 vol.% of serpentine; ca. 370°C). Scale bar is 125 µm. d) sample #18 (ca. 20 vol.% of serpentine; ca. 370°C). Scale bar is 100 µm. For the three deformed samples (b, c, d), on the upper-right corner, the individual black arrow shows the orientation of the torsion axis, whereas the pair of arrow indicates the sense of shear. White-dashed lines in the three deformed samples (b, c, d) delineate locations of grain interfaces where grain embrittlement (grain size reduction) is in a greater extent. White-solid lines in (c) indicates open fractures.

The sample with higher transferred strain (i.e., sample #23, Fig. 4.25c) shows the large grains are elongated. The grains define a shape preferred orientation parallel, or sub-parallel, to the shear. The microstructure of this sample (Fig. 4.25c) also shows (qualitatively) a greater extent of grain embrittlement, fracturing and overall brittle behavior than in the others (Fig. 4.25b, d).

Figure 4.26 show the intracrystalline misorientation for each sample. Figure 4.27 shows a detail of kinked band region of olivine in the most sheared sample (#23).
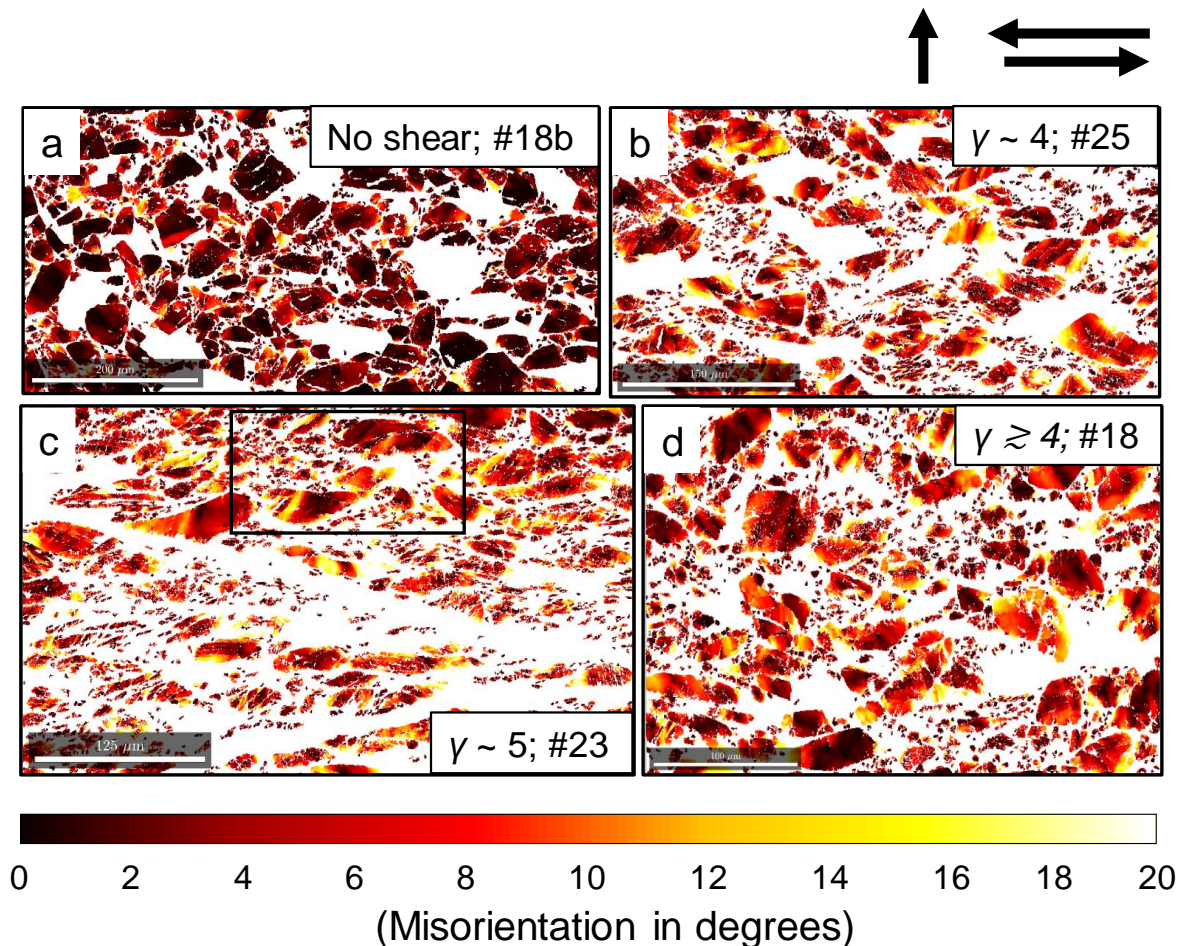
Figure 4. 26. EBSD maps corresponding to samples areas given in Figure 4.25 (a, b, c, d), and showing the extent of intracrystalline misorientation (color-coded) of the olivine grains. The misorientation (from 0° to 20°, see color bar) is computed for each grain with respect to the mean orientation of that grain. γ is the simple shear strain. For the three deformed samples (b, c, d), on the upper-right corner, the individual black arrow shows the orientation of the torsion axis, whereas the pair of arrow indicates the sense of shear. In (c), the black square area corresponds to Figure 4.27.
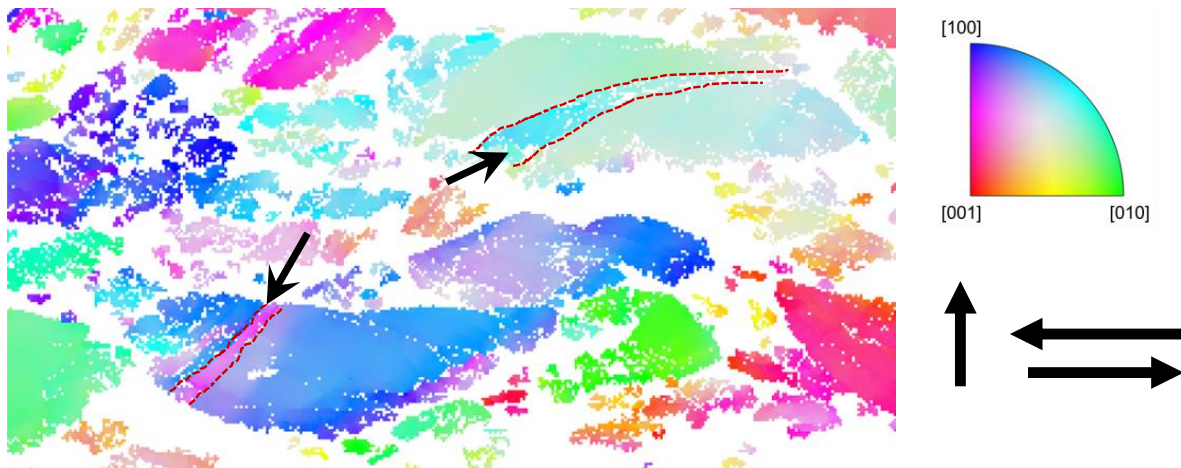
Figure 4. 27. Local color-coded EBSD map acquired within sample #23 (Fig. 4.26c). Color-coding corresponds to crystallographic orientations of the olivine grains (inverse pole figure, upper-right inset). The map shows presence of kink bands in two olivine grains. Black arrows on the map highlight the kink bands location, and the red-dashed lines define the boundaries between the kinked and the unkinked regions within the grains. On the right-hand side, outside the map, the individual black arrow shows the orientation of the torsion axis, whereas the pair of arrows indicates the sense of shear.

The intracrystalline misorientation maps (Fig. 4.16) show the misorientation present in each grain with respect to the mean orientation of that grain. This gives indications on the intracrystalline deformation due to lattice bending or rotation, i.e. intracrystalline plasticity.

In the non-sheared sample (Fig. 4.26a), the overall intracrystalline deformation is low. It is present in either few small grains at the interface between bigger grains, or regions by the edges of bigger grains (Fig. 4.26a). On the other hand, in the deformed samples (Fig. 26b, c, d), the intracrystalline misorientation is developed in larger areas within the grains. In the bigger grains, the intracrystalline misorientation visually results in straight oblique bands, which may be the results of either fracturing or plastic

distortion of the olivine lattice. This is especially true for the sample with higher transferred strain (i.e., sample #23, Fig.4.26c), which also locally developed clear kink bands within the grains (Fig. 4.27). Across the boundaries between the kinked domain and the kinked-free region within the grain, the misorientation is >10°.

The intracrystalline deformation was further investigated in few grains of interest in one sample (i.e., #18, $\gamma \gtrsim 4$, ca. 20 vol.% of serpentine, pressure of ca. 4 GPa, temperature of ca. 370°C) with the local intracrystalline misorientation map (Fig. 4.28). The misorientation is computed with respect to an arbitrary point of reference that defines a local orientation within the individual grain. This reference point was taken by the edge of each grain. The resulting color-coded map shows the lattice distortion propagating from that edge to the other edges of the grain of interest.
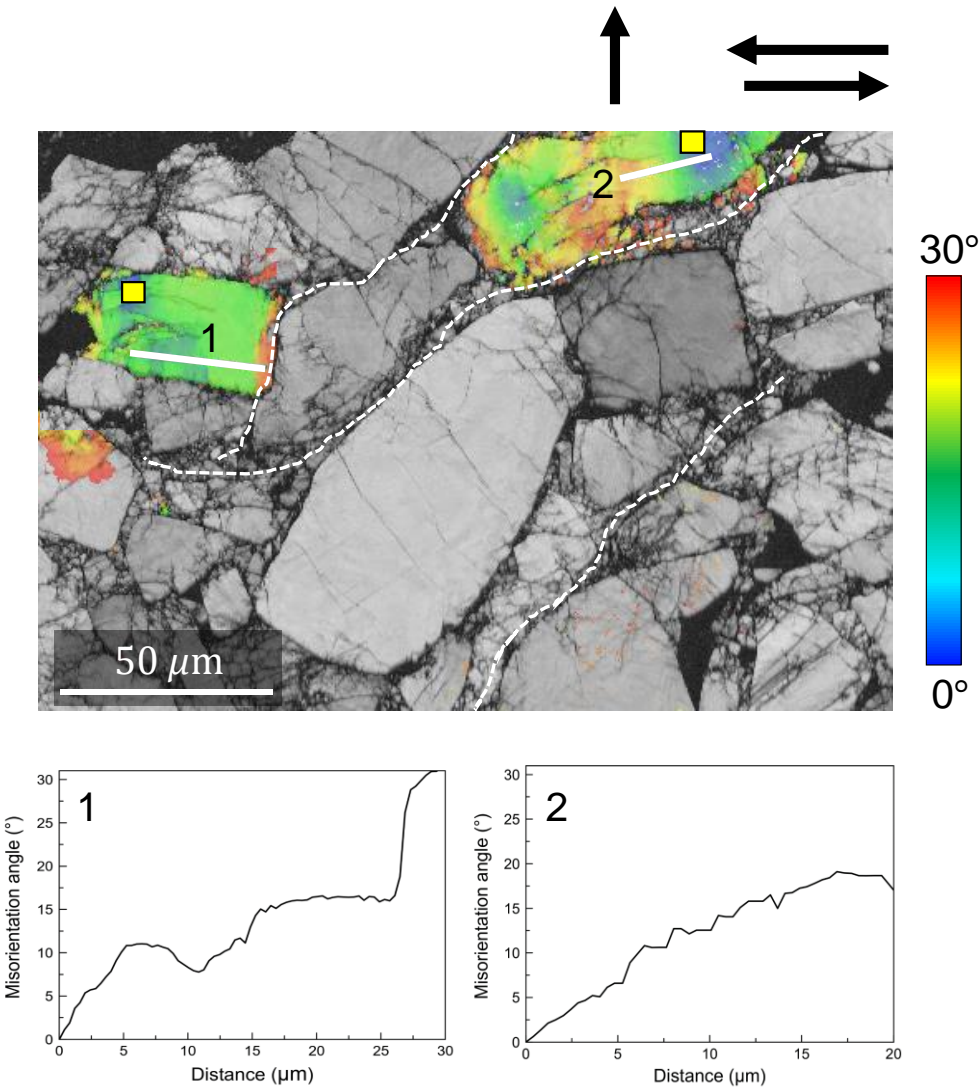
Figure 4. 28. (Top) local EBSD-BC map within sample #18 (i.e., #18, γ ⪆ 4, ca. 20 vol.% of serpentine, pressure of ca. 4 GPa, temperature of ca. 370°C) (see Fig. 4.25d, 4.26d) delineating regions of greater grain embrittlement or crushing (white-dashed lines), and showing superimposed color-coded maps of local misorientation in two grains (from 0° to 30°, color bar). This local misorientation is computed with respect to an arbitrary point of reference within each grain (yellow squares). The white bars (1 and 2) in the grains represent misorientation profiles (below, up to 30°) computed with respect to the starting point (0 µm in distance) of the profiles. On the upper-right corner, the individual black arrow shows the orientation of the torsion axis, whereas the pair of arrow indicates the sense of shear.

In one grain (1, Fig. 4.28, top) the misorientation abruptly increase at the edge of the grain, defining a narrow highly-misoriented region in contact with another adjacent grain. In a second grain, whose distorted shape resembles an undulose or sigmoidal-like structure (2, Fig. 4.28, top), the misorientation continuously increase as we move away from the reference point. The intracrystalline misorientation in these two grains was also measured along linear profiles (Fig. 4.28, below, 1 and 2) that define the lattice distortions across a linear distance from a point of reference, which corresponds to the starting point of the profile. The profile measured in the first grain (1, Fig. 4.28, below) shows an abrupt increase of misorientation (up to ca. 30°) at the end of the profile, corresponding to the abrupt change in intracrystalline orientation in the map (1, Fig. 4.28, top). On the other hand, the profile measured in the second grain (2, Fig. 4.28, below) shows a continuous increase (up to ca. 20°) of the misorientation with increasing distance from the starting point. This emphasizes the continuous lattice distortion visually seen in the map (2, Fig. 4.28, top).

Statistics on the olivine grains morphology were obtained in the areas corresponding to Figures 4.25, 4.26. The parameters are: i) the equivalent grain diameter, i.e. the diameter of an equivalent ellipse or circle fitting the grain shape, and used as an approximation of the grain size; ii) the aspect ratio; iii) the grain orientation spread (GOS), i.e. the average of the misorientation angles (°) to the grain mean orientation (Grain

Orientation Parameters | MTEX (mtex-toolbox.github.io)). These parameters are given in

Figure 4.29 in form of histogram distributions for each sample.
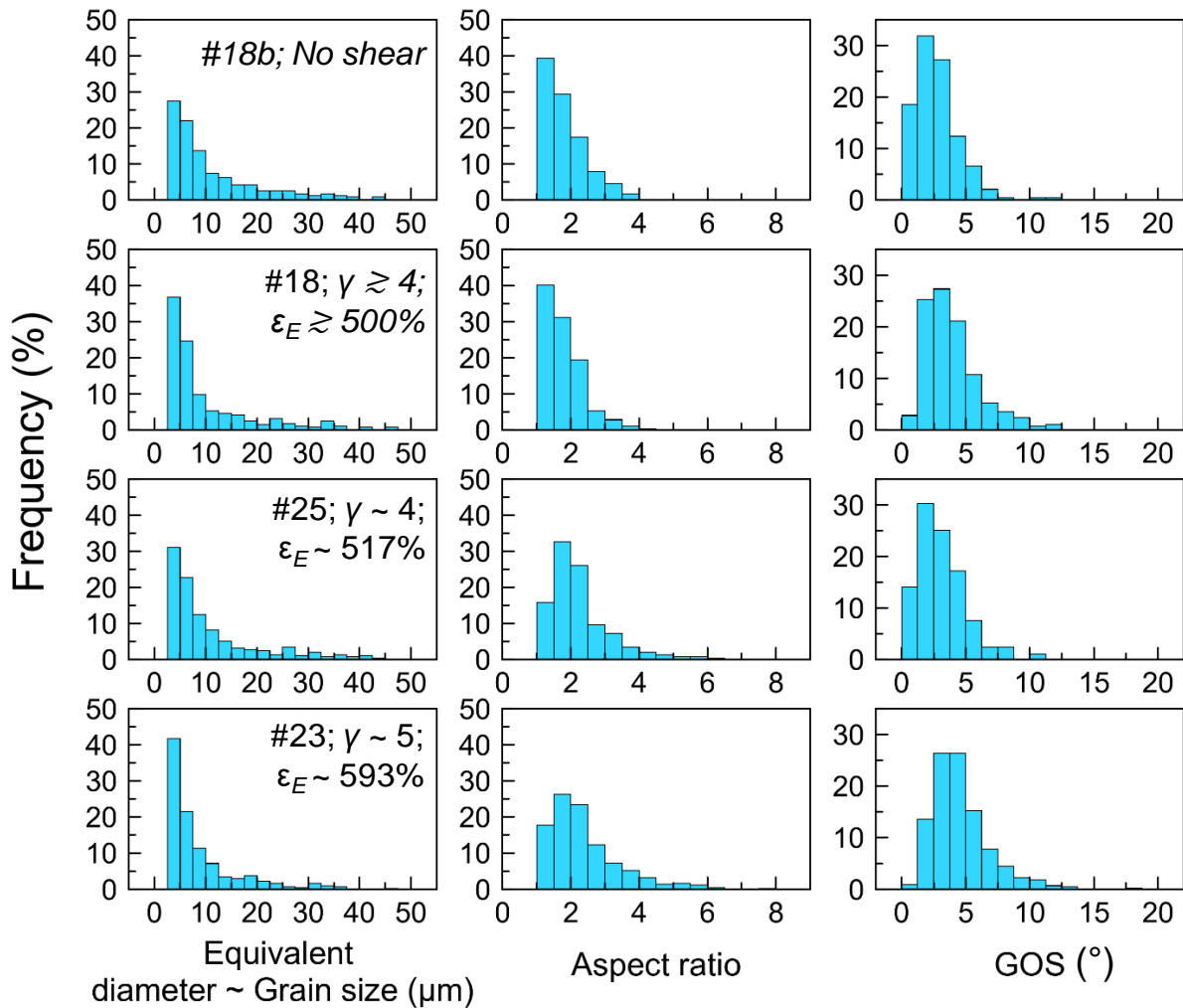
Figure 4. 29. Histograms distribution showing olivine grain statistics on grain size (as equivalent diameter, see text), aspect ratio and grain orientation spread (GOS, see text) for the four samples of interest (labeled as #) comprising the undeformed one and the deformed ones. γ is the shear strain. εE is the equivalent strain.

The grain size reduction in olivine overall increases with increasing transferred strains. This is shown by the population of smaller grains (≤5 μm equivalent diameter) increasing with increasing shear, with their frequency showing values from ca. 25% in the undeformed sample (i.e., #18b) to ca. 40% in the most sheared sample (i.e., #23) (Fig. 4.29).

The aspect ratio distributions overall shift towards higher values with increasing strain (Fig. 4.29). In the undeformed samples (i.e., #18b), the most frequent population (ca. 40%) are represented by grains with aspect ratio of 1-1.5, whereas in the most

sheared sample (i.e., #23), the most frequent population (ca. 25%) is represented by grains with aspect ratio of 2-3. In this sample (#23, $\gamma \sim 5$), a few grains (<10% in frequency) show high aspect ratio of up to ca. 6, as well as in sample #25 ($\gamma \sim 4$). On the other hand, in samples #18b (undeformed) and #18 ($\gamma \gtrsim 4$) the maximum value is 4 (Fig. 4.29).

The GOS distribution overall shift towards higher values as strain increases. It also shows a clear increase in the population at ca. 4-5° from ca. 10% (undeformed sample #18b) to ca. 25% (most-sheared sample #23). The GOS of 4-5° is the most frequent in the sheared sample (#23), whereas in the undeformed sample (#18b) the most frequent GOS is 2.5-3° (Fig. 4.29).

4.4.2. Crystallographic and shape preferred orientations, subgrain misorientation and dislocations types

This section focuses on the main possibly active slip system in olivine at our experimental conditions, as well as on the possibly dominant deformation mechanism. I provide information on: i) the crystallographic preferred orientation (CPO), which is commonly interpreted as a result of crystal plastic deformation mechanisms, where deformation is achieved by the movement of dislocations; ii) low-angle intracrystalline misorientation axes responsible for lattice distortion; iii) intracrystalline dislocations microstructures, which can give confirmation on the main slip system responsible for the plastic crystal deformation.

The olivine crystallographic preferred orientation (CPO) and rotation axes accommodating low-angles misorientation within, and across, olivine subgrains are given in Figure 4.30, for the sheared samples with different strains, as well as for the non-sheared sample shown as a reference. These were computed for the recovered microstructures shown in Figure 4.25, 4.26.

[100]   **[010]**   **[001]**

#18b; No shear

N=875
J=1.3
M=0.008

#18; γ ≳ 4; ε_E ≳ 500%

N=907
J=1.63
M=0.02

#25; γ ~ 4; ε_E ~ 517%

N=1059
J=1.65
M= 0.02

#23; γ ~ 5; ε_E ~ 593%

N=1218
J=1.7
M=0.04
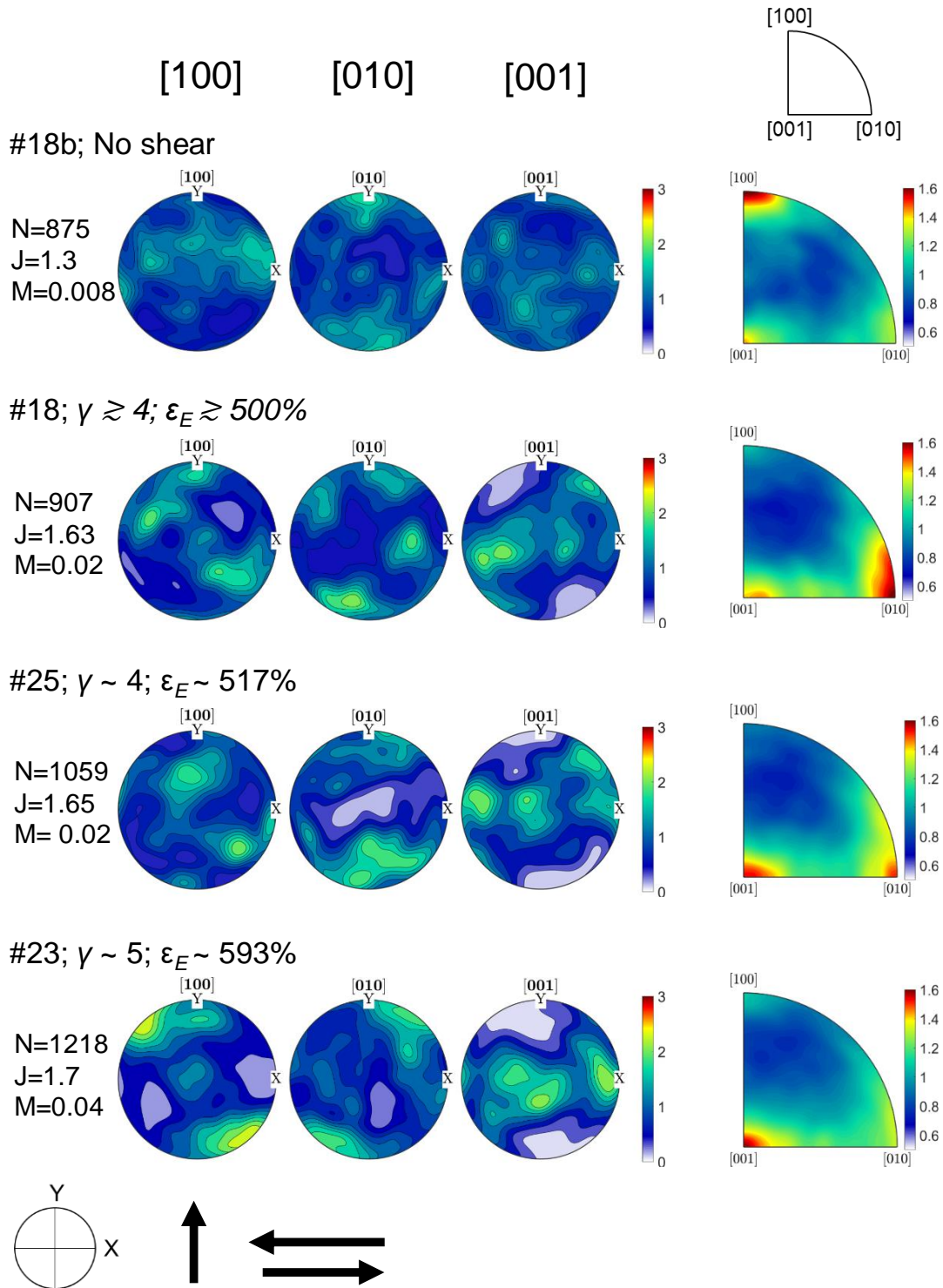
Figure 4. 30. (Left) pole figures (equal area, lower hemisphere projections) showing the crystallographic preferred orientation (CPO) in olivine. The orientation distribution function (ODF) is computed for one point per olivine grain, and is calculated using a half-width of 10°. The color scales of the pole figures are normalized to a maximum multiples of uniform distribution of 3 (color bars). N is the number of grains. J and M are fabric strength indicators (e.g., Mainprice et al., 2015). The samples numbers (#) are given. γ is the shear strain. εE is the equivalent strain. (Right) inverse pole figures showing rotation axes accommodating low-angle misorientation (from 2° to 10°) across subgrain boundaries, and within subgrains, of olivine. On the bottom-left, the torsion axis (individual black arrow) and the sense of shear (pair of arrows) are given with respect to the pole figures reference frame.

The sheared olivine shows an evident CPO present at higher strains, whereas the non-sheared olivine does not show any pattern (Fig. 4.30). At higher shear, the [001] axes are mostly oriented sub-parallel to the shear direction along a girdle (sample #23, Fig. 4.30). The CPO in [100] and [010] become stronger at higher shear, and also oriented almost perpendicular to the shear direction (sample #23, Fig. 4.30). The fabric strength indices (J and M; e.g., Skemer et al., 2005; Mainprice et al., 2015) increase with the transferred strain in olivine (Fig. 4.30, from samples #18b to #23).

The inverse pole figure of low-angle misorientations (right, Fig. 4.30) in the undeformed sample shows the maximum concentration of rotation axes along <100>, which completely disappears in the deformed samples. In one deformed sample (i.e., #18, $\gamma \gtrsim 4$) the maximum concentration is in <010>, with a weaker alignment in <001>. In sample #25 ($\gamma \sim 4$) the concentration is stronger in <001>, with otherwise weaker alignment in <010>. Finally, in sample #23 at higher strain ($\gamma \sim 5$), the only stronger alignment is along <001>. These observations indicate an increase in concentration of low-angle misorientations with rotation axes aligned in <001> as the transferred strain increases.

Figure 4.31 provides the information on the olivine grains major axis orientation (from 0° to 180°) relative to the shear direction (0° and 180° corresponds to the horizontal, i.e. the shear direction). The non-sheared sample is given as a reference (Fig. 4.31). The sheared samples #25 ($\gamma \sim 4$) and #23 ($\gamma \sim 5$) show evidences of developing shape preferred orientation (SPO) of the olivine grains with shear. The results indicate ca. 25% of the population of the grains (frequencies at 0° and 180°) are aligned parallel to the shear in both samples (Fig. 4.31).
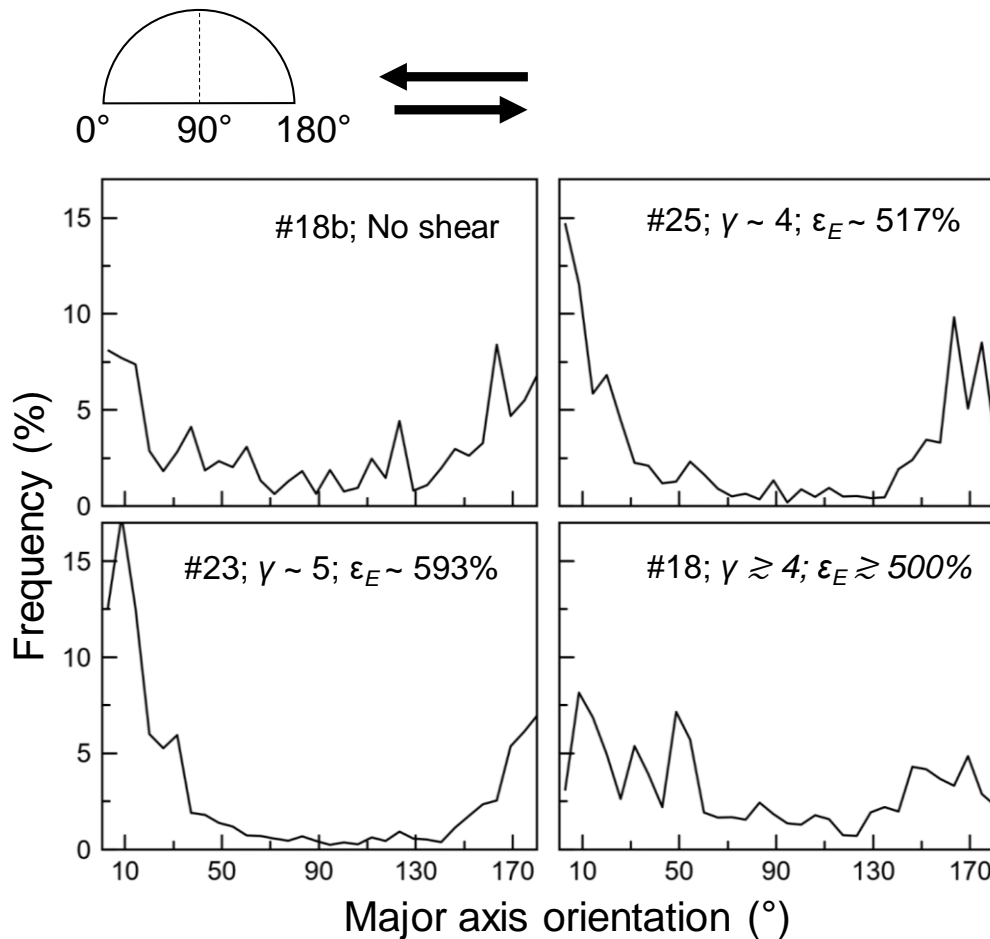
Figure 4. 31. Distributions of the olivine grains major axis orientation (from 0° to 180°) relative to the shear direction. 0° and 180° corresponds to the EBSD maps (Fig. 4.25, 4.26) horizontal, which corresponds to the shear direction. 90° corresponds to the vertical of the EBSD maps, which corresponds to the direction of the torsion axis. Black arrows show the sense of shear. The samples numbers (#) are given. γ is the shear strain. εE is the equivalent strain.

TEM results on olivine dislocations structures are given in Figure 4.32 and 4.33. The purpose of observing and analyzing the dislocations was to confirm the main character of the rotation axes responsible for accommodating the intracrystalline low-angle misorientation (Figure 4.30, inverse pole figures, right).

TEM analyses were carried out on a FIB-lamella (Fig. 4.32) sampled from the sample (#18, given in Fig. 4.25d, 4.26d, 4.28) to analyze the dislocations on the surface perpendicular to the torsion axis (see reference frame in Fig. 4.32a), which corresponds to the plane where the transport direction or shear flow lies (analogue to a portion of the transverse section, TS, in Paterson and Olgaard, 2000; see Fig. 4.23). The FIB-cutting was performed across a grain boundary between an olivine and serpentine crystal (see Fig. 4.23).
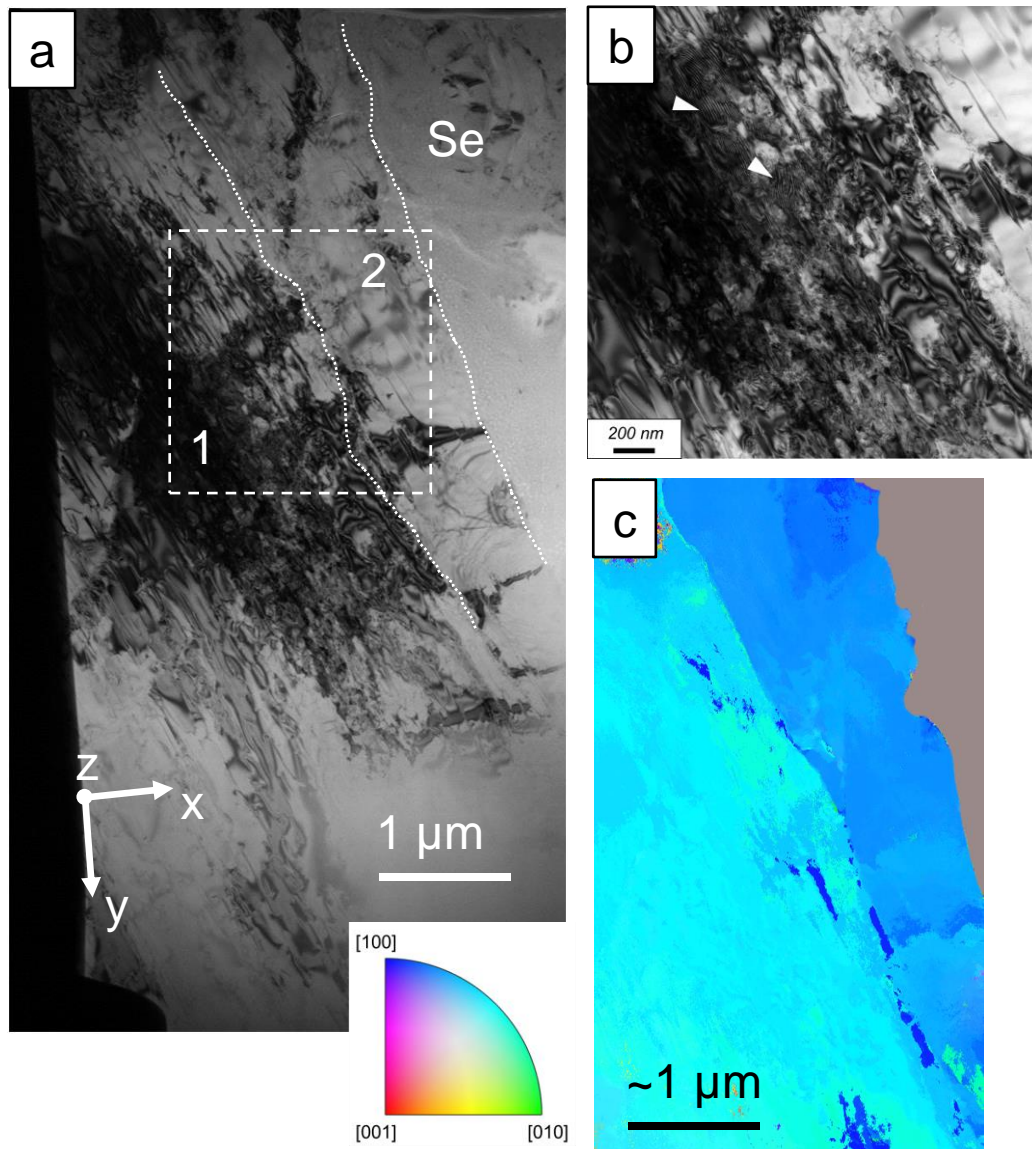
Figure 4. 32. TEM images of the FIB-lamella showing the single crystal of olivine in contact with serpentine (Se). a) STEM-BF (bright field) image of the lamella showing the overview of the olivine crystal. Z is the torsion axis. X is the axis corresponding to the direction of the FIB-cutting. Y is the axis of the FIB-lamella plane. XY defines the FIB-lamella plane perpendicular to the torsion axis Z. 1 and 2 define two different domains in the single crystal of olivine. Between the two domains, the white-dashed line across the olivine crystal corresponds to a subgrain boundary. The other white-dashed line defines the grain boundary with the serpentine (Se). b) STEM-BF image of region within the FIB-lamella (white-dashed square in (a)) showing high density of dislocation interaction (dark contrast) and the presence of narrow fringes of interference (e.g., white triangles). Notice free and long dislocations (bright contrast) on the upper-right (corresponding to domain 2 in (a)). c) Color-coded map (see inset on the bottom, color-coded inverse pole figure) computed from ptychography analysis on the FIB-lamella showing the orientation of the olivine crystal and the misorientation between the two domains. The olivine crystal orientation is close to the ZA (zone axis) [210]. The misorientation between the two domains corresponds to 10-15°.

The overall microstructure in the FIB-lamella can be described by high dislocation density, and also by the presence of possible subgrain boundaries and/or micro-cracking veins (Fig. 4.32a, b). Locally, dislocation interaction is rather pervasive, leading to observation of fringes of interference (Fig. 4.32b).

TEM orientation map analysis revealed the olivine being a single crystal close to [210] orientation (Fig. 4.32c), with misorientation values up to 15° measured across a structural discontinuity developing along the whole lamella section, therefore defining a subgrain boundary sub-parallel to the grain boundary with serpentine (Fig. 4.32a, c).

I labeled the region far from the serpentine boundary and outside the olivine subgrain as domain 1, whereas the region in the proximity of serpentine and within the olivine subgrain as domain 2 (Fig. 4.32a). In comparison with domain 1, domain 2 visually shows a greater population of free and longer dislocation segments (Fig. 4.32b, 4.33a). On the other hand, domain 1 is where the majority of pile-up and tangles of dislocations are located, with also the presence of longer dislocations (Fig. 4.33a). Considering the zone axis (ZA) employed for the DF-imaging mode (Fig. 4.33b), the dominant orientation by which these deformation microstructures develop is parallel to [001] (Fig. 4.33a). Using this ZA, the so-called invisibility criteria (e.g., Williams and Carter, 2008) was employed to infer the main Burgers vector character of the dislocations in the olivine single crystal. By conventional invisibility criteria with reflection g: hkl, I found dislocations being visible with g: $00l$ (Fig. 4.33a), and otherwise invisible dislocations with g: $hl0$ (Fig. 4.33c). This indicates a total Burgers vector $b = <00w>$, where w is a non-zero component. The inferred Burgers vector is therefore consistent with <001> dominant character, which is in agreement with one of the characters of the intracrystalline misorientation observed in the inverse pole figures (Fig. 4.30, right).
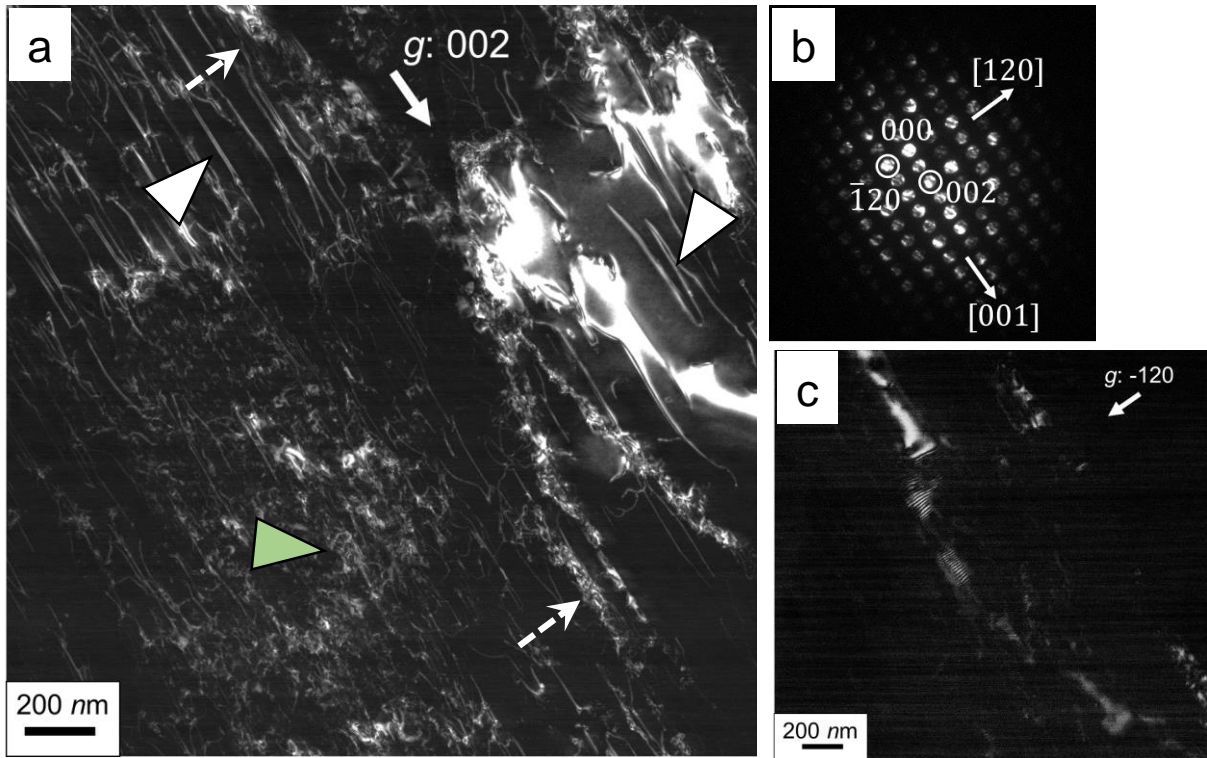
Figure 4. 33. a) STEM DF-image acquired for g: 002. The image corresponds to the area defined by the white-dashed square in Figure 4.32a. The two white-dashed arrows define at the top and on the bottom parts of the subgrain boundary (Fig. 32a) described by dislocation tangles. White triangles show examples of longer dislocations segments (domain 1 and 2). Light-green triangle shows an example of high dislocation interaction and entanglement within the domain 1 (Fig. 32a) of the crystal. b) diffraction pattern showing the ZA [210] of the olivine crystal. White circles showing g reflections of interest (002 and -120) used for the DF (dark field) imaging mode. c) STEM DF-image acquired for g: -120 showing same region of (a) (or white-dashed square in Fig. 4.32a). Note none of the dislocations visible in (a) are not visible at this g reflection condition in (c).

4.5. Discussion

In the following sections, I first discuss the microstructure and deformation behavior for the two phases separately: serpentine deformation (section 4.5.1) and olivine deformation (section 4.5.2). Then, I discuss the overall deformation behavior and scenarios for the olivine+serpentine aggregates (section 4.5.3).

4.5.1. Serpentine deformation

4.5.1.1. Fabric

The serpentine microstructure in the unrolled sections displays sinusoidal-shaped clusters within oblique bands. There are mostly visible at the highest shears and in the samples with 20 vol.% content (Fig. 4.5). These structural features suggest a S-C' fabric (or Riedel-shear bands) (e.g., Passchier and Trouw, 2005). The S-structures corresponds to the sinusoidal-shaped clusters defining the sense of shear, and the C' corresponds to the oblique traces of the bands (Fig. 4.34).
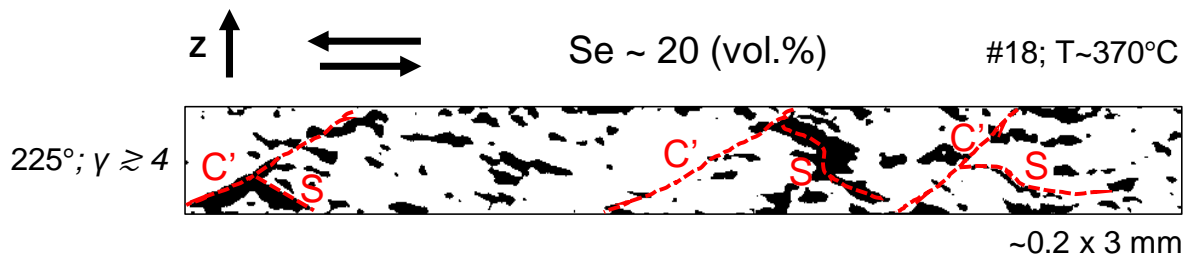
Figure 4. 34. Representative image showing the S-C' fabric (red-dotted lines) described by the serpentine clusters (black) in an experimental sample (#18). Z is the torsion axis. Pair of arrows defines the sense of shear. Se is serpentine. T is temperature. 225° is the anvil twisting angle. γ is the simple shear.

The features of the S-C' fabric can be seen in the statistics of angle distributions of the individual serpentine clusters, displayed by the orientation of major axis of the fitting ellipse to the clusters (e.g., Fig. 4.14), or by the orientation of the clusters boundaries (e.g., Fig. 4.15). With increasing strain, the distribution shows an increase in angles at ca. 30°

or ca. 20° (e.g., Fig. 4.14, 4.15), which can be consistent with the overall orientation of the S-structures or C' cleavage with respect to the shear direction.

The formation of S-C' fabric can also be correlated with the trends of mean aspect ratio and structural layering of serpentine with increasing deformation (numerical results from cluster functions; Fig. 4.16). The trends suggest plateaus from intermediate deformation stages ($\gamma \lesssim 2$) until the end of deformation ($\gamma \gtrsim 4$) (Fig. 4.16), where the mean aspect ratio of the clusters is around a value of ca. 3, and the structural layering shows angles between ca. 5° and ca. 10° with respect to the shear direction (Fig. 4.16). These plateaus could indicate a 'steady-state' serpentine morphology that could correspond to the formation of S-C' fabric in the samples.

The morphology of the minerals in the aggregate, along with the formation of S-C' fabric, are further discussed in section 4.5.3 (and sub-sections therein) with the aggregate deformation scenarios.

4.5.1.2. Interconnectivity

The results of *in-situ* X-ray tomography reveal the serpentine clusters evolving in shape and creating connections with one another (interconnectivity) at HP (ca. 4 GPa) and HT (ca. 330-430°C).

The temperature does not seem to have a detectable influence on the evolution of the serpentine clusters. However, one sample with serpentine content of 10 vol.% deformed at higher temperature (ca. 430 °C; sample #25) shows a higher total connectivity (Fig. 4.21) than another sample at the same serpentine volume but lower temperature (ca. 370°C, sample #23). Therefore, the highest temperature may enhance the formation of connections between clusters, increasing the chances of serpentine interconnectivity with increasing strain.

The interconnectivity of serpentine is primarily influenced by the serpentine content in the samples. The higher the serpentine volume (ca. 20 vol.%), the greater are the chances of connections (or junctions) between neighboring clusters.

In the 2-d skeletonized clusters, the samples with ca. 20 vol.% of serpentine show either a pre-existing, high number of junctions (triple- and quadruple-junctions), or a number of junctions increasing with increasing strain (Fig. 4.19b, c). The density of the junctions seems to prevail over the density of the single branches (individual cluster not forming junctions) in these samples (Fig. 4.18). Conversely, in the samples with ca. 10 vol.%, the number or density of junctions decreases with increasing deformation (Fig. 4.18, 4.19b, c), and only the number and length of single branches (individual clusters) increase (Fig. 4.18, 4.19b, c).

The observations in 2-d agree with the ones in 3-d, where the samples with ca. 20 vol.% shows the serpentine forming large interconnected clusters expanding in the whole RV (Fig. 4.20b), with higher largest-cluster connectivity than the one of samples with ca. 10 vol.% of serpentine (Fig. 4.21).

The increasing number of junctions (interconnectivity) prevailing over the elongation of individual cluster (Fig. 4.17, 4.18, 4.19) with increasing strain is likely what makes the serpentine interconnectivity to develop to larger scale, through the entire sample volume.

However, in one of the samples with 20 vol.% of serpentine (#24) a pre-existing large number of junctions is observed before shear is initiated (green symbols in Fig. 4.18, 4.19). The number of junctions does not increase with increasing deformation for this sample #24, which is in contrast with the case of the other sample with 20 vol.% of serpentine, the #18 (blue-diamond symbols in Fig. 4.18, 4.19). The difference in interconnectivity behavior between these two samples could be due to an initial greater fraction of large clusters in sample #24 than the one in sample #18 (Fig. 4.8, 4.9). The

fraction of large clusters in the former makes almost for the whole serpentine volume (#24, Table 4.5). This significant difference between samples #18 and #24 can be attributed to the two different starting powder batches used (Table 4.1). The two batches of powder mixtures (batch 1 for the sample #18, and batch 2 for sample #24, see Table 4.1) likely differ in particle size distribution, even though presenting the same serpentine volume content and particle size ranges. This resulted in a different cluster size distribution in the hot-pressed samples before deformation, and potentially influenced the formation of pre-exiting large clusters in one sample (#24). The increasing transferred shear strain at this point could only influence the shape or structural layering (preferred orientation) of the clusters in sample #24 (Fig. 4.5, 4.14).

Finally, I suggest scenarios for the serpentine skeletons morphology (Fig. 4.35). At higher serpentine content (ca. 20 vol.%) and lower fraction of large clusters (<15 vol.%), the transferred shear strain (up to $\gamma \gtrsim 4$) can induce an increase in number of junctions and length of the serpentine. This results in a more complex morphology (Fig. 4.35) due to the increasing degree of interconnectivity occurring towards more than one directions. The interconnectivity among the clusters could develop from a local to a global scale (whole sample volume), until the serpentine in the samples is possibly all interconnected. This case could be, however, already valid before shear is initiated if the fraction of large clusters is higher (>15 vol.%). In this scenario, with increasing strain, the interconnected serpentine only changes in distribution and orientation (Fig. 4.35), with the serpentine branches assuming preferential orientations accordingly with the sense of shear. Conversely, at lower serpentine content (ca. 10 vol.%), the transferred shear strain (up to $\gamma \gtrsim 4$) can induce an increase in the length of individual serpentine clusters, without creating new connections between neighboring clusters (Fig. 4.35). This results in a more ordered (layered) and less complex morphology, mainly described by the elongation of the clusters and their alignment with the shear direction (Fig. 4.35).
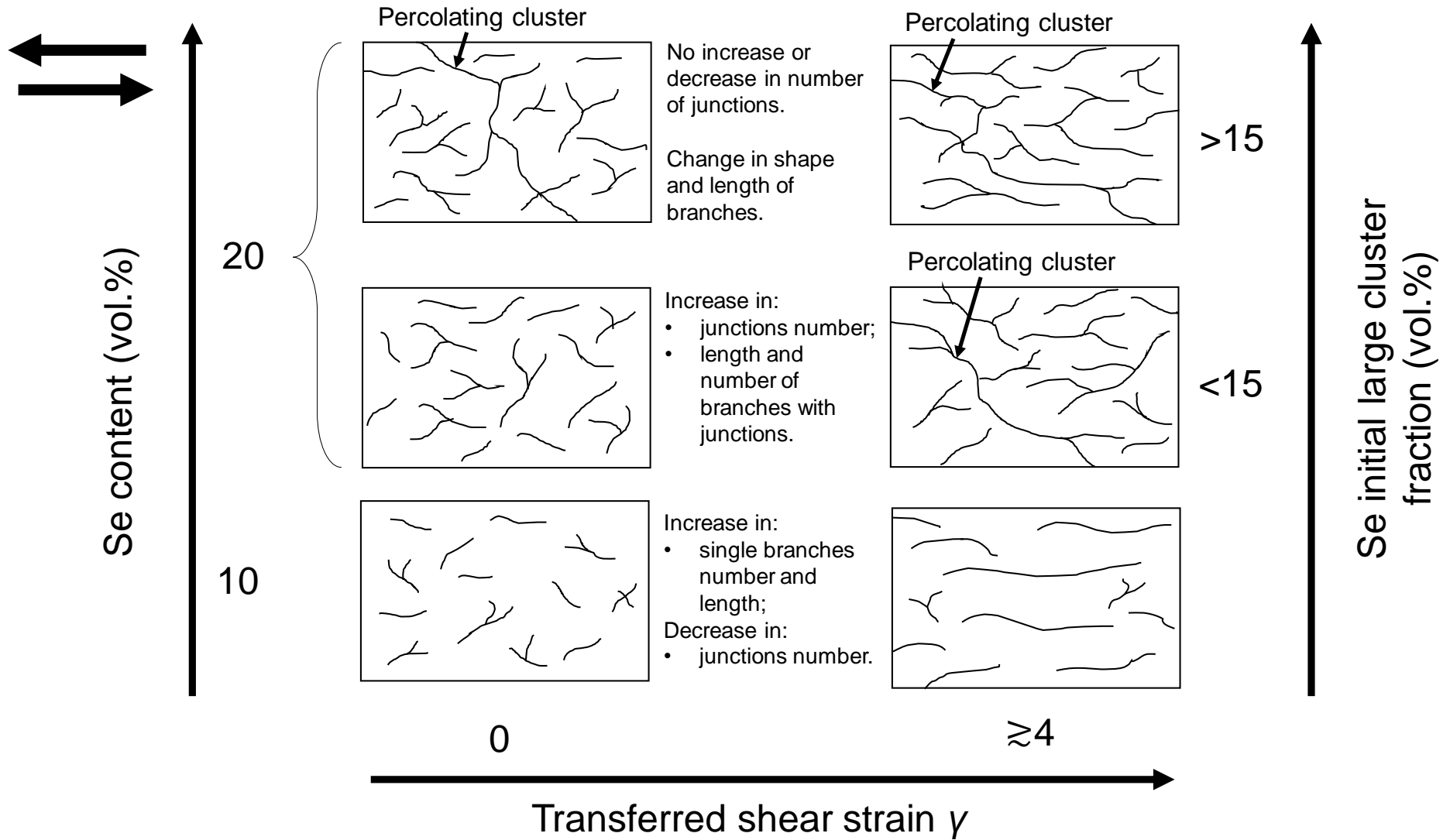
Figure 4. 35. Scenarios for serpentine (Se) morphology (simplified in form of branches) with increasing deformation, as a function of serpentine content (vol.%) and initial fraction of large clusters (vol.%). Pair of arrows defines the sense of shear.

Percolation threshold in the serpentine

The interconnectivity in the serpentine investigated through in-situ XRT is described by the high or increasing number of junctions in the 2-d skeletons (Fig. 4.19, Fig. 4.35) and by the occurrence of large clusters expanding in the whole RV (Fig. 20b), with high largest-cluster connectivity (Fig. 4.21). This high interconnectivity only occurs when the serpentine content is ca. 20 vol.% (samples #18 and #24).

The content of ca. 20 vol.% of serpentine in these samples can be interpreted as the critical content required to potentially have the whole serpentine interconnected and percolating through the sample volume, i.e. a percolation threshold.

The percolation threshold in a mixture or aggregate can be associated with a considerable or drastic change in an aggregate physical properties (Colombier et al., 2020; Guéguen et al., 1997; Karato, 2008; Liu and Lieb, 2021; Stauffer and Aharony, 2003), including mechanical properties.

Based on concepts of percolation theory (see section 4.2) applied to 3-d XRT dataset, the percolation threshold is the minimum concentration of a phase at which that phase is observed to percolate from one end to another of the sample volume, therefore defining the so-called percolating cluster (Liu and Lieb, 2021). This is consistent with the observations (Fig. 4.5, 4.17, 4.20b) and calculations on number of junctions (Fig. 4.19) and cluster connectivity (Fig. 4.21) for the two samples with ca. 20 vol.%, #18 and #24.

However, the occurrence of a percolating cluster in my work cannot be explained with the only concentration of serpentine. In sample #18, it is likely the transferred shear to induce the formation of a percolating cluster at the last stage of deformation, i.e. at $\gamma \gtrsim 4$ (Table 4.5, Fig. 4.20b). Alternatively, in the sample #24, a percolating cluster can be already present before shear is initiated (largest cluster connectivity close to ca. 100% at $\gamma = 0$, Fig. 4.21). The difference between the two samples on the formation of a percolating cluster can be explained with the initial fraction of the large clusters (see also previous

section, Fig. 4.35). Sample #24 shows an initial large clusters fraction in the RV of ca. 18 vol.%, i.e. making almost for the whole serpentine content (Table 4.5), whereas sample #18 shows an initial large clusters fraction in the RV of ca. 13 vol.% (Table 4.5). This suggest that a fraction of larger clusters of serpentine ca. $13 < x < 18$ vol.% in olivine+serpentine aggregates form a percolating cluster throughout the sample without the transfer of the shear. This is consistent with the 2-d serpentine morphology in form of branches (Fig. 4.35).

Ferrand et al. (2017) investigated embrittlement in olivine+serpentine aggregates to explain rapture and earthquakes generation through simple shear experiments at high pressure and temperature. They deformed the aggregates at similar pressure of my work. They integrated the model of percolation theory (e.g., Stauffer and Aharony, 2003) to their results to obtain a critical content at which the serpentine could form a network along which the rupture could occur. Their calculation suggests that above a critical serpentine fraction of ca.18 vol.% the serpentine can form a network at pressure of 3.5 GPa.

The serpentine volume threshold (ca. 20 vol.%) at which serpentine in my sample is interconnected is similar to the critical volume fraction from the calculation by Ferrand et al. (2017).

At constant pressure, my findings emphasize that the formation of a network or percolation threshold for the serpentine within the olivine matrix could not only be explained with the concentration of the serpentine, but also with its clusters size distribution, as well as with the transferred simple shear strain.

Interconnected serpentine in natural rocks

In nature, interconnected or percolating serpentines clusters (or layers), can be comparable to the so-called mesh textures (Viti and Mellini, 1998; Rumori et al., 2004; Andreani et al., 2007; MacKenzie et al., 2016; Viti et al., 2018; Bhilisse et al., 2019) found in serpentinized, or partially serpentinized peridotite.

The mesh texture is a network of longitudinally divided cross-fiber veins (or layers) enclosing olivine cores, or grains. This texture forms by alteration (also called serpentinization) through hydration and metamorphism of originally coarse-grained olivine-rich peridotite (e.g., MacKenzie et al., 2016).

The mesh texture can occur when the serpentinization of the rock is not complete, and can be observable when the serpentine in the rock is ca. 30 vol.% or greater (e.g., Bhilisse et al., 2019). However, contents of serpentine of ca. 10-15 vol.% can be already enough to observe local mesh-like textures or network surrounding olivine grains in partially, or slightly serpentinized peridotite (e.g., Escartín et al., 2001). The contents of ca. ≤20 vol.% of serpentine in my experimental samples are similar or comparable with the contents of serpentine for observing the mesh texture in natural samples (e.g., Escartín et al., 2001; Bhilisse et al., 2019).

Deformed mesh textures can be present in natural retrograde serpentines (e.g., Viti et al., 2018) which can undergo deformation processes during exhumation. During deformation, mesh textures can evolve in size or spatial distribution under deformation. Their morphological changes can influence the stress-strain distribution in retrograde serpentine (Viti et al., 2018), and potentially in the bulk rock.

Escartín et al., (2001) performed deformation experiments on partially serpentinized peridotite with ca. 10-15 vol.% of serpentine. They showed how the presence of a serpentine content of ca. 10 vol.% may already dramatically reduce the strength of the slightly serpentinized peridotite down to that of a pure serpentinite during deformation. One of their samples with ca. 10 vol.% had a pre-existing (prior deformation) locally-developed network (mesh-like texture) of serpentine. This pre-existing network and its possible change in morphology or evolution in size during deformation, might be one of the reasons for the reduction in strength they observed in the rock, therefore playing an important role in its deformation behavior.

Despite mesh textures can primarily form through serpentinization (e.g., Viti and Mellini, 1998; Rumori et al., 2004; Andreani et al., 2007; MacKenzie et al., 2016), if relatively low content (≤20 vol.%) of serpentine are present (i.e., in slightly serpentinized peridotite; Escartin et al., 2001), their morphological development or percolation through the sample surface, or volume, could be explained with deformation, as in the following. With low contents of serpentine, serpentinization process could promote the formation of mesh texture locally; then, the transferred strain could change their morphology (e.g., Viti et al., 2018), such as their spatial distribution and evolution in size. This could lead to the percolation of serpentine interconnected layers (mesh-like) through the samples (Fig. 4.35), which could play a role in the deformation behavior of the bulk rock, and in reducing its strength (e.g., Escartin et al., 2001). Conversely, the mesh texture could be already interconnected and developed in the whole sample. The shear at this point could only influence the morphology of the interconnected serpentine layers, aligning with the shear direction as deformation takes place (Fig. 4.35). The preferential orientation of serpentine developing with increasing transferred deformation could influence the stress-strain distribution in the rock (e.g., Viti et al., 2018), and play a role in the strength reduction.

Finally, I suggest that, if deformation takes places, contents of serpentine >10 vol.% or at ca. 20 vol.% can be interpreted as threshold for the observation of crucial changes in morphology of serpentine mesh textures (i.e., spatial distribution, size, connectivity or percolation) in serpentinized peridotites. This could define the condition of an important change in their deformation behavior or mechanical properties.

4.5.1.3. Deformation regime

The ability of the serpentine in creating connection between neighboring clusters (interconnectivity), until the serpentine can percolate through the sample volume, suggests the occurrence of a distributed (ductile-style) deformation in the mineral rather

than a localized (brittle-style) deformation, at the sample scale. However, it can be questionable whether distributed microcracks (brittle features) possibly observable at smaller scales (e.g., TEM) could also play a role in the deformation of serpentine (e.g., Auzende et al., 2015).

Observations at TEM scale (Fig. 4.24). show rare microcracks (brittle-style) and distributed micro shear bands (analogue to ductile Riedel shear bands or C'; e.g., Marques et al., 2010) developing in the serpentine, which corroborate the occurrence of a dominant ductile style deformation

High-resolution TEM (HRTEM) images show (locally) the absence of lattice planes traces and crystal ordering in the deformed serpentine (Fig. 4.24e). These areas are either in the vicinity of shear bands or chrysotile crystals, where the acquired electron diffraction pattern indicates the presence of continuous (not spotted) rings (Fig. 4.24f). This can agree with the presence of extremely fine-grained serpentine microstructure, or corroborating the lack of crystal ordering (almost amorphization, or destabilization) in the sheared serpentine.

The lack of crystal ordering could potentially be a consequence of delamination of lattice planes in serpentine (e.g., Hansen et al., 2020) due to the relatively high shear. Delamination of lattice planes in serpentine could develop to an extent where loss of crystalline ordering and/or almost amorphization of those planes occur. The (near) amorphization could then enhance the ductile "flow" in serpentine, leading to a more distributed deformation. The lack of crystal ordering, however, could be also due to phase instability.

Based on experimental pressure and temperature of the present study (ca. 4-5 GPa, and ca. 330-430°C), destabilization should occur for chrysotile and lizardite, since they are generally stable at pressures <1GPa and temperatures up to 300°C, whereas the antigorite is stable (e.g., Ulmer and Trommsdorff, 1995; Evans, 2004; Perrillat et al., 2005;

Evans et al., 2013; Schwartz et al., 2013). However, chrysotile was found to be preserved in the deformed serpentine (Fig. 4.24).

Perrillat et al. (2005) studied dehydration kinetics of antigorite (>500° C), and in one of their experiments at 4.1 GPa they showed dehydration reaction starting at ca. 100 min., with a complete antigorite decomposition reached after ca. 180 min. This time frame agrees with the total duration of deformation (twisting) performed in the present work (e.g., Fig. 4.6, 4.20) at similar pressure. Considering the dehydration kinetics of antigorite in Perrillat et al. (2005), and taking it as a proxy for the lizardite and chrysotile, both are expected to fully dehydrate at the pressure and temperature in my experiments (ca. 4-5 GPa, and ca. 330-430°C). Dehydration products should be observed.

However, I did not observe any dehydration products in the recovered samples at SEM scale (Fig. 4.22), and only the local (near) amorphization in the serpentine matrix (mostly lizardite) was observed at TEM scale (Fig. 4.24). This could be explained considering the experimental set-up used. In comparison to the work by Perrillat et al. (2005), where deformation was not carried out and pressure and temperature were kept constant, my experiments consisted of deformation (twisting) at HT (with variations of pressure during twisting; see Fig. 3.17), followed by quenching and subsequent tomography acquisition at room temperature. This was repeated for each twisting step. With this set-up, pressure and temperature were not constant for the entire duration of the experiments, possibly preventing full dehydration of serpentine in the samples.

Therefore, chrysotile or lizardite could be locally destabilized, but not enough to observe a complete destabilization or dehydration in my samples. Yet, this does not explain the observed distributed deformation in the serpentine matrix (mostly lizardite) and the presence of the preserved, non-deformed chrysotile (Fig. 4.24)

However, it could be explained considering that the strength of chrysotile can increase with increasing temperature and pressure (e.g., Moore et al., 2004; Moore and

Lockner, 2007). This can happen after part of the water is driven off the chrysotile, which then approaches to its dry friction coefficient (up to 0.7) (e.g., Moore et al., 2004; Moore and Lockner, 2007). This friction can be higher than the one of lizardite (0.3 to 0.5), and comparable to the one of antigorite (e.g., Reinen et al., 1994; Moore et al., 2004; Moore and Lockner, 2007).

Based on observations and the above speculations, I propose a scenario to explain the deformed microstructure of the serpentine in my samples (Fig. 4.36). With increasing temperature and pressure, part of the water is driven off the chrysotile, which becomes stronger than the most abundant variety, lizardite (Fig. 4.36a). With the shear deformation, the weaker lizardite would show a low-frictional behavior and behaving 'weaker' than chrysotile. This is reflected in the dominant, homogenously distributed deformation (ductile) in the serpentine matrix, with ductile micro shear bands (Fig. 4.24b, 4.36b) and few micro cracks (Fig. 4.24b). The preserved chrysotile becoming "stronger" can act as "clasts" on the otherwise "softer" serpentine matrix mainly comprising the "weaker" lizardite (Fig. 4.36b). This is consistent with a microstructure describing a "semi-brittle" deformation ("harder" clast + "softer" matrix: e.g., White et al., 1980; Passchier and Trouw, 2005; Jammes et al., 2015). Locally, the ductile deformation in the serpentine matrix could be enhanced by shear delamination (e.g., Hansen et al., 2020) due to the high shear, and/or by (near) amorphization mechanism (Fig. 4.36b).

a) Water partially being driven off the chrysotile

b) Sheared, fine-grained matrix, with local phase (near) amorphization or instability

$\gamma \gtrsim 4$

Chrysotile as "clasts" in the fine-grained matrix

Lizardite   Chrysotile   Antigorite
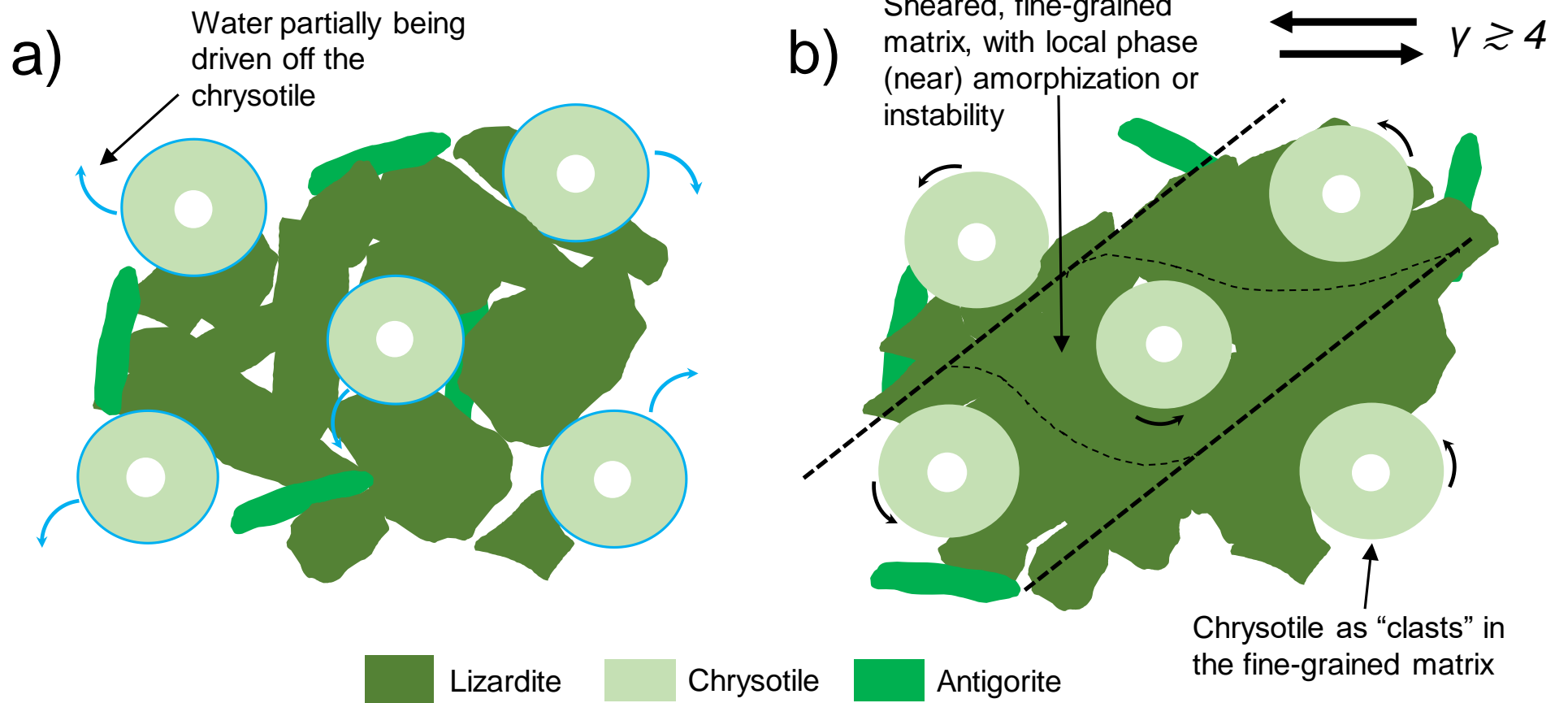
Figure 4. 36. Scenarios for the recovered, deformed microstructure of serpentine composed of lizardite (first most abundant), chrysotile (second most abundant) and antigorite (least abundant). a) Increasing temperature and pressure can make the water drive off the chrysotile. This makes the chrysotile stronger as it approaches to its dry friction coefficient that is higher than the one of lizardite and comparable to the one of antigorite (e.g., Moore et al., 2004; Moore and Lockner, 2007). b) with shear (γ is shear strain), lizardite is behaving as "weaker" phase, showing fine-grained and sheared microstructure in the serpentine matrix, whereas the "stronger" chrysotile is behaving as "clasts". Locally in the matrix, destabilization or (near) amorphization is possible.

Previous experimental studies investigated the ductility of serpentine with a debate on ductility of antigorite (e.g., Escartín et al., 1997; Hilairet et al., 2007; Chernak and Hirth, 2010; Amiguet et al., 2014; Auzende et al., 2015, Proctor and Hirth, 2016; Idrissi et al., 2020; Hansen et al., 2020; Shao et al., 2021).

A recently published experimental work suggested that a brittle or semi-brittle deformation regime mainly control the deformation in antigorite at high pressure and temperature in triaxial or shear deformation (e.g., Shao et al., 2021), with formation of microcracks, local shear bands and kinking in the serpentine microstructure. Proctor and Hirth (2016) initially postulated that a controlled simple shear geometry could induce an easier ductile deformation in antigorite. Their results, however, revealed otherwise, since they observed dominant brittle deformation in all conditions they tested. The shear deformation geometry could, however, play a role in inducting serpentine instability (Shao et al., 2021).

A recent work on uniaxial deformation of olivine+serpentine aggregates by (Hilairet et al., submitted) speculated on the possibility of delamination and/or amorphization in serpentine. They linked their amorphization hypothesis with a decrease in intensity on the basal X-ray diffraction peaks suggesting a loss of crystal ordering at strain of ca. 18%. This strain is lower than the strain ranges transferred to the samples in the present study. If ca. 18% strain can be enough to initiate delamination and/or amorphization (Hilairet et al., submitted), then the strain ranges in the present study would further enhance these processes in serpentine, also promoting a more distributed ductile deformation.

Finally, I suggest the torsional deformation geometry (high shear), together with the water released by the metastable chrysotile as this latter becomes stronger, could lead to a deformation behavior of serpentine that is different from others previously reported in experimental studies at similar conditions of pressures, temperature. The observations

suggest a dominant ductile deformation style that is visible 'macroscopically' (X-ray tomography, interconnectivity and percolation). 'Microscopically' (TEM scale) the observations suggest a deformation that is more consistent with a "semi-brittle" behavior, with the metastable, "stronger" chrysotile acting as "clasts" in a fine-grained, deformed matrix mainly composed by the "weaker" lizardite. Locally, the ductile deformation could be enhanced by shear delamination (e.g., Hansen et al., 2020) due to the high shear, and/or by (near) amorphization (phase instability).

4.5.2. Olivine deformation

The observations and analyses on the recovered microstructure revealed dominant brittle deformation of olivine displayed by the grain embrittlement and "cataclastic flow" (e.g., Fig. 4.25). This agrees with the dominant expected behavior of olivine at temperatures below ca. 900° or ca. 1000° reported in previous work (e.g., Raleigh, 1968; Goetze and Evans, 1979; Demouchy et al., 2009).

The extent of grain embrittlement and cataclastic flow increases with increasing transferred strain in the samples, independently of temperature or serpentine content (e.g., Fig. 4.25, 4.28). The grains crushing between one another generate brittle intracrystalline deformation features. These are displayed by abrupt lattice misorientation (e.g., Fig. 4.25, Fig. 4.28), which are consistent with the formation of microcracks.

However, olivine also locally shows plastic deformation accommodated by a continuous and distributed intracrystalline distortion (continuous lattice misorientation), which is visible when the serpentine content is ca. 20 vol.% (e.g., Fig. 4.28, grain 2). Moreover, strain accommodation through local kinking is also observable (Fig. 4.27), which has been considered as intragranular plasticity in olivine at ranges of temperature of ca. ≤600 °C (e.g., Burnley et al., 2013).

Evidences of plastic deformation in olivine at temperatures of ca. ≤600 °C have been defined in previous experimental studies as low-temperature plasticity (e.g., Gaboriaud et al., 1981; Druiventak et al., 2011; Idrissi et al., 2016). The deformation features associated with olivine low-temperature plasticity, along with extent of work-hardening, can include: i) undulatory extinction associated with high dislocation densities (e.g., Druiventak et al., 2011); ii) dislocations pile-up leading to the formation of either fracture arrays at 300 °C, or deformation lamellae and cellular structures at 600 °C that indicates intragranular work-hardening (e.g., Druiventak et al., 2011) ; iii) active slip systems of (100)[001] or {110}[001], with the former consistent with temperatures lower than 600° C, and the latter consistent with temperature higher than 600°C (Gaboriaud et al., 1981). The slip system of (100)[001] has also been suggested as the dominant slip within individual olivine grains in natural ultramylonitic peridotite (Kaczmarek and Reddy, 2013).

My TEM results on intracrystalline microstructure (Fig. 4.32, 4.33), together with CPO and low-angles misorientation (Fig. 4.30) suggest deformation features associated with work-hardening and (local) low-temperature plasticity, with the dominant intracrystalline slip system of (100)[001]. These findings are in agreement with the previous work on olivine cited above (Gaboriaud et al., 1981; Druiventak et al., 2011; Kaczmarek and Reddy, 2013).

Similar findings on the slip system and CPO of olivine were also reported in a recent study on olivine+serpentine aggregates deformed under uniaxial load (Hilairet et al., submitted) at similar temperatures and pressures. In comparison with Hilairet et al (submitted), the CPO of olivine in the present study is stronger, with higher J-indexes (up to 1.7; compared to ca. 1.07). This could mainly depend on the different deformation geometry employed, and the resulting transferred strain to the samples, resulting in a stronger CPO of the mineral.

The olivine in my samples also shows evidences of SPO, likely promoted by the transferred shear (Fig. 4.31), which influences the crystal shape and orientation. The observable CPO (Fig. 4.30, left) that is expected to form by dislocation glide during shear can be convoluted because of the crystal shape effect (i.e., the SPO) (e.g., Hilairet et al., submitted). This could also question the validity of the possibly dominant slip system in olivine proposed above. However, in my study the proposed slip system remains valid because of the consistency with the low-angle intracrystalline misorientation (Fig. 4.30, right) and inference of the burger vector through TEM observation (Fig. 4.33). Moreover, CPO are visible where SPO are not observable (sample #18, Fig. 4.30, 4.31).

I cannot exclude the effect of SPO on the visible crystallographic texture in olivine (e.g., sample #23; Fig. 4.30, 4.31). However, the above observations suggest a stronger CPO effect and a weaker SPO effect on the resulting crystallographic deformation texture of olivine (Fig 4.30). This again could depend on the different deformation geometry employed in the present work (torsional deformation) compared to previous work, where a uniaxial load was employed, and a weaker CPO with a somewhat stronger SPO was observed (e.g., Hilairet et al, submitted). The resulting transferred strain to the samples due to torsion can efficiently result in a stronger CPO of the mineral, rather than a stronger SPO.

4.5.3. Aggregates deformation

4.5.3.1. Deformation scenarios

The olivine and serpentine in the aggregates suggest two different deformation regimes at the sample scale. Olivine suggests a dominant brittle regime, whereas serpentine suggest a dominant ductile regime. This suggest a general deformation of the aggregates in a semi-brittle regime, i.e. defined by the brittle + ductile deformation features (e.g., Jammes et al., 2015) of the olivine + serpentine, respectively.

The microstructural observations and analyses (*in-situ* X-ray tomography + *post-mortem* electron microscopy) suggest specific deformation scenarios, or morphological configurations, of the aggregates that mainly depend on serpentine content and transferred shear strain, but also on the initial fraction of the large serpentine clusters.

Figure 4.37 shows the different deformation scenarios I proposed for olivine+serpentine aggregates with increasing shear strain, as a function of serpentine content and fraction of large clusters.

At ca. 10 vol.% of serpentine in the samples (Fig., 4.37) olivine likely controls the rheology of the aggregate. With increasing strain, possible rheological weakening would be mainly determined by grain embrittlement (i.e., grain reduction) in olivine. However, olivine could locally display some kinking as a sign of plastic intracrystalline deformation and local strain accommodation (low-temperature plasticity).

At ca. 20 vol.% of serpentine in the samples (Fig. 4.37), the increasing shear (up to at least $\gamma \geq 4$) can induce the serpentine to form large interconnected clusters percolating throughout the samples (percolation threshold), while olivine behaves as clasts. The large interconnected clusters could, however, be formed even before shear is initiated, depending on the initial clusters size distribution (Fig. 4.37). The interconnectivity and percolation of serpentine could also allow rotations of the olivine clasts, with achievement of a favorable grain orientation in order for the slip system to be active and promote local intracrystalline low-temperature plasticity in olivine. A rheology weakening of the aggregate is likely possible thanks to the strain-localized interconnected layers of serpentine developing throughout the sample volume
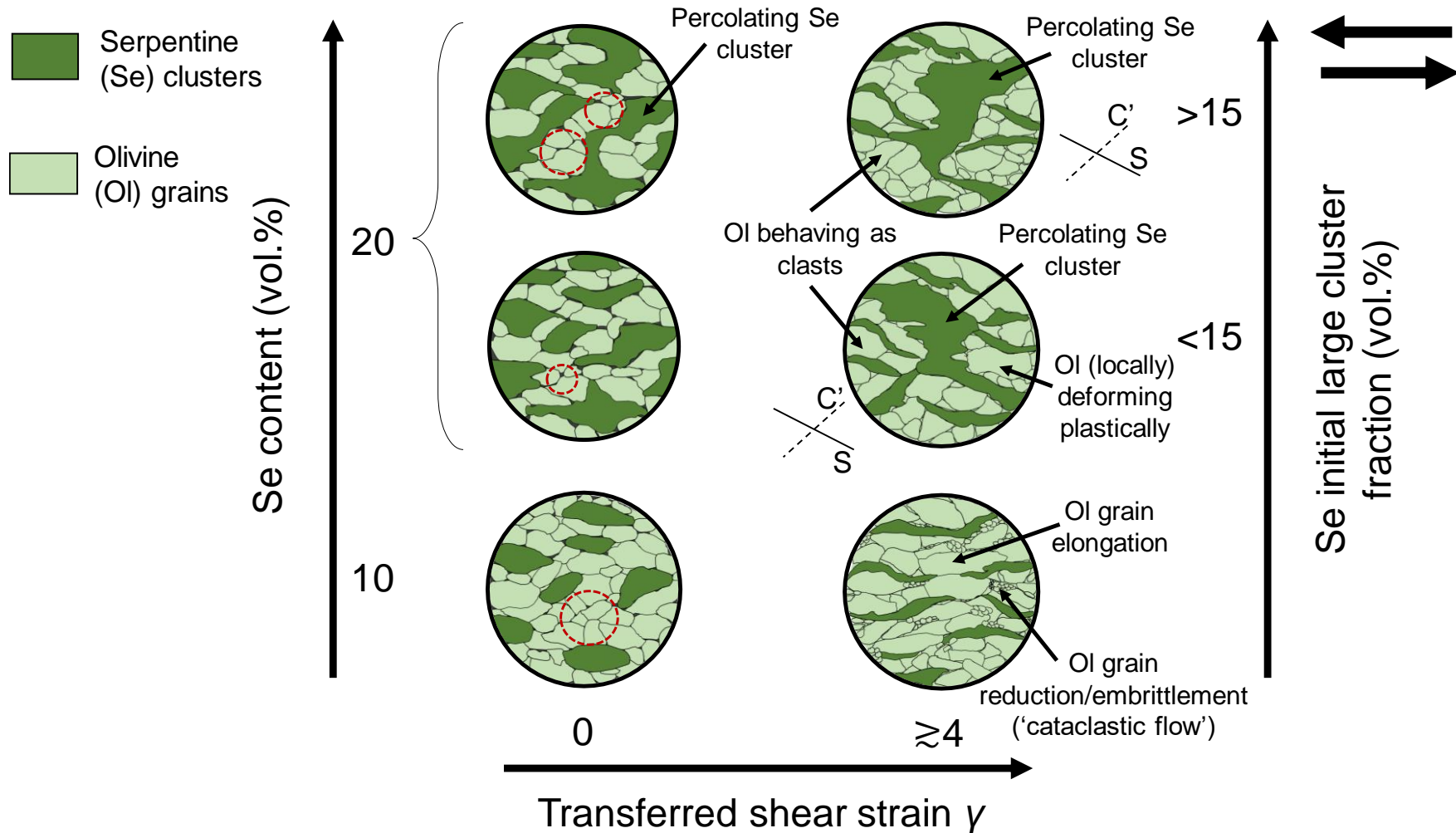
Figure 4. 37. Model of morphological deformation scenarios in olivine+serpentine aggregate depending on transferred shear strain γ, serpentine content (vol.%) and initial (before deformation) large clusters fraction (vol.%) of serpentine. The pair of black arrows indicate the sense of shear. Dark red-dashed circles indicate possible areas of olivine grain size reduction before shear. Small dark-grey areas in the olivine before deformation indicate porosity. For the scenarios at 20 vol.% of Se and γ ≳4, the solid and black-dashed lines define the orientation of the S and C' foliation (i.e., S-C' fabric), respectively.

These deformation scenarios for the two serpentine contents can be consistent with i) a LBF configuration (see section 1.2), for the samples with ca. 10 vol.% of serpentine (Fig. 4.37), and ii) a IWL configuration (see section 1.2, 4.1), for the samples with ca. 20 vol.% of serpentine (Fig. 4.37). These two end-members belong to one of the models for multi-phase rock that gives a first order relation between the stress-strain distribution and the morphology of the phases (e.g., Handy, 1990; 1994; Handy et al., 1999; Karato, 2008; Wang et al., 2011). In the LBF (analogue to a 'dispersed' fabric; term after Montesi et al., 2013; see section 4.1), the strain would be uniform in the samples while the stress would be controlled by the olivine framework. In the IWL (analogue to a 'layered' fabric; term after Montesi et al., 2013; see section 4.1), the strain would be localized in the serpentine interconnected clusters acting as 'weak' layers in the aggregates, which also would influence the strength of the aggregate.

The achievement of a full IWL can correspond to the condition of a percolation threshold, i.e. at 20 vol.% of serpentine, and depending on the shear strain or the initial cluster size distribution.

The above speculation based on microstructural analysis is in agreement with findings by Hilairet et al., (submitted) on stress partitioning in olivine+serpentine aggregates. They found the stress partitioning changing at a threshold between 10 and 20 vol.% of serpentine in the samples. At 20 vol.%, their samples show the stress of olivine in the aggregate reducing, being similar to the one of serpentine in the aggregate, and lower than a polycrystalline olivine deformed together with the olivine+serpentine aggregate (Fig. 2 in Hilairet et al., submitted). Since the olivine is the dominant phase, the reduced stress in olivine can be consistent to the strength reduction of the aggregate. In terms of microstructure, this is consistent with a IWL configuration displayed by the interconnectivity and percolation at 20 vol.% of serpentine as suggested in the present study at simple shear γ of ca. 4 or greater (Fig. 4.35, Fig. 4.37).

4.5.3.2. S-C' fabric

The conditions for a IWL configuration in my samples seem to coincide with the conditions where an S-C' would be more developed in the aggregates (see Fig. 4.5, Fig. 34).

The S-C' fabric, while being a common feature in highly-sheared natural rocks at HP-HT in shear zones (e.g., Passchier and Trouw, 2005), does not form in all rock types. One of the suggested requirements for the S-C' fabric is the formation of an interconnected weak layer that enable the development of a strong anisotropy (Platt and Vissers, 1980; Platt, 1984; Jordan, 1987; Williams and Price, 1990). The experimental findings in the present study support this hypothesis for olivine+serpentine aggregate. Moreover, S-C' fabric related to naturally, highly sheared rocks (such as mylonites) was found where interconnected 'weak' layers of phyllosilicates take up most of the strain, weakening the rock, preventing straining of the 'strong' phase and allowing for more effective strain localization through the entire rock mass (Hunter et al., 2016). This can be consistent with the experimental configuration of the present work for olivine+serpentine aggregate with ca. 20 vol.% of serpentine and deformed at γ of ca. 4 or greater (Fig. 4.35, 4.37).

S-C' fabric is also thought to depend on the rheological contrast of the phases involved in the deformation, as well as on the content of the weak phase in the aggregate (Finch et al., 2020 and references therein). Previous experimental or numerical studies that either have tested different strength ratios (rheological contrast) or different volume proportions of the phases in multi-phase rocks suggested the C' shear bands can form when i) the strength ratio is at least 3 to 5 (Jordan, 1987; Stünitz and Tullis, 2001; Holtzman et al., 2003; Holyoke and Tullis, 2006), ii) when the minimum amount of weak phase is ca. 20 vol.% (e.g., Jordan, 1987), or iii) when the weak phase is ≥15 vol.% (Finch et al., 2020). The present work is in agreement with previous findings for the development of defined C' shear bands (or S-C' fabric) in olivine+serpentine for the two

170

following reasons: i) the strength ratio of olivine/serpentine is at least in the order of ca. 3 (Amiguet et al., 2012; Guillot et al., 2015), and ii) the volume content threshold of the 'weaker' serpentine is ca. 20 vol.% where I observed the S-C' fabric being more developed.

4.5.3.3. Summary and perspectives for the Earth lithosphere

The sheared olivine+serpentine aggregates suggest a semi-brittle deformation under the experimental conditions investigated in the present study. The aggregates suggest a IWL behavior at ca. 20 vol.% content of the 'weaker' serpentine in the samples, whereas a LBF behavior is dominant at ca. 10 vol.% content. The IWL behavior is consistent with a percolation threshold in the aggregates, which can be induced by the transferred shear strain $\gamma \gtrsim 4$. The conditions for IWL in the sample coincide with the ones for the development of S-C' fabric, whose onset can be seen at strain ranges of $\gamma \geq 2$.

The IWL in the samples with ca. 20 vol.% of serpentine can be responsible for an efficient strain localization at $\gamma \gtrsim 4$. Alternatively, at ca. 10 vol.% of serpentine with a LBF behavior, strength reduction in the rock is likely to occur because of the grain size reduction of olivine at $\gamma \gtrsim 4$.

In the lithosphere, during a single deformation event, depending on the degree of serpentinization, a rheological weakening can be induced by either a percolating IWL (e.g., Handy, 1994; Shea and Kronenberg, 1993; Montési, 2013) of the secondary 'weak' phase, serpentine (at ca. 20 vol.%) or by the grain size reduction (e.g., Warren and Hirth, 2006; Kilian et al., 2011) of the dominant 'strong' phase, olivine (at ca. 10 vol.% of serpentine). These mechanisms could lead to shear zones initiation explained with either pre-existing fabric or development of new fabrics and layering (e.g., Gardner et al., 2017; Fossen and Cavalcante, 2017). This can happen at relatively lower strain ranges (up to $\gamma \sim 4$) than the ones usually present in a shear zone ($\gamma \geq 10$, or up to 20; Ramsay and Graham, 1970; Dutruge and Burg, 1997).

If deformation further increases (γ > 4-5) at a constant strain rate, for a lithology with serpentinization of ca. 20 vol.%, the interconnected weak layers of serpentine could develop to higher scale in the lithosphere, with the possible formation of anastomosing shear zones (Fossen and Cavalcante, 2017; Gardner et al., 2017), or resulting in an efficient strain localization up to kilometer-scale that could enable subduction initiation (Montési, 2013; Stern and Gerya, 2018). Alternatively, in a lithology with degrees of serpentinization of ca. 10 vol.%, the grain size reduction of olivine could develop to an extent where homogeneously distributed fine-grained olivine matrix occur. This can be consistent with a ultramylonitic fabric that can efficiently localize the strain in the lithosphere, and maintain weak, ductile shear zones (e.g., Stenvall et al., 2019).

However, I suggest that the above scenarios could change, and transition between different fabrics could occur, if strain rates change.

For instance, an abrupt increase in strain rate could promote an easier strain localization along microcracks or fracture rather than maintaining a homogenous, ductile deformation (Song and Cao, 2021). In this case, for the lithology with serpentinization of ca. 20 vol.%, the serpentine could show a transition from ductile (distributed deformation) to brittle (localized deformation) (Proctor and Hirth, 2016). Microcracks or fracturing would localize along the interconnection between the serpentine, resulting in breaking down the interconnected weak layers (Stenvall et al., 2019), and possibly leading to slips activation in the serpentine (e.g., Moore et al., 2004). This can be consistent with the transition to a fault zone-like fabric, where slips on interconnected layers of phyllosilicate-rich surfaces were suggested to promote fault weakening (e.g., Collettini et al., 2009).

A decrease in the strain rate, on the other hand, could favor the accommodation of a ductile deformation over a brittle deformation in the rock (e.g., Song and Cao, 2021). In this case, for the lithology with the ca. 10 vol.% of serpentine, the ductile deformation

occurring in the serpentine could promote the non-interconnected serpentine segments (already parallel or subparallel to the shear direction; Fig. 4.35, 4.37) to become interconnected along the shear direction. Therefore, a 'layered' fabric (e.g., Jordan, 1987; Handy, 1990, 1994; Ji et al., 2004; Montési, 2007, 2013), described by the interconnected weak layers of serpentine parallel to the shear direction, could occur. This would be consistent with a possible transition between different deformation behavior or fabrics (e.g., Handy, 1990; Handy et al., 1999; Schrank et al., 2008; Gardner et al., 2017), specifically from a LBF-like behavior to a IWL-like behavior, for lithologies with ca. 10 vol.% of serpentinization in the lithosphere.

Based on the above speculations, in terms of strain localization efficiency, I suggest the validity of both mechanisms (interconnected weak layers-sensitive and grain size reduction-sensitive) depending on the weak phase content, and the possible transition from one mechanism to another depending on changes in strains or strain rates.

This could contradict the inference that one mechanism prevails over the other in being the most efficient for strain localization and maintain shear zones in their weakest state (e.g., Shea and Kronenberg, 1993; Handy, 1994; Montési, 2013; Stenvall et al., 2019).

Future numerical models could be performed in polymineralic aggregates (weak+strong phases) under shear deformation ($\gamma \geq 4$) to test the achievement of LBF (with grain size reduction mechanism in the strong phase), IWL or the transition from one to the other, in partially serpentinized peridotite or in other lithologies representative for shear zones (e.g. Fossen and Cavalcante, 2017). The future work could test low values of the weak components (ca. 10 vol.% and 20 vol.%), and mean values of morphological parameters (Fig. 4.16) that in this study were found to be possibly correlated with a stable morphology (e.g., S-C' fabric). These are mean aspect ratio of ca. 3, and a mean structural layering (preferred orientation) with respect to shear direction of ca. 5 to 10° (Fig. 4.16). These parameters could be used to investigate whether the achievement of a "steady-

state" morphology is possible after a certain amount of transferred strain, or rather a fabric transition could be always possible.

General conclusions and perspectives

In this work, I performed shear deformation in multi-phase rocks at high pressure and temperature (HP-HT) in the RoToPEc apparatus coupled with *in-situ* X-ray tomography (XRT).

I successfully imaged and followed the microstructure evolution in two kind of aggregates at different steps of torsional deformation. Evolving deforming features and heterogeneities in the samples were observed and analyzed in a representative volume (RV) preserving the symmetry of the torsion geometry transferred to the samples.

With the outlined image-processing and analyses, I showed some important quantifications that can be used to interpret naturally deformed multi-phase rocks and their microstructural behaviors under shear deformation. This makes the RoToPEc with *in-situ* XRT a suitable, powerful tool to experimentally explore microstructures representative for large shear environments.

Quenching the sample before the acquisition of tomography remains strongly necessary to this date when performing deformation in the RoToPEc. It is crucial to obtain a satisfactory quality of the acquisition, reduce lateral expansion (extrusion of the assembly cell or sample), minimize the loss in oil pressure, and maximize the final strain transferred to the sample. Future work on a different assembly design should be needed to counter the shortcoming of the RoToPEc experimental set-up such us the loss of oil confining pressure, as well as the reduction of the XRT window. The latter cause possible misinterpretation of the acquired data, potentially missing important sample information laying outside the tomography window. This can be countered by performing *post-mortem* electron microscopy analyses on the recovered samples. Moreover, integrating the *in-situ* XRT observations to the electron microscopy analyses permits to link the

evolving microstructure evolution of the phases to their plastic properties and deformation mechanism.

I experimentally explored the evolution of the microstructure with increasing shear deformation in serpentinized peridotite, one of the most common rocks that can be found in multiple tectonic settings of the lithosphere. The main objective was to observe the onset and development of IWL in its microstructure, and determine strain distribution and/or localization, with perspective for shear zone dynamics and shear localization in the lithosphere.

I conducted the experiments (at HP of ca. 4-5 GPa, and HT of ca. 300-400 C°; strain rate of 10^{-4} s^{-1}, simple shear γ up to ca. 5) on aggregates of olivine+serpentine, used as a proxy for serpentinized peridotite. *Post-mortem* electron microscopy analyses were performed to link the *in-situ* XRT observations to the plastic properties of the minerals, and infer the main deformation regime in the rock.

The results showed the deformation regime of the olivine+serpentine aggregates can be described as semi-brittle in all the experimental conditions investigated, with the dominant phase of olivine ('stronger') mainly displaying brittle deformation, whereas the serpentine ('weaker') shows a dominant ductile-style deformation.

The serpentine formed interconnected layers (or interconnected clusters) percolating through the samples when the serpentine content was ca. 20 vol.%, and the transferred shear strain γ ≥ 4. Pre-existing (prior deformation) large clusters also formed when the initial fraction of the large cluster in the samples was >15 vol.%.

The transferred strain (γ ≥ 4), the serpentine volume content (ca. 20 vol.%) and the initial large cluster fraction (>15 vol.%) are conditions that agree with a percolation threshold and IWL configuration for the olivine+serpentine aggregate. These conditions are also consistent with the observation of distributed S-C' fabric in the sample.

Percolation threshold and IWL can correspond to conditions where the strength of the sample likely decreases, and strain localizes in the percolating, interconnected layers of the weak serpentine. At these conditions, the strong olivine grains could behave as clasts, being likely 'free' to rotate among the interconnected weak layers of serpentine.

Alternatively, at serpentine volume contents of < 20 vol.%, interconnected layers of serpentine at the sample volume scale did not occur, independently of strain or initial clusters size distribution of serpentine. Here, olivine grains could be likely 'locked', and during deformation are crashed, causing grain size reduction and accommodating much of the deformation in the rock. This can be consistent with a load-bearing framework (LBF), deformation behavior.

Contents of serpentine >10 vol.% or ca. 20 vol.% seems to be a key for the observation of crucial changes in morphology, connectivity and percolation of the weaker serpentine in serpentinized peridotites. This can define the condition of an important change in deformation behavior and mechanical properties of the rock.

Future work on shear deformation ($\gamma \geq 4$) with stress calculation and partitioning in olivine+serpentine could be performed to corroborate the possible strength reduction of the aggregate, which can be either due to interconnected weak layers of serpentine (at ca. 20 vol.% of serpentine), or grain size reduction in olivine (ca. 10 vol.% of serpentine).

In tectonic settings of the lithosphere, during a single deformation event and depending on the degree of serpentinization, I suggest dynamical weakening can be induced by either IWL of the 'weak' serpentine (ca. 20 vol.% of serpentine), or the LBF behavior with grain size reduction of the 'strong' olivine (ca. 10 vol.% of serpentine). These mechanisms could lead to shear zones initiation that can preferentially develop along fabrics or layering (e.g., Gardner et al., 2017; Fossen and Cavalcante, 2017). This can

happen at relatively lower strain ranges ($\gamma \sim$ 4-5) than the ones usually present in a shear zone ($\gamma \geq$ 10, or up to 20; Ramsay and Graham, 1970; Dutruge and Burg, 1997).

However, if the strain rate changes, a change in the dominant fabric, deformation behavior, or transition from a LBF to IWL could occur in the rock.

I suggest both LBF-like fabric and IWL-like fabric could occur and result in strain localization in the lithosphere with shear zone formation, depending on initial content of weak phase, the evolution of strain and strain rate. This contradicts the inference that one mechanism, interconnected weak layers-sensitive or grain size-sensitive, prevails over the other in being the most efficient for strain localization and maintain shear zones (e.g., Shea and Kronenberg, 1993; Handy, 1994; Montési, 2013; Stenvall et al., 2019).

I suggest the values for i) weaker components (ca. 10 vol.% and 20 vol.%), ii) mean aspect ratio (ca. 3) and iii) mean structural layering with respect to shear direction (ca. 5 to 10°) could be tested as microstructural parameters in future numerical models in deformation of polymineralic rocks, such as serpentinized peridotite or other lithologies representative for shear zones (e.g., Fossen and Cavalcante, 2017). These parameters could be used in a shear geometry at $\gamma \geq$ 4 to investigate i) the IWL vs. LBF behavior, with their possible transition with increasing deformation, and ii) the achievement or not of a "steady-state" morphology after a certain amount of transferred strain.

Bibliography

Álvarez-Murga, M., Perrillat, J.P., Le Godec, Y., Bergame, F., Philippe, J., King, A., Guignot, N., Mezouar, M., Hodeau, J.L., 2017. Development of synchrotron X-ray micro-tomography under extreme conditions of pressure and temperature. J. Synchrotron Radiat. 24, 240–247. https://doi.org/10.1107/S1600577516016623

Amiguet, E., Reynard, B., Caracas, R., Van de Moortèle, B., Hilairet, N., Wang, Y., 2012. Creep of phyllosilicates at the onset of plate tectonics. Earth Planet. Sci. Lett. 345–348, 142–150. https://doi.org/10.1016/j.epsl.2012.06.033

Amiguet, E., Van de Moortèle, B., Cordier, P., Hilairet, N., Reynard, B., 2014. Deformation mechanisms and rheology of serpentines in experiments and in nature. J. Geophys. Res. Solid Earth 119, 4640–4655. https://doi.org/10.1002/2013JB010791

Andreani, M., Mével, C., Boullier, A.M., Escartín, J., 2007. Dynamic control on serpentine crystallization in veins: Constraints on hydration processes in oceanic peridotites. Geochemistry, Geophys. Geosystems 8. https://doi.org/10.1029/2006GC001373

Arganda-Carreras, I., Fernández-González, R., Muñoz-Barrutia, A., Ortiz-De-Solorzano, C., 2010. 3D reconstruction of histological sections: Application to mammary gland tissue. Microsc. Res. Tech. 73, 1019–1029. https://doi.org/10.1002/jemt.20829

Auzende, A.-L., Devouard, B., Guillot, S. phane, Daniel, I., Baronnet, A., Lardeaux, J.-M., 2002. Serpentinites from Central Cuba: Petrology and HRTEM study. Eur. J. Mineral. 14, 905–914. https://doi.org/10.1127/0935-1221/2002/0014-0905

Auzende, A.-L., Pellenq, R.J.-M., Devouard, B., Baronnet, A., Grauby, O., 2006. Atomistic calculations of structural and elastic properties of serpentine minerals: The case of lizardite. Phys. Chem. Miner. 334 33, 266–275. https://doi.org/10.1007/S00269-

006-0078-X

Auzende, A.L., Escartin, J., Walte, N.P., Guillot, S., Hirth, G., Frost, D.J., 2015. Deformation mechanisms of antigorite serpentinite at subduction zone conditions determined from experimentally and naturally deformed rocks. Earth Planet. Sci. Lett. 411, 229–240. https://doi.org/10.1016/j.epsl.2014.11.053

Bai, Q., Kohlstedt, D.L., 1992. High-temperature creep of olivine single crystals, 2. dislocation structures. Tectonophysics 206, 1–29. https://doi.org/10.1016/0040-1951(92)90365-D

Bai, Q., Mackwell, S.J., Kohlstedt, D.L., 1991. High-temperature creep of olivine single crystals: 1. Mechanical results for buffered samples. J. Geophys. Res. 96, 2441–2463. https://doi.org/10.1029/90JB01723

Baronnet, A., Devouard, B., 2005. Microstructures of common polygonal serpentines from axial HRTEM imaging, electron diffraction, and lattice-simulation data. Can. Mineral. 43, 513–542. https://doi.org/10.2113/gscanmin.43.2.513

Bercovici, D., 2003. The generation of plate tectonics from mantle convection. Earth Planet. Sci. Lett. 205, 107–121. https://doi.org/10.1016/S0012-821X(02)01009-9

Bercovici, D., Ricard, Y., 2014. Plate tectonics, damage and inheritance. Nature 508, 513–516. https://doi.org/10.1016/S0012-821X(02)01009-9

Berg, M.T.L., Bromiley, G.D., Butler, I.B., Frost, M., Bradley, R., Carr, J., Le Godec, Y., Montési, L.G.J., Zhu, W., Miller, K., Perrillat, J.P., Mariani, E., Tatham, D., Redfern, S.A.T., 2017. Deformation-aided segregation of Fe-S liquid from olivine under deep Earth conditions: Implications for core formation in the early solar system. Phys. Earth Planet. Inter. 263, 38–54. https://doi.org/10.1016/j.pepi.2017.01.004

Berg, M.T.L., Bromiley, G.D., Le Godec, Y., Philippe, J., Mezouar, M., Perrillat, J.P., Potts, N.J.,

2018. Rapid core formation in terrestrial planets by percolative flow: In-situ imaging of metallic melt migration under high pressure/temperature conditions. Front. Earth Sci. 6, 1–19. https://doi.org/10.3389/feart.2018.00077

Bethe, H.A., 1935. Statistical theory of superlattices 145, 245–270. https://doi.org/10.1142/9789812795755_0010

Bhattacharya, A.R., 2022. Mechanisms of rock deformation. Springer, Cham, pp. 319–335. https://doi.org/10.1007/978-3-030-80795-5_16

Bhilisse, M., Admou, H., Aydda, A., Maacha, L., 2019. Mineralogical and seismic properties of serpentinite of Ait Ahmane fault zone of Bou Azzer ophiolite, central Anti-Atlas of Morocco. Comptes Rendus - Geosci. 351, 303–311. https://doi.org/10.1016/j.crte.2019.01.002

Boulard, E., Denoual, C., Dewaele, A., King, A., Le Godec, Y., Guignot, N., 2020. Following the phase transitions of iron in 3D with X-ray tomography and diffraction under extreme conditions. Acta Mater. 192, 30–39. https://doi.org/10.1016/j.actamat.2020.04.030

Boulard, E., King, A., Guignot, N., Deslandes, J.P., Le Godec, Y., Perrillat, J.P., Clark, A., Morard, G., Itié, J.P., 2018. High-speed tomography under extreme conditions at the PSICHE beamline of the SOLEIL Synchrotron. J. Synchrotron Radiat. 25, 818–825. https://doi.org/10.1107/S1600577518004861

Bromiley, G.D., Redfern, S.A.T., Le Godec, Y., Hamel, G., Klotz, S., 2009. A portable high-pressure stress cell based on the V7 Paris-Edinburgh apparatus. High Press. Res. 29, 306–316. https://doi.org/10.1080/08957950902747411

Brownlee, S.J., Hacker, B.R., Harlow, G.E., Seward, G., 2013. Seismic signatures of a hydrated mantle wedge from antigorite crystal-preferred orientation (CPO). Earth

Planet. Sci. Lett. 375, 395–407. https://doi.org/10.1016/j.epsl.2013.06.003

Bryon, D.N., Atherton, M.P., Hunter, R.H., 1995. The interpretation of granitic textures from serial thin sectioning, image analysis and three-dimensional reconstruction. Mineral. Mag. 59, 203–211. https://doi.org/10.1180/minmag.1995.059.395.05

Burnley, P.C., Cline, C.J., Drue, A., 2013. Kinking in Mg_2GeO_4 olivine: An EBSD study. Am. Mineral. 98, 927–931. https://doi.org/10.2138/am.2013.4224

Butler, I., Fusseis, F., Cartwright-Taylor, A., Flynn, M., 2020. Mjölnir: A miniature triaxial rock deformation apparatus for 4D synchrotron X-ray microtomography. J. Synchrotron Radiat. 27, 1681–1687. https://doi.org/10.1107/S160057752001173X

Byerlee, J., 1978. Friction of rocks. Rock Frict. Earthq. Predict. 615–626. https://doi.org/10.1007/978-3-0348-7182-2_4

Chernak, L.J., Hirth, G., 2010. Deformation of antigorite serpentinite at high temperature and pressure. Earth Planet. Sci. Lett. 296, 23–33. https://doi.org/10.1016/j.epsl.2010.04.035

Collettini, C., Niemeijer, A., Viti, C., Marone, C., 2009. Fault zone fabric and fault weakness. Nature 462, 907–910. https://doi.org/10.1038/nature08585

Colombier, M., Wadsworth, F.B., Scheu, B., Vasseur, J., Dobson, K.J., Cáceres, F., Allabar, A., Marone, F., Schlepütz, C.M., Dingwell, D.B., 2020. In situ observation of the percolation threshold in multiphase magma analogues. Bull. Volcanol. 82. https://doi.org/10.1007/s00445-020-1370-1

Dell'Angelo, L.N., Tullis, J., 1996. Textural and mechanical evolution with progressive strain in experimentally deformed aplite. Tectonophysics 256, 57–82. https://doi.org/10.1016/0040-1951(95)00166-2

Demouchy, S., Schneider, S.E., Mackwell, S.J., Zimmerman, M.E., Kohlstedt, D.L., 2009. Experimental deformation of olivine single crystals at lithospheric temperatures. Geophys. Res. Lett. 36, 1–5. https://doi.org/10.1029/2008GL036611

Denison, C., Carlson, W.D., 1997a. Three-dimensional quantitative textural analysis of metamorphic rocks using high-resolution computed X-ray tomography: Part I. Methods and techniques. J. Metamorph. Geol. 15, 29–44. https://doi.org/10.1111/j.1525-1314.1997.00006.x

Denison, C., Carlson, W.D., 1997b. Three-dimensional quantitative textural analysis of metamorphic rocks using high-resolution computed X-ray tomography: Part II. Application to natural samples. J. Metamorph. Geol. 15, 45–57. https://doi.org/10.1111/j.1525-1314.1997.00007.x

Di Genova, D., Cimarelli, C., Hess, K.U., Dingwell, D.B., 2016. An advanced rotational rheometer system for extremely fluid liquids up to 1273 K and applications to alkali carbonate melts. Am. Mineral. 101, 953–959. https://doi.org/10.2138/am-2016-5537CCBYNCND

Dobson, K.J., Allabar, A., Bretagne, E., Coumans, J., Cassidy, M., Cimarelli, C., Coats, R., Connolley, T., Courtois, L., Dingwell, D.B., Di Genova, D., Fernando, B., Fife, J.L., Fyfe, F., Gehne, S., Jones, T., Kendrick, J.E., Kinvig, H., Kolzenburg, S., Lavallée, Y., Liu, E., Llewellin, E.W., Madden-Nadeau, A., Madi, K., Marone, F., Morgan, C., Oppenheimer, J., Ploszajski, A., Reid, G., Schauroth, J., Schlepütz, C.M., Sellick, C., Vasseur, J., von Aulock, F.W., Wadsworth, F.B., Wiesmaier, S., Wanelik, K., 2020. Quantifying microstructural evolution in moving magma. Front. Earth Sci. 8, 1–22. https://doi.org/10.3389/feart.2020.00287

Druiventak, A., Trepmann, C.A., Renner, J., Hanke, K., 2011. Low-temperature plasticity of olivine during high stress deformation of peridotite at lithospheric conditions: An

experimental study. Earth Planet. Sci. Lett. 311, 199–211.
https://doi.org/10.1016/j.epsl.2011.09.022

Durham, W.B., Goetze, C., 1977. A comparison of the creep properties of pure forsterite
and iron-bearing olivine. Tectonophysics 40, T15–T18.
https://doi.org/10.1016/0040-1951(77)90063-4

Dutruge, G., Burg, J.P., 1997. Strain localisation in an orthogneiss laccolith (the Pinet
Massif, Aveyron, southern France). Tectonophysics 280, 47–60.
https://doi.org/10.1016/S0040-1951(97)00138-8

Escartín, J., Hirth, G., Evans, B., 2001. Strength of slightly serpentinized peridotites:
Implications for the tectonics of oceanic lithosphere. Geology 29, 1023–1026.
https://doi.org/10.1130/0091-7613(2001)029<1023:SOSSPI>2.0.CO;2

Escartín, J., Hirth, G., Evans, B., 1997. Nondilatant brittle deformation of serpentinites:
Implications for Mohr-Coulomb theory and the strength of faults. J. Geophys. Res.
Solid Earth 102, 2897–2913. https://doi.org/10.1029/96jb02792

Evans, B.W., Hattori, K., Baronnet, A., 2013. Serpentinite: What, why, where? Elements 9,
99–106. https://doi.org/10.2113/gselements.9.2.99

Faul, U.H., Fitz Gerald, J.D., Farla, R.J.M., Ahlefeldt, R., Jackson, I., 2011. Dislocation creep
of fine-grained olivine. J. Geophys. Res. Solid Earth 116, 1–12.
https://doi.org/10.1029/2009JB007174

Feldkamp, L.A., Davis, L.C., Kress, J.W., 1984. Practical cone-beam algorithm. J. Opt. Soc.
Am. A 1, 612. https://doi.org/10.1364/josaa.1.000612

Ferrand, T.P., Hilairet, N., Incel, S., Deldicque, D., Labrousse, L., Gasc, J., Renner, J., Wang,
Y., Green, H.W., Schubnel, A., 2017. Dehydration-driven stress transfer triggers
intermediate-depth earthquakes. Nat. Commun. 8, 1–11.

https://doi.org/10.1038/ncomms15247

Finch, M.A., Bons, P.D., Steinbach, F., Griera, A., Llorens, M.G., Gomez-Rivas, E., Ran, H., de Riese, T., 2020. The ephemeral development of C′ shear bands: A numerical modelling approach. J. Struct. Geol. 139, 104091. https://doi.org/10.1016/j.jsg.2020.104091

Fossen, H., 2012. Structural geology. Cambridge University Press.

Fossen, H., Cavalcante, G.C.G., 2017. Shear zones: A review. Earth-Science Rev. 171, 434–455. https://doi.org/10.1016/j.earscirev.2017.05.002

Fusseis, F., Schrank, C., Liu, J., Karrech, A., Llana-Fúnez, S., Xiao, X., Regenauer-Lieb, K., 2012. Pore formation during dehydration of a polycrystalline gypsum sample observed and quantified in a time-series synchrotron X-ray micro-tomography experiment. Solid Earth 3, 71–86. https://doi.org/10.5194/se-3-71-2012

Fusseis, Florian, Steeb, H., Xiao, X., Zhu, W., Butler, I.B., Elphick, S., Mäder, U., 2014. A low-cost X-ray-transparent experimental cell for synchrotron-based X-ray microtomography studies under geological reservoir conditions. J. Synchrotron Radiat. 21, 251–253. https://doi.org/10.1107/S1600577513026969

Fusseis, F., Xiao, X., Schrank, C., De Carlo, F., 2014. A brief guide to synchrotron radiation-based microtomography in (structural) geology and rock mechanics. J. Struct. Geol. 65, 1–16. https://doi.org/10.1016/j.jsg.2014.02.005

Gaboriaud, R.J., Darot, M., Gueguen, Y., Woirgard, J., 1981. Dislocations in olivine indented at low temperatures. Phys. Chem. Miner. 7, 100–104. https://doi.org/10.1007/BF00309460

Gardner, R., Piazolo, S., Evans, L., Daczko, N., 2017. Patterns of strain localization in heterogeneous, polycrystalline rocks: A numerical perspective. Earth Planet. Sci.

Lett. 463, 253–265. https://doi.org/10.1016/j.epsl.2017.01.039

Giovenco, E., Perrillat, J.P., Boulard, E., King, A., Guignot, N., Le Godec, Y., 2021.
Quantitative 4D X-ray microtomography under extreme conditions: A case study on
magma migration. J. Synchrotron Radiat. 28, 1598–1609.
https://doi.org/10.1107/S1600577521007049

Girard, J., Amulele, G., Farla, R., Mohiuddin, A., Karato, S.I., 2016. Shear deformation of
bridgmanite and magnesiowüstite aggregates at lower mantle conditions. Science
(80-.). 351, 144–147. https://doi.org/10.1126/science.aad3113

Goetze, C., Evans, B., 1979. Stress and temperature in the bending lithosphere as
constrained by experimental rock mechanics. Geophys. J. R. Astron. Soc. 59, 463–
478. https://doi.org/10.1111/j.1365-246X.1979.tb02567.x

Guéguen, Y., Chelidze, T., Le Ravalec, M., 1997. Microstructures, percolation thresholds,
and rock physical properties. Tectonophysics 279, 23–35.
https://doi.org/10.1016/S0040-1951(97)00132-7

Guéguen, Y., Palciauskas, V., 1994. Introduction to the physics of rocks. Princeton
University Press, Princeton.

Guillot, S., Schwartz, S., Reynard, B., Agard, P., Prigent, C., 2015. Tectonic significance of
serpentinites. Tectonophysics 646, 1–19.
https://doi.org/10.1016/j.tecto.2015.01.020

Handy, M.R., 1994. Flow laws for rocks containing two non-linear viscous phases: A
phenomenological approach. J. Struct. Geol. 16, 287–301.
https://doi.org/10.1016/0191-8141(94)90035-3

Handy, M.R., 1990. The solid-state flow of polymineralic rocks. J. Geophys. Res. 95, 8647–
8661. https://doi.org/10.1029/JB095iB06p08647

Handy, M.R., Wissing, S.B., Streit, L.E., 1999. Frictional-viscous flow in mylonite with varied bimineralic composition and its effect on lithospheric strength. Tectonophysics 303, 175–191. https://doi.org/10.1016/S0040-1951(98)00251-0

Hansen, L.N., David, E.C., Brantut, N., Wallis, D., 2020. Insight into the microphysics of antigorite deformation from spherical nanoindentation. Philos. Trans. R. Soc. A Math. Phys. Eng. Sci. 378. https://doi.org/10.1098/rsta.2019.0197

Hansen, L.N., Kumamoto, K.M., Thom, C.A., Wallis, D., Durham, W.B., Goldsby, D.L., Breithaupt, T., Meyers, C.D., Kohlstedt, D.L., 2019. Low-temperature plasticity in olivine: Grain Size, strain hardening, and the strength of the lithosphere. J. Geophys. Res. Solid Earth 124, 5427–5449. https://doi.org/10.1029/2018JB016736

Hilairet, N., Guignard, J., Ferrand, T.P., Merkel, S., Raterron, P., Ildefonse, B., Crichton, W., n.d. Stress balance in model serpentinized peridotites deformed at subduction zone pressures. J. Geophys. Res. Solid Earth.

Hilairet, N., Reynard, B., Wang, Y., Daniel, I., Merkel, S., Nishiyama, N., Petitgirard, S., 2007. High-pressure creep of serpentine, interseismic deformation, and initiation of subduction. Science (80-.). 318, 1910–1913. https://doi.org/10.1126/science.1148494

Hirauchi, K. ichi, Michibayashi, K., Ueda, H., Katayama, I., 2010. Spatial variations in antigorite fabric across a serpentinite subduction channel: Insights from the Ohmachi Seamount, Izu-Bonin frontal arc. Earth Planet. Sci. Lett. 299, 196–206. https://doi.org/10.1016/j.epsl.2010.08.035

Hirth, G., Guillot, S., 2013. Rheology and tectonic significance of serpentinite. Elements 9, 107–113. https://doi.org/10.2113/gselements.9.2.107

Hirth, G., Kohlstedt, D.L., 2003. Rheology of the upper mantle and the mantle wedge : A

view from the experimentalists. Geophys. Monogr. Ser. 138, 83–105.

https://doi.org/10.1029/138GM06

Hirth, G., Kohlstedt, D.L., 1996. Water in the oceanic upper mantle: Implications for

rheology, melt extraction and the evolution of the lithosphere. Earth Planet. Sci.

Lett. 144, 93–108. https://doi.org/10.1016/0012-821X(96)00154-9

Holtzman, B.K., Groebner, N.J., Zimmerman, M.E., Ginsberg, S.B., Kohlstedt, D.L., 2003.

Stress-driven melt segregation in partially molten rocks. Geochemistry, Geophys.

Geosystems 4. https://doi.org/10.1029/2001GC000258

Holyoke, C.W., Tullis, J., 2006a. Mechanisms of weak phase interconnection and the

effects of phase strength contrast on fabric development. J. Struct. Geol. 28, 621–

640. https://doi.org/10.1016/j.jsg.2006.01.008

Holyoke, C.W., Tullis, J., 2006b. Formation and maintenance of shear zones. Geology 34,

105–108. https://doi.org/10.1130/G22116.1

Holzer, L., Muench, B., Wegmann, M., Gasser, P., Flatt, R.J., 2006. FIB-nanotomography of

particulate systems - Part I: Particle shape and topology of interfaces. J. Am. Ceram.

Soc. 89, 2577–2585. https://doi.org/10.1111/j.1551-2916.2006.00974.x

Hunter, N.J.R., Hasalová, P., Weinberg, R.F., Wilson, C.J.L., 2016. Fabric controls on strain

accommodation in naturally deformed mylonites: The influence of interconnected

micaceous layers. J. Struct. Geol. 83, 180–193.

https://doi.org/10.1016/j.jsg.2015.12.005

Idrissi, H., Bollinger, C., Boioli, F., Schryvers, D., Cordier, P., 2016. Low-temperature

plasticity of olivine revisited with in situ TEM nanomechanical testing. Sci. Adv. 2.

https://doi.org/10.1126/sciadv.1501671

Idrissi, H., Samaee, V., Lumbeeck, G., van der Werf, T., Pardoen, T., Schryvers, D., Cordier,

P., 2020. In situ quantitative tensile testing of antigorite in a transmission electron microscope. J. Geophys. Res. Solid Earth 125, 1–12. https://doi.org/10.1029/2019JB018383

Ikeda, S., Nakano, T., Nakashima, Y., 2000. Three-dimensional study on the interconnection and shape of crystals in a graphic granite by X-ray CT and image analysis. Mineral. Mag. 64, 945–959. https://doi.org/10.1180/002646100549760

Jammes, S., Lavier, L.L., Reber, J.E., 2015. Localization and delocalization of deformation in a bimineralic material. J. Geophys. Res. Solid Earth 120, 3649–3663. https://doi.org/10.1002/2015JB011890

Jerram, D.A., Higgins, M.D., 2007. 3D analysis of rock textures: Quantifying igneous microstructures. Elements 3, 239–245. https://doi.org/10.2113/gselements.3.4.239

Ji, S., Wang, Q., Marcotte, D., 2004. Mechanical properties of multiphase materials and rocks: a phenomenological approach using generalized means. J. Struct. Geol. 26, 1377–1390. https://doi.org/10.1016/j.jsg.2003.12.004

Jiao, Y., Stillinger, F.H., Torquato, S., 2009. A superior descriptor of random textures and its predictive capacity. Proc. Natl. Acad. Sci. U. S. A. 106, 17634–17639. https://doi.org/10.1073/pnas.0905919106

Jordan, P.G., 1987. The deformational behaviour of bimineralic limestone-halite aggregates. Tectonophysics 135, 185–197. https://doi.org/10.1016/0040-1951(87)90160-0

Kaczmarek, M.A., Reddy, S.M., 2013. Mantle deformation during rifting: Constraints from quantitative microstructural analysis of olivine from the East African Rift (Marsabit, Kenya). Tectonophysics 608, 1122–1137.

https://doi.org/10.1016/j.tecto.2013.06.034

Kaercher, P., Miyagi, L., Kanitpanyacharoen, W., Zepeda-Alarcon, E., Wang, Y., Parkinson, D., Lebensohn, R.A., De Carlo, F., Wenk, H.R., 2016. Two-phase deformation of lower mantle mineral analogs. Earth Planet. Sci. Lett. 456, 134–145. https://doi.org/10.1016/j.epsl.2016.09.030

Karato, S.-I., 2008. Deformation of multi-phase materials, in: Deformation of Earth Materials. Cambridge University Press, Cambridge, p. 482. https://doi.org/10.1017/CBO9780511804892

Karato, S.-I., 2008. Deformation of earth materials: An introduction to the rheology of solid earth, Deformation of Earth Materials: An Introduction to the Rheology of Solid Earth. Cambridge University Press. https://doi.org/10.1017/CBO9780511804892

Karato, S.I., Wu, P., 1993. Rheology of the upper mantle: A synthesis. Science (80-.). 260, 771–778. https://doi.org/10.1126/science.260.5109.771

Kareh, K.M., Lee, P.D., Gourlay, C.M., 2012. In situ, time-resolved tomography for validating models of deformation in semi-solid alloys. IOP Conf. Ser. Mater. Sci. Eng. 33. https://doi.org/10.1088/1757-899X/33/1/012037

Kastner, J., Harrer, B., Requena, G., Brunke, O., 2010. A comparative study of high resolution cone beam X-ray tomography and synchrotron tomography applied to Fe- and Al-alloys. NDT E Int. 43, 599–605. https://doi.org/10.1016/j.ndteint.2010.06.004

Kastner, J., Heinzl, C., 2018. X-Ray Tomography, in: Handbook of Advanced Non-Destructive Evaluation. Springer, pp. 1–72. https://doi.org/10.1007/978-3-319-30050-4_5-1

Kilian, R., Heilbronner, R., Stünitz, H., 2011. Quartz grain size reduction in a granitoid rock and the transition from dislocation to diffusion creep. J. Struct. Geol. 33, 1265–1284. https://doi.org/10.1016/j.jsg.2011.05.004

King, A., Guignot, N., Deslandes, J.P., Pelerin, M., Joosten, I., De Looff, D., Li, J., Bertrand, L., Rosenberg, E., Dewaele, A., Boulard, E., Le Godec, Y., Perrillat, J.P., Giovenco, E., Morard, G., Weitkamp, T., Scheel, M., Perrin, J., Chevreau, H., Itié, J.P., 2019. Recent Tomographic Imaging Developments at the PSICHE Beamline. Integr. Mater. Manuf. Innov. 8, 551–558. https://doi.org/10.1007/s40192-019-00155-2

King, A., Guignot, N., Zerbino, P., Boulard, E., Desjardins, K., Bordessoule, M., Leclerq, N., Le, S., Renaud, G., Cerato, M., Bornert, M., Lenoir, N., Delzon, S., Perrillat, J.P., Legodec, Y., Itié, J.P., 2016. Tomography and imaging at the PSICHE beam line of the SOLEIL synchrotron. Rev. Sci. Instrum. 87. https://doi.org/10.1063/1.4961365

Koeberl, C., Denison, C., Ketcham, R.A., Reimold, W.U., 2002. High-resolution X-ray computed tomography of impactites. J. Geophys. Res. E Planets 107, 1–9. https://doi.org/10.1029/2001je001833

Kohlstedt, D.L., Goetze, C., 1974. Low-stress high-temperature creep in olivine single crystals. J. Geophys. Res. 79, 2045–2051. https://doi.org/10.1029/jb079i014p02045

Le Godec, Y., Álvarez-Murga, M., Bromiley, G., Klotz, S., Mezouar, M., Perrillat, J.P., Philippe, J., Redfern, S.A.T., Solozhenko, V.L., 2012. New scientific opportunities with next-generation portable large-volume high-P/T/stress/tomography cells, in: Acta Crystallographica. Section A, Foundations of Crystallography. https://doi.org/10.1107/s0108767312098984

Le Godec, Y., Hamel, G., Solozhenko, V.L., Martinez-Garcia, D., Philippe, J., Hammouda, T.,

Mezouar, M., Crichton, W.A., Morard, G., Klotz, S., 2009. Portable multi-anvil device for in situ angle-dispersive synchrotron diffraction measurements at high pressure and temperature. J. Synchrotron Radiat. 16, 513–523. https://doi.org/10.1107/S0909049509012928

Liu, J., Lieb, R.K., Hines, C., Liu, K., Gaede, O., Squelch, A., 2009. Improved estimates of percolation and anisotropic permeability from 3-D X-ray microtomography using stochastic analyses and visualization. Geochemistry, Geophys. Geosystems 10. https://doi.org/10.1029/2008GC002358

Liu, J., Regenauer-Lieb, K., 2021. Application of percolation theory to microtomography of rocks. Earth-Science Rev. 214, 103519. https://doi.org/10.1016/j.earscirev.2021.103519

Liu, Z.-Q., 1991. Scale space approach to directional analysis of images. Appl. Opt. 30, 1369. https://doi.org/10.1364/ao.30.001369

Locatelli, M., Verlaguet, A., Agard, P., Federico, L., Angiboust, S., 2018. Intermediate-depth brecciation along the subduction plate interface (Monviso eclogite, W. Alps). Lithos 320–321, 378–402. https://doi.org/10.1016/j.lithos.2018.09.028

Lu, G., Kaus, B.J.P., Zhao, L., Zheng, T., 2015. Self-consistent subduction initiation induced by mantle flow. Terra Nov. 27, 130–138. https://doi.org/10.1111/ter.12140

MacKenzie, W.S., Adams, A.E., Brodie, K.H., 2017. Rocks and Minerals in Thin Section, 2nd ed. CRC press, Taylor and Francis Group. https://doi.org/10.1201/9781315116365

Mainprice, D., Bachmann, F., Hielscher, R., Schaeben, H., 2015. Descriptive tools for the analysis of texture projects with large datasets using MTEX: Strength, symmetry and components. Geol. Soc. Spec. Publ. 409, 251–271.

https://doi.org/10.1144/SP409.8

Marone, F., Schlepütz, C.M., Marti, S., Fusseis, F., Velásquez-Parra, A., Griffa, M., Jiménez-Martínez, J., Dobson, K.J., Stampanoni, M., 2020. Time resolved in situ X-ray tomographic microscopy unraveling dynamic processes in geologic systems. Front. Earth Sci. 7, 1–20. https://doi.org/10.3389/feart.2019.00346

Marques, F.O., Burlini, L., Burg, J.P., 2010. Rheology and microstructure of synthetic halite/calcite porphyritic aggregates in torsion. J. Struct. Geol. 32, 342–349. https://doi.org/10.1016/j.jsg.2010.01.001

McBeck, J., Zhu, W., Renard, F., 2020. The competition between fracture nucleation, propagation, and coalescence in dry and water-saturated crystalline rock. Solid Earth 12, 375–387. https://doi.org/10.5194/se-12-375-2021

McDonough, W., Rudnick, R., 1998. Mineralogy and composition of the upper mantle. Rev. Mineral. Geochemistry 37, 139–164.

Mei, S, Kohlstedt, D.L., 2000. Influence of water on plastic deformation of olivine aggregates 2 . Dislocation creep regime. J. Geophys. Res. 105, 21471–21481. https://doi.org/10.1029/2000JB900180

Mei, S., Kohlstedt, D.L., 2000. Influence of water on plastic deformation of olivine aggregates 1 . Diffusion creep regime. J. Geophys. Res. 105, 21457–21469. https://doi.org/10.1029/2000JB900179

Mellini, M., 1982. The crystal structure of lizardite 1T: hydrogen bonds and polytypism. Am. Mineral. 67, 587–598.

Merli, M., Oberti, R., Caucia, F., Ungaretti, L., 2001. Determination of site population in olivine: Warning on X-ray data treatment and refinement. Am. Mineral. 86, 55–65. https://doi.org/10.2138/am-2001-0107

Mirone, A., Brun, E., Gouillart, E., Tafforeau, P., Kieffer, J., 2014. The PyHST2 hybrid
distributed code for high speed tomographic reconstruction with iterative
reconstruction and a priori knowledge capabilities. Nucl. Instruments Methods
Phys. Res. Sect. B Beam Interact. with Mater. Atoms 324, 41–48.
https://doi.org/10.1016/j.nimb.2013.09.030

Miyazaki, T., Sueyoshi, K., Hiraga, T., 2013. Olivine crystals align during diffusion creep of
Earth's upper mantle. Nature 502, 321–326. https://doi.org/10.1038/nature12570

Mock, A., Jerram, D.A., 2005. Crystal size distributions (CSD) in three dimensions:
Insights from the 3D reconstruction of a highly porphyritic rhyolite. J. Petrol. 46,
1525–1541. https://doi.org/10.1093/petrology/egi024

Montési, L.G.J., 2013. Fabric development as the key for forming ductile shear zones and
enabling plate tectonics. J. Struct. Geol. 50, 254–266.
https://doi.org/10.1016/j.jsg.2012.12.011

Montési, L.G.J., 2007. A constitutive model for layer development in shear zones near the
brittle-ductile transition. Geophys. Res. Lett. 34, 1–5.
https://doi.org/10.1029/2007GL029250

Moore, D.E., Lockner, D.A., 2007. Comparative deformation behavior of minerals in
serpentinized ultramafic rock: Application to the slab-mantle interface in
subduction zones. Int. Geol. Rev. 49, 401–415. https://doi.org/10.2747/0020-
6814.49.5.401

Moore, D.E., Lockner, D.A., 2004. Crystallographic controls on the frictional behavior of
dry and water-saturated sheet structure minerals. J. Geophys. Res. Solid Earth 109,
3401. https://doi.org/10.1029/2003JB002582

Moore, D.E., Lockner, D.A., Shengli, M., Summers, R., Byerlee, J.D., 1997. Strengths of

serpentinite gouges at elevated temperatures 102, 14787–14801. https://doi.org/10.1029/97JB00995

Moore, D.E., Lockner, D.A., Tanaka, H., Iwata, K., 2004. The Coefficient of Friction of Chrysotile Gouge at Seismogenic Depths. Int. Geol. Rev. 46, 385–398. https://doi.org/10.2747/0020-6814.46.5.385

Morales, L.F.G., Mainprice, D., Kern, H., 2018. Olivine-antigorite orientation relationships: Microstructures, phase boundary misorientations and the effect of cracks in the seismic properties of serpentinites. Tectonophysics 724–725, 93–115. https://doi.org/10.1016/j.tecto.2017.12.009

Morard, G., Mezouar, M., Rey, N., Poloni, R., Merlen, A., Le Floch, S., Toulemonde, P., Pascarelli, S., San-Miguel, A., Sanloup, C., Fiquet, G., 2007. Optimization of Paris-Edinburgh press cell assemblies for in situ monochromatic X-ray diffraction and X-ray absorption. High Press. Res. 27, 223–233. https://doi.org/10.1080/08957950601183553

Nakashima, Y., Kamiya, S., 2007. Mathematica programs for the analysis of three-dimensional pore connectivity and anisotropic tortuosity of porous rocks using X-ray computed tomography image data. J. Nucl. Sci. Technol. 44, 1233–1247. https://doi.org/10.1080/18811248.2007.9711367

Navarre-Sitchler, A., Steefel, C., Yang, L., Tomutsa, L., Brantley, S., 2009. Evolution of porosity and diffusivity associated with chemical weathering of a basalt clast. J. Geophys. Res. 114, 1–14. https://doi.org/10.1029/2008JF001060

Niemeijer, A.R., Spiers, C.J., 2005. Influence of phyllosilicates on fault strength in the brittle-ductile transition: Insights from rock analogue experiments. Geol. Soc. Spec. Publ. 245, 303–327. https://doi.org/10.1144/GSL.SP.2005.245.01.15

Padrón-Navarta, J.A., Tommasi, A., Garrido, C.J., López Sánchez-Vizcaíno, V., 2012. Plastic deformation and development of antigorite crystal preferred orientation in high-pressure serpentinites. Earth Planet. Sci. Lett. 349–350, 75–86. https://doi.org/10.1016/j.epsl.2012.06.049

Paganin, D., Mayo, S.C., Gureyev, T.E., Miller, P.R., Wilkins, S.W., 2002. Simultaneous phase and amplitude extraction from a single defocused image of a homogeneous object. J. Microsc. 206, 33–40. https://doi.org/10.1046/j.1365-2818.2002.01010.x

Passchier, C.W., Trouw, R.A.J., 2005. Microtectonics, 2nd ed. Springer.

Paterson, M.S., Olgaard, D.L., 2000. Rock deformation tests to large shear strains in torsion. J. Struct. Geol. 22, 1341–1358. https://doi.org/10.1016/S0191-8141(00)00042-0

Perrillat, J.P., Daniel, I., Koga, K.T., Reynard, B., Cardon, H., Crichton, W.A., 2005. Kinetics of antigorite dehydration: A real-time X-ray diffraction study. Earth Planet. Sci. Lett. 236, 899–913. https://doi.org/10.1016/j.epsl.2005.06.006

Philippe, J., Le Godec, Y., Mezouar, M., Berg, M., Bromiley, G., Bergame, F., Perrillat, J.P., Alvarez-Murga, M., Morand, M., Atwood, R., King, A., Régnier, S., 2016. Rotating tomography Paris–Edinburgh cell: a novel portable press for micro-tomographic 4-D imaging at extreme pressure/temperature/stress conditions. High Press. Res. 36, 512–532. https://doi.org/10.1080/08957959.2016.1221951

Philpotts, Antony R., Ague, J., 2009. Principles of igneous and metamorphic petrology.

Platt, J.P., 1984. Secondary cleavages in ductile shear zones. J. Struct. Geol. 6, 439–442. https://doi.org/10.1016/0191-8141(84)90045-2

Platt, J.P., Vissers, R.L.M., 1980. Extensional structures in anisotropic rocks. J. Struct. Geol. 2, 397–410. https://doi.org/10.1016/0191-8141(80)90002-4

Polder, G., Hovens, H.L.E., Zweers, A.J., Jahnen, A., Moll, C., Kennedy, A.J.F., 2010. Measuring shoot length of submerged aquatic plants using graph analysis. Proc. ImageJ User Dev. Conf. 172–177.

Pringle, D.J., Miner, J.E., Eicken, H., Golden, K.M., 2009. Pore space percolation in sea ice single crystals. J. Geophys. Res. Ocean. 114, 1–14. https://doi.org/10.1029/2008JC005145

Proctor, B., Hirth, G., 2016. "Ductile to brittle" transition in thermally stable antigorite gouge at mantle pressures. J. Geophys. Res. Solid Earth 121, 1652–1663. https://doi.org/10.1002/2015JB012710

Raleigh, C.B., 1968. Mechanisms of plastic deformation of olivine. J. Geophys. Res. 73, 5391–5406. https://doi.org/10.1029/jb073i016p05391

Raleigh, C.B., Paterson, M.S., 1965. Experimental deformation of serpentinite and its tectonic implications. J. Geophys. Res. 70, 3965–3985. https://doi.org/10.1029/JZ070i016p03965

Ramsay, J.G., Graham, R.H., 1970. Strain variation in shear belts. Can. J. Earth Sci. 7, 786–813. https://doi.org/10.1139/e70-078

Reinen, L.A., Weeks, J.D., Tullis, T.E., 1994. The frictional behavior of lizardite and antigorite serpentinites: Experiments, constitutive models, and implications for natural faults. Pure Appl. Geophys. 143, 317–358. https://doi.org/10.1007/BF00874334

Renard, F., Cordonnier, B., Dysthe, D.K., Boller, E., Tafforeau, P., Rack, A., 2016. A deformation rig for synchrotron microtomography studies of geomaterials under conditions down to 10 km depth in the Earth. J. Synchrotron Radiat. 23, 1030–1034. https://doi.org/10.1107/S1600577516008730

Reuschlé, T., 1998. A network approach to fracture: The effect of heterogeneity and loading conditions. Pure Appl. Geophys. 152, 641–665. https://doi.org/10.1007/s000240050170

Riva, A.F., Rosa, A.D., Clavel, C., Sifre, D., Mathon, O., Garbarino, G., Pascarelli, S., 2018. Heat distribution in Paris–Edinburgh press assemblies through finite element simulations. High Press. Res. 38, 303–324. https://doi.org/10.1080/08957959.2018.1485020

Robinson, P., Terry, M.P., Carswell, T., Roermund, H. Van, Krogh, T.E., Tucker, R.D., Solli, A., 2003. Tectono-stratigraphic setting, structure and petrology of HP and UHP metamorphic rocks and garnet peridotites in the Western Gneiss Region, More and Romsdal, Norway. https://openarchive.ngu.no/ngu-xmlui/handle/11250/2665114

Rumori, C., Mellini, M., Viti, C., 2004. Oriented, non-topotactic olivine serpentine replacement in mesh-textured, serpentinized peridotites. Eur. J. Mineral. 16, 731–741. https://doi.org/10.1127/0935-1221/2004/0016-0731

Scambelluri, M., Cannaò, E., Gilio, M., 2019. The water and fluid-mobile element cycles during serpentinite subduction. A review. Eur. J. Mineral. 31, 405–428. https://doi.org/10.1127/ejm/2019/0031-2842

Schrank, C.E., Handy, M.R., Fusseis, F., 2008. Multiscaling of shear zones and the evolution of the brittle-to-viscous transition in continental crust. J. Geophys. Res. Solid Earth 113, 1407. https://doi.org/10.1029/2006JB004833

Schwartz, S., Guillot, S., Reynard, B., Lafay, R., Debret, B., Nicollet, C., Lanari, P., Auzende, A.L., 2013. Pressure-temperature estimates of the lizardite/antigorite transition in high pressure serpentinites. Lithos 178, 197–210. https://doi.org/10.1016/j.lithos.2012.11.023

Shao, T., Zhou, Y., Song, M., Ma, X., Zhang, L., Yao, W., Dang, J., Li, J., 2021. Deformation of antigorite and its geological implications. J. Geophys. Res. Solid Earth 126, 1–24. https://doi.org/10.1029/2021JB021650

Shea, W.T., Kronenberg, A.K., 1993. Strength and anisotropy of foliated rocks with varied mica contents. J. Struct. Geol. 15, 1097–1121. https://doi.org/10.1016/0191-8141(93)90158-7

Shi, H., Hosdez, J., Rougelot, T., Xie, S., Shao, J., Talandier, J., Lacidogna, G., 2020. Digital volume correlation applied to X-ray micro-tomography images in uniaxial creep tests on anisotropic clayey rock. Appl. Sci. 10, 1–15. https://doi.org/10.3390/app10144898

Shi, H.L., Hosdez, J., Rougelot, T., Xie, S.Y., Shao, J.F., Talandier, J., 2021. Analysis of local creep strain field and cracking process in claystone by X-ray micro-tomography and digital volume correlation. Rock Mech. Rock Eng. 54, 1937–1952. https://doi.org/10.1007/s00603-021-02375-5

Skemer, P., Katayama, I., Jiang, Z., Karato, S.I., 2005. The misorientation index: Development of a new method for calculating the strength of lattice-preferred orientation. Tectonophysics 411, 157–167. https://doi.org/10.1016/j.tecto.2005.08.023

Soda, Y., Takagi, H., 2010. Sequential deformation from serpentinite mylonite to metasomatic rocks along the Sashu Fault, SW Japan. J. Struct. Geol. 32, 792–802. https://doi.org/10.1016/j.jsg.2010.05.003

Soda, Y., Wenk, H.R., 2014. Antigorite crystallographic preferred orientations in serpentinites from Japan. Tectonophysics 615–616, 199–212. https://doi.org/10.1016/j.tecto.2013.12.016

Soleimani, M., Pengpen, T., 2015. Introduction: A brief overview of iterative algorithms in X-ray computed tomography. Philos. Trans. R. Soc. A Math. Phys. Eng. Sci. 373. https://doi.org/10.1098/rsta.2014.0399

Song, S., Cao, Y., 2021. Textures and structures of metamorphic rocks, in: Encyclopedia of Geology. Academic Press, pp. 375–388. https://doi.org/10.1016/b978-0-08-102908-4.00052-7

Stauffer, D., Aharony, A., 2003. Introduction to percolation theory, 2nd editio. ed. Taylor & Francis, London.

Stenvall, C.A., Fagereng, Å., Diener, J.F.A., 2019. Weaker than weakest: On the strength of shear zones. Geophys. Res. Lett. 46, 7404–7413. https://doi.org/10.1029/2019GL083388

Stern, R.J., Gerya, T., 2018. Subduction initiation in nature and models: A review. Tectonophysics 746, 173–198. https://doi.org/10.1016/j.tecto.2017.10.014

Stünitz, H., Tullis, J., 2001. Weakening and strain localization produced by syn-deformational reaction of plagioclase. Int. J. Earth Sci. 90, 136–148. https://doi.org/10.1007/s005310000148

Taconet, O., Ciarletti, V., 2007. Estimating soil roughness indices on a ridge-and-furrow surface using stereo photogrammetry. Soil Tillage Res. 93, 64–76. https://doi.org/10.1016/j.still.2006.03.018

Tarplee, M.F.V., van der Meer, J.J.M., Davis, G.R., 2011. The 3D microscopic "signature" of strain within glacial sediments revealed using X-ray computed microtomography. Quat. Sci. Rev. 30, 3501–3532. https://doi.org/10.1016/j.quascirev.2011.05.016

Thielmann, M., Golabek, G.J., Marquardt, H., 2020. Ferropericlase control of lower mantle rheology: Impact of phase morphology. Geochemistry, Geophys. Geosystems 21.

https://doi.org/10.1029/2019GC008688

Thielmann, M., Kaus, B.J.P., 2012. Shear heating induced lithospheric-scale localization: Does it result in subduction? Earth Planet. Sci. Lett. 359–360, 1–13. https://doi.org/10.1016/j.epsl.2012.10.002

Torquato, S., 2010. Optimal design of heterogeneous materials. Annu. Rev. Mater. Res. 40, 101–129. https://doi.org/10.1146/annurev-matsci-070909-104517

Torquato, S., 2002. Random heterogeneous materials, 1st ed. Springer New York, NY, New York. https://doi.org/10.1007/978-1-4757-6355-3

Torquato, S., Beasley, J.D., Chiew, Y.C., 1988. Two-point cluster function for continuum percolation. J. Chem. Phys. 88, 6540–6547. https://doi.org/10.1063/1.454440

Tulley, C.J., Fagereng, Å., Ujiie, K., Piazolo, S., Tarling, M.S., Mori, Y., 2022. Rheology of naturally deformed antigorite serpentinite: Strain and strain-rate dependence at mantle-wedge conditions. Geophys. Res. Lett. 49. https://doi.org/10.1029/2022gl098945

Turcotte, D.L., Schubert, G., 2002. Geodynamics, 2nd ed. Cambridge University Press. https://doi.org/10.1017/CBO9780511807442

Ulmer, P., Trommsdorff, V., 1995. Serpentine stability to mantle depths and subduction-related magmatism. Science (80-.). 268, 858–861. https://doi.org/10.1126/science.268.5212.858

Van De Moortèle, B., Bezacier, L., Trullenque, G., Reynard, B., 2010. Electron back-scattering diffraction (EBSD) measurements of antigorite lattice-preferred orientations (LPO). J. Microsc. 239, 245–248. https://doi.org/10.1111/j.1365-2818.2010.03398.x

Van Geet, M., Swennen, R., Wevers, M., 2001. Towards 3-D petrography: Application of

microfocus computer tomography in geological science. Comput. Geosci. 27, 1091–1099. https://doi.org/10.1016/S0098-3004(00)00154-0

Viti, C., Collettini, C., Tesei, T., Tarling, M.S., Smith, S.A.F., 2018. Deformation processes, textural evolution and weakening in retrograde serpentinites. Minerals. 8, 241 https://doi.org/10.3390/min8060241

Viti, C., Mellini, M., 1998. Mesh textures and bastites in the Elba retrograde serpentinites. Eur. J. Mineral. 10, 1341–1360. https://doi.org/10.1127/ejm/10/6/1341

Voltolini, M., Barnard, H., Creux, P., Ajo-Franklin, J., 2019. A new mini-triaxial cell for combined high-pressure and high-temperature in situ synchrotron X-ray microtomography experiments up to 400°C and 24 MPa. J. Synchrotron Radiat. 26, 238–243. https://doi.org/10.1107/S1600577518015606

Wang, Y., Lesher, C., Fiquet, G., Rivers, M.L., Nishiyama, N., Siebert, J., Roberts, J., Morard, G., Gaudio, S., Clark, A., Watson, H., Menguy, N., Guyot, F., 2011. In situ high-pressure and high-temperature X-ray microtomographic imaging during large deformation: A new technique for studying mechanical behavior of multiphase composites. Geosphere 7, 40–53. https://doi.org/10.1130/GES00560.1

Wang, Y., Uchida, T., Westferro, F., Rivers, M.L., Nishiyama, N., Gebhardt, J., Lesher, C.E., Sutton, S.R., 2005. High-pressure x-ray tomography microscope: Synchrotron computed microtomography at high pressure and temperature. Rev. Sci. Instrum. 76, 1–7. https://doi.org/10.1063/1.1979477

White, S.H., Burrows, S.E., Carreras, J., Shaw, N.D., Humphreys, F.J., 1980. On mylonites in ductile shear zones. J. Struct. Geol. 2, 175–187. https://doi.org/10.1016/0191-8141(80)90048-6

Williams, D.B., Carter, C.B., 2009. Transmission electron microscopy: A textbook for

materials science. https://doi.org/10.1007/978-0-387-76501-3

Williams, P.F., Price, G.P., 1990. Origin of kinkbands and shear-band cleavage in shear zones: an experimental study. J. Struct. Geol. 12, 145–164. https://doi.org/10.1016/0191-8141(90)90001-F

Yamazaki, D., Karato, S.I., 2001. High-pressure rotational deformation apparatus to 15 GPa. Rev. Sci. Instrum. 72, 4207–4211. https://doi.org/10.1063/1.1412858

Yu, T., Wang, Y., Rivers, M.L., 2016. Imaging in 3D under pressure: a decade of high-pressure X-ray microtomography development at GSECARS. Prog. Earth Planet. Sci. 3. https://doi.org/10.1186/s40645-016-0093-6

List of Figures

anvil twisting angle. (b) Sketch of the theoretical transfer of simple shear strain in a cylindrical sample under torsion showing the simple shear strain calculated in our study. H is the image height (X-ray tomography view). L is the actual height of the sample. r is the radius to the marker location. θ is the measured twisting angle in the sample. Red-dotted arrow shows the observed marker motion (AB) defining the arc length of θ. Red vertical line corresponds to half of the height of the sample

3.6. Workflow overview of the X-ray tomography image processing and analyses using Avizo and Fiji softwares. See text for details.

3.7. Change in the reconstructed X-ray tomography volume with increasing twisting angle (a), theoretical transfer of the strain in a solid cylinder and in the representative volume (RV) (b). Z is the torsion axis. a) Arrows showing presence of rings and shading artifacts. Note the decreasing volume size (decrease in height of the image) with increasing anvil twisting angle due to the gap reduction. Phases in the sample image from brightest to darkest: Garnet (secondary mineral); Pyroxene (or omphacite, Omp; matrix mineral); Quartz (accessory mineral). b) γ is strain. r is radius. Red arrow showing the sense of torsion. Black arrows showing the strain gradient along the radius.

3.8. Comparison between two different thresholding segmentation tools, Interactive and Hysteresis, showing when one works better than the another depending on the image quality and/or presence of artefacts. Scale bar refers to a) and b). a) tomography acquired after twisting where artefacts due to sample movements in the grey-scale image are present. In this case, Hysteresis is used. White arrow

the number of grains. J and M are fabric strength indicators (e.g., Mainprice et al., 2015). The samples numbers (#) are given. γ is the shear strain. εE is the equivalent strain. (Right) inverse pole figures showing rotation axes accommodating low-angle misorientation (from 2° to 10°) across subgrain boundaries, and within subgrains, of olivine. On the bottom-left, the torsion axis (individual black arrow) and the sense of shear (pair of arrows) are given with respect to the pole figures reference frame. 144

List of Tables

Microstructural evolution of polymineralic aggregates deformed under high pressure and temperature: an in-situ and post-mortem study on olivine+serpentine

At plate tectonic boundaries, the lithosphere is deformed and strain localization occurs up to kilometers-scale, which can manifest in form of shear zones. The strain localization suggests the strength of the lithosphere is locally weakened. The formation of interconnected layers of weaker minerals in the lithosphere is a potential mechanism to achieve such weakening. Serpentinized peridotite is commonly found within and between tectonic plates. It is mainly composed of olivine and serpentine minerals. The latter is generally accepted to be weaker than olivine at geological strain rates. During deformation, strain is thus expected to preferentially partition into serpentine than into olivine. This can lead to the formation of interconnected weak layers (IWL) of serpentine where strain localizes.

The present work is based on microstructural investigation to infer the strain accommodation in rocks. Olivine+serpentine aggregates with two compositions (10 and 20 vol.% serpentine) are used as a proxy for partially serpentinized peridotites. The aggregates are experimentally deformed in torsion at high pressures (HP, > 2 GPa) and high temperatures (HT, > 300°C) at an equivalent strain rate of 10^{-4} s^{-1}. The experiments are coupled with in-situ absorption contrast X-ray tomography. I obtain 2D and 3D information on connectivity and structural layering in the microstructure of the 'weak' serpentine. Electron microscopy is performed on recovered samples to link the in-situ X-ray tomography observations to the plastic properties of the phases.

I first outline experimental and image-data processing procedures specific to in-situ HP experimental deformation. Then, I study the deformation of the aggregates with increasing shear deformation at multiple scales of observations. The main aim is to observe the onset and development of IWL in its microstructure. The relations between the morphology and plastic properties of the phases in the rock are investigated to understand the strain localization in serpentinized peridotite.

The main results show the deformation regime in olivine+serpentine aggregates can be described as semi-brittle, with the dominant phase of olivine ('stronger') mainly displaying brittle deformation, whereas the serpentine ('weaker') showing a dominant ductile-style deformation. A strain γ of ca. 4-5, serpentine content of ca. 20 vol.%, and initial fraction of large clusters >15 vol.% determine the condition for IWL configuration in the olivine+serpentine aggregates. Conversely, at serpentine content of ca. 10 vol.%, IWL do not occur, independently of strain or initial clusters size distribution of serpentine. This is more consistent with a load-bearing framework (LBF) behavior, where the stronger olivine grains are jammed, and during deformation crush one another, leading to grain size reduction and accommodating much of the deformation in the rock. These findings suggest contents of serpentine >10 vol.% or ca. 20 vol.% define a threshold for crucial changes in the morphology, connectivity, percolation, of the weak serpentine in serpentinized peridotites under shear. This may lead to important changes in deformation behavior and mechanical properties of the rock.

In light of these findings, I give some perspectives for strain localization and shear zones initiation in the lithosphere.